Acoustical Physics, Vol. 48, No. 5, 2002, pp. 511–517. Translated from Akusticheskiĭ Zhurnal, Vol. 48, No. 5, 2002, pp. 581–588.
Original Russian Text Copyright © 2002 by Alekseev, Rybak.

Equations of State for Viscoelastic Biological Media

V. N. Alekseev and S. A. Rybak
Andreev Acoustics Institute, Russian Academy of Sciences,
ul. Shvernika 4, Moscow, 117036 Russia
e-mail: bvp@akin.ru

Received July 9, 2001

Abstract—Several simple models used for viscoelastic media in medical acoustics are analyzed. New versions of equations of state that obey fundamental principles, namely, the causality principle and the principle of entropy increase, are proposed for viscoelastic substances. *© 2002 MAIK “Nauka/Interperiodica”.*

Acoustic studies of biological tissues are often accompanied by studies of the frequency dependence of sound absorption in them. In the latter case, experimental results are often found to disagree with the theoretical predictions. While the application of some initial equations, such as the equations of motion and continuity, is beyond question, the use of other ones is dubious. The equation of motion of a medium in which sound propagation takes place is in essence the Newtonian equation. It is rather strict and usually represented in the form

$$\rho \ddot{u}_i = \frac{\partial \sigma_{ik}}{\partial x_k}. \tag{1}$$

Here, ρ is the substance density, $u_i(\mathbf{r}, t)$ is the particle displacement in the medium at a given point of space and time, and $\sigma_{ik}(\mathbf{r}, t)$ is the stress (force) that acts upon a given particle of the medium. The continuity equation reflects the law of mass conservation of the substance. In the case of a single-phase medium, it has the simplest form,

$$\frac{\partial \rho}{\partial t} + \operatorname{div}\rho\dot{\mathbf{u}} = 0. \tag{2}$$

The two equations given above are insufficient to derive a wave equation for describing the sound propagation in an arbitrary continuous medium. Commonly, the equation of the substance state, which connects the substance parameters involved in Eqs. (1) and (2), is also used. However, in this case, it turns out that the equation of state of the substance already does not have a universal character and has different forms for different substances. In the case of a strict derivation of this equation, new variables appear, which give rise to a series of new equations. These equations are often not as exact as Eqs. (1) and (2) and, in the general case, have a complex, specifically, integro-differential form. Moreover, these additional equations are often phenomenological and depend on specific processes accompanying the sound propagation. An example is the frequently used equation for the measurement of the internal energy of a unit mass of a substance ε:

$$d\varepsilon = TdS - pd(1/\rho) + \sum_i A_i d\xi_i. \tag{3}$$

As one can see from Eq. (3), it is necessary to know the temperature T and the entropy S, apart from the pressure p and the substance density ρ, in order to describe the substance behavior in the field of a sound wave. Moreover, it may be necessary to know a whole set of additional parameters, A_i and ξ_i, to describe the process. The order parameters and the number of dissociated particles, or new particles resulting from the chemical reactions initiated by sound, can be the parameters ξ_i. In the latter case, the corresponding chemical potentials μ_i can serve as the parameters A_i. A classical example of the additional parameter ξ is just “a physical quantity characterizing the state of the body,” which appears in the relaxation theory of sound absorption by Mandel’shtam and Leontovich [1].

It is important to note the fact that writing down all these additional equations in a general form (especially for absorbing media) leads to the loss of their universal character, and additional assumptions, mainly of a phenomenological character, are needed. In this case, it becomes necessary to formulate some inexact assumptions on the substance behavior in given specific conditions. Such a violation of the strictness and generality of the formulated mathematical relations arises in the relations connecting the substance deformations with the forces acting in the medium. The situation becomes even more complicated because of the fact that one has to employ different approximate formulas for different substances by dividing them into classes. For example, in the case of many substances in the liquid state, the stresses arising in the medium when external forces are applied to it are usually proportional to the rate of deformation change. From practice, it was found that, in the first approximation, the shear deformation in a classical Newtonian liquid does not cause stresses. Physically, this fact is closely connected with the main

1063-7710/02/4805-0511$22.00 © 2002 MAIK “Nauka/Interperiodica”

property of a liquid: its fluidity. Formally, the relation between the stress tensor σ_{ik} and the strain u_i is described by the expression [1]

$$\sigma_{ik} = -p\delta_{ik} + \sigma^1_{ik}, \tag{4}$$

where p is the pressure in the liquid and σ^1_{ik} is the so-called tensor of viscous stress equal to

$$\sigma^1_{ik} = \eta\left(\frac{\partial v_i}{\partial x_k} + \frac{\partial v_k}{\partial x_i} - \frac{2}{3}\delta_{ik}\frac{\partial v_m}{\partial x_m}\right) + \zeta\delta_{ik}\frac{\partial v_m}{\partial x_m}. \tag{5}$$

Here, η and ζ are the coefficients of shear and bulk viscosities and $v_i = du_i/dt$ is the particle velocity of the medium $\mathbf{u}$. In particular, from Eq. (4) it follows that, in the limiting case of an ideal liquid, when viscosity is absent, the Pascal law is valid, in which case the stress in the medium is isotropic.

The situation is different with an ideally elastic solid. If external forces are applied to a solid, the stress σ_{ik} arising within it is proportional to the deformation tensor $S_{ik} = (\partial u_i/\partial x_k + \partial u_k/\partial x_i)/2$ and not to its velocity. This property is described formally by Hooke's law, which, for isotropic solids in the case of small deformations, when $S_{ik} = (\partial u_i/\partial x_k + \partial u_k/\partial x_i)/2$, has the form [2]

$$\sigma^s_{ik} = \mu\left(\frac{\partial u_i}{\partial x_k} + \frac{\partial u_i}{\partial x_k} - \frac{2}{3}\delta_{ik}\frac{\partial u_m}{\partial x_m}\right) + K\delta_{ik}\frac{\partial u_m}{\partial x_m}. \tag{6}$$

Here, μ and K are the shear and bulk moduli connected with the common Young modulus E and Poisson's ratio σ by known relations [2]. In a more general case of crystalline solids, Eq. (6) can be written down in dyad form [3, 4]:

$$\sigma = \lambda : S, \tag{7}$$

where σ and S are the stress and strain tensors of the second rank and λ is the fourth-rank tensor of elasticity moduli.

Unlike fluids, Hooke's law for solids reflects the property of ideal elasticity of a medium, and, in the case of the existence of other restrictions, it is valid, strictly speaking, only in statics. In studying the deformation of elastic bodies, it is commonly assumed that the process is reversible. However, it is known that a process is reversible thermodynamically only in the case when it occurs at an infinitely small rate [5]. In this case, at any given moment, there is enough time for the state of thermodynamic equilibrium to be established. However, real motion occurs with a finite velocity, and, therefore, at any given moment, the solid is not in equilibrium. According to the general laws of thermodynamics, the processes tending to bring it to an equilibrium state occur in a body. The presence of these processes leads to irreversibility of motion, which manifests itself, in particular, in the dissipation of mechanical energy transforming finally into heat. The processes of energy dissipation, which are connected with the finiteness of the velocity of motion, are in essence the processes of internal friction or viscosity. In this case, the equation of motion of an elastic medium can be written as before in the common form of Eq. (1). However, the stress tensor now should be understood as the sum of Eqs. (5) and (6). Thus, we must consider the stress tensor on the right-hand side of Eq. (1) as a quantity that is written in a compact dyad form in the following way [4]:

$$\sigma = \lambda : S + \eta : \partial S/\partial t. \tag{8}$$

Here, η is the fourth-rank tensor of viscous moduli.

In the general case, the majority of real media is characterized by the properties that cannot be described within the framework of simple expressions (4)–(6). Real media can have anomalous and structural viscosity, creep accompanied by stress relaxation, elastic aftereffect, etc. The description of motion of a real continuous medium is the subject of rheology, and one has to select a specific equation of state for each substance class. These equations often have rather complex forms. However, there is a large class of substances that can be described in the linear approximation by a simple combination of the properties indicated above. Such media are, in particular, the biological tissues that we are interested in here. Formally, the stress in them depends on both strain and its derivative with respect to time, and, in some cases, it depends also on the higher order derivatives of strain. Therefore, many real materials are viscoelastic in their nature. It should be noted that the response of such media to applied stress is nonlinear in the general case. Hysteresis phenomena can also exist, but we do not consider these phenomena in this paper.

The existing theory of viscoelasticity is basically phenomenological and used for describing the mechanical properties of many macroscopically homogeneous solids and liquids [6]. The equations describing the deformations and flows of viscoelastic media are rheological. Rheology is applied most successfully in the analysis of mechanical properties, flow, and deformations of various polymers in both the solid phase and solutions [7]. However, in fact, starting from the very first experiments on measuring the sound absorption in biological tissues, researchers assumed that the existing theory of viscoelasticity could be applicable to these media also. For example, the author of one of the first papers on this topic successfully simulated a biological tissue with the help of the Voigt element by using the published data on ultrasonic absorption in tissues [8]. He took into account only one relaxation time for describing these data in the frequency range characteristic of medical applications.

The viscoelastic properties of a medium can be described on a macroscopic scale in many ways using various combinations of the elastic and viscous elements mentioned above. As a rule, these elements are conventionally called springs and dampers, respectively. Quite often, to make rheological equations more illustrative and facilitate their generalization, the method of models is used. The simplest mechanical and electric systems obeying the same differential equations as the simulated process are selected for this purpose. The choice of one or another model is arbitrary. For example, electric models can be recommended for those well acquainted with the techniques of calculation used for electric circuits. However, mechanical models are preferable in our opinion, because they are more illustrative and, what is more important, closer to the processes under investigation. It is natural that a formal description of processes can be performed without modeling, but the latter is traditional for rheology. Moreover, as is stated in many textbooks, with the help of models, it is possible to reveal many properties of a medium without any calculations by using only illustrative geometric images [9]. Therefore, according to tradition, we have to mention the existing illustrative images of mechanical models.

Two approaches known as the Maxwell and Voigt models are most popular in medical acoustics [10]. The Maxwell model is well known in both rheology and classical mechanics of continuous media. Its mechanical analog in the one-dimensional case corresponds to the model consisting of a spring and a piston (damper) connected in series. In the case of such a connection, the same force acts upon both elements and their elongations are summed up. It is precisely this model that is used most often for describing macroscopic properties of such viscoelastic materials as polymers and in medical acoustics.

Initially, the Maxwell model was proposed for describing the motion of highly viscous liquids with motion periods that are long in comparison with molecular times. There are many viscous liquids that behave as solids within small time intervals that are, however, large in comparison with molecular times. On the other hand, many amorphous solids, such as glasses, may be treated as the limiting case of liquids with very high viscosities. Formally, the equation of state for such substances is obtained from a simple assumption about the exponential law of the internal stress decrease with time. Taking into account only shear stress and strain, we can write this equation in the form [2]

$$\frac{\partial\sigma_{ik}}{\partial t}+\frac{1}{\tau}\sigma_{ik} = \mu\frac{\partial}{\partial t}\left(\frac{\partial u_i}{\partial x_k}+\frac{\partial u_k}{\partial x_i}\right), \tag{9}$$

where τ is the so-called Maxwell relaxation time, within which the stress decays and which is equal to $\tau \sim \eta/\mu$ in order of magnitude. A more thorough approach to the substantiation of the relaxation theory is connected with the utilization of the additional parameter ξ involved in Eq. (3). In many cases, the change in the internal energy of the medium under investigation affected by the alternating pressure of an acoustical wave occurs not only on account of the change of the kinetic energy of particles and such parameters as the substance density, but also on the account of excitation of the internal degrees of freedom of individual molecules.

In the Voigt model, each element is subjected to equal deformation and the total force acting upon an element is equal to the sum of the forces acting upon a spring and a damper. A viscoelastic medium can be simulated as in the previous case with the help of a set of Voigt elements. The mechanical analog of the Voigt element corresponds to a parallel connection of a spring and a piston. It is a common opinion that such a model represents the viscoelastic properties of many biological media in a more adequate way. Just formally, the Voigt model is described by common equations of the classical theory of solids, but with allowance for the internal friction. This model is known in rheology as the model of the Kelvin medium [9]. The stress arising in such a medium can be represented in the general form of Eq. (8). Here, we present a specific expression for the stress tensor in the case of isotropic solids:

$$\begin{aligned}\sigma_{ik} &= \left(\mu+\eta\frac{\partial}{\partial t}\right)\left(\frac{\partial u_i}{\partial x_k}+\frac{\partial u_k}{\partial x_i}-\frac{2}{3}\delta_{ik}\frac{\partial u_m}{\partial x_m}\right)\\ &\quad+\left(K+\zeta\frac{\partial}{\partial t}\right)\delta_{ik}\frac{\partial u_m}{\partial x_m}.\end{aligned} \tag{10}$$

Both the Maxwell and Voigt models provide an opportunity to obtain the dispersion relations and determine the frequency dependence for the coefficient of sound attenuation $\alpha(\omega)$ in the viscoelastic medium under consideration. The difference between them is the fact that the Maxwell model predicts a stronger dispersion of sound velocity. In addition, the attenuation coefficient α in the Maxwell model increases at first with the frequency growth and then flattens out. According to the Voigt model, the attenuation progressively increases as the frequency increases. In other words, in the case of the Maxwell model, the quantity α/ω^2 drops to zero when frequency tends to infinity, whereas in the case of the Voigt model, it decreases with the growth of frequency and reaches a certain approximately constant value at high frequencies. In the latter case, the frequency dependence of the sound attenuation coefficient is similar to the curve characterizing the influence of a single equilibrium process with two stable states, which acts in combination with the classical processes caused by viscosity and heat conduction.

It was found that the Maxwell theory is applicable mostly for describing the sound propagation in liquids, while the fact of taking into account additional terms in the shear modulus in the Voigt model makes the latter apparently more suitable for describing biological tissues [10]. From physical considerations, it follows that the relaxation processes in the Maxwell model are frequently connected with the rearrangement of the substance structure. Deformations caused by the effect of external forces evolve. Such processes as molecular rearrangement in the vicinity of each selected particle, the development of dislocations, and the growth of

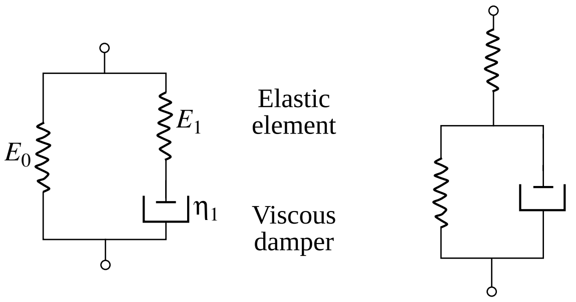

Figure.

cracks in a solid substance take place. Finally, all this leads to an exponential decrease in the internal stress in the medium with time, according to Eq. (9). The dissipative processes in the Voigt model medium are connected mainly with the finiteness of the propagation velocity of interaction forces and are not as strongly connected with the violation of the substance structure. In this connection, we believe that the Maxwell relaxation processes must dominate in liquid-saturated biological tissues and also in many pathological cases when the structure of healthy tissue is destroyed. This fact must manifest itself to the greatest extent when purulent formations appear. In this case, the shift from the Voigt to the Maxwell model must manifest itself more strongly in the low-frequency range.

It is necessary to note that, to describe experimental data correctly, one needs to elaborate simple equations (7)–(10) by combining the Maxwell and Voigt elements and to generalize the corresponding models taking into account the existence of many relaxation times. As we have mentioned before, the model representations help us to proceed in the simplest way to the generalizations and derivations of more complex rheological equations of state. For example, the figure presents two Kelvin models of viscoelastic media whose deformation leads to the Kneser processes [9]. These processes are characterized by the sound prolagation accompanied by the excitation of oscillatory degrees of freedom of the substance in such a way that only a single level is excited, and the role of parameter ξ in Eq. (3) is played by the number of excited molecules. In dyad form, the equation of state that corresponds, e.g., to the model given in the figure on the left has the form

$$\sigma + \tau\dot{\sigma} = (\lambda : S + \eta : \dot{S}) + \tau\lambda : \dot{S}. \tag{11}$$

When longitudinal monochromatic plane waves with frequency ω propagate in a medium with the Kneser relaxation, the use of Eq. (11) leads, as usual, to the renormalization of elastic-viscous moduli. For example, in the scalar version, the employment of Eq. (11) in such media leads to the growth of the imaginary part of the Young modulus according to the rule [9]

$$E = E_0 - \frac{i\omega\eta_1}{1 - i\omega\tau}. \tag{12}$$

We note that the models given in the figure on the left and right are equivalent in their essence and described by the same equations. The difference lies only in the coefficients of the equations, which are expressed through each other being in one-to-one correspondence [9]. In the general case, when we have an arbitrary number of Maxwell relaxation mechanisms, e.g., when excitation of several oscillatory degrees of freedom occurs, the complex modulus is expressed as

$$E = E_0 - i\omega\eta_\infty - \sum_{k=1}^{n} \frac{i\omega\eta_k}{1 - i\omega\tau_k}, \tag{13}$$

where E_0 is the equilibrium Young modulus, η_∞ is the nonrelaxing viscosity, and η_k and $\tau_k = \eta_k/E_k$ are the viscosities and the relaxation times of different mechanisms [9]. The cited monograph [9] gives several more simple generalizations of mechanical models, which were proposed, e.g., by Frenkel' and Obraztsov.

We note that, from the purely mathematical point of view, Eqs. (8), (10), and (11) are different linear combinations of stress and strain tensors, σ_{ik} and u_{ik}, with their first derivatives with respect to time, σ_{ik} and u_{ik}. In this connection, Oldroid suggested a generalized model of a viscoelastic medium, where the linear dependence between the quantities σ_{ik}, $\dot{\sigma}_{ik}$, u_{ik}, and $\dot{u}_{ik}$ was taken into account in the most general form [7]. Using this generalized model, we give here a somewhat modified notation for the equation obtained by Oldroid for isotropic bodies:

$$\begin{aligned}\sigma_{ik} + \tau_1\frac{\partial\sigma_{ik}}{\partial t} &= \mu\left(1 + \tau_2\frac{d}{dt}\right)\left(\frac{\partial u_i}{\partial x_k} + \frac{\partial u_k}{\partial x_i} - \frac{2}{3}\delta_{ik}\frac{\partial u_m}{\partial x_m}\right)\\ &\quad + K\left(1 + \tau_3\frac{\partial}{\partial t}\right)\delta_{ik}\frac{\partial u_m}{\partial x_m},\end{aligned} \tag{14}$$

where τ_1, τ_2, and τ_3 are different relaxation times. Note that, when all times τ_1, τ_2, and τ_3 are equal to zero, Eq. (14) is reduced identically to the classical Hooke equation. When $\tau_2 \neq 0$ and $\tau_3 \neq 0$ but $\tau_1 = 0$, Eqs. (1) and (14) describe the dynamics of a common elastic solid with allowance for the internal friction, i.e., the Kelvin–Voigt model of the medium. In this case, the quantities $\eta = \mu\tau_2$ and $\zeta = K\tau_3$ play the role of the friction coefficients analogous to those used in the theory of viscous liquids [2]. In another limiting case, when $\tau_2 = \tau_3 = 0$ and $\tau_1 \neq 0$, Eq. (14) describes viscoelastic media in the framework of the Maxwell model. In the case of a periodic motion, when the quantities σ_{ik} and u_{ik} depend on time through the factor $\exp(-i\omega t)$, Eq. (14) is formally equivalent to the common Eq. (5), i.e., Hooke's law, but with the complex moduli K and μ. In this case, the quantities K and μ acquire imaginary components that lead to the damping of periodic movements. In this case, the renormalized moduli have the form

$$K \longrightarrow K\frac{1-i\omega\tau_3}{1-i\omega\tau_1}; \quad \mu \longrightarrow \mu\frac{1-i\omega\tau_2}{1-i\omega\tau_1}. \tag{15}$$

The description of the viscoelastic properties of solids by simply adding imaginary components to elastic moduli is widespread. However, Eqs. (15) give specific frequency dependences of the real and imaginary parts of the moduli. A simple analysis of Eqs. (15) shows that, in many cases, and precisely, when the inequalities $\tau_1 > \tau_2$ or $\tau_1 > \tau_3$ are valid, the imaginary parts of elastic moduli become positive, which contradicts the fundamental principles of thermodynamics. The change of the signs of the imaginary parts of the moduli leads to an increase in the amplitude of periodic oscillations and a decrease in the entropy in a closed system. According to this conclusion, the form of Eq. (14) is incorrect. The model of a medium with Kneser relaxation correctly takes into account the principle of entropy increase, but it is not the only one satisfying the basic principles and the causality principle in particular. It is possible to propose one more correct form for the linear combinations of the quantities σ_{ik}, $\dot{\sigma}_{ik}$, u_{ik}, and $\dot{u}_{ik}$ that satisfies general physical principles. In the most general form, an analog of the equation of state for a substance with one relaxation time can be written in dyad form in the following way:

$$\sigma + \tau\frac{\partial\sigma}{\partial t} = \tau\frac{\partial}{\partial t}\left(\lambda : S + \eta : \frac{\partial S}{\partial t}\right). \tag{16}$$

For an isotropic body, this equation takes the form

$$\frac{\partial\sigma_{ik}}{\partial t} + \frac{1}{\tau}\sigma_{ik} = \frac{\partial}{\partial t}\left[\left(\mu + \eta\frac{\partial}{\partial t}\right)\left(\frac{\partial u_i}{\partial x_k} + \frac{\partial u_k}{\partial x_i} - \frac{2}{3}\delta_{ik}\frac{\partial u_m}{\partial x_m}\right) + \delta_{ik}\left(K + \zeta\frac{\partial}{\partial t}\right)\frac{\partial u_m}{\partial x_m}\right]. \tag{17}$$

One can see that the renormalization of the elastic moduli in the case of periodic motion is now performed according to the rule

$$K \longrightarrow K\frac{1-i\omega\zeta/K}{1+i/\omega\tau}; \quad \mu \longrightarrow \mu\frac{1-i\omega\eta/\mu}{1+i/\omega\tau}. \tag{18}$$

The quantity τ coincides here with the Maxwell relaxation time involved in Eq. (9), and it is equal in order of magnitude to the ratio between the shear viscosity η and the shear modulus μ. One can see that, in contrast to Eqs. (15), the imaginary parts of the elastic moduli determined by Eq. (18) are always negative, and, therefore, they never lead to a buildup of oscillations.

As for the substantiation of the newly obtained equations of state that are given above, it is necessary to mention briefly the known dispersion relations. The formulas that establish a connection between the real and imaginary parts of certain analytical functions are often met in various fields of physics. Such formulas are called dispersion relations. The mathematical apparatus of dispersion relations is always the same; i.e., it is the theory of the functions of complex variables, including the Cauchy theory on integration in the complex plane. The physical basis of the dispersion relations is represented by the causality conditions, which must be formulated for every separate problem. We do not repeat here the theory foundations and give its results. We present only several references to the latest studies in this field, as applicable to the mechanics of continuous media [14–16], and make several remarks concerning the problem. In the linear case, when the superposition principle is valid, it is possible to represent the relation between stress and strain in the following most general form:

$$\sigma(t) = \int_0^{\infty} d\tau K_1(\tau) : S(t-\tau). \tag{19}$$

When the strain is the “initial signal” and the resulting stress is “the response,” the integration over time from zero to infinity in Eq. (19) is the mathematical expression of the causality principle. When the kernel $K_1(\tau)$ of the integrand in Eq. (19) is a sharper function than the slowly varying strain function, the function $S(t-\tau)$ can be expanded into the Taylor series in the vicinity of the point $\tau = 0$:

$$S(t-\tau) \approx S(t) - \tau\frac{\partial S}{\partial t} + \frac{(-\tau)^2}{2!}\frac{\partial^2 S}{\partial t^2} + \dots. \tag{20}$$

Substituting Eq. (20) into Eq. (19), we obtain Hooke’s law in the zero approximation, and, in the first approximation, we obtain the equations of state for the Voigt and Kelvin media. Basically, as in the case of the Oldroid approach, it is possible to represent also the left-hand side of Eq. (19) in a form analogous to the right-hand side of the equation with a new kernel $K_2(\tau)$. The corresponding Taylor series expansion finally leads to the general Oldroid equation. However, as we have seen before, in this case, the general principle of entropy increase can be violated, and the sound amplification can be observed instead of its natural absorption. The finiteness of the physical quantities is an important factor in the derivation of the dispersion relations. For example, in the case of Eq. (19), this condition requires that the Fourier image of the kernel $K_1(\omega)$ must not have poles in the upper complex half plane. This fact makes the set of analytical functions narrower by imposing additional restrictions concerning the singularities. In a more general case of the medium description using the kernels $K_1(\tau)$ and $K_2(\tau)$, additional conditions that determine the analytical behavior of the Fourier images of the kernels are necessary.

According to [4, 14], in many cases the losses taken from the measurements of infrasonic and ultrasonic absorption in viscoelastic media are characterized by a simple frequency dependence. In this case, the coefficient of sound attenuation $\alpha = \mathrm{Im}\,k$ characterizing the propagation of a plane monochromatic wave $\exp(i\mathbf{kr} - i\omega t)$ in such media obeys a power law in a very wide range of ω:

$$\alpha(\omega) = \alpha_0 + \alpha|\omega|^y, \tag{21}$$

where y is a positive number, usually smaller than two, and $\alpha_0 \approx 0$ in most cases. In particular, many biological tissues obey this law. For example, in the case of bovine liver, the law given by Eq. (21) is valid in a rather wide frequency range, from 1 to 100 MHz, with the power index equal to $y = 1.3$ [11]. As more precise measurements have shown, many biological tissues that were initially described in the framework of the Voigt model also obey the power law given by Eq. (21) with $1 \le y \le 2$ [12, 13].

A new modification of the equation of state was proposed in [4, 14] for describing the power dependence of acoustic losses on frequency in the viscoelastic media under consideration. The replacement of a viscous damper in the Voigt element by a new formation, namely, the time convolution operator $r(S, t)$, formed the basis of the new approach using the so-called "causal-time" model. As a result of the proposed procedure, Eq. (8) was written down in the following symbolic form [4, 14]:

$$\sigma = \lambda : S + \eta : r(S, t). \tag{22}$$

In this case, it turned out that the convolution operator has different forms, depending on whether the power index y in Eq. (21) is an integer or noninteger, an even or uneven number. For example, in the case of an even number, the modification of Hooke's law now has the form [4, 14]

$$\sigma(t) = \lambda : S(t) - (-1)^{y/2}\eta : \frac{\partial^{y-1}S(t)}{\partial t^{y-1}}. \tag{23}$$

Note that, in the particular case of $y = 2$, Eq. (23) is reduced to Eq. (8), which describes viscoelastic media in the framework of the Voigt model.

When the power index y in Eq. (21) is an uneven number, the equation of state takes the following form [4, 14]:

$$\begin{aligned}\sigma(t) &= \lambda : S(t)\\ &+ 2\eta : \left[(y-1)!(-1)^{(y+1)/2}\frac{H(t)}{\pi t^y}S(t)\right],\end{aligned} \tag{24}$$

where $H(t)$ is the step function (the Heaviside function). Equation (22) takes a simpler form in the very important case when the power index is equal to unity:

$$\sigma(t) = \lambda : S(t) + 2\eta\left[\frac{H(t)}{\pi t}S(t)\right]. \tag{25}$$

Finally, when the power index y in the law given by Eq. (21) is a noninteger, the equation of state is represented as [4, 14]

$$\sigma(t) = \lambda : S(t) - 2\eta : \left[\Gamma(y\sin(\pi y))\frac{H(t)}{\pi|t|^y}S(t)\right], \tag{26}$$

where $\Gamma(y)$ is the gamma-function.

A more detailed description of the properties of the causal-time model given above can be found in [4, 14]. Here, we should note that, in the low-frequency approximation, this model, being more comprehensive and described by Eq. (22), is in fact reduced to the Voigt model. In connection with this model, we suggest ways for further generalization with the consideration of such phenomena as the stress relaxation in the media of interest. This is possible by replacing the viscous damper $\eta : \partial S/\partial t$ in all equations given above by the convolution operator $\eta : r(S, t)$. For example, Eq. (16) proposed by us can be generalized by representing it in the form

$$\sigma + \tau\frac{\partial\sigma}{\partial t} = \tau\frac{\partial}{\partial t}[\lambda : S + \eta : r(S, t)]. \tag{27}$$

The inclusion of the power dependence of acoustic losses in media with Kneser relaxation is possible with the modified Eq. (11), which is represented in the form

$$\sigma + \tau\dot{\sigma} = [\lambda : S + \eta : r(S, t)] + \tau\lambda : \dot{S}. \tag{28}$$

In conclusion, we note that, according to the figurative expression by Morse and Feschbach, which is given in their well-known monograph [17], the exact laws of nature possibly may not fit the Procrustean bed of common integro-differential equations. Probably, this was precisely the reason why the authors of the cited papers [4, 14] had to introduce fractional derivatives. However, in our opinion, the exact description of the phenomena under consideration most probably cannot be reduced to a single differential equation, but they must be described in the framework of a system of integro-differential equations.

ACKNOWLEDGMENTS

This work was supported in part by the Russian Foundation for Basic Research, project nos. 99-02-16161 and 00-02-17855.

REFERENCES

1. L. D. Landau and E. M. Lifshits, *Course of Theoretical Physics*, Vol. 6: *Fluid Mechanics*, 4th ed. (Nauka, Moscow, 1988; Pergamon, New York, 1987).
2. L. D. Landau and E. M. Lifshits, *Course of Theoretical Physics*, Vol. 7: *Theory of Elasticity*, 4th ed. (Nauka, Moscow, 1987; Pergamon, New York, 1986).

3. B. A. Auld, *Acoustic Fields and Waves in Solids*, 2nd ed. (R. E. Krieger, Malabar, Fla, 1990), Vol. 1, Chap. 3.
4. T. L. Szabo and J. Wu, J. Acoust. Soc. Am. **107**, 2437 (2000).
5. L. D. Landau and E. M. Lifshits, *Statistical Physics*, 3rd ed. (Nauka, Moscow, 1976; Pergamon, Oxford, 1980), Part 1.
6. R. M. Christensen, *Theory of Viscoelasticity* (Academic, New York, 1971), p. 346.
7. S. P. Levitskiĭ and Z. P. Shul'man, *Dynamics and Heat Transfer of Bubbles in Polymer Liquids* (Navuka i Tekhnika, Minsk, 1990), p. 268.
8. A. S. Ahuja, Ultrason. Imaging **1**, 136 (1979).
9. I. G. Mikhaĭlov, V. A. Solov'ev, and Yu. P. Syrnikov, *Principles of Molecular Acoustics* (Nauka, Moscow, 1964), p. 312.
10. *Physical Principles of Medical Ultrasonics*, Ed. by C. R. Hill (Ellis Horwood, Chichester, 1986; Mir, Moscow, 1989).
11. J. D. Polhammer, C. A. Edwards, and W. D. O'Brien, Med. Phys. **6**, 692 (1981).
12. N. Kudo, T. Kamataki, K. Yamamoto, *et al.*, in *Proceedings of IEEE Ultrasonic Symposium* (1997), p. 1181.
13. F. A. Duck, *Physical Properties of Tissue* (Academic, New York, 1990), p. 436.
14. T. L. Szabo, J. Acoust. Soc. Am. **97**, 14 (1995).
15. M. O'Donnell, E. T. Jaynes, and J. G. Miller, J. Acoust. Soc. Am. **69**, 696 (1981).
16. T. L. Szabo, J. Acoust. Soc. Am. **96**, 491 (1994).
17. P. M. Morse and H. Feshbach, *Methods of Theoretical Physics* (McGraw-Hill, New York, 1953; Inostrannaya Literatura, Moscow, 1960), Vol. 2.

Translated by M. Lyamshev

Acoustical Physics, Vol. 48, No. 5, 2002, pp. 518–523. Translated from Akusticheskiĭ Zhurnal, Vol. 48, No. 5, 2002, pp. 589–595.
Original Russian Text Copyright © 2002 by Bardyshev.

Acoustic and Combined Methods for Measuring the Levels of Two-Layer Liquids

V. I. Bardyshev
Andreev Acoustics Institute, Russian Academy of Sciences, ul. Shvernika 4, Moscow, 117036 Russia
e-mail: bvp@akin.ru

Received May 30, 2000

Abstract—Methods for the simultaneous measurement of the levels of light and heavy liquid phases in a tank by using electroacoustic transducers, temperature sensors, and hydrostatic pressure gauges are considered. According to the calculations, the measurement of the levels of, e.g., oil, petroleum products, and underlying water is possible with relative standard errors of the order of 0.1–1%. *© 2002 MAIK “Nauka/Interperiodica”.*

Acoustic echo sounding instruments for measuring the levels of liquids in industrial tanks (level meters) are in many cases preferable to level meters using other physical principles (such as float-type, hydrostatic-pressure, capacitance, radar, and optical devices) in a number of technical, operating, and economical characteristics [1]. A study of the accumulated experience and the multipurpose analytical, prognostic, production-related, and patent investigations in countries leading the field of level meter development (Russia, CIS countries, USA, Germany, Great Britain, France, Japan) allows one to conclude that acoustic level meters are most promising, at least for the next 15–20 years [1–5]. They are widely used, in particular, in the oil industry [6]. In Russia, the mass production of echo sounding level meters based on the acoustic signal propagation in air (Ékho-5 [7]) and in liquid (Korvet [8]) is under way. In recent papers, particular attention is given to the accuracy of acoustic level meters [4, 5, 9–11].

The papers cited describe methods for measuring the upper level of a liquid. Below, we consider methods for the simultaneous measurement of the levels or volumes of two immiscible liquid components (phases) of different densities, such as water and oil or a liquid petroleum product (PP). Usually, a PP contains fresh water impurity accumulated at the bottom of a tank during the storage. For determining the quantity of PP in a tank, it is necessary to measure the upper layer of liquid and the position of the interface between the phases. We consider five methods of such measurements that can be easily realized: the hydroacoustic (acoustic signals propagate in liquid), aerohydroacoustic (acoustic signals propagate in gaseous and liquid media), aerohydroacoustic with reference channels for measuring the sound velocity, two-signal aerohydroacoustic (using an echo signal reflected from the surface of the liquid and a signal penetrating into the liquid), and acoustohydrostatic (echo sounding is supplemented with hydrostatic pressure measurement) methods. The first four methods can be used when a distinct interface is available, and the fifth method can be used both with and without the interface, with intermixed liquid phases. These methods differ in the conditions of their application and in measurement accuracy, the calculations of which are presented below.

Level meters that, in addition to acoustic transducers, contain sensors for measuring other physical parameters, e.g., pressure transducers, can be called combined level meters.

In the calculations, we use the following model of a tank. A plane-parallel layer of a light liquid phase of thickness z_1 and density ρ_1 in which the sound velocity is c_1 and temperature T lies on a layer of a heavy liquid phase with the parameters z_2, ρ_2, c_2, and T. The interface is a horizontal plane. The space above the surface of the liquid is occupied by air with the parameters z_3, ρ_3, c_3, and T_3. The level of the liquid is $h = z_1 + z_2$, and the height of the tank is $l = z_1 + z_2 + z_3$ (Fig. 1).

Under these conditions, we consider the accuracy of the known hydroacoustic method that uses pulsed sounding signals and echo signals reflected from the boundaries of the layers, all the signals propagating in the liquid.

The conditions of realization of this method are as follows: $\rho_2 > \rho_1 > \rho_3$ (condition of the phase separation) and $\rho_1 c_1 \neq \rho_2 c_2 \neq \rho_3 c_3$ (condition of the reflection of sound from the layer boundaries). A directional reversible electroacoustic transducer positioned at the bottom of the tank emits a sounding pulse in the upward direction and receives the echo signals reflected from the surface of the liquid and from the interface with the time delays t_1 and t_2, respectively. To increase the reliability and for convenience, the transducer may be fixed at the outer surface of the tank bottom with the transmission and reception of pulses through the bottom, as is done in the Korvet level meter [8].

The coefficients of reflection K and transmission W of the amplitude of a plane sound wave normally incident on the layer boundary are described by Fresnel formulas

$$K = \frac{\rho_1 c_1 - \rho_2 c_2}{\rho_1 c_1 + \rho_2 c_2}, \qquad (1)$$

$$W = \frac{2\rho_1 c_1}{\rho_1 c_1 + \rho_2 c_2}, \qquad (2)$$

where the parameters with the subscript 2 refer to the medium from which the wave is incident on the boundary.

At the temperature $T = +20°C$ (the temperature throughout this paper is measured in degrees Celsius), for light PP, we have $\rho_1 \approx 600–900$ kg/m^3, $c_1 \approx 1100–1500$ m/s, and $\rho_1 c_1 \approx 6.6 \times 10^5–1.35 \times 10^6$ kg/m^2 s; for fresh water, $\rho_2 = 998$ kg/m^3, $c_2 = 1480$ m/s, and $\rho_2 c_2 = 1.48 \times 10^6$ kg/m^2 s; and for air, $\rho_3 = 1.2$ kg/m^3, $c_3 = 343.5$ m/s, and $\rho_3 c_3 = 412$ kg/m^2 s. Since $\rho_1 c_1 \gg \rho_3 c_3$, for the reflection from the liquid surface, we have $|K| \approx 1$. For some sorts of oil at $T < 10°C$, the relation $\rho_1 c_1 \approx \rho_2 c_2$ takes place, the echo signal from the interface is absent, and only h can be measured. Below, we consider the case when $\rho_1 c_1 \neq \rho_2 c_2$ and the echo signals from the liquid surface and the interface considerably exceed the noise level.

Solving the set of equations

$$t_1 = \frac{2z_1}{c_1} + \frac{2z_2}{c_2}, \quad t_2 = 2z_2/c_2, \quad z_1 = 1 + z_2 = h, \qquad (3)$$

we obtain

$$z_1 = (t_1 - t_2)c_1/2, \quad z_2 = t_2 c_2/2,$$
$$h = \frac{1}{2}[(t_1 - t_2)c_1 + t_2 c_2]. \qquad (4)$$

Let the values of c_1 and c_2 be known with the standard random errors σc_1 and σc_2, the values of t_1 and t_2 be measured with the standard errors σt_1 and σt_2, and let these errors be independent. Then, the standard error in determining z_1 is

$$\sigma z_1 = \left[\left(\frac{\partial z_1}{\partial t_1}\sigma t_1\right)^2 + \left(\frac{\partial z_1}{\partial t_2}\sigma t_2\right)^2 + \left(\frac{\partial z_1}{\partial c_1}\sigma c_1\right)^2 + \left(\frac{\partial z_1}{\partial c_2}\sigma c_2\right)^2\right]^{1/2}. \qquad (5)$$

The standard errors σz_2 and σh are calculated similarly.

By using Eqs. (3)–(5), we obtain

$$\sigma z_1 = \frac{1}{2}\left\{c_1^2[(\sigma t_1)^2 + (\sigma t_2)^2] + 4\left(\frac{z_1}{c_1}\sigma c_1\right)^2\right\}^{1/2}, \qquad (6)$$

$$\sigma z_2 = \frac{1}{2}\left[(c_2 \sigma t_2)^2 + 4\left(\frac{z_2}{c_2}\sigma c_2\right)^2\right]^{1/2}, \qquad (7)$$

$$\sigma h = \frac{1}{2}\left\{(c_1 \sigma t_1)^2 + [(c_2 - c_1)\sigma t_2]^2 + 4\left[\left(\frac{z_1}{c_1}\sigma c_1\right)^2 + \left(\frac{z_2}{c_2}\sigma c_2\right)^2\right]\right\}^{1/2}. \qquad (8)$$

Consider an example of the numerical estimation of the accuracy of the hydroacoustic method for the following conditions: $l = 12$ m, $z_1 = 8$ m, and $z_2 = z_3 = 2$ m. The velocity of sound in liquid depends on its temperature T, and this dependence is known. The phases of the liquid are Russian crude oil or light petroleum products obtained from it and fresh water. The empirical dependence $c_1(T)$ for PP is described by the expression

$$c_1(T) = c_{01}(1 + b_1 T). \qquad (9)$$

The empirical values of the coefficients c_{01} and b_1 for Russian PP in the temperature range 5–40°C were obtained by the least-squares method from the data reported in [14], and these values are presented in Table 1.

For fresh water, according to [15], we have

$$c_2(T) = 1410 + 4.21T - 0.037T^2 + 0.0175H, \qquad (10)$$

where $c_2(T)$ is measured in meters per second and H is the depth of the point of measurement in meters.

For $0 < T \leq 20°C$ and $H < 10$ m with an error of no more than 1%, for water one can use approximate expression (9) with the coefficients $c_{02} = 1410$ m/s and $b_2 = 2.99 \times 10^{-3}$ deg^{-1}. The plots of the functions $c(T)$ for PP and fresh water are shown in Fig. 2.

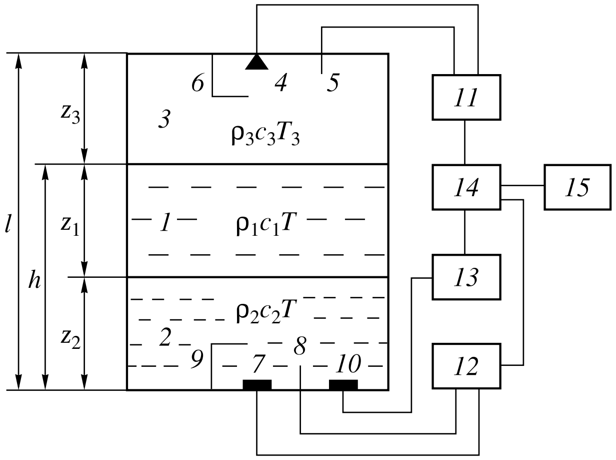

Fig. 1. Simplified block diagram of instrumentation: (*1*) light liquid phase (PP), (*2*) heavy liquid phase (water), (*3*) air space, (*4*) upper reversible electroacoustic transducer, (*5*) air temperature sensor, (*6*) reference reflector of the upper electroacoustic transducer, (*7*) bottom reversible electroacoustic transducer, (*8*) liquid temperature sensor, (*9*) reference reflector of the bottom electroacoustic transducer, (*10*) hydrostatic pressure gauge, (*11*) electronic unit of the upper transducers, (*12, 13*) electronic units of the bottom transducers, (*14*) processor, and (*15*) indicator.

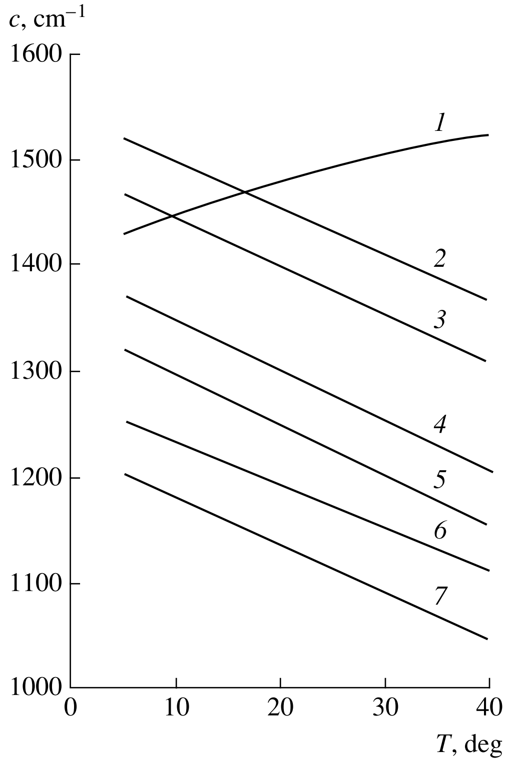

Fig. 2. Dependence of the sound velocity on temperature for the following liquids: (*1*) fresh water, (*2*) oil, (*3*) diesel fuel, (*4*) kerosene, (*5*) AI-95 gasoline, (*6*) AI-92 gasoline, and (*7*) rubber solvent.

Let a piezoceramic element with flexural vibrations, similar to the AP-6 transducer of the Ékho-5 level meter [7], with an effective frequency band $\Delta f = 6$ kHz be used as an electroacoustic transducer. For a signal with a known carrier frequency and a random phase, the standard error of the delay measurement is $\sigma t \approx 1/q\Delta f$, where q is the amplitude signal-to-noise ratio [16]. For $q = 10$ and $\Delta f = 6000$ Hz, we have $\sigma t = 1.6 \times 10^{-5}$ s. Let the temperature of the liquid be measured by a mass-production copper resistance sensor with the standard error $\sigma T = 0.2$°C [17]. This type of sensor is conventionally used for monitoring the temperature in PP storage tanks.

Table 1

PP	c_{01}, m/s	$b_1 \times 10^3$, deg^{-1}
Crude oil	1542	–2.90
Diesel fuel	1490	–3.08
Kerosene	1398	–3.48
AI-95 gasoline	1343	–3.54
AI-92 gasoline	1276	–3.23
Rubber solvent	1250	–4.07

With the dependences $c_1(T)$ and $c_2(T)$ in the form of Eq. (9), for the hydroacoustic method we obtain

$$\sigma z_1(T) = \frac{1}{2}\left\{c_1^2(T)[(\sigma t_1)^2 + (\sigma t_2)^2] + 4\left[\frac{z_1}{c_1(T)}c_{01}b_1\sigma T\right]^2\right\}^{1/2}, \quad (11)$$

$$\sigma z_2(T) = \frac{1}{2}\left\{[c_2(T)\sigma t_2]^2 + 4\left[\frac{z_2}{c_2(T)}c_{02}b_2\sigma T\right]^2\right\}, \quad (12)$$

$$\sigma h(T) = \frac{1}{2}\left\{[c_1(T)\sigma t_1]^2 + [c_2(T) - c_1(T)]^2(\sigma t_2)^2 + 4\left(\frac{z_1 b_1}{1 + b_1 T} + \frac{z_2 b_2}{1 + b_1 T}\right)^2(\sigma T)^2\right\}^{1/2}. \quad (13)$$

According to these expressions, at $T = 20$°C, we have $\sigma z_2 = 1.3$ cm; the values of σz_1 and σh are given in Table 2.

Tests carried out in the laboratory and in tanks of petroleum plants confirmed the efficiency of the hydroacoustic method [18, 19]. The accuracy of echo sounding was near to the calculated estimates shown in Table 2.

The sound velocity in oil depends on its composition and temperature. For PP of a known composition, the dependence $c_1(T)$ can be measured or calculated as in [12] for a three-component liquid. The presence of water impurity and dissolved gases in PP changes this dependence and may lead to an increase in error. The aerohydroacoustic method, which does not require data on c_1, is free from this drawback. The conditions of its realization are as for the previous method. In addition to the bottom electroacoustic transducer, an upper transducer is mounted on the tank's ceiling that emits acoustic pulses in the downward direction and receives the echo signals from the liquid surface with a delay t_3. Then,

$$h = l - 2c_3/t_3, \quad z_2 = 2c_2/t_2, \quad z_1 = h - z_2, \quad (14)$$

$$\sigma h = \sigma z_3 = \frac{1}{2}[(c_3\sigma t_3) + 4(z_3\sigma c_3/c_3)^2]^{1/2}, \quad (15)$$

$$\sigma z_1 = [(\sigma h)^2 + (\sigma z_2)^2]^{1/2}, \quad (16)$$

and σz_2 is estimated by Eq. (7).

Introducing temperature sensors in the air space and in the liquid, one can use the dependences $c_2(T)$ and $c_3(T)$ known for fresh water and air. For the upper and bottom transducers not to interfere with each other, their signals should be separated in frequency or time.

Let us assume that the dependence $c_3(T_3)$ in the air space of the tank is described by the formula (see, e.g., [3])

$$c_3(T_3) = 20.067(T_3 + 273)^{1/2}. \tag{17}$$

For $|T| < 50°\mathrm{C}$ with an error not exceeding 1%, one can use the approximate expression

$$c_3(T_3) = c_{03}(1 + b_3 T_3), \tag{18}$$

where $c_{03} = 331.6$ m/s and $b_3 = 1.83 \times 10^{-3}$ deg^{-1}.

Let the temperature of both liquid and air be measured by copper resistance sensors with the independent standard errors $\sigma T = \sigma T_3 = 0.2°\mathrm{C}$. According to Eqs. (15) and (18), we obtain

$$\sigma h(T_3) = \frac{1}{2}\left\{[c_3(T_3)\sigma t_3]^2 + 4\left[\frac{z_3 b_3 \sigma T_3}{1 + b_3 T_3}\right]^2\right\}^{1/2}. \tag{19}$$

The values of σz_2 and σz_1 are estimated by Eqs. (12) and (16). Under the above conditions and at $T_3 = 20°\mathrm{C}$, we obtain $\sigma h = 2.8$ mm and $\sigma z_1 \approx \sigma z_2 = 1.3$ cm.

If the values of c_2 and c_3 are not known, one should use the aerohydroacoustic method with reference channels. In this case, the level meter is supplemented with devices for measuring the sound velocity (reference channels [3] or reference resonators [9]). In the simplest case, the reference channels are realized by mounting reference reflectors at fixed distances z_{r2} and z_{r3} from the electroacoustic transducers (see Fig. 1), and the time intervals t_{r2} and t_{r3} between the instants of the transmission of sounding signals and reception of echo signals from the reflectors are measured. The reflectors intersect part of the acoustic beam retaining the possibility for receiving the echo signals from the media boundaries. In this case, we have

$$z_2 = z_{r2}t_2/t_{r2}, \quad h = l - z_{r3}t_3/t_{r3}, \quad z_1 = h - z_2, \tag{20}$$

$$\begin{aligned}\sigma z_2 &= \frac{c_2}{2}\left[(\sigma t_2)^2 + \left(\frac{z_2}{z_{r2}}\sigma t_{r2}\right)^2\right]^{1/2} \\ &= \left[\left(z_{r2}\frac{\sigma t_2}{t_{r2}}\right)^2 + \left(z_2\frac{\sigma t_{r2}}{t_{r2}}\right)^2\right]^{1/2},\end{aligned} \tag{21}$$

$$\begin{aligned}\sigma h &= \frac{c_3}{2}\left[(\sigma t_3)^2 + \left(\frac{z_3}{z_{r3}}\sigma t_{r3}\right)^2\right]^{1/2} \\ &= \left[\left(z_{k3}\frac{\sigma t_3}{t_{r3}}\right)^2 + \left(z_3\frac{\sigma t_{r3}}{t_{r3}}\right)^2\right]^{1/2},\end{aligned} \tag{22}$$

and σz_1 is calculated by Eq. (16).

For $z_{r2} = z_{r3} = 0.5$ m, $\sigma t_{r2} = \sigma t_{r3} = 1.6 \times 10^{-5}$ s, and, under the above conditions, from Eqs. (16), (21), and (22) we obtain $\sigma z_1 = 2.8$ cm, $\sigma z_2 = 2.7$ cm, and $\sigma h = 6$ mm. The measurement accuracy can be increased by using shorter high-frequency sounding pulses. In our example, the reference channels provide the measurement of the sound velocity with the relative standard errors $\sigma c_2/c_2 = c_2\sigma t_{r2}/2z_{r2} = 2.4 \times 10^{-2}$ in water and $\sigma c_3/c_3 = 5.5 \times 10^{-3}$ in air. At the same time, hydroacoustic meters using short transmitted pulses at frequencies of about 10^6 Hz and reference bases made of Invar make it possible to measure the sound velocity in water with the relative error $\Delta c/c \approx 6.1 \times 10^{-5}$ [13, 20].

Table 2

PP	σz_1, cm	σh, cm
Oil	1.6	1.2
Diesel fuel	1.6	1.2
Kerosene	1.5	1.1
AI-95 gasoline	1.4	1.1
AI-92 gasoline	1.4	1.1
Rubber solvent	1.3	1.1

If the liquid phases have equal acoustic resistances, no reflection from the interface takes place and the methods considered above are unsuitable for its sounding. In this case, a two-signal aerohydroacoustic method can be used. The conditions of its realization are as follows: $\rho_2 > \rho_1 > \rho_3$, $\rho_1 c_1 \neq \rho_3 c_3$, $c_1 \neq c_2$.

The upper electroacoustic transducer emits a sounding pulse and receives the echo signal from the liquid surface, which provides the measurement of h. The pulse penetrates into the liquid and is received by the bottom transducer with the delay t_2. The coefficients of transmission of the pulse amplitude through the liquid surface, W_{31}, and through the interface, W_{12}, exceed unity. For $\rho_1 c_1 \gg \rho_3 c_3$ and $\rho_2 c_2 \gtrsim \rho_1 c_1$, according to Eq. (2), we have $W_{31} \approx 2$ and $W_{12} \geqslant 1$.

Solving the set of equations

$$\begin{gathered} t_3 = 2z_3/c_3, \quad t_2 = \frac{z_1}{c_1} + \frac{z_2}{c_2} + \frac{z_3}{c_3}, \\ z_1 + z_2 + z_3 = l, \end{gathered} \tag{23}$$

we obtain

$$z_1 = \frac{c_1 c_2}{|c_2 - c_1|}\left[t_2 - \frac{2l + (c_2 - c_3)t_3}{2c_2}\right], \tag{24}$$

$$z_2 = l - \frac{c_3 t_3}{2} - z_1. \tag{25}$$

The value of h is calculated from Eq. (14).

For the errors, we have

$$\begin{aligned}\sigma z_1 = \frac{1}{|c_2 - c_1|}\Bigg\{&(c_1 c_2 \sigma t_2)^2 + \left[\frac{c_1(c_2 - c_1)}{2}\sigma t_3\right]^2 \\ &+ \left(\frac{c_2 z_1}{c_1}\sigma c_1\right)^2 + \left(\frac{c_1 z_1}{c_2}\sigma c_2\right)^2 + \left(\frac{c_1 z_3}{c_3}\sigma c_3\right)^2\Bigg\}^{1/2},\end{aligned} \tag{26}$$

Table 3

PP	$\sigma z_1 \approx \sigma z_2$, cm
Oil	131
Diesel fuel	55
Kerosene	22
AI-95 gasoline	14
AI-92 gasoline	10
Rubber solvent	8.5

σh is estimated by Eq. (15), and

$$\sigma z_2 = [(\sigma h)^2 + (\sigma z_1)^2]^{1/2}. \tag{27}$$

This method is also applicable in the case of frozen water. For ice, $\rho_2 = 940$ kg/m^3, $c_2 = 3980$ m/s [13], and $\rho_2 c_2 = 3.74 \times 10^6$ kg/(m^2 s) $> \rho_1 c_1$. In passing through the liquid–ice boundary, the amplitude of a sound wave increases, and the errors σz_1 and σz_2 decrease due to the increase in the difference $c_2 - c_1$.

Consider an example of a numerical estimate of the accuracy of the two-signal method under the above conditions. Assuming that the dependences $c_1(T)$, $c_2(T)$, and $c_3(T)$ have the form of Eqs. (9) and (18) and the measurements of the temperatures T and T_3 are independent, we obtain

$$\begin{aligned}\sigma z_1(T, T_3) &= \frac{c_1(T)}{|c_2(T) - c_1(T)|}\Bigg\{[c_2(T)\sigma t_2]^2 \\ &+ \frac{1}{4}[c_2(T) - c_3(T_3)]^2(\sigma t_3) + \frac{l}{c_2(T) - c_1(T)} \\ &\times \left[\left[\frac{c_{01}b_1c_2(T)}{c_1(T)} - c_{02}b_2\right]\sigma T\right]^2 + \left[\frac{c_{03}b_3z_3}{c_3(T_3)}\sigma T_3\right]^2\Bigg\}^{1/2},\end{aligned} \tag{28}$$

$$\sigma z_2 = [(\sigma h)^2 + (\sigma z_1)^2]^{1/2}. \tag{29}$$

The values of the errors calculated by these formulas are given in Table 3. As before, according to Eq. (19), $\sigma h = 2.8$ mm and $T = T_3 = 20°\mathrm{C}$.

Under equal conditions, the two-signal aerohydroacoustic method is inferior to the hydroacoustic and aerohydroacoustic methods in the accuracy of the interface localization. When the sound velocities in both phases of the liquid approach each other, the error in measuring the level of the interface sharply increases. When $c_1 = c_2$, the interface is not determined and only h is measured. According to Eqs. (9) and (10) and Table 1, the coincidence of sound velocities in water and oil takes place at $T = 16.4°\mathrm{C}$, and in water and diesel fuel, at $T = 9.5°\mathrm{C}$.

Contrary to the foregoing methods, the acoustohydrostatic method is applicable for measuring the quantity of liquid phases even in the absence of an interface, when the phases are intermixed. The conditions of its application are as follows: $\rho_1 c_1 \neq \rho_3 c_3$ and $\rho_1 \neq \rho_2$. This method requires the use of a reversible electroacoustic transducer fixed on the tank's ceiling and a hydrostatic pressure gauge mounted on the bottom. The level of the liquid is measured by echo sounding, according to Eq. (14). When the interface is present,

$$P = (\rho_1 z_1 + \rho_2 z_2)g, \quad h = z_1 + z_2, \tag{30}$$

where g is the acceleration of gravity. This yields

$$z_1 = (\rho_2 gh - P)/g(\rho_2 - \rho_1), \tag{31}$$

$$z_2 = h - z_1 = (P - \rho_1 gh)/g(\rho_2 - \rho_1). \tag{32}$$

When the liquid is intermixed and the phase separation is absent, Eqs. (31) and (32) hold and the values of z_1 and z_2 are the measures of the quantities of the liquid phases. In a vertical cylindrical tank with the horizontal cross-sectional area S, the volumes V_1, V_2 and the masses m_1, m_2 of the phases are determined by the expressions

$$\begin{aligned} V_1 &= Sz_1, \quad V_2 = Sz_2, \\ m_1 &= \rho_1 Sz_1, \quad m_2 = \rho_2 Sz_2. \end{aligned} \tag{33}$$

By using Eqs. (31)–(33), we obtain

$$\begin{aligned}\sigma z_1 &= \frac{1}{g(\rho_2 - \rho_1)^2}\{[g\rho_2(\rho_2 - \rho_1)\sigma h]^2 \\ &+ [(g\rho_2 h - P)\sigma\rho_1]^2 + [(g\rho_1 h - P)\sigma\rho_2]^2 \\ &+ [(\rho_2 - \rho_1)\sigma P]^2\}^{1/2},\end{aligned} \tag{34}$$

$$\begin{aligned}\sigma z_2 &= \frac{1}{g(\rho_2 - \rho_1)^2}\{[g\rho_1(\rho_2 - \rho_1)\sigma h]^2 \\ &+ [(g\rho_2 h - P)\sigma\rho_1]^2 + [(g\rho_1 h - P)\sigma\rho_2]^2 \\ &+ [(\rho_2 - \rho_1)\sigma P]^2\}^{1/2},\end{aligned} \tag{35}$$

σh is estimated by Eq. (10), and

$$\begin{aligned}\sigma V_1 &= S\sigma z_1, \quad \sigma V_2 = S\sigma z_2, \\ \sigma m_1 &= S[(z_1\sigma\rho_1)^2 + (\rho_1\sigma z_1)^2]^{1/2}, \\ \sigma m_2 &= S[(z_2\sigma\rho_2)^2 + (\rho_2\sigma z_2)^2]^{1/2}.\end{aligned} \tag{36}$$

For the temperature dependences of density of crude oil $\rho_1(T)$ for $10°\mathrm{C} < T < 30°\mathrm{C}$ and of fresh water $\rho_2(T)$ for $T > 5°\mathrm{C}$, the following empirical expressions are valid:

$$\begin{aligned}\rho_1(T) &= \rho_{01}(1 + a_1 T), \quad \rho_{01} = 855.5 \text{ kg/m}^3, \\ a_1 &= -9.2 \times 10^{-4} \text{ deg}^{-1},\end{aligned} \tag{37}$$

$$\begin{aligned}\rho_2(T) &= \rho_{02}(1 + a_2 T^2), \quad \rho_0 = 998.9 \text{ kg/m}^3, \\ a_2 &= -4.78 \times 10^{-6} \text{ deg}^{-2}.\end{aligned} \tag{38}$$

Let us consider an example of a quantitative estimation of the accuracy of the acoustohydrostatic method for the previous conditions by assuming that the dependences $\rho_1(T)$ and $\rho_2(T)$ are known and described by Eqs. (37) and (38). According to Eqs. (31)–(38), we obtain

$$\begin{aligned}\sigma z_1(T) &= [g\Delta\rho(T)]^{-1}\{(\rho_2 g\sigma h)^2 + (\sigma P)^2 \\ &+ [\Delta\rho(T)]^{-2}[2gh\rho_{02}a_2T\Delta\rho(T) \qquad (39) \\ &- [\rho_2(T)gh - P](2\rho_{02}a_2T - \rho_{01}a_1)]^2(\sigma T)^2\}^{1/2},\end{aligned}$$

$$\begin{aligned}\sigma z_2(T) &= [g\Delta\rho(T)]^{-1}\{(\rho_1 g\sigma h)^2 + (\sigma P)^2 \\ &+ [\Delta\rho(T)]^{-2}[gh\rho_{01}a_1\Delta\rho(T) \qquad (40) \\ &- [P - \rho_1(T)gh](2\rho_{02}a_2T - a_1\rho_{01})]^2(\sigma T)^2\}^{1/2},\end{aligned}$$

where $\Delta\rho(T) = \rho_2(T) - \rho_1(T)$.

As previously, according to Eq. (10), we have σh = 2.8 mm.

Let the pressure P be measured by a standard Sapfir-MP pressure gauge with the error $\Delta P = \pm 10^{-3}P_m$, where P_m = 100 kPa is the upper limit of the range of measurement. Taking the standard error $\sigma P \approx 0.6|\Delta P|$ = 60 kPa and using Eqs. (39) and (40), we obtain $\sigma z_1 \approx \sigma z_2$ = 4.8 cm. For a typical vertical cylindrical tank of diameter 19 m and height 12 m, according to Eq. (36), $\sigma V_1/V \approx \sigma V_2/V$ = 0.4%. With a decrease in the difference $\Delta\rho(T)$, these errors grow.

The above calculations showed that the highest accuracy in the simultaneous measurements of the upper level of a two-layer liquid and the position of the layer interface can be achieved with the aerohydroacoustic method, which uses acoustic signals propagating in both liquid and gas space in the tank. In the absence of exact data on the sound velocity, one should use reference channels for its measurement. In the case of intermixed liquid phases with different densities, it is possible to use an electroacoustic transducer and a hydrostatic pressure gauge. The considered methods are intended for measuring the levels and volumes of oil or petroleum products and water accumulated at the tank's bottom during storage. The calculated standard measurement error is about 0.1–1%. An increase in accuracy is possible by extending the frequency band of the sounding acoustic pulses and their optimal processing in the main and reference channels.

One of the considered methods, the hydroacoustic method, has been successfully tested in oil settling tanks. The development of the prototypes of level meters based on other methods is in progress.

REFERENCES

1. A. K. Brovtsyn, Defektoskopiya, No. 5, 73 (1999).
2. O. I. Babikov, *Ultrasonic Control Instruments* (Mashinostroenie, Leningrad, 1985).
3. *Ultrasound. A Small Encyclopedia*, Ed. by I. P. Golyamina (Sovetskaya Éntsiklopediya, Moscow, 1979).
4. F. J. Berto, Oil Gas J., March **10**, 63 (1997).
5. F. J. Berto, Oil Gas J., March **10**, 68 (1997).
6. E. S. Padalka, *Ultrasound in the Oil Industry* (GITL USSR, Kiev, 1962).
7. *EKhO-5 Acoustic Level Meter. Technical Description and Operation Manual* (Staraya Russa, 1991).
8. *Korvet Ultrasonic Level Meters. Advertising Booklet* (Morfizpribor, St. Petersburg, 2000).
9. V. I. Bardyshev, Yu. I. Gromov, A. N. Gromov, *et al.*, Akust. Zh. **46**, 320 (2000) [Acoust. Phys. **46**, 269 (2000)].
10. V. I. Bardyshev, Yu. I. Gromov, A. N. Gromov, *et al.*, RF Patent No. 961210.
11. M. S. Klyuev, S. P. Klyuev, and V. V. Krasnoborod'ko, Akust. Zh. **45**, 825 (1999) [Acoust. Phys. **45**, 743 (1999)].
12. P. Abraham, M. A. Khadar, and J. Jugan, J. Acoust. Soc. Am. **106**, 1284 (1999).
13. *Handbook of Hydroacoustics*, Ed. by A. E. Kolesnikov (Sudostroenie, Leningrad, 1988).
14. P. A. Kolobaev, in *Proceedings of X Session of the Russian Acoustical Society* (Moscow, 2000), Vol. 2, p. 94.
15. V. A. Krasil'nikov, *Sonic and Ultrasonic Waves* (Fizmatgiz, Moscow, 1960).
16. Ya. D. Shirman and V. N. Manzhos, *Theory and Technique of Radar Data Processing against Background Noise* (Radio i Svyaz', Moscow, 1981).
17. *Nomenclature Catalog of Products for General Industrial Application* (ZAO Manometr, Moscow, 2000).
18. S. N. Skorodumov, *A Report of the Acoustics Institute, Russ. Acad. Sci.* (Moscow, 1993).
19. *Liquid Interface Meter for the Oil Industry* (NGTU, Nizhni Novgorod, 1994).
20. K. V. Mackenzie, J. Acoust. Soc. Am. **50**, 1321 (1971).

Translated by A. Svechnikov

Acoustical Physics, Vol. 48, No. 5, 2002, pp. 524–528. Translated from Akusticheskiĭ Zhurnal, Vol. 48, No. 5, 2002, pp. 596–601.
Original Russian Text Copyright © 2002 by Bogdanova, Bulatov, V. Golenishchev-Kutuzov, A. Golenishchev-Kutuzov, Kapralov.

Acoustic Anomalies near Phase Transitions in Manganite

Kh. G. Bogdanova*, A. R. Bulatov*, V. A. Golenishchev-Kutuzov,**
A. V. Golenishchev-Kutuzov, and A. V. Kapralov****
** Zavoĭskiĭ Physicotechnical Institute, Russian Academy of Sciences,*
Sibirskiĭ trakt 10/7, Kazan, 420029 Tatarstan, Russia
*** Kazan State Power Engineering University, Krasnosel'skaya ul. 51, Kazan, 420066 Tatarstan, Russia*
e-mail: adm@kspeu.kcn.ru

Received August 22, 2001

Abstract—The behavior of the velocities and attenuation of ultrasonic waves propagating in $La_{1-x}Sr_xMnO_3$ ($x = 0.175$) manganite at frequencies of 700–800 MHz is studied in the temperature interval from 320 to 180 K, and the effect of magnetic field on the acoustic parameters is investigated. The transformation of acoustic modes in the vicinity of the magnetic phase transition is observed. The changes in the acoustic parameters near the structural and magnetic phase transitions are shown to be related to the strong spin–phonon and electron–phonon interactions. *© 2002 MAIK "Nauka/Interperiodica".*

In the past few years, interest in the physical properties of $R_{1-x}A_xMnO_3$-type manganites (where R stands for a rare-earth metal, namely, La, Pr, or Nd, and A represents an alkali-earth metal, such as Ca, Ba, or Sr) has noticeably increased in connection with the discovery of the giant magnetoresistance phenomenon in these materials [1, 2]. At first, the attention of researchers was mainly concentrated on the effect of the external magnetic field on the transport characteristics of charge carriers. Later, it became clear that the nature of the giant magnetoresistance can be understood only on the basis of a combined study of the crystal, electron, and magnetic structures of manganites and the transformations of these structures under varying external factors (temperature and magnetic field) [3, 4]. Moreover, experimental observations showed that the interrelation between the electron, magnetic, and elastic subsystems determines most of the unusual physical properties of manganites, including such phenomena as the transition from insulator to metallic conduction and the paramagnet–antiferromagnet–ferromagnet transitions. Despite the numerous experiments and theoretical models, both the mechanism governing the temperature dependence of the resistance and the origin of the giant magnetoresistance of manganites remain unclear.

Along with the magnetic, electric, optical, and neutron diffraction methods of studying the physical properties of manganites, an important role can be played by acoustic studies, especially where the structural and magnetic phase transitions in manganites are concerned. Since such acoustic studies have been hitherto uncoordinated and few in number [5–11], their comparison with the data obtained by magnetic, electric, and neutron diffraction methods for similar manganite samples is rather difficult. So far, a comparison has been possible only for specific kinds of composites: $La_{1-x}Sr_xMnO_3$ with $0 \leq x \leq 0.2$ and $La_{1-x}Ca_xMnO_3$ with $x = 0.33$. However, the advantages offered by acoustic studies have not yet been exhausted by the aforementioned experiments. These advantages can be realized only by simultaneously monitoring such acoustic parameters as the velocity and attenuation with the use of much higher frequencies. In addition, the acoustic data should be compared with the measurements of conductivity and magnetization for the same samples. This program was implemented in our investigations. We expected that the increase in the ultrasonic frequencies by two to three orders of magnitude, as compared to the previous experiments, would allow us to study the interaction of acoustic waves with the structural and magnetic changes in the crystal lattice on a microscopic scale.

We studied the temperature dependences of the velocities and attenuation of longitudinal and transverse ultrasonic waves propagating in a $La_{1-x}Sr_xMnO_3$ ($x = 0.175$) crystal for temperatures varying from 325 down to 180 K in magnetic fields 0–1.0 T at frequencies within 700–800 MHz. The results were compared with the experimental data on the temperature dependence of conductivity and the giant magnetoresistance from our previous experiments [11]. The phase diagram [15] shows that the composition under study (with $x = 0.175$) can have several structural, magnetic, and conducting phases (Fig. 1). Since the samples with $x = 0.175$ were found to exhibit the maximal value of giant magnetoresistance, they have been the object of many studies. For these samples, several phase transitions were observed. However, the nature of the transitions at ~200 and ~280 K remains unclear. In one of the publications [7], the phase transition observed at 280 K is attributed to the structural transition from rhombohedral to orthorhombic phase, whereas the authors of another publication [3] believe that this kind of transition occurs near 200 K.

The $La_{1-x}Sr_xMnO_3$ single crystal studied in our experiment was grown at the Moscow Power Institute by the optical zone recrystallization method. To prepare the sample for ultrasonic measurements, the crystal was shaped as a rectangular parallelepiped with the dimensions $4.75 \times 5 \times 8$ mm^3 and with the faces perpendicular to the [100], [010], and [001] axes, respectively. Longitudinal and transverse ultrasonic wave pulses ($\tau \sim 1$ μs) were excited and detected along the [100] axis by lithium niobate bar transducers. To determine the velocities and the attenuation, we used the pulse-echo technique [12].

The sample under study exhibited dramatic changes in both the velocity (V_l and V_t) and attenuation (α_l and α_t) of longitudinal and transverse (respectively) ultrasonic waves in the temperature intervals from 305 to 290, 295 to 275, and 230 to 200 K. In addition, a transformation of the longitudinal mode to the transverse one was observed below 310 K.

The results of our measurements (Fig. 2) showed that the velocity of the longitudinal mode remained virtually constant as the temperature decreased down to $T = 305$ K. In the interval from 305 to 300 K, the first velocity minimum was observed. The second minimum occurred in the temperature interval from 295 to 275 K.

As for the dependence $V_t(T)$ (Fig. 3), a decrease in the velocity was observed beginning from $T = 305$ K down to $T_c = 285$ K with a jump-like velocity increase between 305 and 300 K. The further temperature decrease was accompanied by a gradual velocity increase interrupted by a peak near 230 K.

When a constant magnetic field $H = 0.95T$ was applied, the behavior of the dependences $V_l(T)$ and $V_t(T)$ proved to be much the same as in the absence of magnetic field. However, slight deviations from the behavior described above could be noticed: the anomalies observed in the dependence $V_t(T)$ were shifted to higher temperatures, whereas the anomalies in $V_l(T)$ were shifted to lower temperatures (see Figs. 2 and 3); in addition, at temperatures below 300–290 K, the values of the velocities $V_l(T)$ and $V_t(T)$ observed in the magnetic field were higher.

In the interval between 310 and 290 K, a pronounced minimum was observed in the temperature dependence of attenuation $\alpha_t(T)$. As the temperature decreased further, the attenuation $\alpha_t(T)$ remained constant except for the interval from 230 to 200 K, within which $\alpha_t(T)$ slightly decreased. On the whole, the behavior of $\alpha_l(T)$ and $\alpha_t(T)$ in a constant magnetic field reproduced the corresponding temperature dependences observed at $H = 0$. However, there were some deviations: at $H = 0.95$ T, the attenuation $\alpha_l(T)$ was greater than that at $H = 0$ in the whole temperature range under study, and the attenuation $\alpha_t(T)$ exceeded its value at $H = 0$ in the temperature range $T \le T_c$. In addition, the dependence $\alpha_l(T)$ at $H = 0.95T$ was shifted from its position in a zero magnetic field by ~5 K toward higher temperatures.

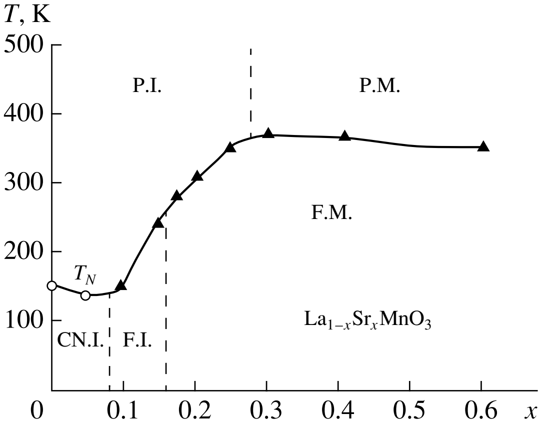

Fig. 1. Phase diagram for $La_{1-x}Sr_xMnO_3$. The empty circles and full triangles show the Néel (T_N) and Curie (T_C) points, respectively. The abbreviations denote a paramagnetic insulator (P.I.), a paramagnetic metal (P.M.), a ferromagnetic insulator (F.I.), and a ferromagnetic metal (F.M.).

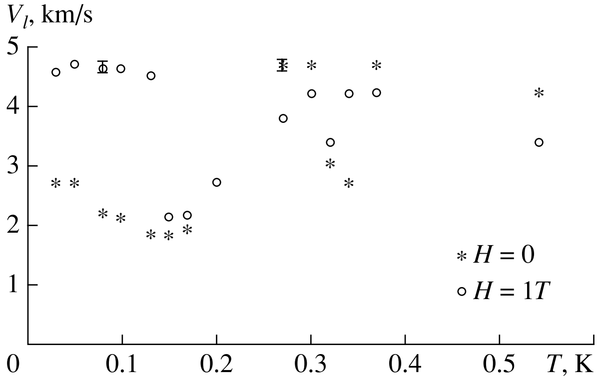

Fig. 2. Velocity of a longitudinal acoustic wave as a function of temperature and magnetic field.

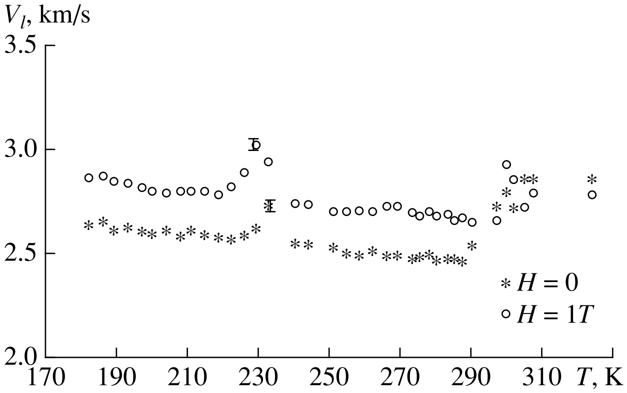

Fig. 3. Velocity of a transverse acoustic wave as a function of temperature and magnetic field.

An unexpected phenomenon observed in the experiment was the transformation of the longitudinal acous-

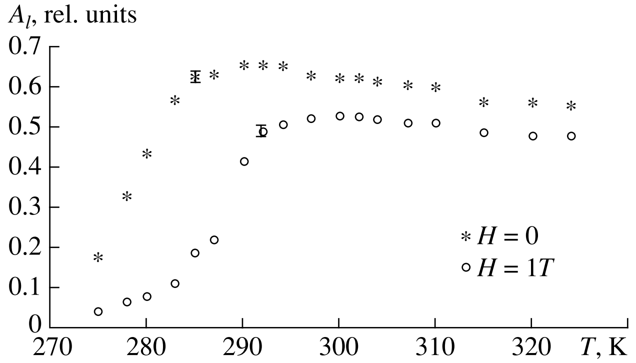

Fig. 4. Amplitude of the longitudinal acoustic mode as a function of temperature and magnetic field.

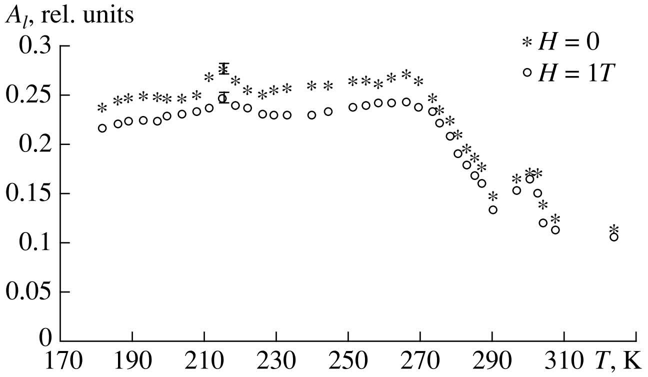

Fig. 5. Amplitude of the transformed transverse acoustic mode as a function of temperature and magnetic field.

tic wave into a magnetoelastic wave with a transverse polarization at temperatures between 315 and 180 K. The experiment showed that, in addition to one pulse, which was attributed to the longitudinal wave according to its velocity, a second pulse appeared with a velocity corresponding to the transverse wave. As the temperature was reduced, the amplitude of the longitudinal pulse transmitted through the sample decreased, whereas the amplitude of the transverse pulse increased. The transformation of acoustic waves manifested itself as a monotone increase in the transverse wave component and a simultaneous monotone decrease in the longitudinal wave component in the temperature interval from 315 to 270 K (Figs. 4 and 5). When purely transverse waves, which were excited by X-cut lithium niobate transducers, were transmitted through the sample, no wave transformation was observed. It should be noted that, according to the theory of elastic wave propagation in anisotropic media, the two transverse waves propagating in a cubic crystal along the [100] direction have the same velocity $V_t = (c_{44}/\rho)^{1/2}$. Since manganites can be classed with quasicubic crystals [6, 7], the observation of a single transverse wave in the magnetoelastic transformation of modes agrees well with theoretical concepts.

To describe our model of the structural and magnetic phase transitions and the transformation of acoustic modes in the temperature interval between 315 and 270 K, we begin with the characterization of the crystalline, magnetic, and electron structures of the composition with $x = 0.175$ above the Curie point. From the phase diagram (Fig. 1), it follows that the sample is in the paramagnetic state and has a rhombohedral structure of the unit cell. The rhombohedral structure results from the distortion of the perfect cubic structure of MnO_3 octahedra by the cooperative Yahn–Teller effect, which is typical of Mn^{3+} ions. In this case, according to the neutron diffraction data [3], all Mn–O bond lengths, as well as bond angles, in the unit cell are equal. This suggests that the cooperative Yahn–Teller ordering of the manganese ion orbitals is incoherent in character, and the conduction in the insulator phase above T_c is of a polaron nature that is related to the free carrier (mainly hole) transport over the Mn^{3+}–O^{2-}–Mn^{4+} ion system (the double exchange model [13]) in conditions of strong spin–phonon and electron–phonon interactions [14]. The presence of such interactions allows one to characterize the carriers as charged magnetoelastic polarons. In this case, the strong spin–phonon interaction is assumed to be responsible for the peak observed in the resistance at a temperature somewhat above T_c for the $La_{1-x}Sr_xMnO_3$ compositions with $0.1 \le x \le 0.3$ [15].

In the sample under study, the suppression of the resistance in magnetic field corresponds to the increase in the acoustic wave velocities observed at $H = 0.95T$ near T_c. As to the anomalies in the behavior of the attenuation and velocities of longitudinal and transverse ultrasonic waves in the temperature intervals 305–290 and 230–200 K, we attribute them to the structural phase transitions from the rhombohedral to the orthorhombic phase. The peak changes in the $V_l(T)$ and $V_t(T)$ near T_c (for our sample, the magnetization measurements and the temperature dependence of the resistance yielded $T_c \approx 285$ K [15]) are in our opinion related to the magnetic phase transition from the paramagnetic to the ferromagnetic state. Some of these transitions were already observed in the previous experiments [6–8, 12].

We believe that the values of the velocities and attenuation of acoustic waves in manganites are determined by both static parameters (distortions of the unit cell, defects, magnetic domains, and, hence, variations in the elastic moduli and in the density of the material) and dynamic parameters (the spin–phonon and electron–phonon interactions).

From this point of view, the increase in the acoustic velocity and the decrease in the resistance observed under the effect of magnetic field in the temperature interval 305–300 K can be explained by the decrease in the incoherent Yahn–Teller distortions of the unit cell.

The two structural transitions interpreted by us as the phase transitions from the rhombohedral (R) to the orthorhombic (O*) phase are caused by the following factors. In the orthorhombic phase, two nonequivalent positions of oxygen ions are present, and, as a result, the MnO_3 octahedron has different bond lengths [3]. The applied magnetic field initiates the R $\longrightarrow$ O* transition in the paramagnetic phase at higher temperatures (see Figs. 2–5). Taking into account that the difference in the elastic energy ΔT between the two structures, ΔE, is small (for the unit cell, $\Delta E = \frac{1}{2}CK\left(\frac{\Delta V}{V}\right)^2$, where V is the unit cell volume, C is the elastic modulus, and ΔV is the change in the cell volume due to the structural transition) and using the known data for the given crystal composition [3], we estimate the quantity $\frac{\Delta E}{k_B}$ as ~5.5 K (k_B is the Boltzmann constant). From Figs. 2 and 3, it follows that the changes in the elastic moduli in the vicinity of the phase transition do not exceed 10–15%, which approximately corresponds to the measurement accuracy for the energy difference ΔE. The above estimate of ΔE was obtained using the average value of C.

On the other hand, for a unit cell in a magnetic field H, the change in the magnetic energy is estimated as $\frac{\Delta E_m}{Hk_B} \approx 6\frac{K}{T}$ [16]. Since, in the paramagnetic phase, an incomplete transformation of the rhombohedral structure to the orthorhombic one takes place, the field $H \sim 1T$ is sufficient for a temperature shift of 3–5 K. The complete formation of the orthorhombic structure occurs at the second transition, already in the ferromagnetic phase, in the temperature interval between 230 and 200 K. When the field $H \sim 1T$ is applied, the degree of ferromagnetic spin ordering increases, which enhances both the velocity increase and the decrease in the attenuation of the longitudinal and transverse acoustic waves that accompany the R $\longrightarrow$ O* structural transition.

Thus, from our experiments with ultrasound, it follows that the strontium concentration ≈0.175 is critical for $La_{1-x}Sr_xMnO_3$ manganite samples: for compositions with $x \leq 0.170$, only one structural transition is observed at 290 K, and for $x \geq 0.180$, also only one transition occurs at 200 K.

The gradual increase in the velocities and the increase in the attenuation of longitudinal and transverse acoustic waves observed below the magnetic phase transition point agree well with the Lee and Min model [14], which predicts a similar behavior of acoustic parameters as a result of the change in the electron–phonon interaction below T_c. According to [14], the mechanism governing this behavior is the considerable suppression of Yahn–Teller distortions in the process of ferromagnetic ordering. The external magnetic field produces a similar effect on the Yahn–Teller distortions, which manifests itself in a further increase in both the velocity and the attenuation of acoustic waves (see Figs. 2–5).

The character of the changes that occur in the acoustic parameters with varying temperature and with magnetic field, together with the temperature and magnetic-field dependences of conductivity observed between 315 and 270 K, suggests that the magnetic ordering plays the key role in these changes. The magnetic ordering process, which consists in the alignment of the spins of Mn^{3+} and Mn^{4+} ions in a ferromagnetic order, is accompanied by a certain suppression of the coherent Yahn–Teller distortions of unit cells. This process also manifests itself in the change from semiconductor to metallic conduction (Fig. 1).

The change from the paramagnetic state of spins to the ferromagnetic one with the formation of a magnetic domain structure allows us to consider the possibility of an acoustic mode transformation at the domain walls [17]. An efficient mode transformation is possible in conditions that allow the presence of magnetostrictive strains in a domain wall. The wave that is directly related to the wall displacement is the longitudinal wave, because the nonuniform strain in the ground state is the longitudinal compressive–tensile strain. In the case of inverse transformation, the more efficient process is the transformation to the longitudinal wave. Transverse waves appear as a result of the local magnetization extending beyond the plane of the domain wall because of its oscillations. Since, according to [7], the matrix of the acoustic wave transformation coefficients, i.e., the ratio of the flux of transformed waves with the polarization i to the initial flux of incident waves with the polarization j, is symmetric, we have $S_{ij} = S_{ji}$. This fact can explain the transformation of longitudinal wave pulses to transverse wave pulses at the front face of the sample. At the rear face, an inverse transformation to longitudinal wave pulses takes place. It should be noted that, in this geometry of the experiment, both transducers were made of Z-cut lithium niobate. The presence of the double transformation described above is also confirmed by the fact that the time difference between two pulses of longitudinal and transverse modes of acoustic vibration does not change after their multiple transmission through the receiving piezoelectric transducer. Presumably, the fact that the acoustic mode transformation was not observed previously [5–10] can be explained by the use of low frequencies (1–10 MHz), because the efficiency of the mode transformation increases when the ultrasonic frequency approaches the eigenfrequency of the domain walls (10^{10}–10^{11} Hz).

The noticeable decrease observed in the intensity of a longitudinal wave pulse transmitted through the sample when the temperature was lowered from 300 K to T_c, as well as the still more substantial increase in the attenuation under the effect of magnetic field, cannot be explained by the mode transformation alone, because the latter process occurs with a violation of the mode intensity balance condition [17]

$$S_{ii} + 2\sum_{j \neq i} S_{ij} + T_i = 1,$$

where S_{ii} is the matrix for the incident longitudinal wave, T_i is the transmission factor for the wave of the given polarization, and S_{ij} is the matrix of the transformed wave. The experimentally measured value of T_i differs from the calculated value by 30–60%. The additional attenuation observed by us for the longitudinal wave and the virtually constant attenuation observed for the transverse wave can be explained by the phenomenological theory of the spin–phonon interaction in magnetic crystals [8]. In this theory, it was assumed that the coupling between the spin system of ions characterized by a strong Yahn–Teller effect and the ultrasonic wave can occur either through single-ion (linear) magnetostriction or bulk magnetostriction. In the first case, an increase in the spin fluctuations gives rise to a simultaneous attenuation of longitudinal and transverse waves. In the second case, the additional attenuation occurs for longitudinal waves only. Presumably, in our case, an increase in the bulk magnetostriction, which occurs when the temperature approaches T_c or when the magnetic field is applied, gives rise to a sharp increase in the attenuation of only longitudinal waves. Since, according to the aforementioned theory [8], we have

$$\alpha_l \sim \omega^2\left(\frac{T - T_c}{T}\right),$$

the substantial increase in α_l with temperature in our experiments, as compared to the experiments at a frequency of 10 MHz [9], can be explained by an increase in frequency by almost two orders of magnitude. On the microscopic scale, the additional attenuation α_l can be explained by the fact that only longitudinal waves strongly affect the length of the Mn–O bonds, which become more rigid when the magnetic field is applied.

Thus, the use of acoustic waves of higher frequencies in our experiments allowed us to investigate finer mechanisms of the interaction of ultrasonic waves with microscopic distortions of the crystal lattice and with the domain structure in a manganite single crystal.

ACKNOWLEDGMENTS

This work was supported by the Russian Foundation for Basic Research, project nos. 99-02-16268 and 01-02-16388.

REFERENCES

1. É. L. Nagaev, Usp. Fiz. Nauk **166**, 833 (1996) [Phys.–Usp. **39**, 781 (1996)].
2. V. M. Loktev and Yu. G. Pogorelov, Fiz. Nizk. Temp. **26** (3), 231 (2000).
3. B. Dabrowski, X. Xiong, Z. Bukowski, *et al.*, Phys. Rev. B **60** (10), 7006 (1999).
4. H. Nakano, Y. Motome, and M. Imada, J. Phys. Soc. Jpn. **69** (5), 1282 (2000).
5. A. P. Ramírez, P. Shiffer, S. W. Cheong, *et al.*, Phys. Rev. Lett. **76** (17), 3188 (1996).
6. H. Fujishiro, M. Ikebe, Y. Konno, and T. Fukase, J. Phys. Soc. Jpn. **66** (12), 3703 (1997).
7. T. W. Darling, A. Miglori, E. G. Moshopoulou, *et al.*, Phys. Rev. B **57** (9), 5093 (1998).
8. Yu. P. Gaĭdukov, N. P. Danilova, A. A. Mukhin, and A. M. Balbashov, Pis'ma Zh. Éksp. Teor. Fiz. **68**, 141 (1998) [JETP Lett. **68**, 153 (1998)].
9. C. Zhu and R. Zheng, Phys. Rev. B **59** (17), 11169 (1999).
10. H. Fujishiro, T. Fukase, M. Ikebe, and T. Kikuchi, J. Phys. Soc. Jpn. **68** (5), 1469 (1999).
11. Kh. G. Bogdanova, A. R. Bulatov, V. A. Golenishchev-Kutuzov, *et al.*, in *EASTMAG'2001* (2001), p. 6.
12. Kh. G. Bogdanova, V. A. Golenishchev-Kutuzov, V. E. Leont'ev, *et al.*, Prib. Tekh. Eksp. **4**, 60 (1997).
13. J. B. Goodenough, *Magnetism and the Chemical Bond* (Interscience, New York, 1963; Metallurgiya, Moscow, 1972).
14. J. D. Lee and B. I. Min, Phys. Rev. B **55** (18), 12454 (1997).
15. A. Urushibara, Y. Morimoto, T. Arima, *et al.*, Phys. Rev. B **51** (20), 14103 (1995).
16. J. W. Tucker and V. W. Rampton, *Microwave Ultrasonics in Solid State Physics* (North-Holland, Amsterdam, 1972; Mir, Moscow, 1975).
17. E. A. Turov and A. A. Lugovoĭ, Fiz. Met. Metalloved. **50** (5), 903 (1980).
18. E. Pyttc and H. Bennet, Phys. Rev. **64** (5), 712 (1967).

Translated by E. Golyamina

Acoustical Physics, Vol. 48, No. 5, 2002, pp. 529–534. Translated from Akusticheskiĭ Zhurnal, Vol. 48, No. 5, 2002, pp. 602–608.

Effect of the Sound Velocity Stratification in the Bottom Sediment Layer on the Diffraction Focusing of an Acoustic Field in a Shallow Sea

E. L. Borodina and Yu. V. Petukhov

Institute of Applied Physics, Russian Academy of Sciences,
ul. Ul'yanova 46, Nizhni Novgorod, 603600 Russia
e-mail: petukhov@hydro.appl.sci-nnov.ru

Received March 27, 2001

Abstract—It is shown that an increase in the sound velocity gradient in the bottom sediment layer results in the formation of additional zones of diffraction focusing of the acoustic field generated by a vertical line array in the water layer. It is also established that, depending on the sound velocity step at the upper boundary of the sediment layer, the diffraction focusing of the acoustic field in the main focusing zones can be enhanced or reduced. *© 2002 MAIK "Nauka/Interperiodica".*

The essentials of the diffraction focusing of acoustic fields in oceanic waveguides due to the interference of adjacent pairs of modes was discussed in detail in our previous studies [1–6]. For shallow-water oceanic waveguides, we investigated the effects of such factors as the sound velocity stratification in the water layer [1, 4], the depth of a sound source and its radiation frequency [3, 4], the acoustic energy absorption in the bottom [3], and the acoustic parameters of an isovelocity fluid sediment layer [6] on the spatial structure of the zones of diffraction focusing.

However, another important question as to how the sound velocity stratification in the bottom sediment layer affects the formation of the zones of diffraction focusing of acoustic fields in shallow-water waveguides still has to be answered. This question is considered in our paper.

To solve the stated problem, we use a fairly simple but credible model of a shallow-water oceanic waveguide (see [7–10]), which includes an isovelocity water layer of depth H with the sound velocity c and density ρ and a fluid sediment layer of thickness h with the sound velocity $c_s(z)$ depending on the depth z,

$$c_s(z) = \frac{c_1}{\sqrt{1-\alpha(z-H)}}, \qquad (1)$$

and the density ρ_s. These layers overlie a homogeneous elastic halfspace with the shear c_t and longitudinal c_l velocities and the density ρ_l. Here, $c_1 = c_s(z = H)$ is the sound velocity near the upper boundary of the sediment layer, and $\alpha > 0$ is the gradient of the square refractive index of acoustic waves in sediments.

We also assume that the source of tonal acoustic radiation with a circular frequency ω is a vertical line array with the aperture D whose center is located at the depth $z_0 = H/2$. Supposing that the amplitude distribution of the excitation coefficient over the array aperture is constant and the phase distribution is absent, we can ignore the contribution of lateral waves to the total field [11]. Using [7–11], we obtain the following expression for the acoustic field intensity $J_0(r, z) = rJ(r, z)$ normalized to the geometric divergence:

$$J_0(r, z) = \left|\sum_{m=0}^{M} A_m(z_0, z, \omega)e^{ikr/u_m}\right|^2. \qquad (2)$$

Here, $A_m(z_0, z, \omega)$ is the amplitude of the mth mode, u_m is its dimensionless (normalized to c) phase velocity, $M = \max\{m\}$ is the number of excited modes, and $k = \omega/c$.

The values of u_m are determined from the dispersion equation corresponding to the given model of the waveguide:

$$\tan\left(kH\frac{\gamma_1}{u_m}\right) = -\frac{\gamma_1}{\beta S}\frac{Rb^4u_m^4\gamma_2U_1 + Sg\beta U_3}{Rb^4u_m^4\gamma_2U_2 + Sg\beta U_4}, \qquad (3)$$

where, for the sake of convenience, the following quantities are introduced:

$$R = \rho/\rho_l, \quad S = \rho/\rho_s, \quad a = c/c_l, \quad b = c/c_t,$$

$$a_1 = c/c_1, \quad a_2 = a_1\sqrt{1-\alpha h},$$

$$\beta = -(\alpha a_1^2/k)^{1/3}u_m, \quad \gamma_1 = \sqrt{u_m^2-1},$$

$$\gamma_2 = \sqrt{1-a^2u_m^2}, \quad \gamma_3 = \sqrt{1-b^2u_m^2},$$

$$\begin{aligned} U_1 &= u(x_1)v(x_2) - v(x_1)u(x_2), \\ U_2 &= u'(x_1)v(x_2) - v'(x_1)u(x_2), \end{aligned} \qquad (4)$$

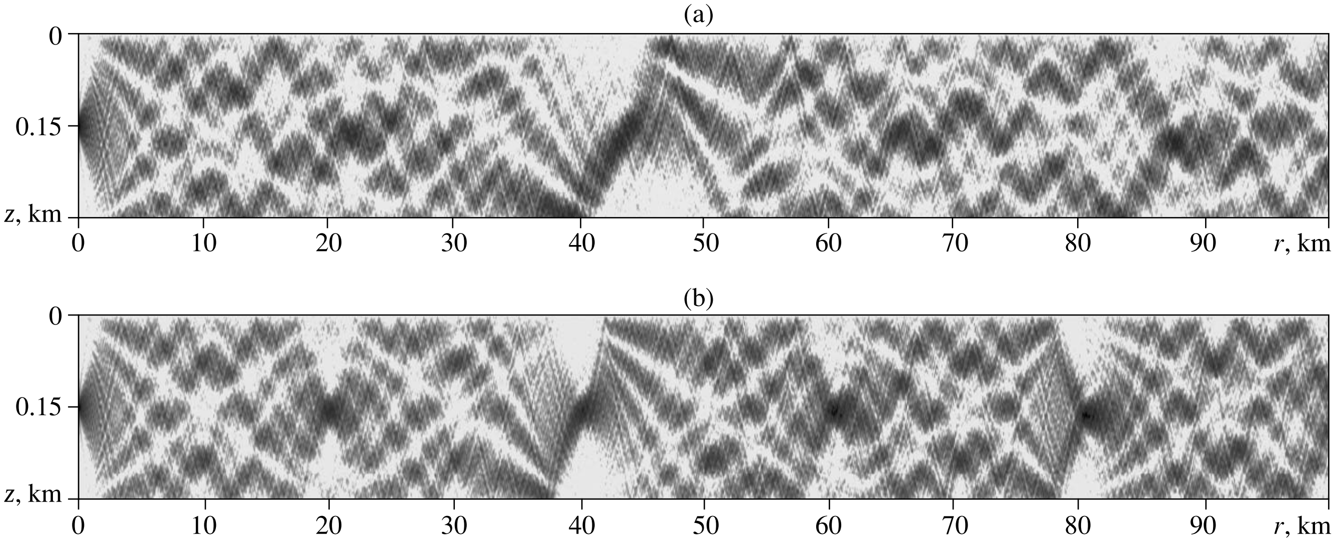

Fig. 1. Spatial distribution of the normalized intensity $J_0(r, z)$ [Eq. (2)] of the acoustic field for $c_1 = 1.45$ km/s and Δc_s = (a) 1 and (b) 30 m/s.

$$U_3 = u(x_1)v'(x_2) - v(x_1)u'(x_2),$$
$$U_4 = u'(x_1)v'(x_2) - v'(x_1)u'(x_2),$$

$$g = (1+\gamma_3^2)^2 - 4\gamma_2\gamma_3,$$
$$x_1 = (1 - a_1^2u_m^2)/\beta^2, \quad x_2 = (1 - a_2^2u_m^2)/\beta^2.$$

Here, $u(x_j)$ and $v(x_j)$ are the Airy functions of the corresponding arguments x_j, $j = 1, 2$ (see [8]).

The modal amplitude is determined from the expression

$$A_m(z_0, z, \omega) = 2\sqrt{\frac{2\pi k}{i}}\frac{F_1(u_m)}{F_2(u_m)}E(z_0, D, u_m)\sin\left(kz\frac{\gamma_1}{u_m}\right), \tag{5}$$

where, for simplicity, the following functions are introduced:

$$F_1(u_m) = i\frac{S\beta}{\sqrt{u_m}}[Rb^4v^4\gamma_2U_2 - Sg\beta U_1], \tag{6}$$

$$\begin{aligned}F_2(u_m) = {} & \frac{1}{2}S\sin\left(2kH\frac{\gamma_1}{u_m}\right)\left[Rb^4u_m^4\left(\beta\left(\frac{\gamma_1}{\gamma_2}+\frac{\gamma_2}{\gamma_1}\right)U_2 + 2\frac{\gamma_1\gamma_2}{\beta}(x_1U_1+U_4)\right)\right.\\ & \left. + S\gamma_1\left(\beta^2\left(\frac{g}{\gamma_1^2} - 4q\right)U_4 + 2g(x_1U_3 + x_2U_2)\right)\right]\\ & + \gamma_1^2\cos^2\left(kH\frac{\gamma_1}{u_m}\right)\left[Rb^4u_m^4\left(\frac{U_1}{\gamma_2} + 2\frac{\gamma_2}{\beta^2}(U_3+U_2)\right)\right.\\ & \left. - 2S\left(2q\beta U_3 - \frac{g}{\beta}(U_4 + x_2U_1)\right)\right]\\ & - SkH\frac{\beta}{u_m}[Rb^4u_m^4\gamma_2U_2 + Sg\beta U_4],\end{aligned} \tag{7}$$

$$q = 2\gamma_2\gamma_3 + \frac{\gamma_2}{\gamma_3} + \frac{\gamma_3}{\gamma_2} - 2(1+\gamma_3^2), \tag{8}$$

$$\begin{aligned}E(z_0, D, u_m) = \frac{u_m}{Dk\gamma_1}\left\{\cos\left[kz_0\frac{\gamma_1}{u_m}\left(1 - \frac{D}{2z_0}\right)\right]\right.\\ \left. - \cos\left[kz_0\frac{\gamma_1}{u_m}\left(1 + \frac{D}{2z_0}\right)\right]\right\}.\end{aligned} \tag{9}$$

Note that Eq. (9) describes the directional pattern of the radiating array for the mth mode.

In the numerical modeling of the spatial distribution of the normalized acoustic field intensity with the use of Eqs. (2), (3), and (5), we (as in [6], to provide the succession of the results) choose the following parameters for the radiation, the water layer, and the bottom: $f = \omega/2\pi = 300$ Hz, $z_0 = 150$ m, $D = 10c/f$, $H = 300$ m, $c = 1.45$ km/s, $\rho = 1 \times 10^3$ kg/m^3, $h = 0.1H$, $\rho_s = 1.4\rho$, $c_t = 1.7$ km/s, $c_l = 2.4$ km/s, and $\rho_l = 1.6\rho$. The values of the sound velocities near the upper c_1 and lower $c_2 = c_s(H + h)$ boundaries of the sediment layer varied.

Figures 1–3 present the results of the numerical calculation of $J_0(r, z)$ in a dynamic range of 16 dB. From these results, one can draw the following conclusions.

First, when the sound velocities coincide on both sides of the upper boundary of the sediment layer, $c = c_1$, the increase in the increment of the sound velocity, $\Delta c_s = c_2 - c_1$, within this layer leads to a monotone

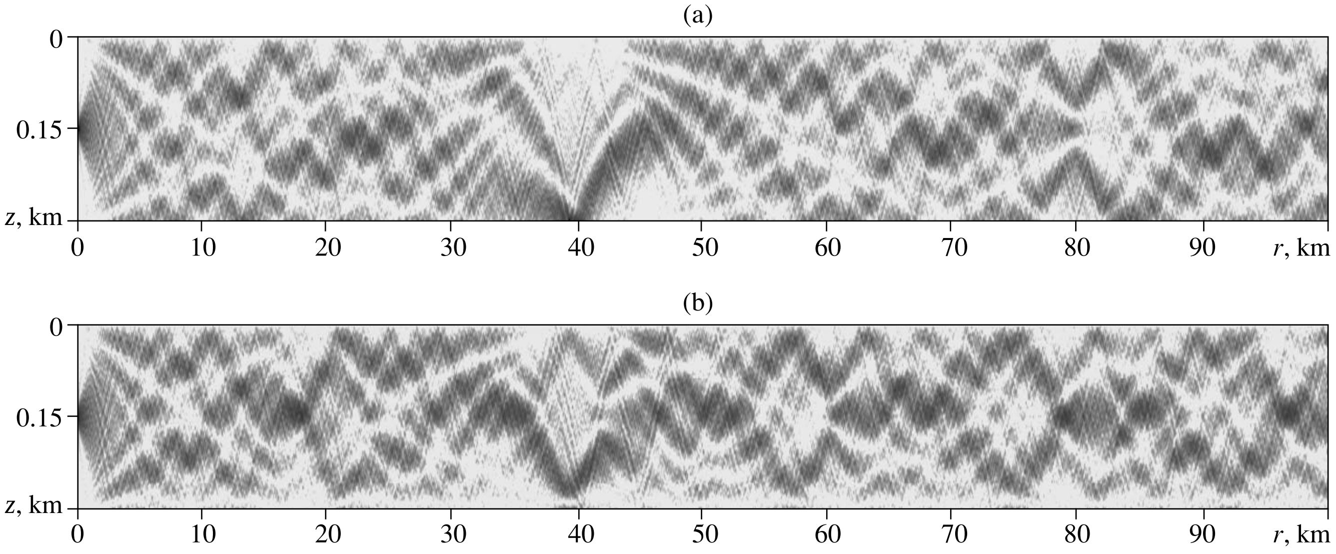

Fig. 2. The same as in Fig. 1 for $c_1 = 1.44$ km/s.

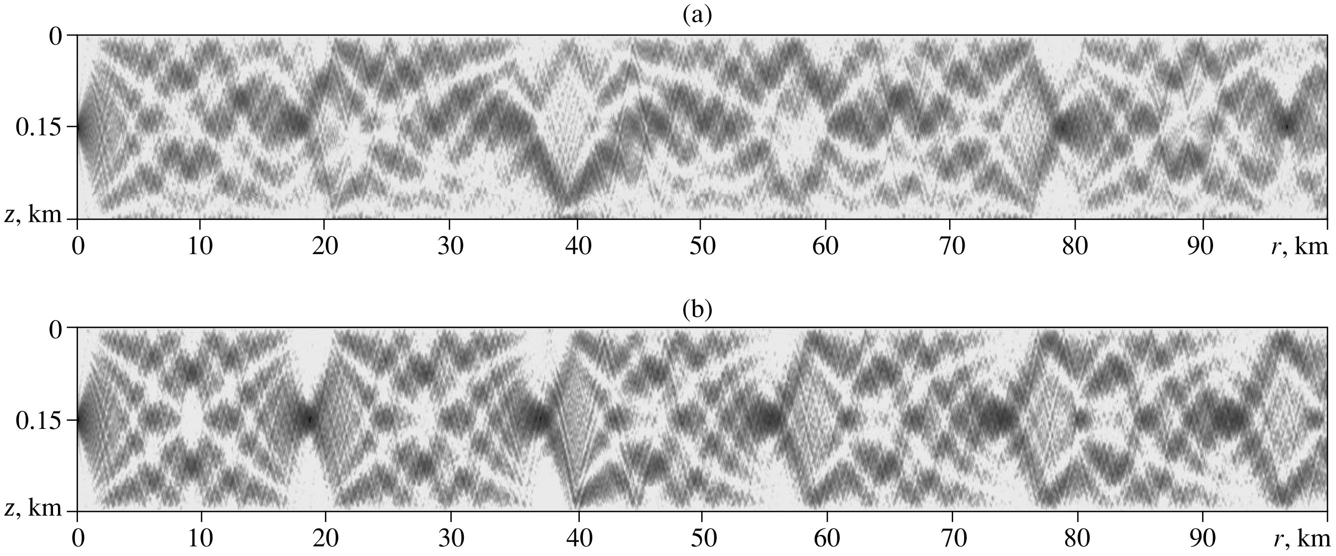

Fig. 3. The same as in Fig. 1 for $c_1 = 1.42$ km/s.

enhancement of the effect of diffraction focusing of the acoustic field (see Fig. 1). As in [6], its enhancement at the principal focal points, whose spatial repetition period R_0 is rather accurately estimated from the simple relationship

$$R_0 = 4(H+h)^2/\lambda, \qquad (10)$$

where $\lambda = c/f$ (see [3, 6]), is caused by smoothing the dependence of the quantity

$$R_g(m, m+1;\, m+1, m+2) = \frac{R_{m,\,m+1}R_{m+1,\,m+2}}{|R_{m,\,m+1} - R_{m+1,\,m+2}|} \qquad (11)$$

on the mode number m, $1 \le m \lesssim 10$ (see Fig. 4), with an increase in Δc_s. The quantity R_g given by Eq. (11) corresponds to the period of changes in the interference structure of the field of two adjacent pairs of modes with the corresponding interference periods

$$R_{m,\,m+1} = \frac{2\pi}{|k_m - k_{m+1}|}, \qquad R_{m+1,\,m+2} = \frac{2\pi}{|k_{m+1} - k_{m+2}|} \qquad (12)$$

and the frequency dependences of the horizontal wave numbers $k_m = k/u_m$. Therefore, in the waveguide under study, it characterizes the interference of adjacent pairs of modes with numbers $1 \le m \lesssim 10$, for which $R_g \approx R_0$,

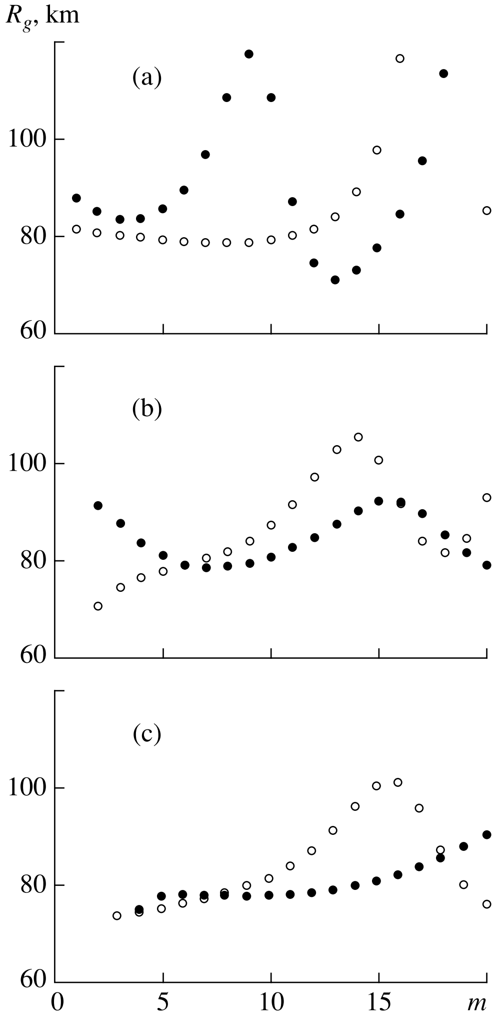

Fig. 4. Dependence of the spatial period R_g [Eq. (11)] on the mode number m in the interval $1 \le m \le 20$ for c_1 = (a) 1.45, (b) 1.44, and (c) 1.42 km/s and for Δc_s = 1 m/s (full circles) and 20 m/s (empty circles).

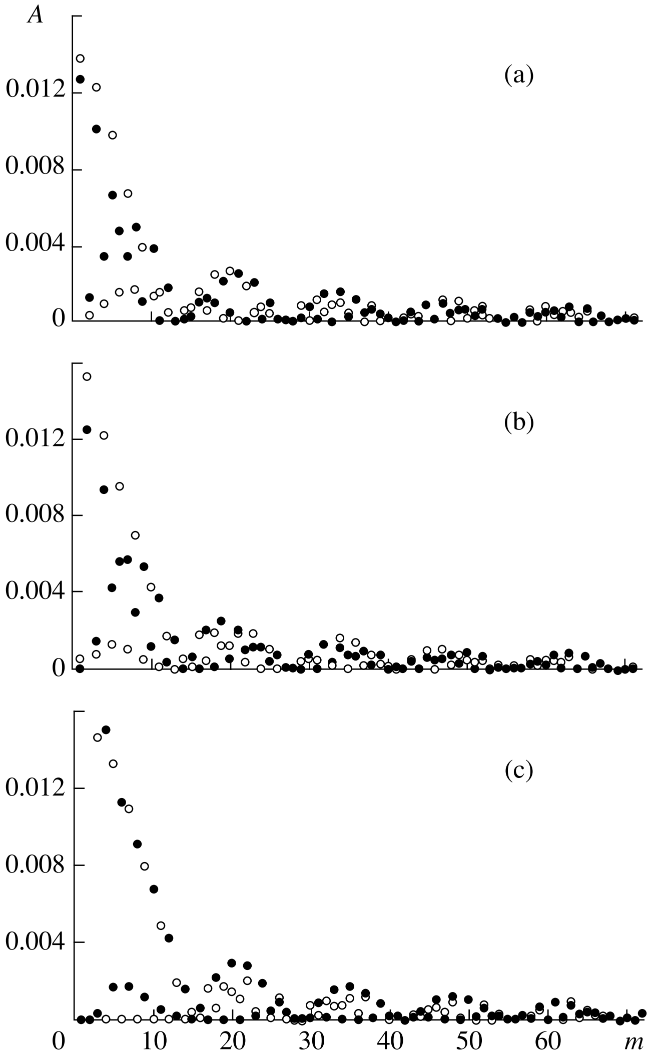

Fig. 5. Dependences of the normalized mode amplitudes $A = |A_m|/\max\{|A_m|\}|_{h=0}$ on the mode number m for c_1 = (a) 1.45, (b) 1.44, and (c) 1.42 km/s and for Δc_s = 1 m/s (full circles) and 30 m/s (empty circles).

since they do not take part in the formation of weakly divergent acoustic beams [12].

Second, for $c \le c_1$, with increasing Δc_s, the diffraction focusing begins to manifest itself with a spatial period noticeably smaller than R_0:

$$R_1 = \frac{1}{4}R_0. \qquad (13)$$

Such a behavior of $J_0(r, z)$ is caused by the fact that the interference structure of the acoustic field, in contrast to that of optical waveguides [13, 14], begins to be formed by only the modes of the same parity: either by the odd modes, as in a given waveguide (see Fig. 5), or by the even modes.

The validity of Eq. (13) can rather rigorously be proved analytically using an even more simplified model of the oceanic waveguide that consists of an isovelocity water layer of thickness $H + h$ overlying a rigid halfspace. In the framework of such a model, the horizontal wave numbers of the modes are determined from the expression

$$\begin{aligned} k_m &= k\sqrt{1-y_m^2}, \\ y_m &= \pi\left(m-\frac{1}{2}\right)/k(H+h) \quad (m = 1, 2\ldots). \end{aligned} \qquad (14)$$

From this expression, in the paraxial approximation, i.e., accurate to $y_m^2 \ll 1$, we obtain the formula for the interference period of the modes with the numbers m and n:

$$R_{m,n} \approx \frac{8(H+h)^2}{\lambda}\frac{1}{n^2-m^2+m-n} \qquad (15)$$

$$(m = 1, 2\ldots, n = 1, 2\ldots).$$

Expression (15) allows us to obtain the simple relationships

$$R_{m,\,m+1} \approx \frac{4(H+h)^2}{\lambda}\frac{1}{m} = \frac{R_0}{m}, \qquad (16)$$

$$Rg(m, m+1;\, m+1, m+2) \approx \frac{4(H+h)^2}{\lambda} = R_0, \quad (17)$$

which are valid for the modes of adjacent numbers $n = m + 1$; in addition, we determine the quantities

$$R_{m,\,m+2} \approx \frac{4(H+h)^2}{\lambda}\frac{1}{2m+1} = \frac{R_0}{2m+1}, \qquad (18)$$

$$R_g(m, m+2;\, m+2, m+4) \approx \frac{R_0}{4} = R_1, \qquad (19)$$

corresponding to the adjacent modes of even numbers $m = 2m_1$ and $n = m + 2$ or the adjacent modes of odd numbers $m = 2m_1 - 1$ and $n = m + 2$ ($m_1 = 1, 2\ldots$).

Dependences (17) and (19) prove Eq. (13), which was obtained from the numerical modeling with a more realistic model of the oceanic waveguide. In addition, these expressions show that the spatial periods of the diffraction focusing of the field formed by either even or odd modes in an isovelocity acoustic waveguide coincide, in contrast to the case of similar optical waveguides where the period for the odd modes is two times smaller than the period for the even modes (see [13, 14]).

Here, it is significant to note that the increase in Δc_s in the layered waveguide under consideration leads to a predominance of odd mode contributions to the total field not only through the increase in their amplitudes but also through a decrease in the amplitudes of the even modes (see Fig. 5).

Third, as the sound velocity at the upper boundary of the sediment layer decreases, the increase in Δc_s, beginning from a certain value $c_1 = c_p < c$, contributes to the formation of additional focal points (see Figs. 2, 3). However, in this case, the diffraction focusing of the acoustic field at the principal focal points is reduced (see Fig. 3). The latter fact is caused by an increase in the interval of the variation of R_g [Eq. (11)] for modes with the numbers $1 \le m \lesssim 10$, which are responsible for the formation of the zones of the diffraction focusing in the waveguide under consideration [3–6]. As the value of c_1 decreases, the diffraction focusing is reduced when $c_p < c_1 < c$ (see Figs. 1, 2) and enhanced when $c_1 < c_p$ (see Fig. 3). For example, for $c_1 = 1.44$ km/s $> c_p$ (Fig. 2), the effect of the diffraction focusing is less pronounced than for $c_1 = c$ (see Fig. 1) and $c_1 = 1.42$ km/s $< c_p$ (see Fig. 3). This is caused by the noticeably greater interval of the variation of R_g [Eq. (11)] for the corresponding numbers $1 \le m \lesssim 10$ of modes in the first case (see Fig. 4).

Thus, the results of the theoretical investigations presented above allow us to conclude that the increase in the sound velocity gradient in the bottom sediment layer results in the formation of additional zones of diffraction focusing of the acoustic field generated in a shallow sea by a vertical line array with a given aperture dimension and a given position in the water layer. In this case, depending on the sound velocity step at the upper boundary of the sediment layer, the diffraction focusing can be enhanced or reduced.

It should also be noted that the diffraction focusing features established here and in [1–6] can be used for the focusing of acoustic radiation in shallow-water oceanic waveguides. Such an approach may be preferable to that based on the method of wave conjugation [15]. The latter needs an extended aperture with rather complicated laws of amplitude and phase distributions of the excitation coefficients.

In closing, we present a qualitative consideration of the effect of acoustic energy absorption in the bottom on the formation of the zones of diffraction focusing of acoustic fields in shallow-water oceanic waveguides. To this end, we use the results of the theoretical investigations of mode attenuation in a shallow sea [16–26].

For waveguide models with an isovelocity water layer and a homogeneous absorbing bottom [16–19] or with a homogeneous, high-velocity, absorbing sediment layer [20, 21], the attenuation coefficients of modes increase with the mode number. According to [3], in such situations, along with the natural decrease in the sound intensity in the zones of diffraction focusing, these zones can be relatively more pronounced in a certain interval of distances, as compared to the case without absorption in the bottom. Beyond this interval, these zones will be less pronounced. Such a behavior of the acoustic field is determined by the fact that the modes of higher numbers, which attenuate with distance more noticeably, shade the zones of the diffraction focusing (see [3]).

In the case of acoustic field generation by a vertical line array with optimal aperture, which significantly suppresses the excitation of the modes with higher numbers, the absorption of acoustic energy in the bottom will lead only to a natural attenuation of the acoustic field in the zones of diffraction focusing.

If the homogeneous absorbing sediment layer is a low-velocity one with respect to the water layer, the modal attenuation coefficients can reach minimal values for the modes of relatively high numbers (see [22–24]). Therefore, in such a situation, the attenuation of the acoustic field in the zones of diffraction focusing will be more pronounced than in the case of a high-velocity sediment layer.

Less obvious features of the formation of the zones of diffraction focusing can manifest themselves when the low-velocity absorbing sediment layer has a positive gradient of sound velocity, which results in considerable quantitative differences in the attenuation coefficients of modes of different parity (see [25, 26]). The latter, even with a point source of the acoustic field, can lead to a noticeable manifestation of additional zones of diffraction focusing with a smaller spatial period in a certain interval of horizontal distances [see Eq. (19)].

It is natural that, for the initial generation of modes of a single parity with the use of the vertical array, the formation of additional zones of diffraction focusing in a certain interval of horizontal distances will be more pronounced, if just these modes have the minimal attenuation coefficients. Otherwise, both main and additional zones of diffraction focusing will only be reduced in the whole range of distances.

ACKNOWLEDGMENTS

This work was supported by the Russian Foundation for Basic Research (project no. 00–05-64604) and the Competition Center for Basic Natural Studies.

REFERENCES

1. Yu. V. Petukhov, Akust. Zh. **46**, 384 (2000) [Acoust. Phys. **46**, 327 (2000)].
2. D. I. Abrosimov and Yu. V. Petukhov, Akust. Zh. **46**, 149 (2000) [Acoust. Phys. **46**, 113 (2000)].
3. D. I. Abrosimov and Yu. V. Petukhov, Akust. Zh. **46**, 5 (2000) [Acoust. Phys. **46**, 1 (2000)].
4. E. L. Borodina and Yu. V. Petukhov, Akust. Zh. **47**, 313 (2001) [Acoust. Phys. **47**, 262 (2001)].
5. E. L. Borodina and Yu. V. Petukhov, Akust. Zh. **47**, 451 (2001) [Acoust. Phys. **47**, 384 (2001)].
6. E. L. Borodina and Yu. V. Petukhov, Akust. Zh. **47**, 590 (2001) [Acoust. Phys. **47**, 511 (2001)].
7. W. M. Ewing, W. S. Jardetsky, and F. Press, *Elastic Waves in Layered Media* (McGraw-Hill, New York, 1957).
8. L. M. Brekhovskikh, *Waves in Layered Media*, 2nd ed. (Nauka, Moscow, 1973; Academic, New York, 1960).
9. B. G. Katsnel'son and V. G. Petnikov, *Acoustics of a Shallow Sea* (Nauka, Moscow, 1997).
10. N. R. Chapman, C. T. Tindle, and E. K. Westwood, J. Acoust. Soc. Am. **100**, 3631 (1996).
11. E. L. Borodina and Yu. V. Petukhov, Akust. Zh. **46**, 437 (2000) [Acoust. Phys. **46**, 373 (2000)].
12. D. I. Abrosimov and Yu. V. Petukhov, Akust. Zh. **43**, 437 (1997) [Acoust. Phys. **43**, 373 (1997)].
13. L. A. Rivlin and V. S. Shil'dyaev, Izv. Vyssh. Uchebn. Zaved., Radiofiz. **11**, 572 (1968).
14. E. E. Grigor'eva and A. I. Semenov, Kvantovaya Élektron. (Moscow) **5** (9), 1877 (1978).
15. T. Akal, C. Ferla, D. R. Jackson, *et al.*, J. Acoust. Soc. Am. **105**, 1597 (1999).
16. V. K. Kuznetsov, Akust. Zh. **27**, 901 (1981) [Sov. Phys. Acoust. **27**, 499 (1981)].
17. E. A. Rivelis and S. Yu. Slavyanov, Akust. Zh. **32**, 705 (1986) [Sov. Phys. Acoust. **32**, 443 (1986)].
18. N. S. Ageeva and V. D. Krupin, Akust. Zh. **25**, 340 (1979) [Sov. Phys. Acoust. **25**, 192 (1979)].
19. V. D. Krupin, Akust. Zh. **18**, 556 (1972) [Sov. Phys. Acoust. **18**, 460 (1972)].
20. N. S. Ageeva and V. D. Krupin, Akust. Zh. **26**, 161 (1980) [Sov. Phys. Acoust. **26**, 89 (1980)].
21. N. S. Ageeva and V. D. Krupin, Akust. Zh. **29**, 721 (1983) [Sov. Phys. Acoust. **29**, 427 (1983)].
22. N. S. Ageeva and V. D. Krupin, Akust. Zh. **30**, 577 (1984) [Sov. Phys. Acoust. **30**, 341 (1984)].
23. N. S. Ageeva and V. D. Krupin, Akust. Zh. **31**, 1 (1985) [Sov. Phys. Acoust. **31**, 1 (1985)].
24. N. S. Ageeva and V. D. Krupin, Akust. Zh. **27**, 669 (1981) [Sov. Phys. Acoust. **27**, 372 (1981)].
25. N. S. Ageeva and V. D. Krupin, Akust. Zh. **34**, 391 (1988) [Sov. Phys. Acoust. **34**, 228 (1988)].
26. N. S. Ageeva and V. D. Krupin, Akust. Zh. **35**, 385 (1989) [Sov. Phys. Acoust. **35**, 229 (1989)].

Translated by Yu. Lysanov

Acoustical Physics, Vol. 48, No. 5, 2002, pp. 535–539. Translated from Akusticheskiĭ Zhurnal, Vol. 48, No. 5, 2002, pp. 609–613.
Original Russian Text Copyright © 2002 by Galanin, Kononenko.

Diffraction Effects in the Ultrasonic Field Generated by an Oscillating Piezoelectric Disk Fixed along the Edge

V. V. Galanin* and V. S. Kononenko**
** Samara Institute of Railway Transport Engineers, Pervyĭ Besymyannyĭ per. 18, Samara, 443066 Russia*
*** Samara State Technical University, Pervomaĭskaya ul. 18, Samara, 443100 Russia*
e-mail: physics@sstu.samara.ru

Received November 23, 2001

Abstract—The diffracted field of an oscillating piezoelectric disk fixed along the edge is calculated with consideration for the spectrum of the disk’s eigenfrequencies and the corresponding oscillation amplitude distribution. The diffraction corrections are calculated as functions of the system parameters, including the Q-factor of the piezoelectric plate and the frequency of radiation. *© 2002 MAIK “Nauka/Interperiodica”.*

In most cases, ultrasound is radiated with the use of a planar piezoelectric transducer, whose simplest model is the piston source. However, multiple experimental investigations [1–7] show that, in certain cases, the measured diffracted field of an ultrasonic transducer correlates with the theoretical calculations for a piston transducer only within an order of magnitude. Several researchers investigated the radiation of piezoelectric transducers without considering their natural oscillations [8–10]. There is no general solution to the problem of the plate oscillations. For this reason, to gain an insight into the problem, we consider a circular piezoelectric plate fixed along the edge and radiating into a liquid layer; we also assume that the opposite side of the layer is represented by a plane hard screen with a receiving circular piezoelectric plate built into it. We seek an approximate solution for a narrow-band signal of finite duration under the assumption that the radiated and reflected signals are separated in time and that multiple reflections can be ignored. In addition, the effect of transverse and Lamb waves is negligible to a first approximation for sufficiently thin piezoelectric disks [11], so that we can exclude the shear oscillations of the piezoelectric plate from our consideration. With these assumptions, we can easily obtain the solution to the formulated problem and consider the behavior of the diffraction corrections as functions of the system parameters.

Consider oscillations of a circular isotropic piezoelectric plate of radius a fixed by the edge in a hole of an infinite hard screen of the same thickness. A similar piezoelectric plate is used as the receiver. We use the cylindrical coordinate system with the coordinates r, φ, and z. Let the transmitting and receiving plates have the same radius a and thickness d and be located at a distance L from each other. The z axis passes through the centers of the plates. The surfaces of the transmitting piezoelectric plate correspond to $z = -d$ and $z = 0$, and the surfaces of the receiving plate, to $z = L$ and $z = L + d$.

Since the plates are rigidly fixed along their contours, the following boundary conditions must be satisfied:

$$\begin{gathered} u_1 = 0 \text{ and } u_3 = 0 \text{ for } r = a, \\ u_{2,1} = 0 \text{ for } r \ge a, \quad z = 0 \text{ and } z = L, \end{gathered} \tag{1}$$

where u_1, $u_{2,1}$, and u_3 are the displacements of particles in the radiating piezoelectric plate, the liquid layer, and the receiving piezoelectric plate, respectively. The solution to the wave equation for liquid must take into account the pulsed nature of the ultrasonic signal; we assume that, during the exciting pulse, the oscillations in the disk are steady and the radiation is stationary. Because the exciting pulse and the reflected signal are separated in time, no reflected signal is present in the liquid at the boundary $z = 0$. On the contrary, the reflected wave must be considered in the boundary condition at $z = L$. On the basis of these speculations with consideration for the sound field symmetry about the z axis and boundary conditions (1), we can represent the solution to the wave equation in the form

$$u_1 = \sum_{n=1}^{\infty} J_0\left(\frac{\nu_{0n} r}{a}\right)\left(A_n e^{-ik_n z} + B_n e^{ik_n z}\right) \quad \text{for } -d \le z \le 0, \tag{2}$$

$$u_{2,1} = \int_0^{\infty} e^{-i\beta z} J_0(\alpha r) f(\alpha) \alpha d\alpha = C(r, z) e^{-ikz} \quad \text{for } 0 \le z < L, \tag{3}$$

$$u_{2,3} = C(r,z)e^{-ikz} + D(r,z)e^{ikz} = u_{2,1} + u_{2,2} \quad \text{for} \quad 0 < z \le L, \tag{4}$$

$$u_3 = \sum_{m=1}^{\infty} J_0\left(\frac{\nu_{0m} r}{a}\right)(E_m e^{-ik_m z} + F_m e^{ik_m z}) \quad \text{for} \quad L \le z \le L + d, \tag{5}$$

where the wave numbers $k_m^2 = k_0^2 - \nu_{0m}^2/a^2$ and $k_n^2 = k_0^2 - \nu_{0n}^2/a^2$ determine the fundamental oscillation frequencies of the transmitting and receiving piezoelectric plates; k_0 and k are the wave numbers for the piezoelectric plates and liquid, respectively; ν_{0n} and ν_{0m} are the roots of the zero-order Bessel functions; $\beta^2 = k^2 - \alpha^2$; α is the integration variable; $f(\alpha)$ is the distribution function of the radial wave amplitudes (this function is determined from the boundary conditions); and A_n, B_n, E_m, F_m, $C(r, z)$, and $D(r, z)$ are the quantities related to the amplitudes of waves propagating along the z axis in the positive and negative directions. For the liquid layer, we have two expressions allowing for the pulsed nature of the piezoelectric plate excitation. Formula (3) describes the ultrasonic field at the transmitting piezoelectric plate with no signal reflected from the receiving piezoelectric plate, and formula (4) describes the ultrasonic field at the receiving piezoelectric plate with both incident and reflected waves in the liquid.

The boundary conditions at the surfaces of the piezoelectric plates have the form:

$$T_1 = 0 \quad \text{for} \quad z = -d, \tag{6}$$

$$T_1 = T_2 \quad \text{for} \quad z = 0, \tag{7}$$

$$u_1 = u_{2,1} \quad \text{for} \quad z = 0, \tag{8}$$

$$T_2 = T_3 \quad \text{for} \quad z = L, \tag{9}$$

$$u_{2,3} = u_3 \quad \text{for} \quad z = L, \tag{10}$$

$$T_3 = 0 \quad \text{for} \quad z = L + d, \tag{11}$$

where T_1 and T_3 are the elastic stresses in the transmitting and receiving plates, the quantity $T_2 = c_2^D(\partial u_2/\partial z)$ determines the sound pressure in the liquid, $c_2^D = \rho c_2^2$, and ρ and c_2 are the density and sound velocity in the liquid, respectively.

For the longitudinal oscillation mode, equations of the piezoelectric effect have the form [12]

$$T_i = c_i^D \frac{\partial u_i}{\partial z} - hD_i, \tag{12}$$

$$E_i = -h\frac{\partial u_i}{\partial z} + \beta^s D_i, \tag{13}$$

where E_i and D_i are the strength and induction of the electric field in the transmiting ($i = 1$) and receiving ($i = 3$) piezoelectric plates; $c_i^D = \rho_{0i}c_{0i}^2$ are the elastic moduli at a constant induction; ρ_{0i} and c_{0i} are the plate densities and sound velocity in the plates, respectively; h is the piezoelectric constant; and β^s is the inverse dielectric permittivity.

Substituting Eqs. (2)–(5) and (12) in boundary conditions (6)–(11), we obtain six equations in six unknowns A_n, B_n, E_m, F_m, $C(r, z)$, and $D(r, z)$. Solving these equations, we find the displacement u_3 as a function of voltage at the output of the receiving plate. Consider this solution step by step. Substitute the displacements u_1 and $u_{2,1}$ given by Eqs. (2) and (3) in Eqs. (6)–(8), multiply the resulting equations by the factor $(r/a^2)J_0(\nu_{0m}r/a^2)$, and integrate them over r from 0 to a. By the orthogonal property of the Bessel functions, the terms with $m \neq n$ will vanish in the sum. From the system of equations thus obtained in three unknowns A_n, B_n, and $C(r, 0)$, we derive an expression for $C(r, 0)$:

$$C(r,0) = \frac{4ihD_1}{c_1^D}\sum_{n=1}^{\infty} J_0\left(\frac{\nu_{0n}r}{a}\right)\frac{k_n R_n}{\nu_{0n}J_1(\nu_{0n})}\sin^2\frac{k_n d}{2}, \tag{14}$$

where $R_n^{-1} = \gamma_n \cos k_n d + i \sin k_n d$ and $\gamma_n = c_2^D k/(c_1^D k_n)$.

To determine $u_{2,1}$, we write boundary conditions (1) for $z = 0$ from the side of the liquid layer in the following form:

$$\begin{cases} u_{2,1} = C(r,0), & 0 \le r < a \\ u_{2,1} = 0, & r \ge a. \end{cases} \tag{15}$$

By applying the Hankel integral transformation to Eq. (3) with allowance for condition (15) and calculating the known integral of the Bessel functions, we obtain

$$f(\alpha) = \frac{4ihD_1 a^2}{c_1^D}\sum_{n=1}^{\infty}\frac{k_n}{k}R_n \sin^2\frac{k_n d}{2}\frac{J_0(x)}{(\nu_{0n}^2 - x^2)},$$

where $x = a\alpha$.

With this result, we obtain an expression for $u_{2,1}$ from Eq. (3):

$$u_{2,1} = \frac{4ihD_1}{c_1^D}\sum_{n=1}^{\infty}\frac{R_n}{k_n}\sin^2\frac{k_n d}{2}\int_0^{\infty} e^{-i\beta z} J_0\left(\frac{rx}{a}\right)\frac{J_0(x)x\,dx}{(\nu_{0n}^2 - x^2)}. \tag{16}$$

This expression describes the diffracted field produced by an oscillating piezoelectric plate fixed along the edge.

Using boundary conditions (8)–(10), we find expressions for E_m and F_m. We substitute Eqs. (4) and (5) in Eqs. (8)–(10), multiply the resulting expressions by the factor $(r/a^2)J_0(\nu_{0m}r/a^2)$, and integrate them over r

from 0 to a. As a result, we obtain an expression for the displacements on the receiving piezoelectric plate u_3:

$$u_3 = \frac{16ihD_1}{c_1^D}\sum_{m=1}^{\infty} J_0\left(\frac{\nu_{0m}r}{a}\right)\frac{\nu_{0m}R_m}{J_1(\nu_{0m})} \times \cos(k_m(z-L-d))\sum_{n=1}^{\infty}\frac{R_n}{k_n}\sin^2\frac{k_nd}{2}I_{mn}, \qquad (17)$$

where

$$I_{mn} = \int_0^{\infty} e^{-i\beta z}\frac{xJ_0^2(x)dx}{(\nu_{0m}^2-x^2)(\nu_{0n}^2-x^2)}. \qquad (18)$$

Setting $D_3 = 0$ and using Eq. (13), we determine the voltage amplitude at the receiving piezoelectric plate

$$U = \frac{2h}{a^2}\int_L^{L+d} dz\int_0^a(\partial u_3/\partial z)rdr.$$

Substituting expression (17) for u_3 in this equality, we obtain

$$U = \frac{64ih^2D_1}{kc_2^D}U_{mn},$$

$$U_{mn} = \sum_{m=1}^{\infty}\gamma_m R_m\sin^2\frac{k_md}{2}\sum_{n=1}^{\infty}\gamma_n R_n\sin^2\frac{k_nd}{2}I_{mn}.$$

Taking into account that $h = k_t c_{01}\sqrt{\rho_{01}/\varepsilon_1\varepsilon_0}$, $D_1 = \varepsilon_1\varepsilon_0 U_1/d$ [12], and $k_0 d = \pi$, we obtain the desired expression for U:

$$U = \frac{64ik_t^2U_1}{\gamma\pi}U_{mn}, \qquad (19)$$

where $\gamma = c_2^D k/c_1^D k_0$ is the liquid-to-plate acoustic resistance ratio, k_t is the coefficient of electromechanical coupling, ε_1 is the relative dielectric permittivity at constant strain, $\varepsilon_0 = 8.85 \times 10^{-12}$ F/m, and U_1 is the voltage amplitude at the transmitting piezoelectric plate.

In formula (19), n is the number of a frequency in the oscillation spectrum of the transmitting piezoelectric plate, and m is the number of a frequency in the oscillation spectrum of the receiving piezoelectric plate.

Calculations by formula (19) were performed with the use of a special computer program that calculated the complex-valued singular integrals (18) and summed them over indexes n and m. The diffraction damping decrement A and the diffraction increment of velocity $\Delta c/c$ were calculated as functions of the parameters ka, $s = \lambda z/a^2$, and γ by the formulas $A = 20\log(|U_0|/|U|)$ and $\Delta c/c = \psi/kz$, where U_0 is the value of U at $s = 0$ and ψ is the argument of U_{nm}. The ratio k/k_0 was set equal to 4 and the liquid-to-plate acoustic resistance ratio γ was set equal to 0.1.

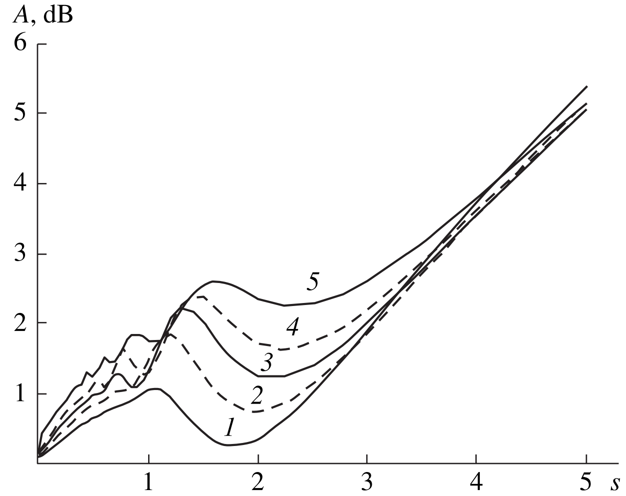

Fig. 1. Diffraction damping decrement A as a function of the generalized distance s for $\gamma = 0.1$ and different values of the parameter ka: (*1*) 100, (*2*) 140, (*3*) 200, (*4*) 300, and (*5*) 3000.

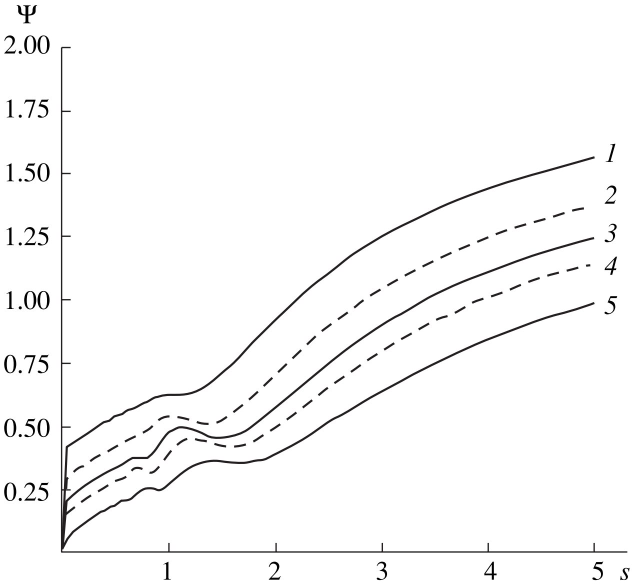

Fig. 2. Diffraction phase ψ as a function of the generalized distance s for $\gamma = 0.1$ and different values of the parameter ka: (*1*) 100, (*2*) 140, (*3*) 200, (*4*) 300, and (*5*) 3000.

Figures 1 and 2 show the parameters A and ψ as functions of s for different ka. The diffraction damping decrement A and the diffraction phase ψ calculated as functions of the generalized distance for $ka \geq 3000$ (which corresponds to fairly great ratios of the piezoelectric disc radius to the wavelength) coincide with the corresponding quantities for the field of a piston transducer within 0.1% despite the fact that the initial formulas for these cases are drastically different. Unlike the formula for the piston transducer, formula (19) includes terms dependent on the wave numbers $k_{n,m}$, i.e., on the natural frequencies of the piezoelectric

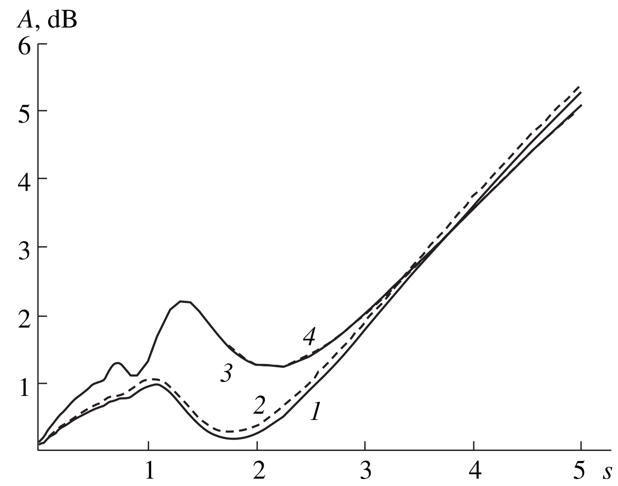

Fig. 3. Function $A(s)$ for different liquid-to-plate acoustic resistance ratios γ and different parameters ka: (*1*) $\gamma = 0.01$, $ka = 300$; (*2*) $\gamma = 0.1$, $ka = 100$; (*3*) $\gamma = 0.1$, $ka = 200$; and (*4*) $\gamma = 0.01$, $ka = 630$.

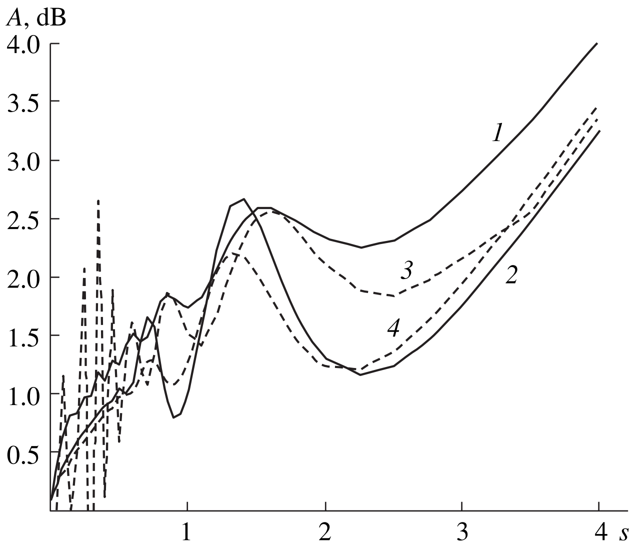

Fig. 4. Function $A(s)$ for $\gamma = 0.1$, $ka = 630$ and different relative frequencies ν: (*1*) 0.95, (*2*) 1.00, (*3*) 1.002, and (*4*) 1.02.

plates. When the parameter ka is great, a great number of natural frequencies are excited, and their sum forms an oscillation close in shape to the piston transducer oscillation. Consequently, an edge-fixed piezoelectric plate with a low Q-factor oscillates practically as a piston transducer.

For lower values of ka, the behavior of the diffraction damping decrement $A(s)$ for $s \leq 2$ differs from that of the field of the piston transducer. The decrement A decreases with decreasing ka, and the maxima and minima of the curve are shifted toward smaller values of s. The existence of this shift is supported experimentally [3, 7].

The changes in the behavior of the curve in Fig. 1 are explained by the fact that, for smaller ka, only several natural oscillations with small n and m form the major contribution to the oscillation amplitude distribution at the surface of the piezoelectric plate. From the expression for $R_{n,m}$, it follows that $R_{n,m} \sim 1/\gamma_{n,m}$ near the resonance frequency, and the smaller the parameter $\gamma_{n,m}$, the sharper the resonance characteristics of the nth and mth peaks. As the wave number k decreases, the relative interval between the peaks increases, and they may not overlap at all. However, for a large n, the amplitude of the corresponding resonance peak can be very small, because the fundamental frequency of this peak may be much higher than the excitation frequency. In addition, the parameters $k_{n,m}$ must be positive and the number of the resonance frequencies of the piezoelectric plate, which are determined by the numbers n and m, is finite and decreases with decreasing ka.

In the case of a piezoelectric plate with a small Q-factor, the diffraction corrections to the field of the piston transducer are in reasonably good agreement with experimental data [1, 3]. A fairly good agreement also occurs for a piezoelectric plate glued in a hole of a screen [2, 5]. Conversely, in the case of a piezoelectric plate with a high Q-factor, which is realized for operation in gases, the amplitude distribution of the piezoelectric plate oscillations will be governed, due to the small values of γ_n, only by one or a few resonance oscillations with small n and m.

As our calculations show, different curves correspond to the same values of ka but different values of the parameter γ. However, for arbitrary values of ka, the values of γ can be chosen so that the curves will be identical. The diffraction curve depends on the quantity $(ka)^2\gamma$ and, because of the relation $\gamma \sim Q^{-1}$, on $\varepsilon = (ka)^2/Q$ in the general case. Figure 3 shows four curves; curves *1* and *2*, as well as curves *3* and *4*, correspond to nearly the same values of ε and practically coincide.

In contrast to the field of a piston transducer, the diffraction field of an oscillating piezoelectric plate must additionally depend on the frequency f of the exciting signal. In formula (19), we represent the quantity $k_{n,m}d$ in the form $k_{n,m}d = k_0d(1 - \nu^2_{0n,m}/(k_0a)^2)^{1/2}$, where $k_0d = \pi f/f_0$, $f_0 = v_0/2d$ is the fundamental frequency of the piezoelectric plate, and v_0 is the longitudinal wave velocity in the plate. At the resonance frequency, we have $k_0d \approx \pi$ and the relative frequency $\nu = f/f_0 \approx 1$. In the calculations, we set the following values: $ka = 630$ and $\gamma = 0.01$. The maximal value of $|U|$ calculated by Eq. (19) corresponds to a frequency $f > f_0$. Figure 4 shows the functions $A(s)$ obtained near the resonance frequency for different values of f. From these curves, it follows that the oscillation amplitude of the quantity $A(s)$ increases with increasing ν. The smallest oscillation occurs at $\nu = 0.95$, which corresponds to an excitation frequency lower than f_0 (curve *1*). As the relative frequency ν slightly increases from 1 to 1.002 (curves *2* and *3*), the amplitude of oscillation considerably increases, curve *3* corresponding to the relative frequency at which the resonance amplitude decreases by 23%. The ν-dependent increase in these oscillations is explained by the fact that, as the excitation frequency increases, the oscillations with small indexes *n* and *m* make a decreasing contribution to the diffraction field while the oscillations with great indexes *n* and *m* make an increasing contribution. Our calculations showed that the functions $A(s)$ remain intact when the parameter ka decreases from 630 to 200 with a simultaneous increase in ν from 1.002 to 1.02. This means that the quantity $\chi = (\nu - 1)(ka)^2$ = const determines a family of identical curves.

Thus, this paper offers an exact solution to the diffraction problem for the ultrasonic field generated by an oscillating piezoelectric plate fixed along its edge. The resulting expressions essentially differ in form from the corresponding formulas for the field of a piston transducer and include terms dependent on the natural oscillation frequencies of the piezoelectric plates. The calculations make it possible to estimate and analyze the diffraction damping and the diffraction increment of velocity as functions of the generalized interplate distance, the *Q*-factors of the piezoelectric plates, and the deviation of the ultrasound excitation frequency from the fundamental frequency of the piezoelectric plate.

REFERENCES

1. M. Reewood, Proc. Phys. Soc. London **70**, 721 (1957).
2. E. F. Garome, J. M. Witting, and P. A. Fleury, J. Acoust. Soc. Am. **30**, 1417 (1961).
3. P. Tabuchi, Y. Tanaca, and T. Okuda, Mem. Inst. Sci. Ind. Res., Osaka Univ. **27**, 1 (1970).
4. Y. Tanaca, Acustica **23** (6), 328 (1970).
5. K. Brendel and C. Ludwig, Acustica **32** (2), 110 (1979).
6. R. C. Chivers, J. Acoust. Soc. Am. **68**, 80 (1980).
7. J. D. Aindov, A. Markiwicz, and R. C. Chivers, J. Acoust. Soc. Am. **78**, 1519 (1985).
8. B. Laulagnet, J. Acous. Soc. Am. **103**, 2451 (1998).
9. T. Imamura, Bull. NRLM **47** (4), 45 (1998).
10. L. Shuyu, Acust. Acta Acust. **86** (2), 388 (2000).
11. V. S. Kononenko and P. K. Khabibullaev, Dokl. Akad. Nauk **340** (1), 39 (1995).
12. D. Berlincour, D. Kerran, and H. Jaffe, in *Physical Acoustics: Principles and Methods*, Ed. by W. P. Mason (Academic, New York, 1964; Mir, Moscow, 1966), Vol. 1, Part A, pp. 204–326.

Translated by A. Vinogradov

Acoustical Physics, Vol. 48, No. 5, 2002, pp. 540–545. Translated from Akusticheskiĭ Zhurnal, Vol. 48, No. 5, 2002, pp. 614–620.
Original Russian Text Copyright © 2002 by Galkin, Kulakov, Popov.

Vertical Variability of Sound Fields in a Coastal Wedge

O. P. Galkin, A. V. Kulakov, and R. Yu. Popov
Andreev Acoustics Institute, Russian Academy of Sciences,
ul. Shvernika 4, Moscow, 117036 Russia
e-mail: bvp@akin.ru

Received September 3, 2001

Abstract—The results of measuring the vertical variability of sound fields are presented for a coastal wedge off the Pacific shelf of the Kamchatka peninsula. It is shown that the vertical radius of sound field correlation can reach ~30 m for frequencies within 600–800 Hz. The scatter of the specific parameters of the variability is in rather wide limits depending on the location of a vertical chain of receiving hydrophones, the hydrological conditions, the azimuth angle of the sound source, and the relief and bottom structure of the coastal wedge. *© 2002 MAIK “Nauka/Interperiodica”.*

One of the basic problems arising in monitoring the ocean by acoustic methods is the necessity to detect and locate sources of weak noiselike signals on a background of noise. For example, such problems are the control over the illegal activity of ships in a protected economic sea zone, the estimation of the tsunamigenic properties of underwater earthquakes, and some other problems of both fundamental and applied character. In order to overcome the arising difficulties, one has to use space-developed receiving arrays and optimal or quasi-optimal methods of data processing. Such methods, in one way or another, must use knowledge of the transfer function (the response function) of a channel. The calculation of the latter with a desired accuracy is, however, almost impossible because of the lack of data on the hydrological situation in the region and on the bottom characteristics at the site of the array location, and also because it is necessary to calculate the structure of the sound fields with the accuracy of a fraction of the phase of the received signal.

For a specific location of extended receiving arrays, a real way to estimate the parameters of an oceanic waveguide is to use a set of benchmark low-power sources of well-known signals. With their help, one can measure the transfer functions and the time period of their quasi-stability. In other words, it is necessary to study the characteristics of the spatial and temporal variability of the sound field in the test region. We note that many works (see, e.g., [1–3]) are devoted to studies of the variability of sound fields in the ocean. In this paper, we analyze one of the important issues of this problem, namely, the variability of sound fields at depth in the northwestern Pacific.

The experiment was carried out off the Kamchatka peninsula. Figure 1a presents the test region and the acoustic tracks, one of which is almost perpendicular to the general line of isobaths, while the other is oriented at an angle of ~45° to the first track. The numbers denote the points where ships were located: the receiving ship was anchored at point *1* and the transmitting ship drifted at points *2*–*5*. Figures 1b and 1c show the bottom profiles along the tracks between points *1*–*3* and *1*–*5*. Points *2* and *4* were at a distance of ~210 km from the point of reception, and points *3* and *5*, at ~312 km. At each of points *2*–*5*, the transmitter was lowered from the transmitting ship to a depth of 100 m; during 30 min it generated a train of pulse signals frequency-modulated by a linear law (LFM signals). The frequency deviation was in a band of 600–800 Hz. The duration of each pulse was 1 s; the pulse repetition period was 3–5 s. The signals were received by a vertical chain of 10 hydrophones with a total length of 96 m. The hydrological conditions (the sound velocity profile $c(z)$) at the site of reception are shown in Fig. 2. The upper hydrophone of the receiving chain was at a depth of 6 m, i.e., above the thermocline, and the lower hydrophone was at a depth of ~102 m, i.e., below the sound channel axis. The depths of all hydrophones are also shown in Fig. 2a. The sea depth at the point of reception was ~150 m. During the measurements, the sea roughness was less than Beaufort 3.

After filtering, the signals received by different hydrophones were entered in a computer and were subjected to a spectral-correlation analysis. In particular, the cross-correlation function of the signals received by various pairs of hydrophones was determined for different hydrophone separations in depth Δz:

$$\Phi(t, \tau) = \frac{1}{T}\int_{t}^{t+T} A_p(\eta)e^{j\omega\eta}A_k(\eta-\tau)e^{j\omega(\eta-\tau)}d\eta,$$

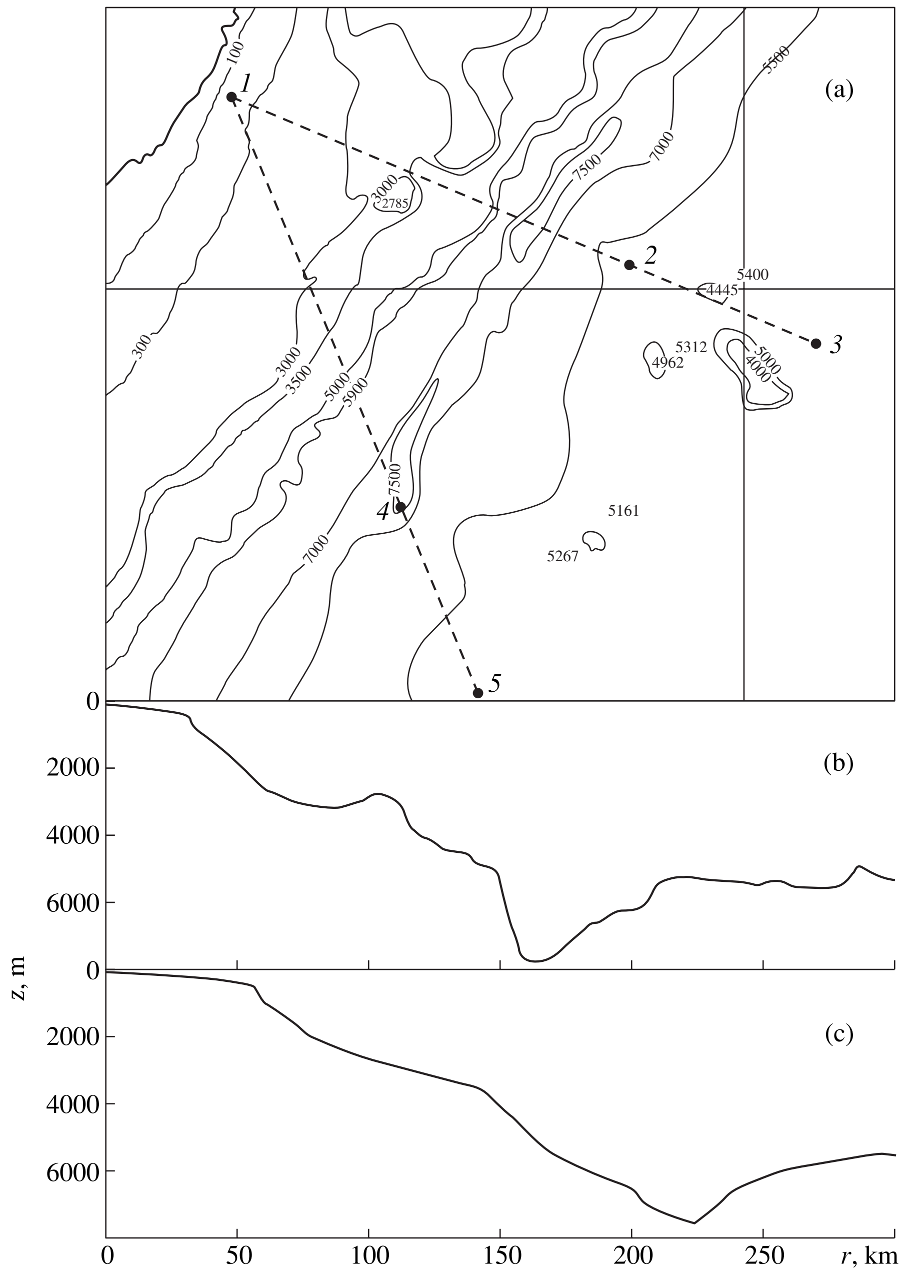

Fig. 1. (a) Test region and (*1–3*, *1–5*) the acoustic tracks with the positions of (*1*) the receiving array and (*2–5*) the transmitting ship. The bottom profiles along track (b) *1–3* and (c) track *1–5*.

where $A_p(t)e^{j\omega t}$ and $A_k(t)e^{j\omega t}$ are the signals received by hydrophones with numbers p and k, t is the running time, T is the integration time equal to the duration of the pulse in the train, $\omega = 2\pi f$, f is the sound frequency, and τ is the relative time delay between signals received by different hydrophones.

Let $A(t + a)e^{j\omega t}$ be a transmitted signal, where $A(t) = 1$ for $t \le a$ and $A(t) = 0$ for $t > a$. Such a form represents the pulsed character of the signal (a is the pulse duration). A multipath signal propagating in an oceanic waveguide and arriving at the pth hydrophone, which is located at distance r from the source, can be written as

$$S_p(t) = \sum_i^M A_p(t - t_i + a)e^{j\omega(t - t_i)}, \qquad (1)$$

where M is the number of the signals arriving at the pth hydrophone along p different rays, i is the index of the ray, and $A_p(t) = 1$ for $t_i \le t \le t_i + a$ and 0 outside this interval. The signals received by another hydrophone,

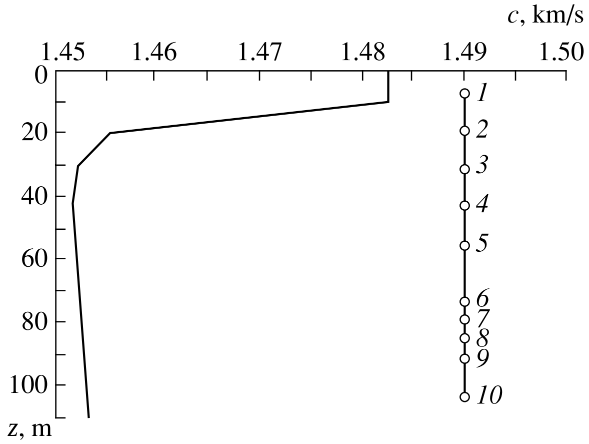

Fig. 2. Dependence of sound velocity c on depth z at the point of reception (left) and the depths of hydrophones (*1*–*10*) of the receiving chain (right).

q, separated from hydrophone p are described by a similar expression

$$S_q(t) = \sum_k^N A_q(t - t_k + a)e^{j\omega(t - t_k)}, \qquad (2)$$

where N is the number of rays over which signals arrive at the qth hydrophone and k is the number of a ray.

The cross-correlation coefficient of the signals received at points p and q can be presented as

$$R(t, \tau) = \frac{1}{T}\int_t^{t+T} \frac{S_p(\eta)S_q(\eta - \tau)}{\left[\frac{1}{T}\int_t^{t+T} S_p^2(\eta)d\eta \frac{1}{T}\int_t^{t+T} S_q^2(\eta)d\eta\right]^{1/2}} d\eta. \qquad (3)$$

In explicit form, expression (3) is very cumbersome, but the basic information is carried by only a limited number of its terms. We make some simplifying assumptions, for which purpose we consider a rather simple case of a homogeneous waveguide with the corresponding points located almost at the same depth somewhat off the channel axis. The last assumption is necessary to simplify the ray analysis. We assume that the signals arrive at every point of reception with the same focusing factors along the rays symmetric with respect to the horizontal plane (i.e., under grazing angles of equal magnitude but opposite signs). When the transmitted signal is a wide-band one (however, its band Δf is narrow enough to satisfy the condition of a weak variation of the quantity $R(t)$ within the interval a), we assume that, for most signals arriving along individual rays, the following inequality is valid:

$$t_{i+1} - t_i \ge \frac{1}{\Delta f},$$

where $1/\Delta f$ is the interval of autocorrelation of the initial signal.

Substituting Eqs. (1) and (2) into Eq. (3), we obtain that only the diagonal elements of the correlation matrix will differ from zero. Assume now that the points of reception p and q are separated in depth by the interval Δz, which is sufficiently small to neglect the wave front curvature in the vertical plane for every arriving signal [4]. In this case, from simple geometric considerations, we obtain

$$t_k = t_i + \frac{\partial t_i}{\partial z}\Delta z = t_i \pm \frac{\sin\chi_i}{c}\Delta z,$$

where χ_i is the grazing angle at the point of reception, and the sign between the terms depends on the sign of the angle of the signal arrival along the ith ray.

Then, equation (1) takes the form (under the assumption that $M = N$)

$$R_{p,q}(t, \tau) = \frac{\sum_i^M \cos\omega_0\left(\pm\frac{\sin\chi_i}{c}\Delta z - \tau\right)\int_t^{t+T} A_p(\eta - t_i - \tau)A_p\left(\eta - t_i \pm \frac{\sin\chi_i}{c}\Delta z\right)d\eta}{\left[\int_t^{t+T}\left|\sum_i^M A_p(\eta - t_i)\right|^2 d\eta \int_t^{t+T}\left|\sum_i^M A_p\left(\eta - t_i \mp \frac{\sin\chi_i}{c}\Delta z\right)\right|^2 d\eta\right]^{1/2}}. \qquad (4)$$

Taking into account the assumptions that the amplitude of each partial signal within the interval a near t_i is virtually constant and equal to unity and, therefore, the ratio of integrals in Eq. (4) is also close to unity, we obtain (after trivial trigonometric transformations)

$$R_{p,q}(t, \tau) \approx 2\cos\omega_0\tau\sum_i^M \cos\left[\omega_0\frac{\sin\chi_i}{c}\Delta z\right].$$

Hence, we obtain that there are two independent conditions for the occurrence of the main maximum of the correlation function:

$$\omega_0\tau = 0, \quad \frac{\omega_0\Delta z\sin\chi_i}{c} = \min.$$

From Eq. (4), it follows that, for a pulsed signal, there is a temporal sequence of correlation maxima appearing at times of signal arrival along a correspond-

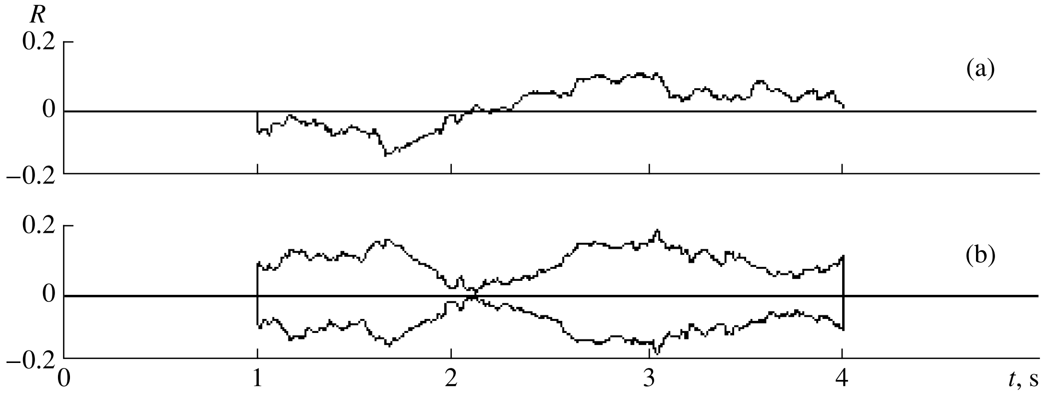

Fig. 3. (a) Dependence of the normalized short-term correlation function R of signals received by two hydrophones on the running time t for $\tau = 0$; (b) envelope of the curves similar to those presented above (Fig. 3a) for different τ; $r = 210$ km, $f = 600$–800 Hz and $\Delta z = 12$ m.

ing ray i. The change in the amplitude of these maxima with a specific index i (i.e., within the length of a spread multipath signal) is approximated by the cosine factor under the summation sign, which depends only on the angle of signal arrivals χ_i. Thus, for any fixed value $\Delta z \neq 0$ at $\tau = 0$, the correlation is maximal for all (any) signals arriving along rays; the specific value of this maximal correlation is different for different signals and is determined by the argument of the cosine in the sum in Eq. (4). In particular, if we assume that the ray number is i and the frequency ω_0 and the interval Δz satisfy the condition

$$\frac{\omega_0 \Delta z \sin\chi_i}{c} = \frac{\pi}{2}(l-1),$$

where l is an even integral number, we obtain that a specific value of the ith correlation maximum is close to zero for any delay τ. It is precisely this pattern that is observed in the measurements of the short-term cross-correlation function for real LFM signals received by a vertical chain of hydrophones at fixed values of ω_0 and Δz and at different values of τ. The above-mentioned results are illustrated in Fig. 3, which exhibits a dependence of the short-term correlation coefficient R on the time t for $\tau = 0$ (curve *a*) and the envelope of the family of such curves for different τ (plot *b*). In the plots $R(t)$, one can clearly see a region where the correlation is minimal (the so-called “neck”).

Now, we consider other features of the results obtained. Figure 4 shows the behavior of the envelopes of normalized correlation functions obtained from 29 realizations of the LFM signals received by two hydrophones separated in depth by 6 m (the depths are ~74 and ~80 m). The pulse repetition period in a train was 3 s. The signals were generated at point *2* (see Fig. 1a) located at a distance of ~210 km from the hydrophones. The mean peak value of the correlation coefficient (from 29 realizations) was $\bar{R} \cong 0.5$ for the standard deviation $\sigma \cong 0.03$. If the distance between the hydrophones increases by a factor 2 ($\Delta z = 12$ m), we obtain $\bar{R} \cong 0.43$ with $\sigma \cong 0.02$ (the mean depth of the receiving base is ~56 m). The sufficient length of the chain of hydrophones allowed one to carry out measurements at a constant separation of the receiving elements ($\Delta z = 12$ m) located, however, at different depths in the water layer. In this case, the value of $\bar{R}$ varies from 0.12 (when the hydrophones are located in the thermocline) to 0.43–0.45 (for the central part of the chain); the maximal values of $\bar{R}$ correspond to the position of hydrophones near the sound channel axis. A further increase in the separation of hydrophones in depth, Δz, allowed us to estimate the vertical correlation radius ρ as a measure of the vertical variability of the sound field. When the correlation radius is defined as such a value of Δz at which $\bar{R}$ decreases by a factor of e, its value in the considered series of experiments will be close to 24 m; if it is defined as Δz at which $\bar{R}$ decreases to the background level, we obtain $\rho \cong 30$ m. Note that, for signals arriving along each individual ray (of the multiray bundle of signals), the values of $\bar{R}$ must be greater than those mentioned above [5]. This is related to the fact that the values of $\bar{R}$ were determined in our experiment for the total sum of signals received, i.e., in the presence of an additional interference. It was produced by signals that arrived within the averaging time T but were not cross-correlated when the difference in the arriving times over different rays exceeded the autocorrelation interval of the initial signal ($1/\Delta f$). Such an interference is usually called additive signal interference.

It should be noted that, at different depths of reception, the sound field variability can be much greater, particularly, near the velocline in the profile $c(z)$.

Similar measurements carried out at a distance of 312 km from the source (point *3*, in Fig. 1) yielded almost the same estimates of the radius of the sound

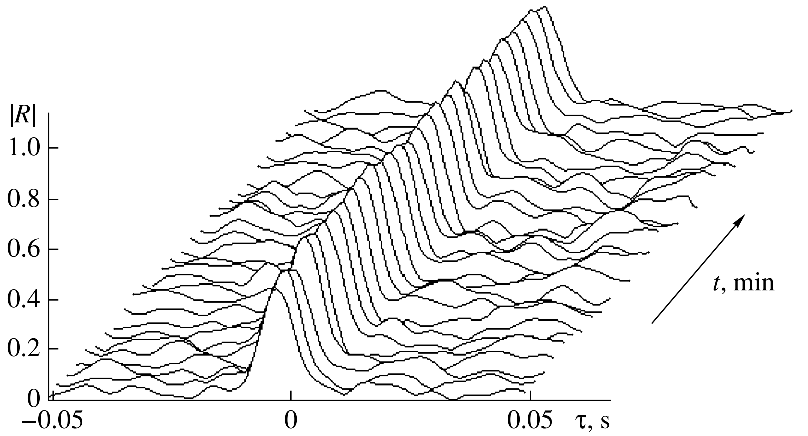

Fig. 4. Envelopes of normalized correlation functions within a 3-min-long initial part of the train for the LFM signals received by two hydrophones separated by $\Delta z = 6$ m, for $\tau = 0$. The signals are generated at point *2* of the first track (Fig. 1a); $r = 210$ km.

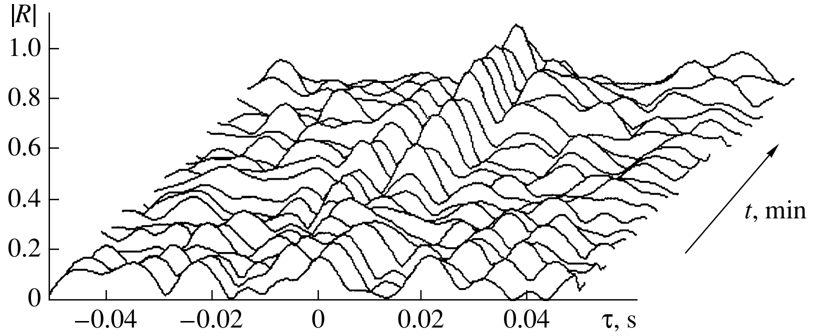

Fig. 5. The same as in Fig. 4 with the signal generation at point *4* of the second track (Fig. 1a). The data refers to a 3-min-long terminal part of the train of the LFM signals.

field variability with the same standard deviations σ (0.01–0.02).

Entirely different results were obtained with a change of the azimuth angle of the source, i.e., with the sound radiation at points *4* and *5* of the second track (Fig. 1). Figure 5 presents a plot similar to that in Fig. 4 but obtained for the source located at point *4* (the only difference was in the pulse repetition period in the train, which was increased up to 5 s). As seen from Fig. 5, the values of $\bar{R}$ are mainly at the background level. Only in the last 3 min of the total 30-min radiation period did the values of $\bar{R}$ begin to exceed the background ($\bar{R} \cong 0.22$ with $\sigma \cong 0.07$). The allowance made for the speed and direction of the drift of the transmitting ship (the measurements were carried out with a satellite navigation system) showed that the length of the track increased by 1.3–1.5 km within 30 min. A detailed calculation of the sound field characteristics given an increase in the track length by almost the same value (from 210 to 212 km) at the depths 72, 78, and 84 m (hydrophones *6*, *7*, and *8* in Fig. 2) showed that, even within such a small interval of distances, the sound field structure can undergo significant changes. Figure 6 presents the sound field intensity calculated at the mean frequency of the range used (700 Hz) with allowance for the phase shifts of the received signals in the aforementioned interval of distances. Figure 6a refers to the track oriented almost normally to the general direction of isobaths in the region of the coastal slope (tracks *1–3* in Fig. 1a). Figure 6b refers to the track lying at an angle of 45° (tracks *1–5* in Fig. 1a). Note that the calculation was carried out for smoothed bottom geometry of a real coastal wedge for the selected tracks. As seen from these plots, the sound field level is very low at several distances (for example, 210.3 and 210.8 km in Fig. 6a and 210.7 and 211.6 km in Fig. 6b) due to the interference of the arriving signals. Therefore, the cross-correlation coefficient between the signals received by hydrophones separated in depth will be close to the background level determined by the noise at the point of reception in the case when a signal at one (or more) of the hydrophones is very weak or even absent. At the same time, at those distances where the intensity of the total signal for the considered depths is high (for example, at distances 211.1 and 211.7 km in Fig. 6a and 210.4 and 211.1 km in Fig. 6b), one can expect maximal values of the correlation coefficient. Therefore, we can assume that the dependences illustrating the behavior of envelopes of the normalized correlation func-

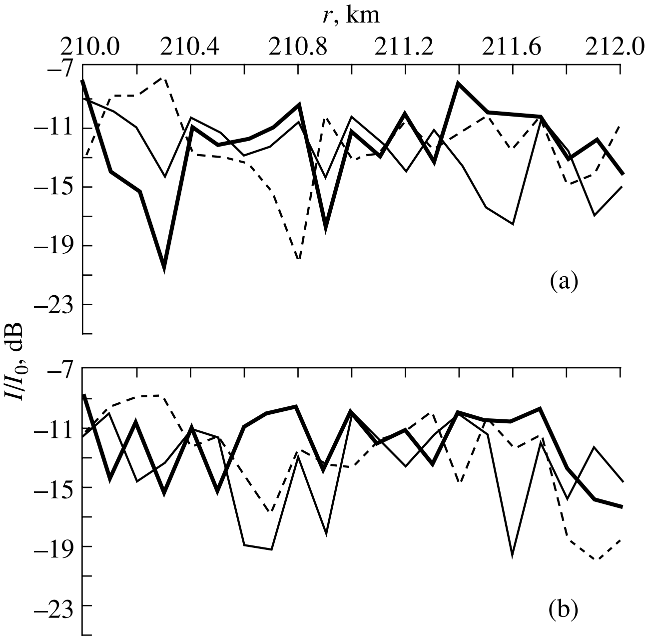

Fig. 6. Dependence of the normalized intensity I/I_0 (I_0 is the intensity at the distance $r = 1$ km) on the distance r with allowance for the phase of the arriving signals: (a) track *1–2*; (b) track *1–4*. The depths of reception are 72 m (thick solid lines), 78 m (thin solid lines), and 84 m (dotted lines).

tions, which are presented in Figs. 4 and 5, are mainly related to the change of distance due to the drift of the transmitting ship.

It should be noted that the values of the vertical radii of spatial correlation, ρ, at points *3* and *5,* i.e., at distances of ~300 km, are close to those presented for the distance 210 km, although, on the southern track, they were always somewhat less.

Thus, on the basis of the full-scale measurements and calculations, we can conclude that the vertical variability of sound fields in the frequency band 600–800 Hz is essentially anisotropic in the azimuth plane, because it depends not only on the hydrological conditions and positions of the hydrophones in depth, but also on the geometry of the coastal wedge. The latter undergoes significant changes when the acoustic track is rotated in the azimuth direction. Besides, in the narrow-band analysis of the experimental data, there are certain parts of a multiray signal related to the arrival of individual signals at such angles at which, for a given frequency ω_0 and a fixed separation of hydrophones in depth Δz, the short-term correlation coefficient is close to the background level at any time delay τ. In this case, the so-called necks of the envelope of the correlation function are formed. The signs of the cross-correlation coefficient are different for the signals arriving before and after the neck, and, therefore, the value of the correlation coefficient averaged over the total spreading time of a multiray continuous signal can be very low. However, this fact does not characterize the true extent of the sound field coherence, because, in the experiments under consideration, the spatial resolution of signals propagating along individual rays was absent [6].

In summary, we can state that, in the specific summer–autumn conditions of the northeastern region of the Pacific Ocean (off the Kamchatka peninsula), the sound field variability in depth was considerable. When the corresponding points were located near the sound channel axis, the vertical interval of the sound field correlation in the coastal wedge was no greater than 30 m (for frequencies within 600–800 Hz). As the hydrophones were displaced from the channel axis, the correlation interval decreased, especially, when the receiving elements were displaced toward the thermocline. Clearly, in other regions of the ocean with different hydrological and oceanological characteristics of the waveguide, the values of the vertical correlation interval of the sound field in a coastal wedge can differ from those presented above.

ACKNOWLEDGMENTS

We thank Yu.I. Tuzhilkin who suggested the approach for analyzing the vertical variability of the sound fields produced by underwater explosions, and we are grateful to A.E. Lents, who carried out the necessary calculations.

This work was supported by the Russian Foundation for Basic Research, project no. 00–02–17694.

REFERENCES

1. Kwang Yoo and T. C. Yang, J. Acoust. Soc. Am. **106**, 3255 (1999).
2. O. P. Galkin, A. V. Mikryukov, O. E. Popov, and R. Yu. Popov, Akust. Zh. **43**, 616 (1997) [Acoust. Phys. **43**, 529 (1997)].
3. V. M. Baronkin, M. V. Zheleznyakov, and R. Yu. Popov, in *Acoustics in the Ocean* (Nauka, Moscow, 1992), pp. 127–135.
4. O. P. Galkin, N. N. Komissarova, B. L. Lyutarevich, and E. A. Kharchenko, Akust. Zh. **40**, 575 (1994) [Acoust. Phys. **40**, 509 (1994)].
5. O. P. Galkin and S. D. Pankova, Akust. Zh. **45**, 479 (1999) [Acoust. Phys. **45**, 426 (1999)].
6. O. P. Galkin, R. Yu. Popov, Yu. V. Semenov, and E. V. Simakina, Akust. Zh. **47**, 616 (2001) [Acoust. Phys. **47**, 534 (2001)].

Translated by Yu. Lysanov

Acoustical Physics, Vol. 48, No. 5, 2002, pp. 546–551. Translated from Akusticheskiĭ Zhurnal, Vol. 48, No. 5, 2002, pp. 621–626.
Original Russian Text Copyright © 2002 by Egerev, Fokin, Szurkowski.

Photoacoustic Express Diagnostics of Lubricating Oil: Model Investigations

S. V. Egerev*, A. V. Fokin*, and J. Szurkowski**

** Andreev Acoustics Institute, Russian Academy of Sciences, ul. Shvernika 4, Moscow, 117036 Russia*
e-mail: egerev@akin.ru
*** Institute of Experimental Physics, University of Gdansk, Wita Stwosza 57, Gdańsk, PL-80952 Poland*

Received October 20, 2001

Abstract—The possibility of evaluating the size of metallic inclusions in lubricating oil by photoacoustic measurements in a gas-microphone cell is investigated. The photoacoustic spectra of suspensions of microscopic spherical steel particles with diameters from 5 to 70 μm in an oil layer with a thickness of 20 μm are measured. A semiquantitative model of the photoacoustic effect in a suspension layer is proposed for inclusions of both small and large size in comparison with the layer thickness. It is demonstrated that the body of information obtained from the measurements considerably increases when the thickness of the oil layer is close to the size of inhomogeneous inclusions. © *2002 MAIK "Nauka/Interperiodica".*

One of the most important problems of vehicle servicing is a timely change of lubricating oil in engines and transmissions. A too frequent change of oil increases running expenses and a too rare one affects the safety of operation. Therefore, special attention is given to the development of techniques for the express diagnostics of industrial oils. Informational symptoms of oil aging are the processes of oil decomposition and the appearance of a considerable amount of metallic particles in it. The diagnostics is based on exactly these symptoms. Common spectrophotometric methods of diagnostics are rarely applied to optically dense liquids like industrial oils. On the contrary, photoacoustic techniques offer good opportunities for analyzing optically dense suspensions.

The conventional gas-microphone version of the photoacoustic diagnostics of solids and liquids is as follows. A sample to be studied is placed into a sealed (as a rule) photoacoustic cell consisting of one or several chambers filled with air [1]. The cell has one or several windows through which the sample is heated by intensity-modulated radiation from a laser or from some other source. The heat transfer between the sample and the air surrounding it in the cell gives rise to pressure oscillations (a photoacoustic signal), which are detected by a microphone. These signals depend on the sample's properties and are used for its diagnostics [2, 3].

A sample may be additionally characterized by measuring the dependence of the pressure amplitude in the cell on the wavelength of the optical source. Such a dependence is called the photoacoustic spectrum of a sample. The gas-microphone photoacoustic technique alone or in combination with differential scanning calorimetry can be used for the determination of the thermodynamic properties of a sample [4] and for analyzing strongly scattering samples [5]. This method is also used for the depth profiling of multilayer structures [6] and the monitoring of biomass [7] and exciton structures [8].

The photoacoustic analysis of lubricating oil samples has a history. For example, a technique for the photoacoustic detection of the processes of oil decomposition is described in [9]. The present paper concentrates on another feature; namely, we examine the gas-microphone photoacoustic response of an inhomogeneous sample represented by a suspension of microscopic particles in oil. It is of interest to examine the case of an especially small inhomogeneous sample, when the initial liquid layer is rather thin and its thickness is close to the size of inhomogeneities in it. Indeed, the impurities present in a sample affect the form of the photoacoustic spectrum differently, depending on whether they are immersed in oil completely or project above the surface, which can make their detection and analysis easier. Thus, the main purpose of this work is the study of the process of photoacoustic conversion in conditions when the particle size is comparable with the thickness of the oil layer with the aim to answer the question of what information on the quantity, size, and characteristics of the particles can be obtained by measuring the photoacoustic spectra at different ratios between the oil layer thickness and the size of inclusions.

It was found that the measurement of the photoacoustic spectra of an oil sample of a fixed thickness with steel spherical microscopic particles of various diameters is a sufficiently good model for the process of microscopic particle detection in oil by measuring the photoacoustic spectra for samples of different thicknesses.

1063-7710/02/4805-0546$22.00 © 2002 MAIK "Nauka/Interperiodica"

Figure 1 shows the scheme of the utilized photoacoustic gas-microphone cell of special design. The cell was made of aluminum, and its upper and lower windows were made of quartz. The total height of the cell was 4 mm, and its diameter was 30 mm. A condenser microphone by Bruel and Kjaer (model 4144) was used as a sound receiver. The photoacoustic measurements were conducted within a wavelength range of 400–750 nm. A 400-W xenon arc lamp combined with a grating monochromator and controlled by a personal computer was used as a light source. The frequency of light modulation was 20 Hz.

Industrial lubrication oil Transol SP-100 was used as the initial liquid for sample preparation. A sample was prepared in the thin-layer version (the layer thickness was 20 μm). Calibrated microscopic spherical steel particles were added to the layer. Particles of only one size were present in each sample. It was possible to select particles with diameters from 5 to 70 μm. Thus, we had both samples with totally immersed inhomogeneities and samples with the particles noticeably projecting above the oil surface. The volume concentration of particles was 0.1%.

The results measuring the photoacoustic spectra for several inhomogeneous samples differing in the size of their inclusions are given in Fig. 2. The photoacoustic spectrum for the initial oil is given also. Its decrease with the wavelength indicates that oil becomes more transparent in the red and infrared ranges.

It is worth noting that, in the range of small wavelengths up to 500 nm, the curves corresponding to oil with particles are close to each other, although the particle diameters change considerably. The corresponding spectra of inhomogeneous samples qualitatively reproduce the curve for the initial spectrum of pure oil but noticeably exceed it in their levels.

Near a wavelength of 500 nm, the family of photoacoustic spectra of inhomogeneous samples splits into two groups, depending on the ratio between the particle size and the layer thickness. In the case of samples containing only small particles, the amplitude of the photoacoustic signal decreases with increasing wavelength. The second group of curves corresponds to large particles, which project over the oil surface. Here, the photoacoustic amplitude almost does not depend on the radiation wavelength. In both groups, the amplitude of the photoacoustic signal depends weakly on the particle size. It is worth noting that, in the group of small particles immersed in oil, the amplitude of the photoacoustic signal decreases with the growth of the particle diameter, while in the case of large particles, it increases. This fact indicates that the photoacoustic conversion for small and large particles occurs in different conditions. Indeed, large particles touch the cell bottom and part of their surface is not covered with oil. Therefore, compared to small particles, new factors come into play, such as the heat transfer through the cell bottom, the radiation absorption, and the heating of air directly by a part of the particle surface without the intermediate layer of oil. The role of these factors is examined further on the basis of a theoretical model.

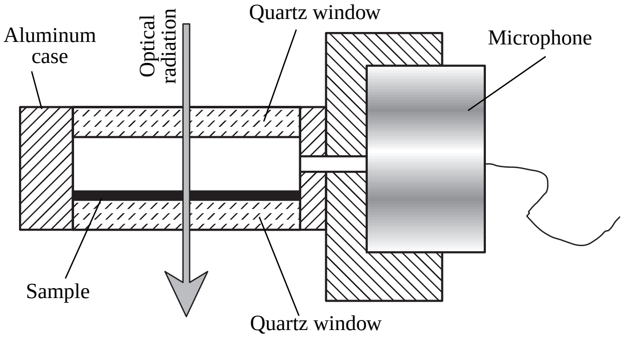

Fig. 1. Schematic diagram of a photoacoustic gas-microphone cell.

The following model of the phenomenon was developed to interpret the experimental results. It is possible to calculate the amplitude of the photoacoustic signal in a general case by taking into account the scattering of optical radiation by the particles in oil. However, the basic experimentally determined features of the photoacoustic conversion, i.e., the splitting of the curve family into two branches (depending on whether the particle diameter exceeds the thickness of the oil layer or not) and the weak dependence on the particle diameter in each of the branches, can be explained within the framework of the semiquantitative model considered below. It is based on the fact that the scattering changes the shape of the photoacoustic spectrum only slightly, even when it is large, and it changes the amplitude of the photoacoustic signal considerably, as demonstrated in [10].

The process of the formation of a photoacoustic signal represented by pressure pulsations in the cell chamber occurs as follows. Optical radiation with the intensity

$$I = I_0(1 + \cos\omega t)/2$$

modulated with the frequency $f = \omega/2\pi$ is absorbed by both oil and metallic particles present in it. As a result of radiation-free oscillatory-translational relaxation, the absorbed electromagnetic energy is converted into heat, which leads to heating and, as a consequence, to the thermal expansion of the particles, the oil, and the layer of air adjoining the oil. By virtue of the linearity of the photoacoustic conversion, the amplitude of the photoacoustic signal is represented by the sum of the signals produced by the thermal expansion of the oil, particles, and air. The problem of the ratio of contributions from the expansion of the condensed medium (oil in our case) and air is considered quantitatively in [11], where it is demonstrated in particular that the first component is negligible when the thickness of the oil layer is equal in its order of magnitude or small in comparison with the penetration depth of a temperature wave in air $\mu_g = (2\chi_g/\omega)^{1/2}$. Here, the index g denotes air; $\chi =$

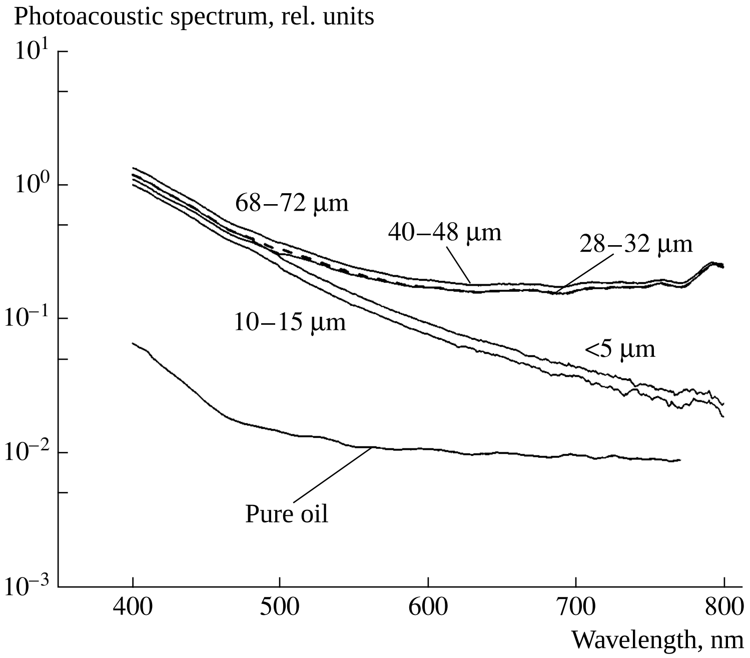

Fig. 2. Photoacoustic spectra of pure oil and inhomogeneous samples with admixture of steel particles with different diameters (the diameters are indicated in the plot). The thickness of the oil layer is 20 μm. The volume concentration of particles is 0.1% for all samples.

$\kappa/\rho C_p$ is the thermal diffusivity; and κ, ρ, and C_p are the heat conductivity, density, and specific heat (at constant pressure). In our experiment (the modulation frequency is 20 Hz), we have $\mu_g = 560$ μm, which far exceeds the thickness of the oil layer $h_l = 20$ μm. Therefore, the only source of the photoacoustic signal is the thermal expansion of air. It can be easily demonstrated that the presence of particles in oil does not influence the obtained conclusion.

The air heating is determined by the absorption of optical radiation both in oil and particles. Taking into account the linear character of photoacoustic conversion, the amplitude of the photoacoustic signal can presented in the form

$$p = p_l + p_p, \tag{1}$$

where p_l is the component describing the response of oil and p_p is that for particles.

Strictly speaking, Eq. (1) is valid for the sum of complex quantities. However, it is possible to ignore the phase shift and make estimates using real quantities in the case under study. This can be explained by the fact that the penetration depth of a temperature wave in oil μ_l (for the frequency $f = 20$ Hz) is approximately equal to 40 μm and exceeds the sample thickness. The penetration depth of a temperature wave in particles also exceeds their diameters. Thus, the phase shift between the aforementioned components arises only because of the propagation of heat from particles along the oil surface. As will be demonstrated further, its value does not exceed $\pi/4$ and can be ignored in our estimations.

As demonstrated in [10], the signal component corresponding to the response of the initial liquid can be presented (taking into account the scattering by metallic particles) in the form

$$p_l = AR\beta I_0/2, \tag{2}$$

where β is the absorption coefficient of optical radiation in oil; A is the factor describing the contribution of both the configuration of the photoacoustic cell and the thermoelastic parameters of oil and gas filling the cell, which does not depend on the optical parameters of oil and particles; and R is the factor taking into account the scattering. The last depends on the relationship between the lengths of absorption and scattering of optical radiation, the penetration depth of a temperature wave in oil, and the thickness of the oil layer.

In the general case, the dependence of the quantity R on the absorption and scattering, which are determined by the optical characteristics of the oil and particles and the particle size, has a complex nonmonotonic character. In the case of small values of the scattering coefficient, the value of R grows with its increase because of the increase in the quantity of the energy absorbed in the sample due to the decrease in the number of photons leaving the sample through its rear nonirradiated surface. In the case of very large values of the scattering coefficient, the value of R decreases with its increase, since the number of photons leaving the sample through its front irradiated surface increases. There is a rather large range of values of the scattering coefficient for which the indicated mechanisms partially compensate each other and the value of R, sometimes exceeding unity, depends only slightly on the scattering and absorption.

Precisely this case is observed in our experiment. Indeed, in the wavelength range $\lambda < 500$ nm, where the magnitude of the photoacoustic signal is determined by the absorption in oil and the contribution from the absorption in particles is inessential, the curves corresponding to different values of the absorption coefficient in particles (and therefore, to different values of the scattering coefficient as well) almost coincide and repeat in their shape the photoacoustic spectrum of pure oil.

The photoacoustic component connected with the radiation absorption in particles is described in a more complex way. Let us consider qualitatively the process of the formation of a photoacoustic signal in the case of radiation absorption by a single particle with the diameter d. First of all, we are interested in the dependence of the photoacoustic signal on the particle diameter. The character of this dependence depends essentially on the relationship between the particle diameter and the thickness of the oil layer.

Consider the case when the particle diameter is small in comparison with the thickness of the oil layer. According to the results of [11], the magnitude of the photoacoustic response is proportional to the average (over the surface) amplitude of temperature oscillations of the oil surface. To evaluate the amplitude, we use the relation describing a temperature wave in the oil surrounding a particle with the surface temperature changing according to the harmonic law $T_0\exp(i\omega t)$ [11, 12]:

$$T(r) = T_0\frac{R}{r}\exp\left[-\frac{1+i}{\mu_l}(r-R)+i\omega t\right], \qquad (3)$$

where r is the distance from the particle center and $R = d/2$ is the particle radius. The assumption that the particle heating is uniform is valid, since the penetration depth of the temperature wave far exceeds the particle size in the conditions of the experiment.

As was mentioned above, the thickness of the oil layer is small in comparison with the penetration depth of the temperature wave. Therefore, according to Eq. (3), the estimate $T_s \sim T_0(R/h)$ is valid for the amplitude of temperature oscillations T_s at the oil surface at the point located directly over the particle (the focus of heating), where h is the distance from the particle center to the oil surface. In calculating the amplitude of oscillations of the average temperature of the oil surface, it is necessary to take into account only the exponential drop of temperature that is described by the second factor in Eq. (3). Indeed, the surface temperature decreases in inverse proportion to r when the distance from the heating focus grows. However, in the process of calculating the average temperature, this decrease is compensated by the growth of the effectively heated area in proportion to r. Thus, ignoring the phase shift of about $\pi/4$, we obtain the following estimate for the amplitude of average temperature oscillations:

$$\bar{T}_s \sim T_0\frac{R}{h}\frac{\mu_l^2}{D^2}, \qquad (4)$$

where D is the characteristic diameter of the sample that is determined by the size of the photoacoustic cell. It is assumed that $\mu_l < D$.

For a system of particles immersed in oil with the concentration n (the number of particles per unit volume), the photoacoustic signal is the sum of individual responses, and, finally, we obtain the following estimate for the component of the amplitude of pressure fluctuations in the cell p_p that is connected with the radiation absorption in particles:

$$p_p \sim BnVT_0\frac{R}{\bar{h}}\frac{\mu_l^2}{D^2}, \qquad (5)$$

where the factor B depends on both the thermoelastic parameters of the air filling the cell and on its size, V is the volume of the oil layer, $\bar{h} = h_l/2$ is the distance to the sample surface that is averaged over the particle ensemble, and h_l is the thickness of the oil layer.

The amplitude of temperature oscillations T_0 can be estimated proceeding from the law of energy conservation. Taking into account the fact that the energy of optical radiation absorbed during the time $1/f$ is converted into the thermal energy concentrated in a particle and the layer of oil surrounding it that has a thickness of the order of magnitude of μ_l, we obtain the following estimate for T_0:

$$T_0 \sim \frac{\sigma I_e f^{-1}}{d^3(\rho C_p)_p + \mu_l^3(\rho C_p)_l}, \qquad (6)$$

where σ is the absorption cross section of optical radiation, I_e is the effective value of optical radiation intensity, C_p is the specific heat at constant pressure, and ρ is the density. The subscripts p and l indicate that this quantity belongs to particles or oil, respectively.

In the general case, the absorption cross section can be represented in the form

$$\sigma = S_{pl}(m_{lp}, \lambda/d)\pi d^2/4,$$

where m_{lp} is the complex refractive index of a particle with respect to oil [13]. In our case, the dimensions of particles are large in comparison with the wavelength of optical radiation. Therefore, the dependence of the function S_{pl} on λ/d is weak, and it may be ignored in our estimations assuming that $S_{pl}(m_{lp}, \lambda/d) = S_{pl}(m_{lp})$. In the general case, $I_e = KI_0$, where the factor K depends on the optical parameters of the liquid and particles as well as on their dimensions. The character of this dependence is analogous in many ways to the dependence of the factor R involved in Eq. (2) on the indicated quantities, and this dependence can be also ignored.

Taking into account the fact that the volume concentration of particles n_v is maintained constant in our experiment, i.e.,

$$n_v = \pi n d^3/6V = \text{const},$$

we obtain the following estimate for the amplitude of the photoacoustic response of a particle ensemble from Eqs. (5) and (6):

$$p_p \sim B n_v V^2 I_e \frac{\mu_l^2}{f h_l D^2} \frac{S_{pl}(m_{lp}, \lambda/d)}{d^3(\rho C_p)_p + \mu_l^3(\rho C_p)_l}. \qquad (7)$$

Since the specific heat of metallic particles is close to that of oil, the terms in the denominator are of the same order of magnitude for $d \sim \mu_l \sim 40$ μm. Thus, if the particle diameter is small in comparison with both the thickness of the oil layer and μ_l, the magnitude of the photoacoustic signal almost does not depend on the particle diameter d, but it decreases when d becomes close to μ_l. This is observed in the experiment (see the curves corresponding to the particles with diameters <5 μm and 10–15 μm in Fig. 2).

Another case is that of large particles with dimensions exceeding the thickness of the oil layer. In this case, Eq. (7) takes on the form

$$p_p \sim B n_v V^2 I'_e \frac{\mu_l^2}{f D^2} \frac{S_{pg}(m_{lp}, m_{lg}, \lambda/d, h_l/d)}{d^3(\rho C_p)_p + \mu_s^3(\rho C_p)_s} \frac{1}{d}, \qquad (8)$$

where m_{lg} is the complex refractive index of a particle with respect to air, and the subscript s indicates that this quantity refers to quartz. In deriving this estimate, we took into account the fact that particles touch the quartz bottom, and the main part of heat is transferred into it. The presence of the additional factor $1/d$ in Eq. (8) in comparison with Eq. (7) is connected with the absence of temperature decrease in the process of propagation of a temperature wave from the particle surface to the oil surface, which is described by the factor d/h in Eq. (4).The replacement of I_e by I'_e indicates a change in the scattering character due to the fact that, when $d > h_l$, a part of the particle surface is not covered by oil and the optical radiation heats it directly and not through the oil layer. We introduce a more general function S_{pg} instead of S_{pl}, since the cross sections of scattering and absorption differ for two types of boundaries, namely, the particle–air and oil–particle boundaries.

Taking into account the fact that the specific heats of particles and quartz are close, the terms in the denominator are of the same order of magnitude at $d \sim \mu_s \sim 1$ mm. Thus, since the diameter of the particles used in the experiment is smaller than 1 mm, the dependence of p_p on the particle diameter is involved only in the term S_{pg}/d. The agreement with the experiment is attained if we assume that S_{pg} grows with an increase in particle diameter faster than the first power of d, which is quite reasonable, since the area of a particle irradiated directly by the incident radiation and not by the one transmitted through the oil layer increases with the growth of d. The splitting of curves into two families corresponding to the particles completely covered by oil and those only partially covered by oil is explained by the change in the scattering character, which formally corresponds to the change of I_e for I'_e and S_{pl} for S_{pg}. To describe the character of curve splitting more precisely, it is necessary to know the dependences of I_e, I'_e, S_{pl}, and S_{pg} on the relationship between the particle diameter, the wavelength of optical radiation, and the thickness of the oil layer.

Substituting expressions for p_l and p_p into Eq. (1), we obtain the following estimate for the photoacoustic response of a liquid with particles:

$$p = AR\beta I_0/2$$

$$+ \begin{cases} B n_v V^2 I_e \dfrac{\mu_l^2}{f h_l D^2} \dfrac{S_{pl}(m_{lp}, \lambda/d)}{d^3(\rho C_p)_p + \mu_l^3(\rho C_p)_l}, & d < h_l \\[2ex] B n_v V^2 I'_e \dfrac{\mu_l^2}{f D^2} \dfrac{S_{pg}(m_{lp}, m_{lg}, \lambda/d, h_l/d)}{d^3(\rho C_p)_p + \mu_s^3(\rho C_p)_s} \dfrac{1}{d}, & d > h_l. \end{cases} \qquad (9)$$

These expressions qualitatively describe the experimental results presented above. The first term in Eq. (9) plays the main role within the range of wavelengths smaller than 500 nm, where the absorption in oil is essential and it is possible to ignore the absorption (but not the scattering) in the particles. Therefore, the curve for the spectrum of an inhomogeneous sample reproduces the curve of the spectrum for pure oil by exceeding it in level on account of factor R taking into account the scattering.

On the contrary, the absorption in oil can be ignored in the range of wavelengths greater than 500 nm. The dominant role belongs to the second term in Eq. (9). Already its form demonstrates that the spectra for inhomogeneous samples split into two groups, depending on whether the particles are immersed in oil or project over the surface. It is necessary to note that, as was shown above, the derived expressions also qualitatively explain the behavior of the spectra depending on the particle diameters within each group.

The study described above demonstrates that gas-microphone photoacoustic spectroscopy is effective for analyzing very small amounts of inhomogeneous samples. In this case, if the thickness of the sample layer is comparable with the dimensions of inclusions, the character of the photoacoustic spectrum in the wavelength range where the absorption in particles is essential allows one to conclude whether small or large particles dominate in the sample. Moreover, performing measurements for different thicknesses of the sample under analysis, it is presumably possible to obtain information on the distribution of particles in size. Thus, gas-microphone photoacoustic measurements, being inferior to direct photoacoustic detection in sensitivity [14], are advantageous from the point of view of the amount of information they provide.

ACKNOWLEDGMENTS

We are grateful to the Warsaw Institute of Aviation and personally Dr. B. Wislicki for the assistance in the sample preparation. We are also grateful Dr. J. Motylewski for the fruitful discussion of the results. The theory of the phenomenon was developed under the Cooperation Agreement between Gdańsk University (Poland) and the Scientific Council on Acoustics of the Russian Academy of Sciences.

REFERENCES

1. A. E. Pashin and A. V. Fokin, Akust. Zh. **39**, 715 (1993) [Acoust. Phys. **39**, 376 (1993)].
2. A. Rosencwaig, *Photoacoustics and Photoacoustic Spectroscopy* (Wiley, New York, 1980).
3. S. V. Egerev, A. V. Fokin, and A. E. Pashin, Rev. Sci. Instrum. **67** (8), 2691 (1996).
4. T. G. Vassile, Thermochim. Acta **330** (1–2), 145 (1999).
5. M. Grus and A. Sikorska, Physica B (Amsterdam) **266** (3), 139 (1999).
6. M. Halttunen, J. Tenhunen, T. Saarinen, and P. Stenius, Vibr. Spectrosc. **19** (2), 261 (1999).
7. K. Schmidt and D. Beckmann, Sens. Actuators B **51** (1–3), 261 (1998).
8. G. Sundararajan, Y. V. G. S. Murti, and A. R. Dhobale, Solid State Commun. **106** (4), 193 (1998).
9. J. Motylewski, J. Szurkowski, T. Zmiercak, *et al.*, Prog. Nat. Sci. **6** (Suppl.), S-634 (1996).
10. P. Helander, I. Lundstrom, and D. McQueen, J. Appl. Phys. **51** (7), 3841 (1980).
11. F. A. McDonald and G. C. Wetsel, in *Physical Acoustics*, Ed. by W. P. Mason and R. N. Thurston (Academic, New York, 1988), p. 502.
12. H. S. Carslaw and J. C. Jaeger, *Conduction of Heat in Solids*, 2nd ed. (Oxford Univ. Press, Oxford, 1959), p. 40.
13. H. C. van Hulst, *Light Scattering by Small Particles* (Wiley, New York, 1957).
14. S. V. Egerev and A. V. Fokin, Proc. SPIE **3916**, 210 (2000).

Translated by M. Lyamshev

Acoustical Physics, Vol. 48, No. 5, 2002, pp. 552–557. Translated from Akusticheskiĭ Zhurnal, Vol. 48, No. 5, 2002, pp. 627–632.
Original Russian Text Copyright © 2002 by Eliseevnin, Tuzhilkin.

The Directivity of a Radiating Line Array Slightly Deflected from Vertical in a Waveguide

V. A. Eliseevnin and Yu. I. Tuzhilkin
Andreev Acoustics Institute, Russian Academy of Sciences, ul. Shvernika 4, Moscow, 117036 Russia
e-mail: bvp@akin.ru

Received July 19, 2001

Abstract—The azimuth directivity of a line array in a waveguide is studied for the case of its deflection from the vertical under the effect of underwater currents. The modal composition and the interference pattern of the field radiated by such an array is considered. *© 2002 MAIK “Nauka/Interperiodica”.*

Vertical arrays are widely used in experiments on sound propagation in the ocean. Lacking directivity in the horizontal plane, they allow one to measure the vertical arrival angles of signals and to determine their modal composition. This is very important for the determination of the distance to a sound source and its depth by the methods of matched field processing [1] or matched-beam processing [2]. A vertical array is convenient for use in experiments. It can be lowered from a ship or anchored. Its vertical position is maintained by the mass of the load or by the buoyancy of a subsurface buoy.

Some difficulties arise in the presence of underwater currents disturbing the array shape. In this case, the experimental equipment must be supplemented by a system for determining the array shape, which considerably complicates the experiment [3]. Results of studying the methods for the determination of the array shape with allowance for real disturbing factors are presented in [4]. The effect of the array slope on the efficiency of the signal reception is considered in [5]. In the signal processing, data on the deviations of the array elements in the plane containing the source are taken into account. Simpler ways to reduce the effect of the shape distortions of the receiving array are, in particular, the use of special multifrequency signals [6] and cepstrum analysis [7].

The problem becomes more complicated when the sound source is represented by a vertical radiating array that is also subjected to deformations. Such an array was used by Kuperman *et al* [8, 9] in the experiments on the phase conjugation. In these experiments, the signal from a distant source was received by a vertical array and reradiated by it as a time-reversal signal, which provided its concentration in the region near the source. The monitoring of this region was realized by another vertical array.

The difficulties increase further when several reradiating arrays or reflectors are present or when their azimuth is unknown. In this case, the radiating array, despite its deflection from vertical, should be directed to the source azimuth. In contrast to the receiving array, whose information can be processed in parallel with allowance for the deviations of its elements for all values of the azimuth, the transmitting array cannot be compensated for a simultaneous omnidirectional radiation in the horizontal plane. In this connection, it is of interest to consider the problem of the azimuth directivity of a deformed vertical array.

In this paper, we consider the simplest case of deformation: a line array deflected from vertical without disturbing its shape, and the simplest form of waveguide: a homogeneous water layer with pressure-release upper and rigid lower boundaries. Without aspiring to universal results, such an approach allows us to show the basic features of the phenomenon under study.

In the absence of currents, a line array anchored to the bottom and stretched by a neutral buoyancy near the surface assumes a vertical position. Its aperture covers all the waveguide thickness H. The radiated sound field is represented as a sum of a finite number of modes (normal waves) propagating in the waveguide without attenuation [10]. To study a single mode, the distribution of the sensitivity of the array elements over its aperture is set to be proportional to the distribution of the field of this mode along the vertical, i.e., the array is tuned to the radiation of this mode. Due to the orthogonality of the waveguide eigenfunctions, the total radiated sound energy becomes concentrated in a single mode to which the array is tuned.

The sound field potential produced at the point (Z, R) of the waveguide by a continuous vertical line array radiating a monochromatic signal is given by the expression

$$U_a(Z, R, t) = \int_0^H \cos(b_q z) U(z, Z, R, t) dz. \qquad (1)$$

Here, Z is the depth of the point of reception, R is the horizontal distance between the array and the receiver, t is the running time, and z is the depth of the zth element of the array. It is assumed that the origin of coordinates is at the bottom and the z axis is directed upward; $b_q = (q - 0.5)\pi/H$ is the vertical component of the wave vector of the qth mode; $\cos(b_q z)$ is the eigenfunction of this mode, to the radiation of which the array is tuned; and $U(z, Z, R, t)$ is the sound field potential produced at the point (Z, R) by the array element located at the depth z. Considering this element as an omnidirectional point source, the sound field potential at large distances from the array can expressed as [10]

$$U(z, Z, R, t) = \frac{A}{\sqrt{R}} \sum_{l=1}^{m} \frac{1}{\sqrt{\xi_l}} \cos(b_l z) \cos(b_l Z) \exp(j\xi_l R - j\omega t), \tag{2}$$

$$A = -j \frac{V_0}{\sqrt{2\pi H}} \exp\left(-j\frac{\pi}{4}\right).$$

Here, V_0 is the source strength, m is the number of modes propagating in the waveguide without attenuation, $\xi_l = \sqrt{k^2 - b_l^2}$ is the horizontal component of the wave vector of the lth mode, $k = \omega/C$ is the wave number, ω is the circular frequency, and C is the sound velocity in the water column.

Substituting Eq. (2) into Eq. (1) and making the necessary transformations, with allowance for the orthogonality of the waveguide eigenfunctions

$$\int_0^H \cos(b_q z) \cos(b_l z) dz = H/2 \tag{3}$$

for $q = l$ and 0 for $q \neq l$, we obtain

$$U_a(Z, R, t) = \frac{A}{\sqrt{R}} \frac{H}{2} \frac{\cos(b_q Z)}{\sqrt{\xi_q}} \exp(j\xi_q R - j\omega t). \tag{4}$$

From this expression, it follows that the vertical line array covering the whole waveguide thickness and tuned to the radiation of the qth mode radiates only this single mode. Due to the cylindrical symmetry of the problem, the directional pattern of the array in the horizontal plane is a circle.

Let the array, as a whole, deflect from the vertical by the angle γ without any deformations. The geometry of the problem is shown in Fig. 1. In this case, the depth of each element of the array decreases to $z = \varsigma\cos\gamma$, where ς is the coordinate along the aperture. The integration with respect to z must be carried out from zero to $z_M = H\cos\gamma$. The direction of the horizontal axis R coincides with that of the array slope.

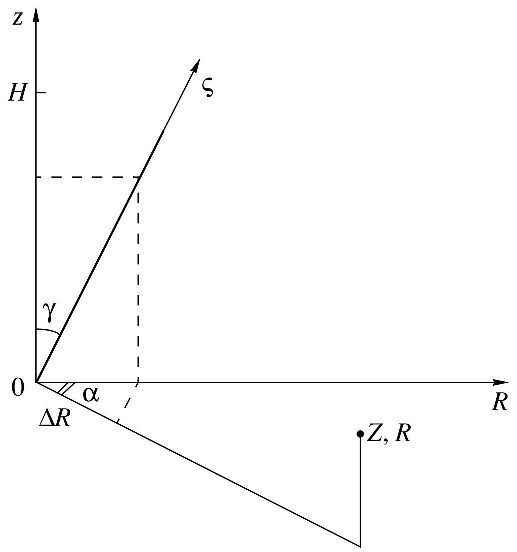

Fig. 1. Geometry of the problem.

An array element with the coordinate ς obtains the increment ΔR to the distance to the point of reception. In the plane of the array slope, $\Delta R = \varsigma\sin\gamma$ and, as follows from Fig. 1, the distance at any azimuth α is equal to

$$R - \Delta R = R - \varsigma\sin\gamma\cos\alpha = R - z\tan\gamma\cos\alpha.$$

For a sloping array, the excitation function of the qth mode takes the form $\cos(b_q z/\cos\gamma)$. The sound potential generated by such an array is determined by the expression

$$\begin{aligned} U_a(Z, R, \alpha, t) &= \frac{A}{\sqrt{R}} \exp(-j\omega t) \sum_{l=1}^{m} \frac{\cos(b_l Z)}{\sqrt{\xi_l}} \\ &\times \exp(j\xi_l R) \int_0^{z_M} \cos(b_q z) \exp(-\xi_l \tan\gamma\cos\alpha z) dz \\ &= \frac{A}{\sqrt{R}} \exp(-j\omega t) \frac{z_M}{4} \sum_{l=1}^{m} \frac{\cos(b_l Z)}{\sqrt{\xi_l}} \\ &\times [a(l, \alpha) + jb(l, \alpha)] \exp(j\xi_l R); \end{aligned} \tag{5}$$

$$a(l, \alpha) = \sum_{i=1}^{4} \frac{\sin(c_i z_M)}{c_i z_M},$$

$$b(l, \alpha) = \sum_{i=1}^{4} \left(\frac{1}{c_i z_M} - \frac{\cos(c_i z_M)}{c_i z_M}\right),$$

$$\begin{aligned} c_1 z_M &= kH(G_1 - w), \quad c_2 z_M = kH(G_2 - w), \\ c_3 z_M &= kH(-G_2 - w), \quad c_4 z_M = kH(-G_1 - w), \end{aligned} \tag{6}$$

$$G_{1,2} = b_q/k \pm b_l/k \cos\gamma,$$

$$w = \sqrt{1-(b_l/k)^2}\sin\gamma\cos\alpha.$$

As a result of the array departure from the vertical position, not only the radiation of the qth mode, to which the array is tuned, will occur, but also modes of other numbers will be radiated. When the vertical array is tuned, the total radiated power is carried by the single qth mode. The power radiated by the same array deflected from the vertical will be distributed between the qth mode and a group of adjacent modes.

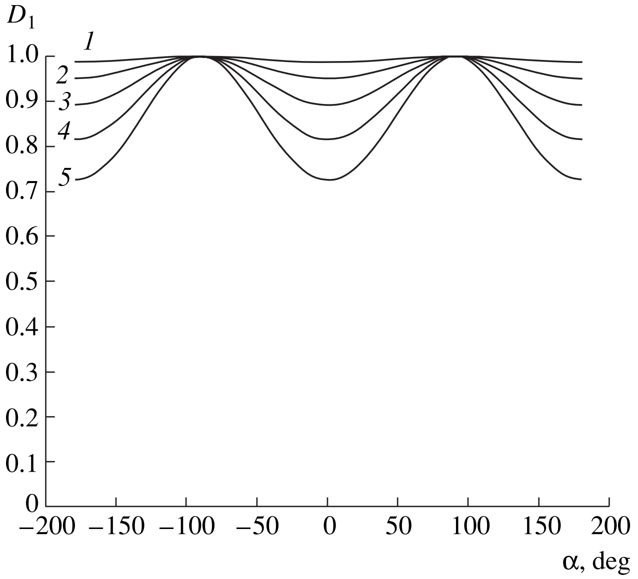

Fig. 2. Directional pattern in a shallow-water waveguide for $H = 2.5\lambda$, $q = 1$, and γ = (*1*) 2°, (*2*) 4°, (*3*) 6°, (*4*) 8°, and (*5*) 10°.

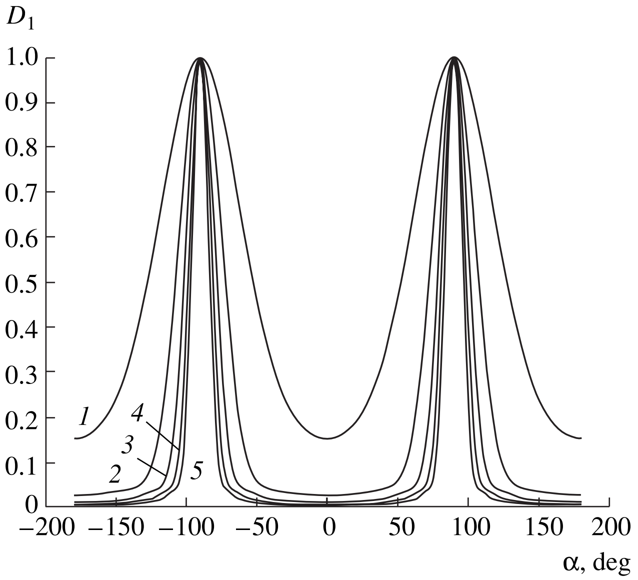

Fig. 3. Directional pattern in a deep-water waveguide for $H = 30\lambda$, $q = 1$, and γ = (*1*) 2°, (*2*) 4°, (*3*) 6°, (*4*) 8°, and (*5*) 10°.

Besides, the array departure from vertical leads to the appearance of a horizontal component of its aperture, which results in the appearance of the array directivity in the horizontal plane; i.e., the directional pattern ceases being circular. In this case, the effect of the directivity will occur for all radiated modes.

Since the radiation of the qth mode is of interest, we will characterize the array directivity in the horizontal plane by its directional pattern for the qth mode:

$$D_q(\alpha) = \frac{P_q P_q^*}{\max\{P_q P_q^*\}} = a^2(q,\alpha) + b^2(q,\alpha), \tag{7}$$

where the sound pressure is $P = j\rho\omega U$ [10, 12].

As examples, we carried out calculations for two waveguides: a shallow-water waveguide $H = 2.5\lambda$ and a deep-water waveguide $H = 30\lambda$, where λ is the sound wavelength in the water column. For a frequency of 300 Hz (λ = 5 m), the depth of the shallow-water waveguide is H = 12.5 m and that of the deep-water waveguide is H = 150 m. In the shallow-water waveguide, m = 5 modes can propagate, and in the deep-water waveguide, m = 60 modes. Figures 2 and 3 exhibit the directional patterns $D_1(\alpha)$ for the first mode of the line arrays located in these waveguides. The arrays are tuned to the radiation of the first modes and are deflected from vertical by various angles γ (2°, 4°, 6°, 8°, and 10°). From Figs. 2 and 3, one can see that even a slightly inclined array acquires a directivity in the horizontal plane, which is most pronounced in the deep-water waveguide. The radiation maxima correspond to the directions perpendicular to the array slope. In contrast, in the direction of the slope, as well as in the opposite direction, the array does not radiate the first mode already at the angle $\gamma = 4°$ in the deep-water waveguide. The beamwidth of the pattern in the transverse directions is close to 35° (Fig. 3). For the 150-m waveguide, the horizontal projection of the array aperture is $H\sin(4°)$ = 10.46 m. A rectangular vertical array of such a width at a frequency of 300 Hz would have a beamwidth of 27° in the horizontal plane.

As the array slope increases, the efficiency of the first mode radiation decreases. Together with the first mode, the array begins to radiate modes of higher numbers, which gives rise to an interference pattern of the field, depending on the azimuth and distance. As an

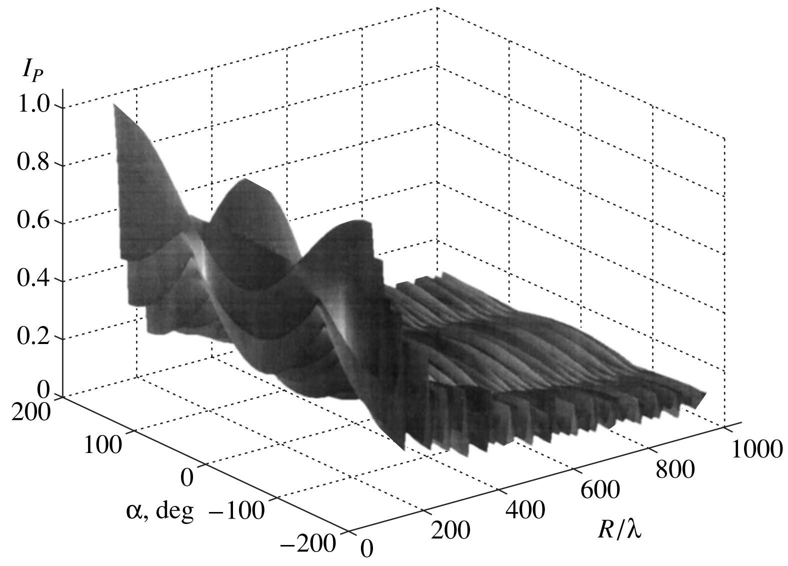

Fig. 4. Sound intensity in a shallow-water waveguide for $H = 2.5\lambda$, $m = 5$, $\gamma = 5°$, $\alpha = 0°$, and $q = 1$.

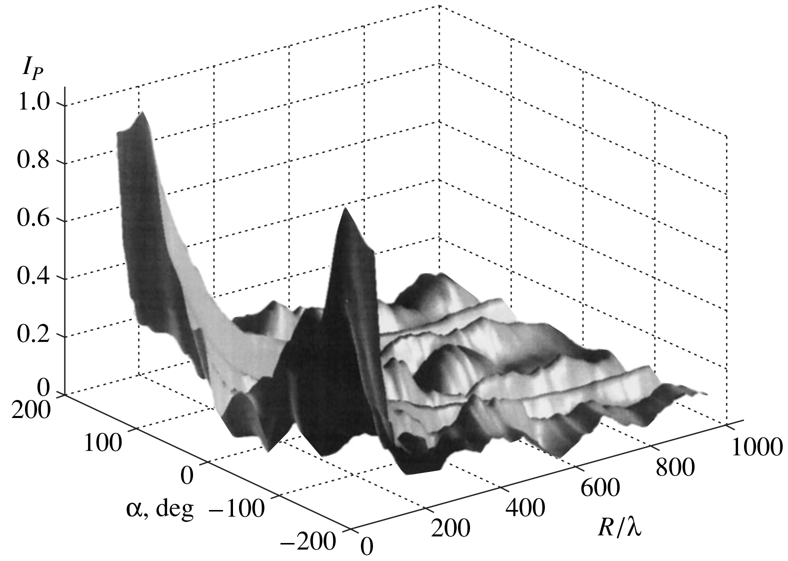

Fig. 5. Sound intensity in a deep-water waveguide for $H = 30\lambda$, $m = 60$, $\gamma = 5°$, $\alpha = 0°$, and $q = 1$.

example, Figs. 4 and 5 show three-dimensional dependences of the normalized sound intensity on the azimuth α and distance R for the shallow- and deep-water waveguides ($\gamma = 5°$ and $Z = 0.5H$):

$$I_P(Z, R, \alpha) = \frac{P_a(Z, R, \alpha)P_a^*(Z, R, \alpha)}{\max\{P_a(Z, R, \alpha)P_a^*(Z, R, \alpha)\}}, \tag{8}$$

$$\begin{aligned} P_aP_a^* = (\omega\rho)^2\frac{AA^*}{R}\left(\frac{z_M}{4}\right)^2\Bigg\{&\left(\sum_{l=1}^{m}\frac{\cos(b_lZ)}{\sqrt{\xi_l}}[a(l,\alpha)\cos(\xi_lR) - b(l,\alpha)\sin(\xi_lR)]\right)^2 \\ &+\left(\sum_{l=1}^{m}\frac{\cos(b_lZ)}{\sqrt{\xi_l}}[a(l,\alpha)\sin(\xi_lR) + b(l,\alpha)\cos(\xi_lR)]\right)^2\Bigg\}. \end{aligned} \tag{9}$$

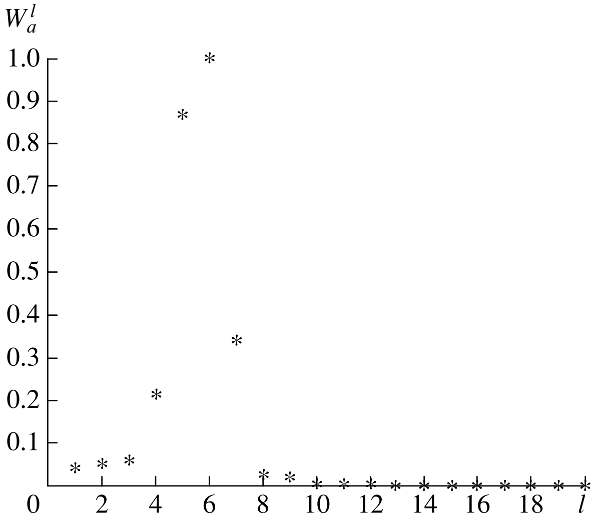

Fig. 6. Distribution of the power radiated by an inclined array over the modes in a deep-water waveguide for $H = 30\lambda$, $m = 60$, $\gamma = 5°$, and $q = 1$.

Figures 4 and 5 show that the total field has a complex structure, especially in the deep-water waveguide. The average decay law is proportional to $1/R$, as in any waveguide without attenuation. The pattern is symmetrical about the plane of the array slope ($\alpha = 0°$). However, the field intensity maxima observed at $\alpha = \pm 90°$ are not the largest ones for all distances R. At some distances, the interference of the modes of high numbers gives relatively high field levels for the azimuth values at which the field level of the first mode was low (Fig. 3).

It is of interest to consider the distribution of the sound energy radiated by an inclined array between modes of different numbers. The power radiated by a compensated vertical array in a waveguide was calculated in [11]. Using a similar approach, we assume that the sound energy radiated by an inclined array is transferred through the side surface of the cylinder of a large radius R. The array is located near the cylinder axis, the bottom and the surface of the waveguide being totally reflective. The radiated acoustic power W_a is determined by integrating the horizontal component of the power density flux J_a over the cylindrical surface

$$W_a = \int_0^H \int_0^{2\pi} J_a(Z, R, \alpha) R d\alpha dZ. \qquad (10)$$

According to [10, 12], the quantity J_a is determined as

$$J_a(Z, R, \alpha) = \frac{1}{2}\mathrm{Re}(P_a V_{aR}^*) = \frac{1}{2}\mathrm{Re}\left(j\rho\omega U_a \frac{\partial U_a}{\partial R}\right), \qquad (11)$$

where P_a and V_{aR} are the pressure and the horizontal component of the particle velocity of the sound field at the point (Z, R, α) of the waveguide. Using the Eq. (5) for the sound potential U_a and performing the necessary transformations, we obtain the radiation power of the inclined array in the waveguide as a sum of the powers radiated through different modes:

$$W_a = \frac{1}{2}\rho\omega H A A^* \left(\frac{z_M}{4}\right)^2 \times \sum_{l=1}^{m} \int_0^{2\pi} [a^2(l, \alpha) + b^2(l, \alpha)] d\alpha = \sum_{l=1}^{m} W_a^l. \qquad (12)$$

Thus, in the shallow-water waveguide ($H = 2.5\lambda$, $m = 5$, $\gamma = 5°$, and $q = 1$), the sound energy is mainly transferred by the first mode. The second mode transfers only about 7% of the energy of the first mode. The remaining three modes are not excited at all. In the deep-water waveguide ($H = 30\lambda$, $m = 60$, $\gamma = 5°$, and $q = 1$), the situation is different: the fifth and sixth modes play the main role, and the remaining modes are almost not excited (Fig. 6 presents only the 20 first modes).

Thus, a vertical array that is omnidirectional in the horizontal plane becomes directional as a result of its deflection from the vertical position. The directivity is fairly small when the slope does not exceed several degrees and the waveguide depth is no greater than several sound wavelengths. However, the directivity becomes considerable in waveguides whose depth reaches several tens of wavelengths. The directional pattern of the array in the horizontal plane acquires deep minima in the direction of the inclination and maxima in the transverse directions. The mode composition of the radiation changes significantly. In addition to the mode to which the array is tuned, modes of other numbers (and with higher intensities) come into play, which leads to the formation of a complex interference pattern of the field. The distortions of the shape of the receiving array are usually determined using additional means and are taken into account at the point of reception of signals arriving from given horizontal directions. These signals can be processed in parallel or sequential regimes. However, the array slope can be a significant obstacle when the array is a radiating one and the signal should be transmitted over all horizontal directions simultaneously.

REFERENCES

1. A. B. Baggeroer and W. A. Cuperman, NATO ASJ Ser., Ser. C **388**, 79 (1993).
2. T. C. Yang, K. Yoo, and T. Yates, J. Acoust. Soc. Am. **104**, 2174 (1998).
3. W. S. Hodgkiss, D. E. Ensberg, J. J. Murray, *et al.*, IEEE J. Ocean Eng. **21**, 393 (1996).

4. S. E. Dosso and B. J. Sotirin, J. Acoust. Soc. Am. **106**, 3445 (1999).
5. M. Snellen and D. G. Simons, J. Acoust. Soc. Am. **109**, 514 (2001).
6. V. A. Burov, O. N. Sergeev, and N. P. Sergievskaya, Akust. Zh. **38**, 350 (1992) [Sov. Phys. Acoust. **38**, 187 (1992)].
7. V. A. Zverev and A. A. Pavlenko, Akust. Zh. **47**, 352 (2001) [Acoust. Phys. **47**, 297 (2001)].
8. W. A. Kuperman, W. S. Hodgkiss, H. C. Song, *et al.*, J. Acoust. Soc. Am. **103**, 25 (1988).
9. W. S. Hodgkiss, H. C. Song, W. A. Kuperman, *et al.*, J. Acoust. Soc. Am. **105**, 1597 (1999).
10. L. M. Brekhovskikh and Yu. P. Lysanov, *Fundamentals of Ocean Acoustics* (Gidrometeoizdat, Leningrad, 1982; Springer, New York, 1991).
11. V. N. Golubeva and V. A. Eliseevnin, Akust. Zh. **45**, 117 (1999) [Acoust. Phys. **45**, 104 (1999)].
12. M. A. Isakovich, *General Acoustics* (Nauka, Moscow, 1973).

Translated by Yu. Lysanov

Acoustical Physics, Vol. 48, No. 5, 2002, pp. 558–563. Translated from Akusticheskiĭ Zhurnal, Vol. 48, No. 5, 2002, pp. 633–639.
Original Russian Text Copyright © 2002 by Kapustina, Kolesnikova, Reshetov, Romanova.

Optical Properties of Acoustically Induced Domains in Liquid Crystals

O. A. Kapustina, N. A. Kolesnikova, V. N. Reshetov, and O. V. Romanova
Andreev Acoustics Institute, Russian Academy of Sciences, ul. Shvernika 4, Moscow, 117036 Russia
e-mail: bvp@akin.ru

Received June 20, 2001

Abstract—Optical properties of acoustically induced domains in planar liquid crystal layers are considered: the diffraction of light and the focusing of light by domains. *© 2002 MAIK “Nauka/Interperiodica”.*

The acoustic action upon an oriented layer of a liquid crystal (LC) in certain conditions leads to the formation of stationary structures (domains) of different scales and configurations [1], which act on the incident light as phase diffraction gratings. The investigation of the interaction of light with acoustic domains seems very promising in connection with the opportunity to obtain information on the orientation of the director $\vec{n}$ in the domains, their structure, and the properties of diffracted light, as well as opportunities to use the effects in devices and elements of systems for the coherent optical processing of information.[1]

This paper presents the results of an experimental study of the optical properties of a system of acoustic domains formed in planar layers of nematic and cholesteric LC under acoustohydrodynamic effect at frequencies at which the relation between the viscous and elastic wavelengths λ_v and λ in LC, the thickness d, and the layer length L satisfy the following inequalities:

$$d < \lambda_v \ll L, \quad \lambda \gg L.$$

In these conditions, the domain formation has a threshold character and is related to the development of the orientation instability [2–4].

Experiments on the observation of the focusing and diffraction of light by a system of acoustic domains formed in an LC cell are conducted using a common scheme: the LC fills in a flat capillary formed by glass plates *1* and *2* with the inner surfaces processed according to the conventional technique [5] to obtain a planar orientation of molecules of the LC *3* in the layer plane (the *OXY* plane in Fig. 1a).[2] A possibility for microdisplacements of plate *1* in the direction of the *Z* axis was provided in the experiment. This allowed us to vary the distance between plates *1* and *2*, which determined the LC layer thickness, within a required range (20–100 μm). This distance was controlled by an interferometric technique with an accuracy of ±5 μm [6]. Plate *2* performed vibrations in the *OXY* plane in the direction of the *Y* axis. The vibrations were caused by an exciter fed by a generator. The amplitude of vibrations of this plate was measured according to the displacements of a hairline drawn at its lateral surface. The measurements were performed using a micrometer eyepiece of a microscope, which was calibrated preliminarily using a test object (a grid with a step of 500 μm). The optical part of the setup provided an opportunity to observe the domains by both polarization-optical and diffraction methods. The light source of the polarization microscope was supplemented by interference filters. The optical system had the following transmission bands: 0.35 ± 0.03, 0.45 ± 0.03, 0.52 ± 0.5, and 0.63 ± 0.6 μm. The intensity of the diffracted light was measured using a photomultiplier installed behind a screen at which the diffraction pattern was formed. The voltage drop due to the photocurrent through a resistor in the photomultiplier circuit was measured by a voltmeter.

Two series of experiments with planar samples of nematic (an MBBA/EBBA mixture) and cholesteric (CC/MBBA/EBBA) LC were conducted.[3] The acoustic frequency was varied within the range 25–500 Hz.

The first series of experiments was conducted using NLC samples with the thickness 20–75 μm. A typical optical pattern of distortion is given in Fig. 2a. The pattern was observed in polarized light ($\vec{E} \parallel X$) through a microscope lens after attaining the threshold amplitude of vibrations ξ_{0y} ($d = 75$ μm and $f = 330$ Hz). It represents a system of alternating dark and light stripes parallel to the *Y* axis with the period $\Lambda_x = 2\pi/q_x$ along the *X* axis. (Here, q_x is the wave number of the structure

---

[1] The term “director” common in LC physics means a unit vector coinciding with the direction of the preferred orientation of molecules.

[2] A coating of polyvinyl alcohol was applied to the surfaces of the plates limiting the LC in order to obtain a planar orientation of molecules in the layer. The coating was polished in a certain direction.

[3] The abbreviations common to LC physics are used here: MBBA is metoxibenzilidene-*n*-butylaniline, EBBA is etoxibenzilidene-*n*-butylaniline, and CC is cholesteryl chloride.

periodic along the X axis.) If a monochromatic light beam is transmitted through a layer where such a domain system is formed, a diffraction pattern in the form of a chain of spots located in the plane perpendicular to the domains appears on the screen positioned behind the layer. The angular distribution of the diffraction maxima and minima obeys a common law of a diffraction grating with the period Λ, namely, $\Lambda \sin\beta = m\lambda_0$, where β is the diffraction angle, λ_0 is the light wavelength, and $m = 0, 1, 2, \ldots$. At $\lambda_0 = 0.63$ μm and $\Lambda = 75$ μm, we have the diffraction angle $\beta = 28.8'$ that can be observed readily in the experiment. Observations show that the diffraction patterns obtained with linear domains near the threshold of their formation contain only the maxima of the zeroth and first orders of diffraction. Curves *1* and *2* in Fig. 3a illustrate the changes in the light intensity in the zeroth (I_0) and first (I_1) diffraction maxima, respectively, in the case of an increase in the vibration amplitude ξ_{0y} over the threshold of the domain formation for an LC layer with the thickness 75 μm at the frequency 330 Hz (the light wavelength is 0.63 μm). Here, the values of I_0 and I_1 are normalized to their own maximal values $I_0^{\max}$ and $I_1^{\max}$. In this experiment, $I_1^{\max} = 1.42 I_0^{\max}$. It is essential that, in these measurements, the electric vector $\vec{E}$ of an electromagnetic wave was perpendicular to the longitudinal axis of the domains (the Y axis) when the diffraction pattern was most pronounced. As observations showed, in the case of orientation of the vector $\vec{E}$ parallel to the Y axis, there is no diffraction, but an effective light scattering by the domains is observed. In this case, the character of scattering as a function of the vibration amplitude and the layer thickness is determined by the dependences typical of the effect of acoustic dynamic light scattering in LC, which is described in [7, 8].

It was found that the intensity and the form of the diffraction spots are very critical to the change in vibration amplitude at a fixed frequency. An increase in the amplitude ξ_{0y} leads sometimes to a complex redistribution of the light intensity among the diffraction maxima, an increase in their number, and their spreading. Figure 3b gives as an example the anomalous evolution of the intensity distribution in the zeroth, first, and second maxima of diffraction with the increase in the vibration amplitude expressed in relative units through the parameter $\delta = (\xi_{0y} - \xi_{0y}^{th})/\xi_{0y}^{th}$, where ξ_{0y}^{th} is the threshold value of vibration amplitude. One can see that the intensity in the second maximum of diffraction increases with the growth of ξ_{0y}, and at $\delta \geq 0.43$, it exceeds the light intensity in the first maximum ($d = 60$ μm and $f = 300$ Hz). Apparently, this anomaly is caused by a rearrangement of the LC spatial structure that leads to the formation of a phase grating with a complex profile of phase delay, which is different from the sinusoidal one. In the typical situation of a phase grating with a sinusoidal profile, only the maxima of the zeroth and first orders are present in the diffraction pattern, as was indicated above, and their half-width Δ depends on the number of illuminated periods. In these conditions, the relation between the light intensity in the first diffraction maximum and the vibration amplitude at values of ξ_{0y} that differ little from the threshold one is a power law of the form $I_1 \sim \xi_{0y}^2$ (Fig. 3c, plot *1*).

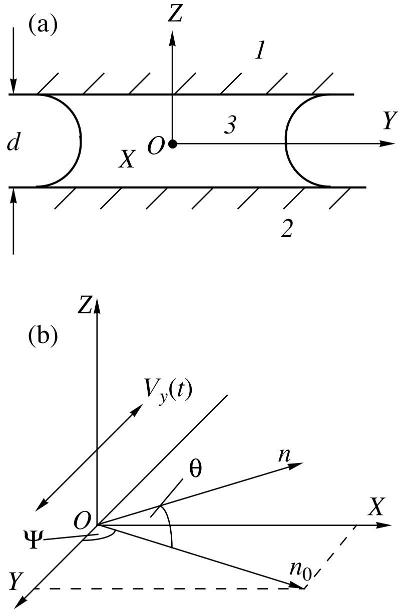

Fig. 1. (a) Schematic diagram of the experiment: (*1*, *2*) glass plates and (*3*) the LC layer. (b) Geometry of the problem: $\vec{n}$ and $\vec{n}_0$ are the current and initial positions of the director, θ is the angle between the deflected director $\vec{n}$ and the *OXY* layer plane, and Ψ is the angle between the velocity vector of the oscillatory Couette flow and $\vec{n}_0$.

As observations show, the light polarization in the diffraction maxima at all vibration amplitudes used in the experiment remains fundamentally linear and coincides with the polarization of the light source. The plot illustrating the dependence of the light intensity in the first maximum on λ_0 is given in Fig. 3d. It allows one to judge the influence of the light wavelength within the interval 0.35–0.63 μm on the diffraction pattern corresponding to the structure of linear domains in the nematic LC.

The second series of experiments was conducted with cholesteric LC (CC/MBBA/EBBA) with the helix pitch $P_0 = 4$ μm using samples with a thickness of 30–110 μm in the frequency range 90–500 Hz. The optical distortion pattern characteristic of this type of LC and observed in polarized light is given in Fig. 2b ($d = 35$ μm and $f = 150$ Hz). It is a regular square grid with the spatial periods $\Lambda_x = 2\pi/q_x$ (along the X axis) and $\Lambda_y = 2\pi/q_y$ (along the Y axis), where q_x and q_y are the wave numbers of the structure periodic along the X

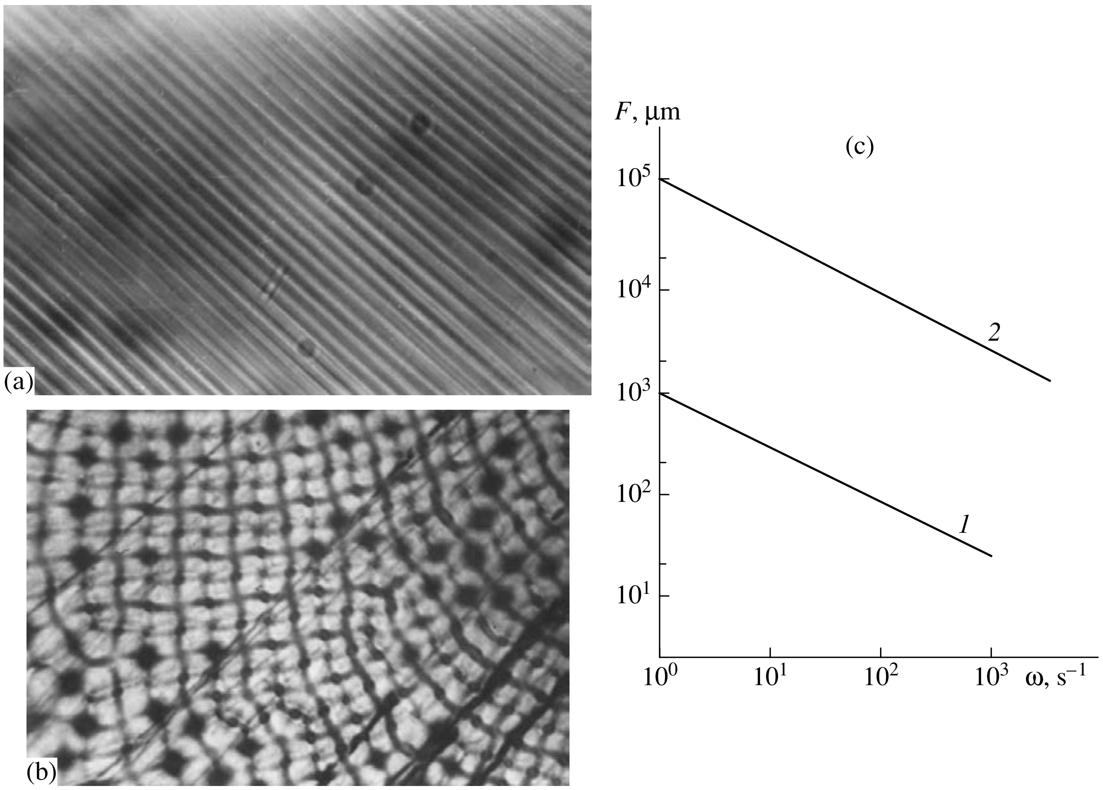

Fig. 2. Optical patterns of the distortion in planar samples of (a) nematic and (b) cholesteric LC. (c) Focal distance of the cylindrical lenses formed in layers of nematic LC (*1*) 20 and (*2*) 200 μm thick as a function of the frequency of vibrations.

and Y axes, respectively. As a rule, the values of Λ_x and Λ_y coincide, and their relation with the layer thickness and the helix pitch is determined by the law of the form $(P_0d)^{1/2}$ [7], which is typical of this type of distortion of the planar structure of a cholesteric LC at all other kinds of external action [9]. The diffraction pattern formed by such a two-dimensional system of domains is more complex: it is equidistant chains of spots located one after another. Nevertheless, the laws revealed in the experiments and determining the characteristic parameters of this diffraction pattern are analogous to those obtained for nematic LC. For example, the difference in the plots representing the amplitude dependence of the light intensity in the first diffraction maximum in comparison with the same dependence for nematic LC (Fig. 3a, plot *2*) is only the value of the threshold amplitude ξ_{0y}^{th}. It is higher in cholesteric LC (see Fig. 3a, plot *3*; here, ξ_{0y}^{th} = 2.84 μm, d = 75 μm, f = 330 Hz, and λ_0 = 0.63 μm). As in the case of nematic LC, in the range of values of ξ_{0y} insignificantly differing from the threshold one, the light intensity in the first maximum is related to ξ_{0y} by the function $I_1 \sim \xi_{0y}^2$ (Fig. 3c, plot *2*).

Let us make some numerical estimates of the parameters determining the properties of domains as optical phase gratings. We use the simplest model reasoning as the basis. We consider the following physical situation: an LC layer is located between the planes $Z = \pm d/2$. The ends of this layer are open. The external action on the LC is determined by an oscillating flow with a linear velocity profile. The director $\vec{n}_0$ lies in the OXY layer plane and makes the angle ψ with the flow direction (the Y axis) (Fig. 1b). Let us consider a situation when the action of this flow leads to the formation of a regular director distribution in the LC layer with the form

$$\theta(x, y, z, t) \cong \theta(t)\cos(q_x x)\cos(q_z z). \tag{1}$$

Here, θ is the angle between the deflected position of the director $\vec{n}$ and the OXY layer plane, q_x and q_z are the wave numbers characterizing the orientation distortions arising along the OX and OZ axes, $q_x = 2\pi/\Lambda_x$ and $q_z = \pi/d$, and $\theta(t)$ is the function representing the time dependence of the deflection angle of the director. Since the director motion occurs with a velocity that is much lower than the light velocity, the optical pattern observed in the LC layer at each time moment corresponds to the instantaneous values of $\theta(t)$, and, in analyzing the light propagation through the domain system, we may assume the director distribution given by Eq. (1) to be static. We assume also that the deviation of the front of a light wave within the LC layer from a plane front is very small.

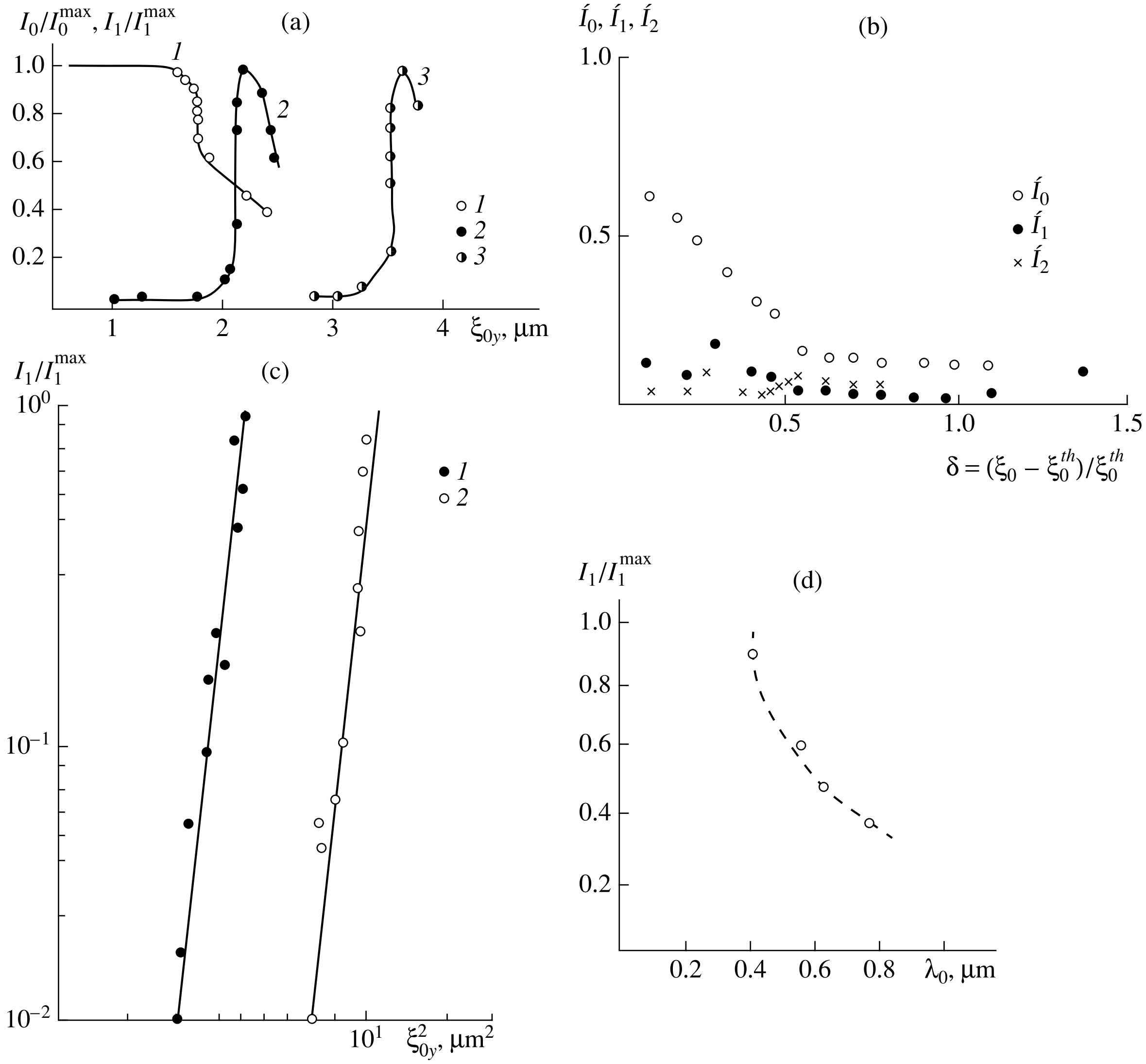

Fig. 3. (a) Variation of the light intensity in the zeroth (I_0) and first (I_1) diffraction maxima with an increase in the vibration amplitude ξ_{0y} in the case of one-dimensional linear domains [(*1*) I_0 and (*2*) I_1] and two-dimensional [(*3*) I_1] domains. (b) Example of an anomalous evolution of the light intensity distribution in the (*1*) zeroth, (*2*) first, and (*3*) second diffraction maxima with increasing amplitude parameter δ for linear domains in a nematic LC with $d = 60$ μm at $f = 300$ Hz. (c) Relation between the light intensity in the first diffraction maximum and the vibration amplitude in overthreshold conditions at $\xi_{0y} < \xi_{0y}^{max}$ for linear domains in (*1*) nematic and (*2*) cholesteric LC. (d) Influence of the light wavelength λ_0 on the light intensity in the first diffraction maximum for linear domains; $d = 75$ μm, $f = 330$ Hz, and $\xi_{0y} = 2.2$ μm.

Proceeding from the known equation of the ellipsoid of refraction indices [6], it is possible to determine the changes in the refraction indices that are caused by the distortions of the director field. In the case when these distortions are regular and the director distribution is described by Eq. (1), we obtain, according to [10], the effective refraction index n_{eff} along the Z axis in the following form:

$$n_{\text{eff}}(x, z, t) = n_e + 0.5 n_e (n_0^2 - n_e^2)\theta^2(t)\cos^2(q_x x)\cos^2(q_z z)/n_0^2. \tag{2}$$

Here, n_0 and n_e are the refraction indices of the ordinary and extraordinary light rays. We assume that a plane monochromatic wave with the homogeneous intensity I_0 is polarized in such a way that the vector $\vec{E}$ coincides with the director $\vec{n}_0$ and is incident upon the layer in the direction of the Z axis (the case of normal incidence).[4] When the wave leaves the layer, it has an alternating

---

[4] The medium is homogeneous for the wave polarized orthogonally to this direction, and there is no modulation of the refraction index [6]. This means that such a wave propagates through the LC layer without distortions.

phase determined by the spatial distribution of the refraction index n_{eff} and equal to

$$\Phi(x, z, t) = (2\pi/\lambda_0)\int_{-d/2}^{d/2} n_{\text{eff}}(x, z, t)dz. \tag{3}$$

Taking into account Eq. (3) and ignoring the constant phase difference in the plane corresponding to the exit from the layer, we arrive at the following relation for the phase difference:

$$\begin{aligned}\Delta\Phi(x, t) &= -\pi d n_e(n_e^2 - n_0^2)\theta^2(t)\\ &\times[1 + \cos(2q_x x)]/4n_0^2\lambda_0.\end{aligned} \tag{4}$$

Expanding the function $\cos(2q_x x)$ involved in Eq. (4) into a series in the small parameter $\Delta x = x - x_0$, we determine the equation describing the profile of the wave front at the exit from the layer:

$$\begin{aligned}&\cos(2q_x x) \approx \cos(2q_x x_0)\\ &- \sin(2q_x x_0)2q_x\Delta x - 1/2\cos(2q_x x_0)(2q_x)^2(\Delta x)^2.\end{aligned} \tag{5}$$

It follows from Eq. (5) that, if $\sin(2q_x x_0) = 0$, the wave front has a parabolic profile: at $\cos(2q_x x_0) = -1$, the rays converge, and at $\cos(2q_x x_0) = 1$, they diverge. From these estimates, it follows that, for a plane wave with the vector $\vec{E}$ along the director $\vec{n}_0$ (the *OX* axis), the LC layer under study is a phase grating of collecting and diverging lenses.

The focal distance of these lenses *F* can be determined according to the curvature radius of the wave front, $1/F = \Delta\Phi''(x, t)/k_0 n_g$. Here, n_g is the refraction index of the glass plates bounding the layer and $k_0 = 2\pi/\lambda_0$. If we assume that $n_g = n_e$, we obtain

$$F = \pm[(n_e^2 - n_0^2)d\theta^2(t)q_x^2/2n_0^2]^{-1}. \tag{6}$$

The result of the action of this lens system is shown in Fig. 2a for the situation when the microscope is focused at a distance equal to *F* over the layer surface. Plots *1* and *2* in Fig. 2c show the frequency dependence of the focal distance of the lenses that follows from Eq. (6) for the layers with the thicknesses 20 and 200 μm. It is assumed here that $n_0 = 1.56$, $n_e = 1.83$, $\theta = 0.03$ rad, $q_x \approx 10^{-2}(q_z\omega)^{1/3}$ μm^{-1} [3], and $q_z = \pi/d$. From plot *2*, it follows that, at $\omega = 10^3$ s^{-1}, for the layer with the thickness 200 μm, the focal distance is 10 μm. It is evident that, in this case, the above assumption, i.e., that within the LC layer the deviation of the wave front from a plane is small, is not valid, and to analyze the situation correctly, it is necessary to take into account the fact that the LC refraction index depends on the angle between the propagation direction of a light wave and the position of the director $\vec{n}$. The solution of this problem goes beyond the framework of our study. However, using these estimates as the basis, it is possible to determine the criterion of applicability of the conclusions following from the analysis given above. The criterion is determined by the inequality $d/F \ll 1$. Taking into account Eq. (6), it can be written in the form $0.2d^2\theta^2(t)q_x^2 \ll 1$.

Let us consider a diffraction pattern in the far wave field of this system of cylindrical lenses. According to [11], in the case of an illuminated area with the dimension $L \gg 1/q_x$, the electric field strength *E* of a light wave in the observation direction making the angle β with the layer normal can be written in the form

$$\begin{aligned}E(\beta) &= 1/2E_0[\cos\Phi_1(\beta)\cos\Phi_0\\ &+ \sin\Phi_1(\beta)\sin\Phi_0]dx.\end{aligned} \tag{7}$$

Here, $\Phi_1(\beta)$ and Φ_0 are the functions describing the spatial phase distribution for the direction determined by the angle β and the direction of the primary beam (β = 0), respectively. For the distribution of the refraction index determined by Eq. (2), we have

$$\begin{aligned}\Phi_1(\beta) &= \omega t - xk_0n_e/\sin\beta - zk_0n_e/\cos\beta\\ &- k_0n_ed/[1 - (n_e^2 - n_0^2)\theta^2(t)/8n_0^2],\end{aligned} \tag{8}$$

$$\Phi_0 = k_0n_e(n_e^2 - n_0^2)d\theta^2(t)\cos(2q_x x)/8n_0^2. \tag{9}$$

Transforming Eq. (7) with the help of the Jacobi identity $\exp(im\cos\alpha) = \sum_{-\infty}^{\infty} J_n(m)\exp(in\alpha)$ [12], we determine the basic characteristics of the diffraction pattern: the light intensity I_n in even and uneven maxima (at the values of Φ_1 equal to 0 and π/2, respectively), the diffraction angle β_n, and the width of a maximum $\Delta\beta_n$. The relations determining these characteristics are given below.

$$I_n = J_n^2(\Phi_0) \cong (1/2\Phi_0)^n/n!, \tag{10}$$

$$\beta_n = n[2q_x\sin\psi/k_0], \tag{11}$$

$$\Delta\beta_n = \pi/k_0L\cos\beta_n. \tag{12}$$

Here, $J_n(\Phi_0)$ is the Bessel function of the *n*th order. The light intensity in the direction of the primary light beam (β = 0) is $I_0 \approx J_0^2(\Phi_0)$. From the form of the function Φ_0 characterizing the diffraction efficiency of a domain system, it follows that the relation for the light intensity in the first diffraction maximum has the form

$$I_1 \cong k_0n_e(n_e^2 - n_0^2)d\theta^2(t)/16n_0^2. \tag{13}$$

This means that $I_1 \sim 1/\lambda_0$, which coincides with the results of measurements (see Fig. 3d). Since the character of the time dependence of light intensity in the maximum of the *n*th order is determined according to Eqs. (9) and (10) by the quantity $[\theta(t)]^{2n}$, it is possible, using the experimental values of $I_n(t)$ and $\langle I_n(t)\rangle$, to determine the character of variation and the absolute value of the squared angle $\theta(t)$ characterizing the director deflection.

It is necessary to note that the diffraction efficiency of a domain system can be increased by directing a light beam at a certain angle φ_0 with respect to the LC layer normal. Indeed, if this beam lies in the *OXZ* plane and the angle φ_0 is small, the effective refraction index is equal to

$$n_{\text{eff}} = n_0\{1 - 0.5(n_e^2 - n_0^2)[\varphi_0 + \theta(t)]^2/n_0^2\}, \quad (14)$$

and the diffraction efficiency is

$$\Phi_0^* \cong k_0 n_e(n_e^2 - n_0^2) d\varphi_0\theta(t)\cos(q_x x)/2n_0^2, \quad (15)$$

which is higher than the value corresponding to the conditions of the normal incidence of light on the layer (see Eq. (9)). In this situation, the light intensity in the diffraction maximum of the *n*th order is proportional to $\varphi_0\theta(t)$, and the director deflection caused by the escape of molecules from the layer plane can be observed directly.[5] It follows also from the form of Eq. (15) that the spatial period of domains along the *OX* axis changes and becomes equal to $\Lambda_x = 2\pi/q_x$. In this case, according to Eq. (11) the diffraction angle β_n decreases by a factor of 2.

The evidence in favor of the estimates given above are the experimental data on the dependence of the light intensity in the first diffraction maximum on the vibration amplitude ξ_{0y} and the light wavelength λ_0 in the conditions of normal light incidence upon the layer, which are given in Fig. 3. However, it is necessary to note that these estimates are valid for large-scale domains formed in thin LC layers (<10 μm), when the wave numbers q_x are comparable with, or smaller than, $q_z = \pi/d$. But if the wave number of domains far exceeds q_z, which occurs in thick LC layers, the restriction $d/F \ll 1$ introduced above is not valid: the focal distances of cylindrical lenses, which are calculated under the assumption of small perturbations of the wave front according to Eq. (6), become comparable to, or smaller than, the layer thickness. In this case, the correct description of the phenomenon can apparently be obtained only by taking into account the refraction of light within the domain structure. From the above analysis, it also follows that, according to our estimates, the spatial period of the domains corresponding to the conditions of oblique incidence of light upon the layer is two times greater than the structure period in the case of the normal light incidence ($2\pi/q_x$ and π/q_x, respectively). This difference can be interpreted as follows: in the case of normal light incidence, the sign of the director deflection angle $\theta(t)$ is inessential, because the effects of focusing and light diffraction are determined by the square of this angle (see Eqs. (6) and (9)); in contrast, in conditions of oblique light incidence, the sign of this angle becomes important, because the optical effects now depend on $\theta(t)$ (see Eq. (15)), and, in this case, the spatial period is doubled taking the value $2\pi/q_x$. This value corresponds to that observed in the experiments with normal light incidence on the LC layer. In our opinion, this fact also proves that, in the analysis of light propagation through a domain structure with the period $\Lambda \ll d$ ($q_x \gg q_z$), it is necessary to take into account the light refraction within a domain and the dependence of the local values of the refraction index $n(x, y, z, t)$ on the angle between the direction of light propagation and the director. This problem goes beyond the framework of this paper and needs further study.

In conclusion, we note that, from the study of the light diffraction by a domain structure, it is possible not only to obtain comprehensive and diversified information on the character and magnitude of the director deflection in a planar LC layer under acoustic action, but also to evaluate various properties of acoustically activated optical phase gratings formed on the basis of LC, specifically, in conditions of oblique incidence of light on the layer.

ACKNOWLEDGMENTS

This work was supported by the Russian Foundation for Basic Research, project no. 00-02-17732.

REFERENCES

1. *Handbook of Liquid Crystal*, Ed. by D. Demus, J. Goodby, G. W. Gray, H. W. Spiess, and V. Vill (Wiley–VCH, Germany, 1998), No. 1, pp. 549–568.
2. E. Guyon and P. Pieranski, Phys. Rev. A **9** (1), 404 (1974).
3. D. I. Anikeev and O. A. Kapustina, Zh. Éksp. Teor. Fiz. **110**, 1328 (1996) [JETP **83**, 731 (1996)].
4. E. Dubois-Violette, E. Guyon, I. Janossy, *et al.*, J. Mec. Theor. Appl. **16** (5), 733 (1997).
5. P. De Gennes, *The Physics of Liquid Crystals* (Clarendon, Oxford, 1974; Mir, Moscow, 1977).
6. A. Sommerfeld, *Optics* (Academic, New York, 1954; Inostrannaya Literatura, Moscow, 1953).
7. *Physical Properties of Liquid Crystals*, Eds. D. Demus *et al.* (Wiley–VCH, Germany, 1999), pp. 447–466.
8. O. A. Kapustina and V. N. Lupanov, Akust. Zh. **23**, 390 (1977) [Sov. Phys. Acoust. **23**, 218 (1977)].
9. S. A. Pikin, *Structural Transformation in Liquid Crystals* (Nauka, Moscow, 1981).
10. E. Guyon, I. Janossy, P. Pieranski, and J. M. Jonathan, J. Opt. (Paris) **8** (6), 357 (1977).
11. N. I. Kalitievskiĭ, *Wave Optics* (Vysshaya Shkola, Moscow, 1978).
12. H. B. Dwight, *Tables of Integrals and Other Mathematical Data*, 4th ed. (Macmillan, London, 1961; Nauka, Moscow, 1983).

Translated by M. Lyamshev

---

[5] Comparison of Eqs. (9) and (15) leads to the ratio $\Phi_0^*/\Phi_0 \cong 2\varphi_0\theta(t)/\theta^2(t) = 2\varphi_0\theta(t) \gg 1$. The typical values of the angle θ are 0.02 and 0.07 rad near the threshold of domain formation and in the case of an almost fully developed instability, respectively.

Acoustical Physics, Vol. 48, No. 5, 2002, pp. 564–571. Translated from Akusticheskiĭ Zhurnal, Vol. 48, No. 5, 2002, pp. 640–648.
Original Russian Text Copyright © 2002 by Korobov, Ékonomov.

The Effect of Heat Treatment and Static Deformations on the Acoustic Nonlinearity of Copper Wires

A. I. Korobov and A. N. Ékonomov

Physics Faculty, Moscow State University, Vorob'evy gory, Moscow, 119899 Russia

e-mail: akor@att.phys.msu.su

Received May 3, 2001

Abstract—The results of an experimental study of the effect of heat treatment and static deformations on the nonlinear acoustic properties of copper wire samples are presented. The nonlinear properties of wires are studied by measuring the stress–strain curve, the dependence of the velocity of acoustic waves in the samples on their deformation, and the transformation of the spectrum of the initial harmonic wave. The values of the static and dynamic Young moduli and the values of the static, quasistatic, and dynamic nonlinear parameters are determined. From the metallographic and X-ray diffraction analyses of the samples, the correlation between their internal structure and acoustic properties is revealed. © *2002 MAIK "Nauka/Interperiodica".*

Investigation of the physical properties of solids under deformation is an urgent problem [1, 2]. New possibilities for studying the strained state of a solid appeared with the development of methods of nonlinear acoustics [3]. These methods made it possible to conduct extensive studies of the mechanisms of nonlinearity and nonlinear acoustic phenomena in various solids. In materials with defects, along with the nonlinearity of molecular forces (the physical nonlinearity) resulting in a nonlinear relation between the stress σ and strain ε, a structural nonlinearity shows up. This nonlinearity is determined by a supramolecular internal structure of a solid (dislocations, microcracks, local internal stresses, etc.) and may exceed the physical nonlinearity by two to four orders of magnitude [4–7]. It is of interest to investigate the acoustic properties of metals in the process of changes that occur in their internal structure under various types of machining or other treatment, such as plastic deformation, annealing, and hardening.

This paper describes an experimental study of the effect of external static loads on the elastic properties of samples of a copper wire subjected to various types of heat treatment.

The creation of considerable static deformations (including plastic ones) in metals with a simultaneous excitation of acoustic waves in them involves some experimental difficulties. Therefore, as an object of investigation, we chose samples of thin electrotechnical copper wire. The advantages of studying the acoustic properties of this kind of objects are obvious: (a) the simplicity of manufacturing the samples and (b) the fact that, in a thin wire, it is easy to create plastic deformations and generate acoustic waves with large amplitudes.

For investigating the nonlinear properties of metal wire samples, three methods were used: static, quasistatic, and dynamic.

The static method consists in the measurement of the stress-strain (σ–ε) relationship (Fig. 1). Hooke's law for a thin rod or a wire with consideration for the quadratic nonlinearity of the dependence $\sigma = \sigma(\varepsilon)$ in the vicinity of any value of static deformation ε_s can be written as

$$\begin{aligned}\sigma(\varepsilon_s) &= E(\varepsilon_s)\varepsilon + \frac{1}{2}E_2(\varepsilon_s)(\varepsilon)^2 \\ &= E(\varepsilon_s)[\varepsilon - \Gamma_{st}(\varepsilon_s)(\varepsilon)^2],\end{aligned} \qquad (1)$$

where $E(\varepsilon_s) = \left(\frac{\partial\sigma}{\partial\varepsilon}\right)_{\varepsilon = \varepsilon_s}$ is the static Young's modulus of the second order [1], $E_2(\varepsilon_s) = \left(\frac{\partial E}{\partial\varepsilon}\right)_{\varepsilon = \varepsilon_s} = \left(\frac{\partial^2\sigma}{\partial\varepsilon^2}\right)_{\varepsilon = \varepsilon_s}$ is the Young's modulus of the third order, and $\Gamma_{st}(\varepsilon_s) = -\frac{E_2(\varepsilon_s)}{2E(\varepsilon_s)}$ is the static quadratic nonlinear acoustic parameter. Thus, the experimental stress–strain dependence $\sigma = \sigma(\varepsilon)$ makes it possible to find the static values of $E(\varepsilon_s)$, $E_2(\varepsilon_s)$, and $\Gamma_{st}(\varepsilon_s)$ as functions of strain [8].

The quasistatic method is based on the measurement of the dependence of the velocity of acoustic waves in a solid on the constant external forces or fields applied to it [9]. The process of propagation of acoustic waves in thin metal wires essentially differs from the propagation in an unbounded medium: it is of a mode character and, as a rule, exhibits a geometric dispersion [10]. In the experiments, we used the lowest mode of a normal

1063-7710/02/4805-0564$22.00 © 2002 MAIK "Nauka/Interperiodica"

longitudinal acoustic wave that exists down to the zero frequency *f*. For the case when the wire diameter *D* is much less than the acoustic wavelength $\lambda = C/f\ (D \ll \lambda)$, the dispersion of this mode is insignificant and its velocity *C*, the so-called rod velocity, is determined as

$$C = \sqrt{\frac{E_d}{\rho}}, \tag{2}$$

where E_d is the dynamic Young's modulus and ρ is the density of the material that in all following calculations is considered to be constant.

The measurement of the velocity $C = C(\varepsilon_s)$ of longitudinal acoustic waves in a wire makes it possible to find the dependence of the dynamic Young's modulus on the static strain

$$E_d(\varepsilon_s) = \rho(C(\varepsilon_s))^2 \tag{3}$$

and determine the quasistatic nonlinear acoustic parameter

$$\Gamma_{qst}(\varepsilon_s) = -\frac{E_{2s}(\varepsilon_s)}{2E_d(\varepsilon_s)}, \tag{4}$$

where $E_{2s}(\varepsilon_s) = \left.\frac{\partial E_d(\varepsilon_s)}{\partial \varepsilon}\right|_{\varepsilon = \varepsilon_s} = \left.\frac{\partial[\rho(C(\varepsilon_s))^2]}{\partial \varepsilon}\right|_{\varepsilon = \varepsilon_s} =$ $(C(\varepsilon_s))^2\left.\frac{\partial \rho}{\partial \varepsilon}\right|_{\varepsilon = \varepsilon_s} + 2\rho(C(\varepsilon_s))\left.\frac{\partial(C(\varepsilon_s))}{\partial \varepsilon}\right|_{\varepsilon = \varepsilon_s}$ is the mixed Young's modulus of the third order (similarly to the mixed moduli of elasticity of the third order [9]).

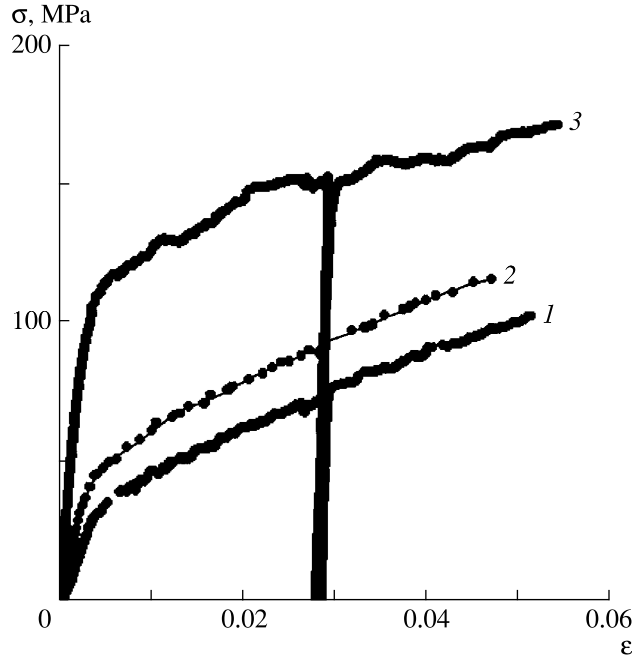

Fig. 1. Stress–strain curves for the samples of (*1*) an annealed wire, (*2*) a hardened wire (every twentieth experimental point is shown, and the solid line is an approximating curve), and (*3*) an untreated wire.

The dynamic method is based on the interaction of acoustic waves (the generation of harmonics or combination frequencies) in a nonlinear medium and consists in the measurement of the amplitudes of fundamental and combination frequencies in the spectrum of the investigated signal. In the experiment, we used a modulation method [11]. Let the length of a thin rod (wire) X_0 along which a sinusoidal acoustic wave propagates with the frequency $\omega = 2\pi f$ and amplitude A_0

$$A = A_0 \sin(\omega t - kX) = A_0 \sin(\omega t - \varphi) \tag{5}$$

be modulated with a sine of frequency Ω:

$$X = X_0 + \Delta X \sin\Omega t = X_0(1 + \varepsilon_0 \sin\Omega t), \tag{6}$$

where ΔX is the amplitude of the sample length variation, $\varphi = kX = \frac{\omega X}{C}$, and $\varepsilon_0 = \Delta X/X_0$. We assume that the conditions $\Delta X \ll X_0$ and $\omega \gg \Omega$ are satisfied. For $X_0 \ll C/\Omega$, the deformation caused by the modulation with the frequency Ω can be considered as constant along the whole length of the wire. Due to the nonlinearity of Hooke's law (1), with the deformation of the sample, the value of Young's modulus E_m in it varies with the frequency Ω:

$$\begin{aligned} E_m &= \frac{\partial \sigma}{\partial \varepsilon} = E_d + E_{2d}\varepsilon_0 \sin\Omega t \\ &= E_d(1 - \Gamma_{dn}\varepsilon_0 \sin\Omega t), \end{aligned} \tag{7}$$

where σ is the stress, E_d is the dynamic Young's modulus of the material under study in the absence of modulation of the sample length, E_{2d} is the dynamic Young's modulus of the third order, and $\Gamma_{dn} = -\frac{E_{2d}}{E_d}$ is the nonlinear acoustic parameter. From Eqs. (2) and (7), it follows that the velocity of acoustic waves in the sample will also change with time:

$$C = \sqrt{\frac{E_m}{\rho}} = \sqrt{\frac{E_d(1 - \Gamma_{dn}\varepsilon_0 \sin\Omega t)}{\rho}}.$$

For $|\Gamma_d \varepsilon_0| \ll 1$, this expression is simplified:

$$C = C_0\left(1 - \frac{\Gamma_{dn}}{2}\varepsilon_0 \sin\Omega t\right), \tag{8}$$

where C_0 is the velocity of acoustic waves in the absence of modulation. Taking into account Eqs. (6) and (8), the expression for the phase φ in Eq. (5) can be written as

$$\varphi = \frac{\omega X}{C} = \frac{\omega X_0(1 + \varepsilon_0 \sin\Omega t)}{C_0\left(1 - \frac{\Gamma_{dn}}{2}\varepsilon_0 \sin\Omega t\right)}$$

$$= \frac{\omega X_0}{C_0}\left((1+\varepsilon_0\sin\Omega t)\left(1+\frac{\Gamma_{dn}}{2}\varepsilon_0\sin\Omega t\right)\right)$$

$$= \frac{\omega X_0}{C_0}\left(1+\frac{\Gamma_{dn}}{4}\varepsilon_0^2+\frac{2+\Gamma_{dn}}{2}\varepsilon_0\sin\Omega t+\frac{\Gamma_{dn}}{4}\varepsilon_0^2\cos 2\Omega t\right).$$

For $\varepsilon_0 \ll 1$, omitting the terms proportional to ε_0^2, we have

$$\varphi = \frac{\omega X_0}{C_0}\left(1+\frac{2+\Gamma_{dn}}{2}\varepsilon_0\sin\Omega t\right). \qquad (9)$$

Substituting Eq. (9) into Eq. (5), we obtain

$$\begin{aligned} A &= A_0\sin\left(\omega t-\frac{\omega X_0}{C_0}-\frac{\omega X_0}{C_0}\frac{2+\Gamma_{dn}}{2}\varepsilon_0\sin\Omega t\right) \\ &= A_0\sin[(\omega t-k_0X_0)-\varphi_0\sin\Omega t] \\ &= A_0[\sin(\omega t-k_0X_0)\cos(\varphi_0\sin\Omega t) \\ &\quad -\cos(\omega t-k_0X_0)\sin(\varphi_0\sin\Omega t)], \end{aligned} \qquad (10)$$

where $k_0 = \frac{\omega}{C_0}$ and $\varphi_0 = \frac{\omega X_0}{C_0}\frac{2+\Gamma_{dn}}{2}\varepsilon_0$.

Using the formulas for Bessel functions, we derive from Eq. (10):

$$\begin{aligned} A &= A_0J_0(\varphi_0)\sin(\omega t-k_0X_0) \\ &+ A_0\sum_{n=1}^{\infty}J_n(\varphi_0)\{\sin[(\omega t+n\Omega)-k_0X_0] \\ &+ (-1)^n\sin[(\omega t-n\Omega)-k_0X_0]\}; \end{aligned} \qquad (11)$$

i.e., a harmonic signal propagating along the sample undergoes phase modulation and, as a consequence, frequency modulation (FM) [12]. For $\varphi_0 \ll 1$, Eq. (10) can be simplified:

$$\begin{aligned} A &= A_0[\sin(\omega t-k_0X_0)-\cos(\omega t-k_0X_0)\varphi_0\sin\Omega t] \\ &= A_0\sin(\omega t-k_0X_0)-\frac{A_0\varphi_0}{2} \\ &\times\{\sin[(\omega+\Omega)t-k_0X_0]-\sin[(\omega-\Omega)t-k_0X_0]\}. \end{aligned} \qquad (12)$$

For $\varphi_0 \ll 1$, the spectrum of the FM signal with a sinusoidal modulation of the sample length is similar to the spectrum of an amplitude-modulated signal and consists of three components: the carrier frequency ω and two side frequencies $(\omega-\Omega)$ and $(\omega+\Omega)$ [11]. According to Eq. (12), the ratio of amplitudes M (the modulation depth) of one of the side frequencies and the carrier frequency is determined by the expression

$$M = \frac{A(\omega-\Omega)}{A(\omega)} = \frac{A(\omega+\Omega)}{A(\omega)}$$

$$= \frac{A(\omega-\Omega)+A(\omega+\Omega)}{2A(\omega)} = \frac{\varphi_0}{2} = \frac{\omega X_0}{C_0}\frac{2+\Gamma_{dn}}{2}\varepsilon_0$$

$$= \frac{\omega}{C_0}X_0\frac{2+\Gamma_{dn}}{2}\frac{\Delta X}{X_0} = k_0\Delta X\frac{2+\Gamma_{dn}}{2},$$

which yields

$$\Gamma_{dn} = \frac{2M}{k_0\Delta X}-2. \qquad (13)$$

Expression (13) makes it possible to calculate the absolute value of the dynamic acoustic nonlinear parameter Γ_{dn} from the experimentally determined values of the modulation depth M and the amplitude of the wire length variation ΔX [11].

For the experimental investigation of the nonlinear properties of wire samples, an automated measuring system [13] was used. The system makes it possible, concurrent with the measurement of the stress-strain curve $\sigma = \sigma(\varepsilon)$, to determine the amplitude and change in the time of propagation of acoustic waves in the sample in an automated mode of operation. The errors in the determination of the sample elongation did not exceed 0.5 μm, of the force applied to the sample, 0.03 N, and of the change in propagation time, 0.5 ns. The use of a vibration-testing machine allowed us to obtain small sinusoidal variations of the wire length. The amplitude and form of vibrations generated by the vibration-testing machine were monitored with an accelerometer. The spectral components of acoustic waves were measured by a spectrum analyzer.

Three types of polycrystalline samples made of PEV-1 electrotechnical copper wire of various diameters (D = 0.75 and 0.9 mm) were investigated. The first set of samples was made of an annealed wire. In the annealing, the samples were heated in a furnace up to 600°C, held at this temperature for 4 h, and then slowly cooled to 20°C. The second set of samples was made of a hardened wire. The hardening consisted in a fast cooling of a sample in transformer oil after annealing. The samples of the third set were manufactured of a wire not subjected to heat treatment.

In the samples with the length X_0 = 1.10–1.15 m, pulses of longitudinal acoustic waves of the frequency $\omega \sim 160$ kHz and duration 30–50 μs were excited. As a rule, we observed a sequence of several acoustic pulses. By measuring the time of propagation τ_0 and the amplitude of these pulses, we determined the attenuation and velocity of acoustic waves. At a frequency of 160 kHz, the attenuation did not exceed 5 dB/m and the velocity C_0 in the untreated wire was equal to (3600 ± 100) m/s, in the annealed wire, (3700 ± 100) m/s, and in the hardened wire, (3800 ± 100) m/s. These values coincide with the data for rod velocity [14]. Since the acoustic wavelength $\lambda \geq 2$ cm was much greater than the diameter D of the wire samples ($\lambda/D > 25$), the geometric dispersion of the velocity of acoustic waves did not exceed one tenth of a percent and was neglected in the calculations.

The further procedure of the experiment was the same for the samples of all three sets. After the determination of the initial velocity C_0 and the absorption of acoustic waves, the relationship between the stress σ and the sample elongation ΔL was measured. The force applied to a sample was slowly increased until reaching the strain $\varepsilon = \Delta L/X_0 \sim 0.03$ (loading of the sample), which corresponded to the plastic deformation region, and then the force was slowly reduced to zero (unloading of the sample); then, the force was again increased (repeated loading). On reaching the strain $\varepsilon \cong 0.05$, the experiment was terminated. After unloading, a residual deformation was observed in all samples. The measurements were made in an automated mode of operation. Every experiment lasted for 4 h, during which no less than 2500 cycles of measurement were made. The experimental dependences $\sigma = \sigma(\varepsilon)$ are shown in Fig. 1. The concurrent measurements of the changes in the time of propagation of acoustic waves in a sample, $\Delta\tau = \Delta\tau(\varepsilon)$, and the strain made it possible to determine the change in the velocity of acoustic waves, $\frac{\Delta C}{C_0} = -\frac{\Delta\tau}{\tau_0} + \frac{\Delta L}{X_0}$, and to calculate the dependence of the dynamic Young's modulus $E_d(\varepsilon_s)$ on the strain:

$$E_d(\varepsilon) = \rho C_0^2\left[1 + 2\left(\frac{\Delta C}{C_0}\right) + \left(\frac{\Delta C}{C_0}\right)^2\right]. \qquad (14)$$

These dependences for the three types of wire are presented in Fig. 2b.

The form of the dependences $\sigma = \sigma(\varepsilon)$ (Fig. 1) obtained for the wires of all types studied is typical of the materials with elastoplastic linear hardening [15]. The effect of the heat treatment on the elastic properties of the samples is clearly seen. The transition to the plastic region in all samples took place approximately at the same strain $\varepsilon \sim 0.004$. However, the stresses σ arising in this case were noticeably different: $\sigma \sim 100$ MPa in the untreated wire, $\sigma \sim 40$ MPa in the hardened wire, and $\sigma \sim 30$ MPa in the annealed wire. Figure 2a shows the dependences of the static Young's modulus on the strain in the investigated samples; the dependences were obtained by differentiation of the relations $\sigma = \sigma(\varepsilon)$ displayed in Fig. 1. The dependences consist of a set of discrete experimental points and are not continuous functions. In addition, due to the Savart–Masson effect, the dependence $\sigma = \sigma(\varepsilon)$ is represented by a step curve [1]. Therefore, before differentiation, these dependences were smoothed out by polynomials. For zero strain, the values of the static Young's moduli $E(\varepsilon_s)$ are as follows: (14 ± 1) GPa for the annealed wire, (17 ± 1) GPa for the hardened wire, and (60 ± 3) GPa for the untreated wire. These values are much smaller than the tabular data (according to [14], the static Young's modulus of copper lies within 110–130 GPa). Under deformation, the modulus $E(\varepsilon_s)$ decreases and, for $\varepsilon \geq 0.01$ in all samples, it reaches a value of about 1 GPa. However, in the loading-unloading region, $E(\varepsilon_s)$ considerably increases and, in all samples, becomes equal to (115 ± 5) GPa (Fig. 2a), which is consistent with the tabular data for the Young's modulus of copper [14].

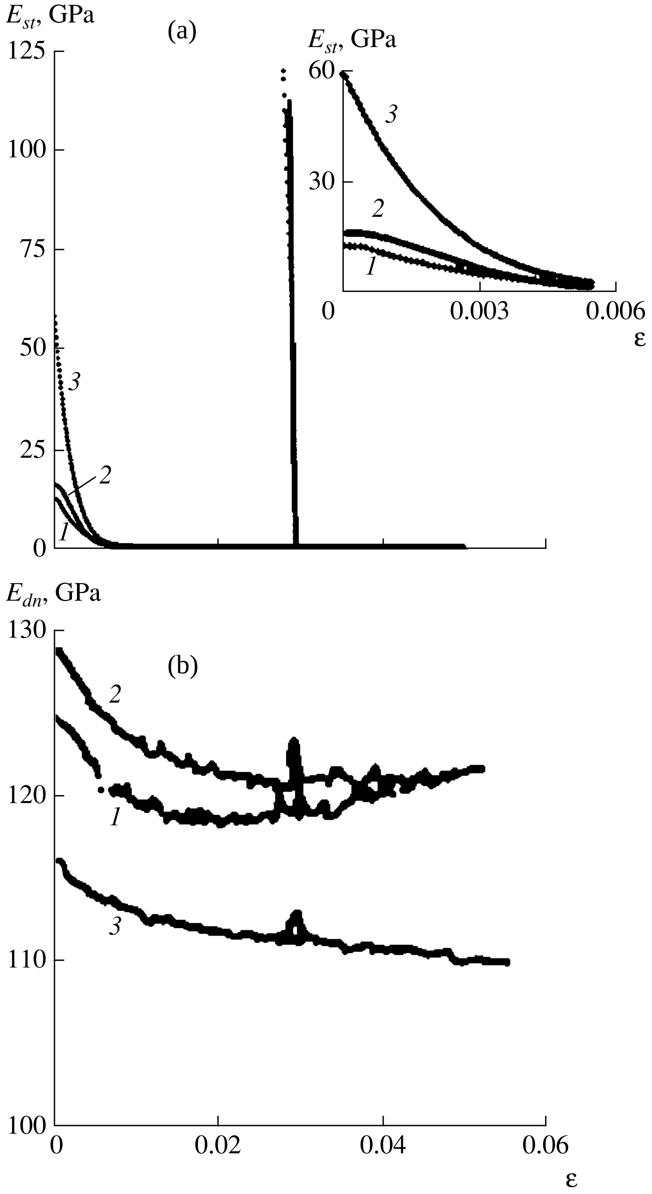

Fig. 2. Dependence of the (a) static and (b) dynamic Young moduli on the strain for the samples of (*1*) an annealed wire, (*2*) a hardened wire, and (*3*) an untreated wire.

The behavior of the dynamic Young's modulus $E_d(\varepsilon_s)$ under deformation essentially differs from the corresponding dependence for the static Young's modulus. In undeformed samples, the values of the modulus $E_d(\varepsilon_s)$ are different ((120 ± 5) GPa for annealed, (128 ± 5) GPa for hardened, and (115 ± 5) GPa for untreated wires), but, within the accuracy of the experiment, they coincide with the tabular data for copper. With an increase in deformation, the decrease in $E_d(\varepsilon_s)$ by no more than 5% is observed. In this case, while in the untreated wire $E_d(\varepsilon_s)$ steadily decreases, in the annealed and hardened wires $E_d(\varepsilon_s)$ begins to increase

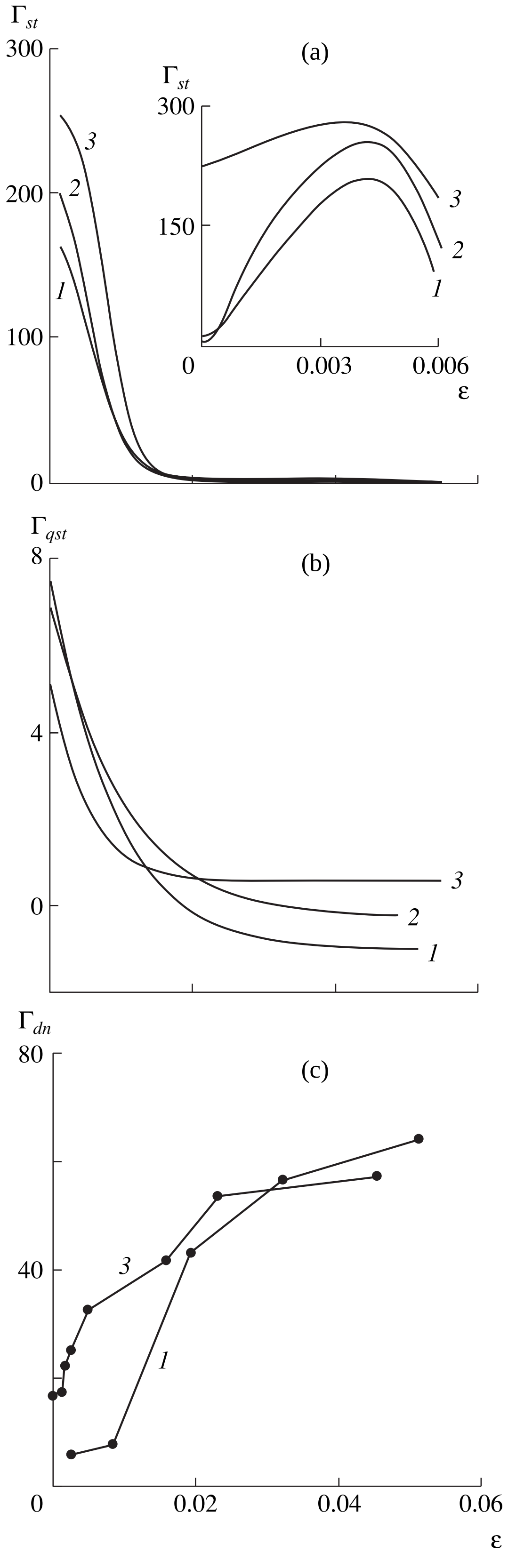

Fig. 3. Dependence of the (a) static, (b) quasistatic, and (c) dynamic nonlinear parameters on the strain for the samples of (*1*) an annealed wire, (*2*) a hardened wire, and (*3*) an untreated wire.

slowly at $\varepsilon > 0.02$. In the loading-unloading region, $E_d(\varepsilon_s)$ in all samples increases to some extent but does not reach its value for the zero strain (Fig. 2b).

From the experimental results displayed in Figs. 1 and 2, according to Eqs. (1) and (4), the static $\Gamma_{st}(\varepsilon_s)$ and quasistatic $\Gamma_{qst}(\varepsilon_s)$ nonlinear parameters were determined. These parameters are presented in Figs. 3a and 3b. As is seen from these figures, in the region of static deformations $\varepsilon \sim 0.004$, the parameter $\Gamma_{st}(\varepsilon_s)$ has a maximum equal to 220 ± 30 for annealed, 250 ± 30 for hardened, and 280 ± 30 for untreated wires and practically becomes zero for $\varepsilon > 0.02$. In the region of zero deformations, the parameter $\Gamma_{st}(0)$ equals 7 ± 2 for hardened and 15 ± 2 for annealed wires, while for an untreated wire $\Gamma_{st}(0) = 220 \pm 30$. The quasistatic parameters $\Gamma_{qst}(\varepsilon_s)$ gradually decrease from the values 5 ± 1, 7 ± 1, and 8 ± 1 in the samples of annealed, hardened, and untreated wires, respectively, in the absence of deformation and reach an approximately constant level for $\varepsilon > 0.02$. The parameter $\Gamma_{qst}(\varepsilon_s)$ changes sign at $\varepsilon \cong 0.018$ for an annealed wire and at $\varepsilon \cong 0.032$ for a hardened wire.

The measurements of the nonlinear dynamic parameter Γ_{dn} were made at the carrier frequency of acoustic waves $f \sim 160$ kHz and the modulation frequency $\Omega/2\pi = 205$ Hz. The strain produced by acoustic waves did not exceed 10^{-6}. For $\Delta X > 10^{-5}$ m, in the acoustic wave spectrum, components appeared at the frequencies $(\omega \pm n\Omega)$, where $n = 1, 2, 3, \ldots$, and, for computing Γ_{dn}, one should use Eq. (11). For the amplitude of length modulation $\Delta X \le 10^{-5}$ m, in the acoustic wave spectrum three components were observed: at the carrier frequency ω and at two side frequencies $(\omega - \Omega)$ and $(\omega + \Omega)$. The amplitudes of the components depended linearly on both ΔX and the carrier amplitude A_0. (In the experiment, the change in the sample length ΔX in the presence of modulation did not exceed 10^{-5} m, and Γ_{dn} was calculated according to Eq. (13).) The results of these measurements for untreated and annealed wires are shown in Fig. 3c. The parameter Γ_{dn} at small strains in an untreated wire is approximately three times as great as in an annealed wire. With the transition to plastic deformations, both wires exhibited an increase in Γ_{dn} by a factor of more than 3 for an untreated wire and by an order of magnitude for an annealed wire.

It is logical to suggest that the changes in the elastic properties of the samples are connected with the changes in their internal structure. In the manufacture of a wire by a drawing method, a fine grain structure forms in it, and this structure changes under subsequent heat treatment, which affects the elastic properties of the samples [16–19]. To determine the correlation between the elastic properties and the internal structure of the samples, metallographic and X-ray diffraction analyses of the samples were performed before and after their plastic deformation. The results of the metallographic analysis of the sample structure are presented

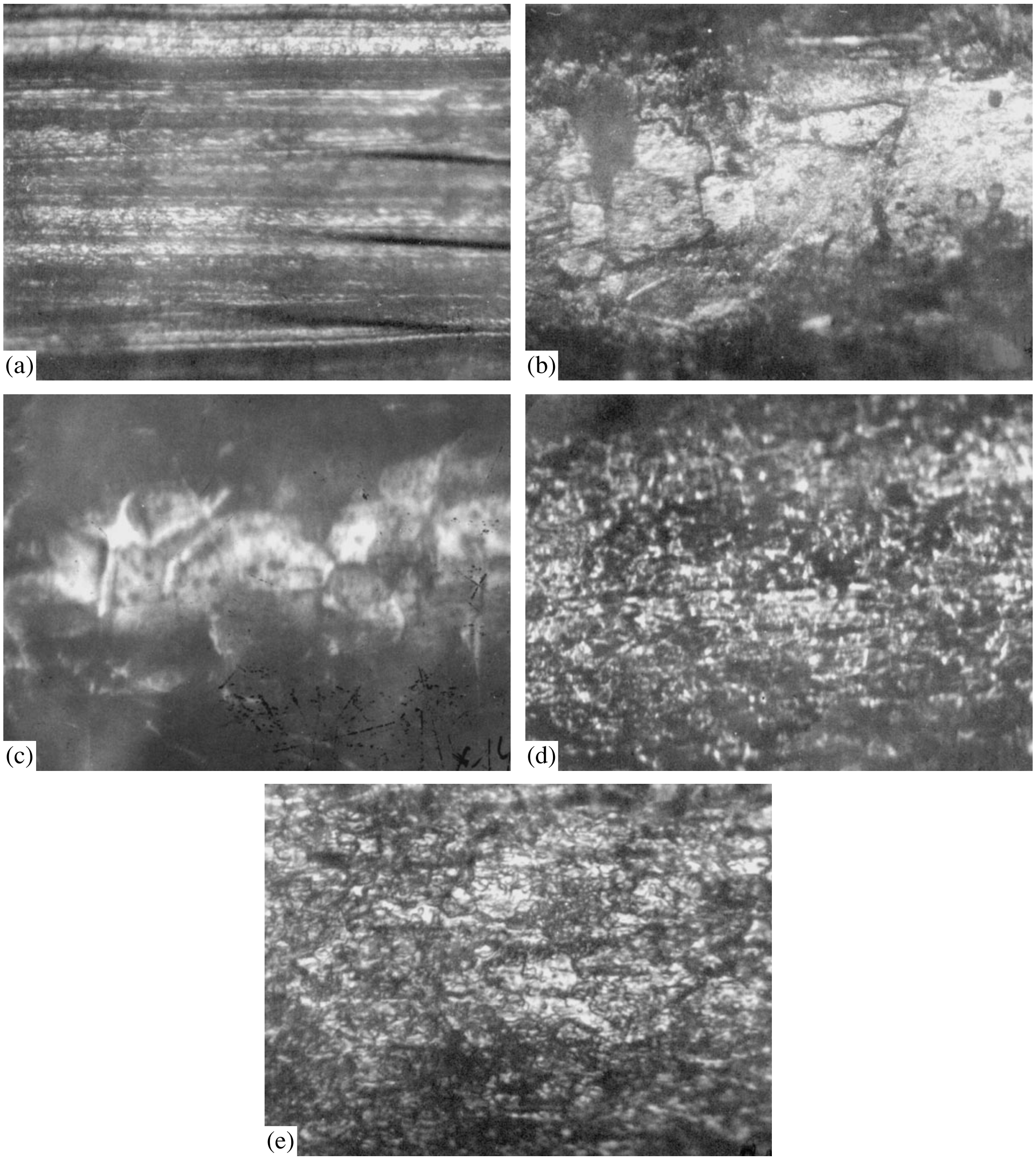

Fig. 4. Micrographs of the samples (140× magnification) of an untreated wire (a) before and (d) after its plastic deformation; (b) an annealed wire and (c) a hardened wire before and (e) after their plastic deformation.

in Fig. 4. In Fig. 4a, it is seen that, inside the wire, during its manufacture, a columnar microstructure forms with the sizes of grains within the columns ~5–10 μm. The X-ray diffraction analysis showed that, in these samples, the [100] texture with a misorientation up to ±25° relative to the sample axis was formed. As a result of annealing, single crystal blocks 35–150 μm in size with sharp narrow boundaries were formed in the wire (Fig. 4b). The blocks had an arbitrary crystallographic orientation. After hardening, the sizes of crystallites and their orientation practically did not change; however, the structure of a hardened wire, compared to the annealed one, proved to be more closely packed and its boundaries were less sharply defined (Fig. 4c). Plastic deformation of an untreated wire resulted in the decrease in crystallite sizes to 5 μm (Fig. 4d) and the appearance of the [111] texture in addition to the [100] texture. However, the amount of the [100] texture was considerably greater, and its misorientation was reduced from ±25° to ±5°. The plastic deformation of annealed and hardened wires resulted in the formation of the predominant [111] texture in them with grain sizes of 3–40 μm (Fig. 4e). This allows us to conclude that the plastic deformation of the samples leads to a decrease in crystallite sizes to 5 μm and to the establishment of a certain crystallographic orientation relative to the wire axis. The analysis of the results of metallographic and X-ray diffraction studies of the samples makes it possible to explain qualitatively the differences in their elastic properties. After the application of a load, a change in the sample length may occur due to various mechanisms: the deformation of crystallites, the multiplication of dislocations, slips and rotations of crystallite blocks relative to each other, and a decrease in the sizes of crystallites (fragmentation). (The presence of the rotation of crystallites is confirmed by the fact that, after plastic deformation, the decrease in the misorientation of the [100] texture in an untreated wire and the establishment of the [111] texture in annealed and hardened samples takes place.) The internal structures of the samples subjected to different kinds of heat treatment differ from one another, and, hence, the contributions of the mentioned mechanisms to the change in the static Young's modulus under deformation are different for different wires. This leads to the differences in the stress-strain curves $\sigma = \sigma(\varepsilon)$ of these samples (Fig. 1).

Different values of the dynamic Young's modulus $E_d(\varepsilon_s = 0)$ of undeformed wire samples are also explained by the internal structure of these samples. In polycrystalline copper samples, the velocity of longitudinal acoustic waves is $V_{\mathrm{pcr}} = 4700$ m/s [14]. In copper single crystals, the velocity of longitudinal acoustic waves along the [100] direction is $V[100] = 4340$ m/s, along the [110] direction, $V[110] = 4960$ m/s, and along the [111] direction, $V[111] = 5160$ m/s [20]. Thus, for longitudinal waves in copper, the following inequality is valid: $V[100] < V_{\mathrm{pcr}} < V[110] < V[111]$. (It can be shown that, in copper, a similar inequality is also satisfied for the rod velocity C [21].) Therefore, in an untreated wire, in which the texture [100] was formed in the course of its manufacture, the rod velocity (and, consequently, the dynamic Young's modulus $E_d(\varepsilon_s = 0)$) is smaller than the corresponding velocities in polycrystalline samples of annealed and hardened wires. Under the deformation of the samples of an untreated wire, a change in the acoustic wave velocity takes place due to the physical nonlinearity, as well as due to the decrease in the misorientation of the [100] texture from ±25° to ±5°. These mechanisms lead to the reduction in the value of $E_d(\varepsilon_s)$. In polycrystalline samples of annealed and hardened wires, the change in the dynamic Young's modulus under strains less than 0.2 is mainly determined by the physical nonlinearity resulting in the decrease in $E_d(\varepsilon_s)$. The increase in the deformation of polycrystalline samples leads to the formation of the [111] texture and, as a consequence, to an increase in the velocity of acoustic waves. At strains greater than 0.2, this mechanism becomes dominant and leads to an increase in the dynamic Young's modulus (Fig. 2b). A similar explanation applies to the change of sign of the quasistatic nonlinear parameter $\Gamma_{qst}(\varepsilon_s)$ in the wire samples subjected to heat treatment in the region of static strains near 0.2 (Fig. 3b).

The increase in the acoustic dynamic nonlinear parameter Γ_{dn} in the region of plastic deformations is connected with the reduction in the sizes of crystallites that results in the growth of the area of their boundaries and, consequently, in an increase in the structural nonlinearity arising at the grain boundaries [4–7]. This is confirmed by the fact that, in an untreated wire under small deformations, the sizes of crystallites are considerably smaller than in an annealed wire, and the nonlinear parameter Γ_{dn} is greater than in an annealed wire. With an increase in deformation, the decrease in the size of structure in annealed samples led to a steeper increase in the parameter Γ_{dn}, as compared to an untreated wire. In the region of plastic deformation, when the sizes of crystallites in both wires become approximately equal, the values of the parameters Γ_{dn} in these wires coincide within the accuracy of the experiment (Fig. 3c).

Thus, we described the results of combined experimental investigations of the elastic nonlinearity of samples of copper wires subjected to various types of heat treatment by static, quasistatic, and dynamic methods in the range of static deformations ($\varepsilon \sim 0$–0.05). The effect of the heat treatment and plastic deformation on the internal structure of the samples was investigated by using metallographic and X-ray diffraction methods. The correlation between the elastic properties and internal structure of the samples was revealed. The values of the quasistatic nonlinear parameter $\Gamma_{qst}(0)$ in all samples and the values of the static parameter $\Gamma_{st}(0)$ in annealed and hardened wires, as well as the value of the parameter Γ_{dn} at small static deformations in an annealed wire, coincide within the accuracy of the experiment with the values of the nonlinear acoustic parameter calculated for copper single crystals by using the literature data for the moduli of elasticity of the second and third orders [20]. This allows us to assume that, at small static deformations, the indicated parameters are determined basically by the physical nonlinearity. At small deformations, the value of the parameter Γ_{dn} in the samples of an untreated wire is approximately two times greater than the corresponding value for an annealed wire. This points to the fact that, together with the physical nonlinearity, in these samples even in the absence of static deformation, a considerable contribution to the value of Γ_{dn} is made by the structural nonlinearity. In the region of plastic deformation, a considerable difference in the values of the nonlinear parameters was observed for the samples that had identical structure but were measured by different methods. This result is associated with the fact that, in this deformation region, the contribution to the values of the nonlinear parameters is made by different physical mechanisms. The static nonlinear parameter $\Gamma_{st}(\varepsilon_s)$ is determined by the specific features of the plastic deformation of polycrystalline samples: the multiplication of dislocations, the slips and rotations of crystalline blocks relative to each other, and a decrease in the crystallite sizes (fragmentation). The value of the quasistatic parameter $\Gamma_{qst}(\varepsilon_s)$ in the plastic deformation region is affected not only by the nonlinearity of intermolecular forces, but also by the processes of fragmentation of individual crystallites and the establishment of a certain crystallographic orientation in them relative to the wire axis. The considerable change in the nonlinear parameter Γ_{dn} in the plastic deformation region is connected with the increase in the structural nonlinearity due to the crystallite fragmentation and the resulting increase in the area of the grain boundaries.

ACKNOWLEDGMENTS

We are grateful to N.A. Khattanova for assistance in conducting the metallographic and X-ray diffraction analyses.

This work was supported by the Russian Foundation for Basic Research, project no. 02-02-16186, and by the President's grant for the Support of Leading Scientific Schools, project no. 00-15-96530.

REFERENCES

1. J. F. Bell, *The Experimental Foundations of Solid Mechanics* (Springer, Berlin, 1984; Nauka, Moscow, 1984).
2. G. A. Malygin, Usp. Fiz. Nauk **171** (2), 187 (2001).
3. L. K. Zarembo and V. A. Krasil'nikov, *Introduction to Nonlinear Physical Acoustics* (Nauka, Moscow, 1966).
4. O. V. Rudenko, Defektoskopiya, No. 8, 24 (1993).
5. A. S. Korotkov, M. M. Slavinskiĭ, and A. M. Sutin, Akust. Zh. **40**, 84 (1994) [Acoust. Phys. **40**, 71 (1994)].
6. I. Yu. Solodov and R. G. Maev, in *Emerging Technologies in NDT* (Brookfield, Rotterdam, 2000), pp. 137–144.
7. Y. Zheng, R. G. Maev, and I. Yu. Solodov, Can. J. Phys. **77** (12), 927 (1999).
8. A. I. Korobov, Yu. Brazhkin, and A. N. Ekonomov, in *Sixth Annual International Conference on Composites Engineering* (Orlando, Florida, 1999), p. 89.
9. R. N. Thurston and K. Brugger, Phys. Rev. A **133**, 1604 (1964).
10. J. E. May, in *Physical Acoustics: Principles and Methods*, Ed. by W. P. Mason (Academic, New York, 1964; Mir, Moscow, 1966), Vol. 1, Part A, pp. 489–565.
11. A. I. Korobov, Yu. A. Brazhkin, E. Yu. Grin', and A. N. Ékonomov, in *Proceedings of X Session of the Russian Acoustic Society* (Moscow, 2000), Vol. 2, p. 107.
12. A. A. Kharkevich, *Linear and Nonlinear Systems* (Nauka, Moscow, 1973).
13. A. I. Korobov, Yu. A. Brazhkin, and A. N. Ékonomov, Izmer. Tekh., No. 7, 48 (2000).
14. *Physical Quantities. Handbook*, Ed. by I. S. Grigor'ev and E. Z. Melikhov (Énergoatomizdat, Moscow, 1991).
15. *Encyclopedia of Physics* (BSE, Moscow, 1992), Vol. 3.
16. R. Z. Valiev and R. K. Islamgaliev, Fiz. Met. Metalloved. **85** (3), 161 (1998).
17. N. A. Tyapunina, E. K. Naimi, and G. V. Bushueva, *Effect of Ultrasound on Defect Crystals* (Mosk. Gos. Univ., Moscow, 1999).
18. A. I. Korobov, A. V. Batenev, and Yu. A. Brazhkin, Defektoskopiya, No. 2, 39 (2000).
19. V. E. Nazarov, Akust. Zh. **37**, 150 (1991) [Sov. Phys. Acoust. **37**, 75 (1991)].
20. R. Truell, C. Elbaum, and B. B. Chick, *Ultrasonic Methods in Solid State Physics* (Academic, New York, 1969; Mir, Moscow, 1972).
21. Yu. I. Sirotin and M. P. Shaskol'skaya, *Fundamentals of Crystal Physics* (Nauka, Moscow, 1975).

Translated by A. Svechnikov

Acoustical Physics, Vol. 48, No. 5, 2002, pp. 572–575. Translated from Akusticheskiĭ Zhurnal, Vol. 48, No. 5, 2002, pp. 649–652.
Original Russian Text Copyright © 2002 by Kotov.

Acoustooptic Multiplication of the Frequency Shift of Optical Radiation on the Basis of Bragg Polarization Splitting

V. M. Kotov

Institute of Radio Engineering and Electronics, Russian Academy of Sciences,
pl. Vvedenskogo 1, Fryazino, Moscow oblast, 141120 Russia
e-mail: vmk277@ire216.msk.su

Received February 17, 2000

Abstract—A technique for the acoustooptic multiplication of the frequency shift of an optical beam is proposed. The technique is based on the cascade diffraction of the beam by a single acoustic wave with the use of Bragg polarization splitting in a uniaxial crystal. The fundamental possibility of the practical realization of the technique is confirmed experimentally by using anisotropic acoustooptic diffraction in $LiNbO_3$. *© 2002 MAIK "Nauka/Interperiodica".*

Acoustooptic techniques are widely used for controlling optical radiation [1–3]. One of the advantages of acoustooptic diffraction is the simplicity of obtaining a frequency shift of an optical beam as a result of the reflection of light from a traveling acoustic grating. In this case, the light frequency ν is shifted by the frequency of the sound wave *f*. In many practical applications, it is necessary to shift the frequency of light by greater values. The simplest way to do this is to utilize Raman–Nath diffraction. However, in this case, the intensities of diffracted beams are highly nonuniform, the number of the diffraction orders is practically uncontrollable, and the major part of the light energy propagates in the zero diffraction order [1–3]. In this connection, techniques based on Bragg diffraction should be preferable.

In this paper, cascade diffraction, which consists in a repeated Bragg interaction of light with a single acoustic wave (see, e.g., [4]), is proposed as a method for obtaining relatively large frequency shifts.

The type of cascade acoustooptic interaction studied previously [4] can be realized only on the basis of a gyrotropic crystal. The present paper proposes a technique that allows one to obtain a cascade diffraction in crystals without gyrotropy. This extends the range of acoustooptic materials suitable for acoustooptic multiplication of the frequency shift of optical radiation in Bragg diffraction conditions. The technique is based on the specific features of the diffraction of light by sound in an anisotropic medium when two diffraction modes exist for different angles of light incidence [1–3]. The optical scheme of an acoustooptic cell using this feature is presented in Fig. 1. The initial optical radiation I_0 with the polarization corresponding to the ordinary beam (a negative crystal is considered for definiteness, though this is not fundamentally important) is incident on the input optical plane of a crystal at the angle γ_1 and is refracted within the crystal at the angle Θ_1. As the result of the anisotropic diffraction by a traveling acoustic wave with the wave vector **q** and frequency *f*, this beam deviates, with its polarization changing to orthogonal and is incident on the output plane of the cell at the angle $\Theta_2 < \Theta_1$. The beam going out at the angle γ_2 is reflected from the external mirror M_1 and then again directed to the acoustooptic cell at the angle γ_4 with respect to its optical plane. After the refraction within the crystal at the angle Θ_4, this beam is diffracted by the same acoustic wave **q** and, after one more anisotropic diffraction, is incident on the opposite optical plane at the angle Θ_3. Going out of the crystal at the angle γ_3, this beam is reflected from the mirror M_2 and is again directed at the acoustooptic cell at the angle γ_1,

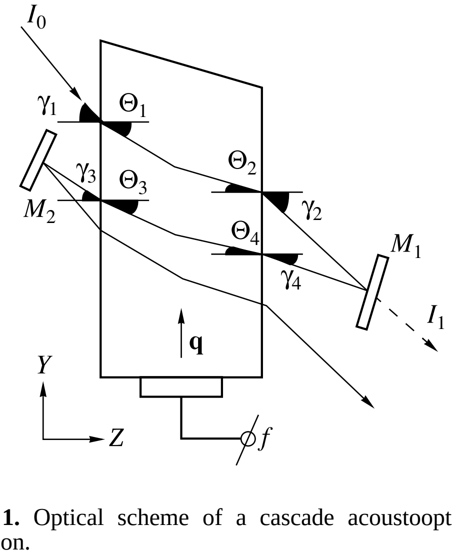

Fig. 1. Optical scheme of a cascade acoustooptic diffraction.

1063-7710/02/4805-0572$22.00 © 2002 MAIK "Nauka/Interperiodica"

and so on. The process can be repeated many times. Thus, the cascade acoustooptic diffraction of light by a single acoustic wave is realized, and the frequency of optical radiation increases by the sound frequency after each act of diffraction ($\Theta_2 < \Theta_1$ and $\Theta_4 < \Theta_3$). All diffraction acts occur at different points of the crystal, which makes it possible to spatially separate all diffracted beams. If the mirrors M_1 and M_2 are semitransparent, part of the radiation can be led out of the system after each act of diffraction (as the radiation I_1, for example).

Figure 2 shows the vector diagram of acoustooptic interaction that serves as the basis for the cascade diffraction. The diffraction occurs in a uniaxial crystal, and the diffraction plane is inclined at the angle α to the optical axis OZ of the crystal. The beams $\mathbf{K}_1$ and $\mathbf{K}_4$ are diffracted in the directions $\mathbf{K}_2$ and $\mathbf{K}_3$, respectively, as a result of their interaction with the same acoustic wave $\mathbf{q}$. The angles Θ_1–Θ_4 in Fig. 2 fully correspond to the angles Θ_1–Θ_4 in Fig. 1. The sequence of the diffraction acts is as follows: the initial radiation $\mathbf{K}_1$ diffracts in the direction of the beam $\mathbf{K}_2$, which propagates in the direction of the beam $\mathbf{K}_4$ after reflection from the external mirror; the latter beam diffracts in the direction of the beam $\mathbf{K}_3$, which returns to the crystal along the direction of the beam $\mathbf{K}_1$ after reflection from the second external mirror, and so on. Such a chain of acoustooptic interactions provides the spatial separation of the diffraction acts in the crystal. The process can be repeated many times, and the diffraction region moves along the acoustooptic cell as the number of the acts of this process grows.

The beams $\mathbf{K}'_3$ and $\mathbf{K}'_4$ that are the symmetric reflections of the beams $\mathbf{K}_3$ and $\mathbf{K}_4$ with respect to the point O are shown in Fig. 2 to stress the presence of two kinds of diffraction in an anisotropic medium. In this case, the beams $\mathbf{K}_1$, $\mathbf{K}_2$, $\mathbf{K}'_3$, and $\mathbf{K}'_4$ lie within the same quadrant, and one can see that $\Theta_1 \neq \Theta'_3$ and $\Theta_2 \neq \Theta'_4$. To obtain the diffraction parameters, one can use a common method described, e.g., in [2, 3], where the processes of acoustooptic interaction near and far from the optical axis of a crystal are considered. However, the practical utilization of acoustooptic elements imposes some additional restrictions on the choice of the diffraction conditions. In practice, it is desirable to use the conditions with the optical radiation incident on an acoustooptic cell at comparatively small angles. This simplifies the problem of the antireflection treatment of optical planes, reduces the crystal dimensions, etc. From this point of view, the optimal choice seems to be the utilization of Bragg polarization splitting [5], which is characterized by the fact that the optical radiation is deviated simultaneously into two diffraction orders (+1 and –1). This idea realized completely in a uniaxial crystal serves as the basis of the proposed type of cascade diffraction.

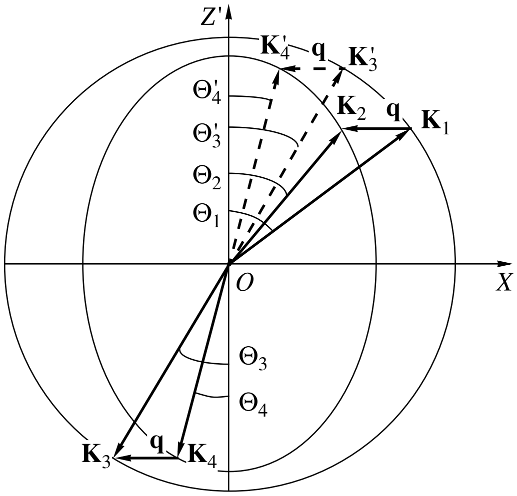

Fig. 2. Vector diagram of the cascade acoustooptic diffraction.

For convenience, we will operate with the vectors $\mathbf{K}_1$, $\mathbf{K}_2$, $\mathbf{K}'_3$, and $\mathbf{K}'_4$ and not with $\mathbf{K}_1$, $\mathbf{K}_2$, $\mathbf{K}_3$, and $\mathbf{K}_4$, which is of no fundamental importance from the point of view of mathematics. We denote the vector magnitudes by K_1, K_2, K_3, and K_4, respectively. Further, we change to the projections of these quantities on the OX axis:

$$\begin{aligned} A_1 &= K_1 \sin\Theta_1; \quad A_3 = K_3 \sin\Theta_3; \\ A_2 &= K_2 \sin\Theta_2; \quad A_4 = K_4 \sin\Theta_4. \end{aligned} \tag{1}$$

For a uniaxial negative crystal, it is evident that $K_1 = K_3 = 2\pi n_0/\lambda_0$, where n_0 is the refraction index of the ordinary beam for the light wavelength λ_0. In our experiments (see below), the acoustic wave is propagated normally to the optical OZ axis of the crystal. Therefore, we assume that $\mathbf{q} \perp OZ$ in our calculations. Moreover, we assume that $A_2 = A_3$ (the condition for the realization of the Bragg polarization splitting). Taking into account that $K_1\cos\Theta_1 = K_2\cos\Theta_2$ and $K_3\cos\Theta_3 = K_4\cos\Theta_4$, which follows from the orthogonality of $\mathbf{q}$ and OZ, the relation between the quantities A_1–A_4 can be obtained:

$$\begin{gathered} A_2^2 = \left(\frac{n_e}{n_\alpha}\right)^2 (A_1^2 + K_1^2 m), \\ A_4^2 = \left(\frac{n_e}{n_\alpha}\right)^2 (A_3^2 + K_1^2 m), \quad A_2 = A_3, \quad 2A_3 = A_1 + A_4, \end{gathered} \tag{2}$$

where $m = \dfrac{n_\alpha^2}{n_0^2} - 1$, $n_\alpha = \dfrac{n_0 n_e}{\sqrt{n_0^2 \sin^2\alpha + n_e^2 \cos^2\alpha}}$, n_0 and n_e are the main refractive indices of the crystal, and α is the inclination angle of the diffraction plane to the opti-

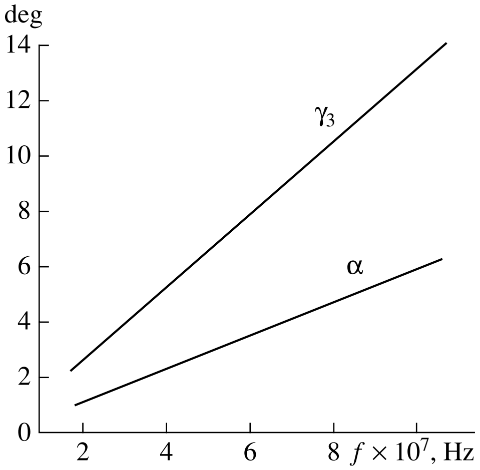

Fig. 3. Dependences of the angles γ_3 and α on the frequency of sound f.

cal OZ axis of the crystal. Solving the system of equations (2) with respect to A_3, we obtain

$$A_3 = \frac{K_1^2 m\left[1-\left(\frac{n_e}{n_\alpha}\right)^2\right]}{\left(\frac{n_\alpha}{n_e}-\frac{n_e}{n_\alpha}\right)^2-4} \times\left[1 \pm \sqrt{1-\frac{\left[1+\left(\frac{n_e}{n_\alpha}\right)^2\right]^2\left[\left(\frac{n_\alpha}{n_e}-\frac{n_e}{n_\alpha}\right)^2-4\right]}{\left(\frac{n_\alpha}{n_e}\right)^2\left[1-\left(\frac{n_e}{n_\alpha}\right)^2\right]^4}}\right]. \quad (3)$$

The value of the wave vector of sound q is determined as

$$q = A_1 - A_2 = A_3 - A_4. \quad (4)$$

The angles Θ_1–Θ_4 are determined by the expressions

$$\sin\Theta_3 = \frac{A_3\lambda_0}{2\pi n_0};$$

$$\sin^2\Theta_2 = \frac{n_0^2\sin^2\Theta_3}{n_\alpha^2 + n_0^2\sin^2\Theta_3\left(1-\frac{n_\alpha^2}{n_e^2}\right)}; \quad (5)$$

$$\sin^2\Theta_1 = \frac{n_\alpha^4}{n_0^2 n_e^2}\frac{\sin^2\Theta_2}{1+m\sin^2\Theta_2} - m;$$

$$\sin^2\Theta_4 = \frac{\sin^2\Theta_3 + m}{\frac{n_\alpha^4}{n_0^2 n_e^2} + \left(1-\frac{n_\alpha^2}{n_e^2}\right)(\sin^2\Theta_3 + m)}.$$

The angles γ_1–γ_4 are determined on the basis of Snell's law for anisotropic media. Taking into account Eq. (4), the sound frequency f is represented in the form

$$f = \frac{V n_0}{\lambda_0}\left(\sqrt{\frac{n_\alpha^2}{n_e^2}\sin^2\Theta_3 - m} - \sin\Theta_3\right). \quad (6)$$

Here, V is the velocity of the sound wave.

Figure 3 shows the dependences of the angles α and $\gamma_3 = \arcsin(n_0 \sin\Theta_3)$ on the acoustic wave frequency f that are calculated on the basis of Eqs. (3)–(6). It is assumed that diffraction occurs in $LiNbO_3$ by a transverse acoustic wave with the velocity $V = 3.84 \times 10^5$ cm/s, the wavelength of optical radiation is $\lambda_0 = 0.63 \times 10^{-4}$ cm, and the refractive indices are $n_0 = 2.286$ and $n_e = 2.202$. In the calculations, the plus sign was chosen in Eq. (3), because only with this sign was the value of A_3 positive. One can see that the angular dependences have a linear character within the frequency range from 0 to ~110 MHz, and the angle γ_3 increases more than two times faster than the angle α. At higher frequencies, the angle γ_3 begins to increase exponentially and reaches a value of 90° at $f = 350$ MHz. In other words, the maximal shift frequency that can be obtained in every diffraction act using the Bragg polarization splitting in $LiNbO_3$ does not exceed 350 MHz.

The possibility of realizing cascade diffraction in $LiNbO_3$ was tested experimentally. We selected the single crystal dimensions 8 × 8 × 10 mm along the directions [100], [010], and [001], respectively. A transverse acoustic wave with a frequency of 102 MHz (the third harmonic of a piezoelectric transducer made of $LiNbO_3$) was generated along the [010] direction with the [100] direction of the shear. A He–Ne laser of LG-207-A type was selected as the source of optical radiation. It generated light with the wavelength $\lambda = 0.63 \times 10^{-4}$ cm. First of all, the conditions of Bragg polarization splitting were obtained with two diffracted beams formed on both sides of the incident radiation. These beams were in strict Bragg synchronism with the incident radiation; i.e., they appeared or vanished simultaneously at angular detuning. The polarization of the incident radiation was oriented at an angle of 45° to the [100] direction to provide the best and equal conditions of diffraction on both sides of the incident beam. For the input electrical power $P_{el} \sim 1$ W, the efficiency of the diffraction in each order was ~12% of the incident radiation. The diffraction angle was ~1°. The effect of splitting was obtained reliably and taken as the basis for the realization of the cascade diffraction. For this purpose, the crystal was oriented in a corresponding way, according to Fig. 1. The input polarizer was positioned so that the ordinary beam propagated through it. The angle of light incidence on the crystal was 20°, and the diffraction efficiency was 20%. The diffracted beam was again directed into the acoustooptic cell under the Bragg angle with the help of an external mirror, and the secondary diffraction with an efficiency of ~4% of the initial beam was realized. The diffracted beam was again directed at the crystal under the angle corresponding to the incidence angle of the initial beam with the help of the second mirror. The next diffracted beam (the third diffraction act) was obtained by the angular adjustment of the second mirror. The intensity of this beam was ~0.5% of the initial incident beam. The experiment did not aim to determine the limiting parameters of the frequency multiplication (in particular, it is possible to increase the length of acoustooptic interaction and thereby decrease the diffraction into other orders whose efficiency was 10–15%, to optimize the sound field within the sample, etc.). Our aim was to confirm the fundamental possibility of realizing Bragg polarization splitting for the tasks of multiplication of the frequency shift of an optical signal.

The following conclusions can be made on the basis of the investigation described:

(1) The existence of two diffraction types at different angles of light incidence provides an opportunity to realize a cascade acoustooptic diffraction with the spatial separation of the regions of acoustooptic interaction in the crystal.

(2) The conditions of Bragg polarization splitting are the best from the practical point of view. They provide two types of diffraction that occur at different angles of light incidence on the crystal, the incidence angles being the smallest in this case.

(3) The fundamental possibility of realizing a cascade diffraction on the basis of polarization splitting is confirmed experimentally using an acoustooptic cell made of $LiNbO_3$. A three-cascade diffraction with an output beam efficiency of 0.5% with respect to the incident beam is obtained.

ACKNOWLEDGMENTS

This work was supported in part by the Russian Foundation for Basic Research, project no. 01-01-00545.

REFERENCES

1. L. N. Magdich and V. Ya. Molchanov, *Acoustooptic Devices and Their Applications* (Sovetskoe Radio, Moscow, 1978; Gordon and Breach, New York, 1988).
2. V. I. Balakshiĭ, V. N. Parygin, and L. E. Chirkov, *Physical Foundations of Acoustooptics* (Radio i Svyaz’, Moscow, 1985).
3. J. Xu and R. Stround, *Acoustooptic Devices: Principles, Design, and Applications* (Wiley, New York, 1992).
4. V. M. Kotov, Kvantovaya Élektron. (Moscow) **30** (4), 373 (2000).
5. V. M. Kotov, Avtometriya, No. 3, 109 (1992).

Translated by M. Lyamshev

Acoustical Physics, Vol. 48, No. 5, 2002, pp. 576–583. Translated from Akusticheskiĭ Zhurnal, Vol. 48, No. 5, 2002, pp. 653–660.
Original Russian Text Copyright © 2002 by Matveev, Mityugov.

Determination of the Parameters of Motion for an Underwater Object

A. L. Matveev and V. V. Mityugov

Institute of Applied Physics, Russian Academy of Sciences,
ul. Ul'yanova 46, Nizhni Novgorod, 603600 Russia
e-mail: matveyev@hydro.appl.sci-nnov.ru

Received August 22, 2001

Abstract—Experimental data on the observation of a moving underwater acoustic screen by simplest antenna arrays extended in both vertical and horizontal directions are presented. New signal processing algorithms are proposed. *© 2002 MAIK "Nauka/Interperiodica".*

In the last decade, much attention has been paid to using vertical multielement arrays to observe moving inhomogeneities in shallow underwater sound channels. High efficiency and reliability were attained with the method of an incoherent accumulation of the signal outputs over the array elements [1–4]. With the signals received by the array, one can advantageously use the mode expansions of the sound field for a given sound speed profile [5–7] to solve the problem of estimating the position of a distant sound source [8] and solve many other problems. Such studies have been repeatedly performed in both in-sea experiments [9, 10] and computer simulations [1, 2, 11].

In this paper, we consider the forward-scattering observations in which a compact object (an acoustically opaque or other type of inhomogeneity) moves in space between the array and a cw sound source across the propagation path.

According to numerous experimental observations, a vertical array, on average, provides higher noise immunity and reproducibility in comparison with a horizontal one. The reason is that, because of the multimode sound propagation in a shallow-water sound channel, the signal output produced by the inhomogeneity that shadows the source proves to be vertically distributed in a highly nonuniform manner. Therefore, a horizontal array can miss some valid signals in depth, while the vertical one monitors the whole water column or most of it. The situation is somewhat better with multifrequency cw transmission but, even in this case, the vertical array has certain advantages [10].

The inherent drawback of a vertical array is that, in most practical-purpose applications, it is unable to determine the direction at which the moving inhomogeneity crosses the propagation path, although the corresponding projection of the velocity vector can be measured to a good accuracy by means of quasi-holographic matched filtration with computer algorithms for searching over the filter parameters [2].

The evident way to overcome this difficulty consists in using arrays of a more general type, which, in addition to the advantages of the vertical array, provide a sufficient horizontal base to indicate the direction of the inhomogeneity movement. Below, we present experimental results for two implementations of such arrays: a binary pair that consists of two vertical arrays aligned in the plane that is perpendicular to the propagation path and an inclined array that forms an angle of $\pi/4$ with the vertical axis in the same plane. The experiments were carried out at the Sankhar Lake (Vladimirskaya oblast, Russia) in 1999 [10].

Let us briefly recall the algorithms of signal processing for forward-scattering observations with a single vertical array, which were used in [2–4]. Let $x_{kj}(t)$ be the current complex amplitude of the signal that has the carrier frequency f_j and is received by the kth hydrophone of the array:

$$x_{kj}(t) = X_{kj}(t)e^{i\varphi_{kj}(t)}, \tag{1}$$

where X_{kj} and φ_{kj} are the real amplitude and phase, respectively.

The preliminary procedure of subtracting the strong initial signal of the source, along with the most significant low-frequency fluctuations, consists in forming the normalized amplitude and phase variables:

$$Y_{kj}^{(a)}(t) = \frac{X_{kj}(t)}{\tilde{X}_{kj}(t)} - 1, \tag{2}$$

$$Y_{kj}^{(\varphi)}(t) = \varphi_{kj}(t) - \tilde{\varphi}_{kj}(t), \tag{3}$$

where $\tilde{X}_{kj}(t)$ and $\tilde{\varphi}_{kj}(t)$ are the results of smoothing the respective initial quantities by the sliding filter producing a window of τ in duration (about several tens of seconds, see [1–4]). From the resulting quadrature components, the following complex variables are formed:

$$Y_{kj}(t) = Y_{kj}^{(a)}(t) + iY_{kj}^{(\varphi)}(t). \tag{4}$$

In the signal processing, to separate the diffraction-shadow perturbations caused by the moving inhomogeneity, these variables are match-filtered,

$$F_{kj}(t) = \left|\int Y_{kj}(t')\Phi_j^*(t-t')dt'\right|, \tag{5}$$

with the linear filter constructed on the basis of *a priori* theoretical information [2, 12] on the structure of the valid signal. Namely,

$$\Phi_j(t) = C_j \exp\left[-\frac{V^2}{h\lambda_j}\left(i\pi + \frac{2l^2}{h\lambda_j}\right)t^2\right], \tag{6}$$

where V is the velocity component across the propagation path, l is the projection of the screen length on the same direction, h is the adjusted distance of the path from the array, and λ_j is the depth-averaged wavelength at the jth observation frequency. Remember here that the adjusted distance h is determined from length L of the propagation path and the physical distance R of the diffractor from the array at the point where the path crosses the trajectory of motion:

$$h = R\left(1 - \frac{R}{L}\right). \tag{7}$$

The constant C_j is found from the normalization condition

$$C_j^{-1}\int|\Phi_j(t)|^2 dt = 1. \tag{8}$$

After all the aforementioned procedures, the transformed signal outputs are incoherently accumulated:

$$F_j(t) = \frac{1}{N}\sum_{k=1}^{N}|F_{kj}(t)|, \tag{9}$$

where N is the number of array elements. If several frequencies are studied in the experiment, the resulting output signals are additionally averaged over the frequencies.

Let us consider an experiment with a binary pair of two vertical arrays: array 1 (left with respect to the direction towards the source) and array 2 (right). Let B be the horizontal base between the arrays along the line perpendicular to the propagation path. According to simple kinematic considerations, the delay time t_d between the signal outputs of the arrays of the aforementioned pair can be expressed as

$$t_d = \frac{B}{|V|}\left(1 - \frac{R}{L}\right), \tag{10}$$

the signs "+" or "–" being in an evident manner related to the direction at which the inhomogeneity crosses the path.

The experimental record, slightly less than 12 min in its duration, is presented below to illustrate three cases of crossing the path by the model screen. The model was a cylindrical body, 3 m in length and 0.45 m in diameter. This model was towed across the middle of the 300-m path, nearly perpendicularly to it, with a speed of 0.6 m/s. The depth of towing was 6 m.

The signals were received by two 64-element vertical arrays, which were horizontally separated by 4.5 m. Each array had the length 12 m and covered nearly the entire thickness of the underwater waveguide. The insonification was performed at three frequencies: f_1 = 2117 Hz, f_2 = 2499 Hz, and f_3 = 2995 Hz. As the transmitting system, a horizontal array consisting of 16 sound sources and phased towards the receiving arrays was used.

Figure 1 (curve *a*) shows the result of averaging the outputs of array 1 over the three frequencies. Before averaging, the signals were processed according to the mentioned procedures, namely: the normalizing subtraction of the main part of the initial signal, the matched filtration (5) and (6) of complex variables $Y_{kj}(t)$, and the incoherent accumulation over the array elements. The following abbreviations and parameter values are used in Fig. 1a: max = 0.065 is the maximal value of the signal outliers after averaging over three peaks, snr = 20.05 is the signal-to-noise ratio averaged over three peaks, ave = 0.025 is the constant noise background, and rms = 0.002 is the standard deviation for the remaining fluctuations.

Figure 1 (curve *b*) presents a similar result for array 2. The detailed comparison of the two plots shows that the time separation t_d of the two correspondent peaks is 3.75 s. This value agrees with the estimate yielded by Eq. (10) for the given speed $|V|$ = 0.6 m/s of the model that crosses the middle of the path, with signal reception by the binary arrays horizontally separated by B = 4.5 m.

The sign of the observed delay also allows one to determine the direction of crossing the path by the model: from left to right for the first and third (in time) signal peaks and from right to left for the second one. The aforementioned feature is well pronounced in Fig. 2 that illustrates the difference signal

$$F^{(-)}(t) = \frac{1}{3}\sum_{j=1}^{3}[F_j^{(1)}(t) - F_j^{(2)}(t)], \tag{11}$$

i.e., the result of subtracting the curves of Fig. 1.

The structure of sign-varying curve of Fig. 2 offers another interesting possibility to improve the noise immunity of the observations, namely, by performing the secondary matched filtration of the difference-signal perturbations to obtain sharpened peaks of the same signs, with higher levels relative to the remaining noise.

Let us consider the corresponding model for the filter. Again, we make use of the theoretical model for the diffraction signal, which was introduced in our previ-

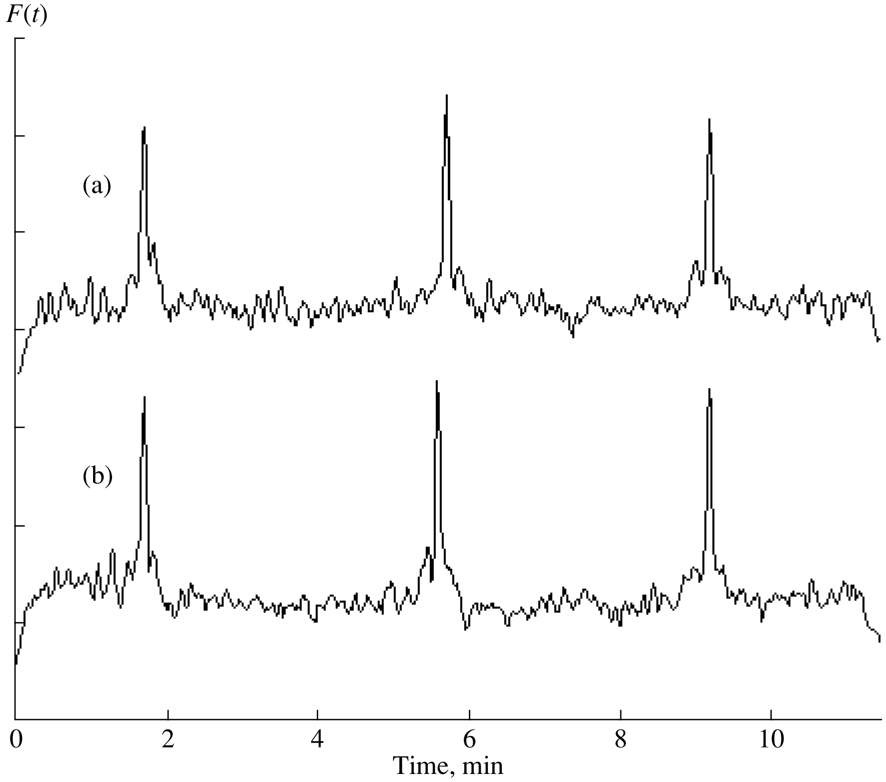

Fig. 1. Results of the incoherent accumulation of the transformed signal outputs averaged over three frequencies: arrays (a) 1 and (b) 2.

ous studies [2–4], but this time, it is applied to arrays 1 and 2 of the binary pair:

$$Y_j^{(1,2)}(t) = a_j \exp\left[-\frac{V^2}{h\lambda_j}\left(i\pi + \frac{2l^2}{h\lambda_j}\right)(t \pm t_d/2)^2\right]. \quad (12)$$

Here, a_j is the amplitude of the diffraction-shadow perturbation, which is expressed through the acoustic cross section σ of the model according to the semi-empirical formula [2]

$$a_j = \mu\frac{\sigma}{H\sqrt{h\lambda_j}}. \quad (13)$$

In this equation, H is the channel thickness and, for the experiments at the Sankhar Lake, $\mu \simeq 1.7$ is the empirical factor that allows for the multiray nature of sound propagation.

Let us perform the integration in Eq. (5). By substituting Eq. (12) into Eq. (5), with the calculated normalizing constant

$$C_j = \pi^{\frac{1}{2}}\frac{h\lambda_j}{2l|V|}, \quad (14)$$

and extracting the full square in the exponent, we obtain

$$F_j^{(1,2)}(t) = a_j \exp\left[-V^2\left(\frac{l^2}{h\lambda_j} + \frac{\pi}{4l^2}\right)(t \pm t_d/2)^2\right]. \quad (15)$$

Specifying $t_d = B/2|V|$ (which corresponds to crossing the path in its midpoint), we construct the difference filter

$$D_j(t) = A_j e^{-\alpha_j t^2} \times 2\sinh(\alpha_j t t_d), \quad (16)$$

where

$$\alpha_j = V^2\left(\frac{l^2}{h\lambda_j} + \frac{\pi}{4l^2}\right). \quad (17)$$

The constant A_j is found from the condition

$$A_j^{-1}\int|D_j(t)|^2 dt = 1. \quad (18)$$

With such a normalization, in the resulting convolutions

$$S_j(t) = \left|\int[F_j^{(1)}(t') - F_j^{(2)}(t')]D(t-t')dt'\right|, \quad (19)$$

we can again use the estimating expression (13) to determine the height of the signal peak.

Figure 3 shows the result of applying algorithm (19) to the binary-difference signals of the same record (with averaging over three frequencies). The signal-to-noise ratio becomes higher by a factor of 1.5, and there is nearly no noise “basement” of the signal. It seems

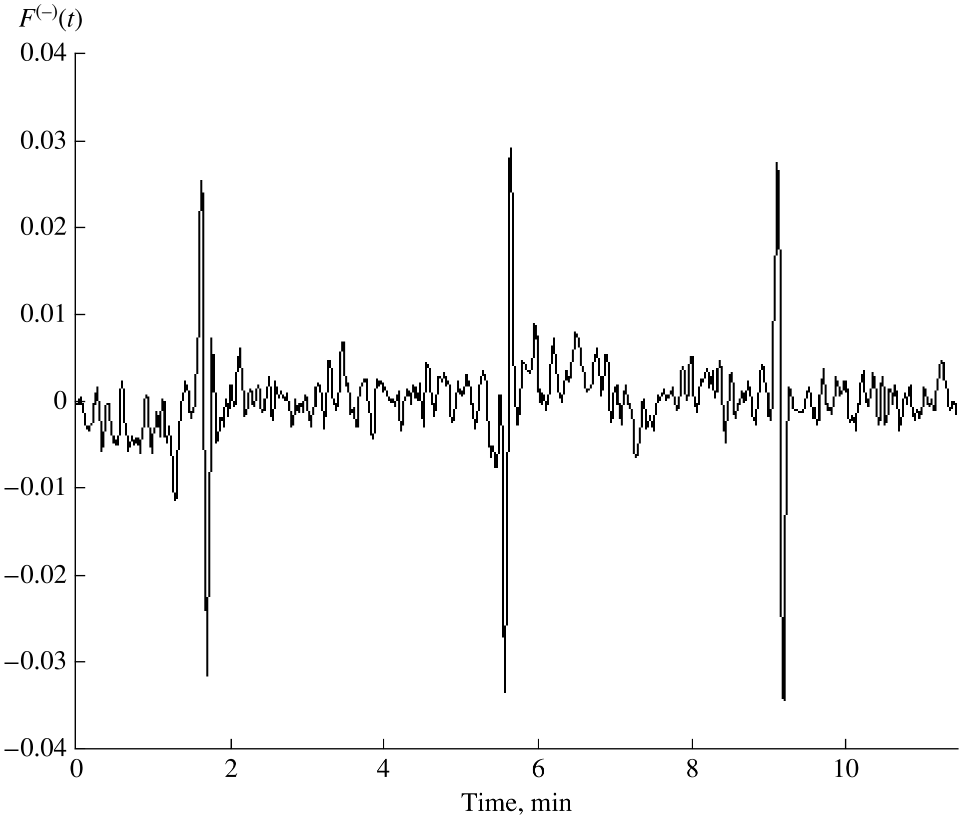

Fig. 2. Difference output of the binary pair.

that here we approach the fundamental limit of noise immunity, which can ever be attained with the principle of incoherent accumulation of signal outputs for vertical arrays.

Another simplest representation of the array that is both vertically and horizontally extended is an inclined linear array. In the experiment, we used a 64-element 12-m array forming an angle of π/4 with the vertical in the plane perpendicular to the direction towards the source. In this case, the cw sound field of frequency 2499 Hz was generated by a vertical array of 16 sound sources whose phasing was chosen to maximally suppress the excitation of modes with higher numbers in order to decrease the fluctuations caused by the nonstationary intermode interference.

The main specificity of incoherent signal accumulation over the elements of the inclined array is the need to take into account the time delays between the sharpened signal peaks associated with the moving inhomogeneity. Instead of Eq. (9), now one should use the algorithm of accumulation with shifting:

$$F_j(t) = \frac{1}{N}\sum_{k=1}^{N}|F_{kj}(t \pm k\Delta)|, \qquad (20)$$

where k is the ordinal number of the hydrophone and Δ is the time delay between the pair of adjacent array elements.

If the parameters of the inhomogeneity motion are not known in advance, the time delays Δ between the adjacent hydrophones and the signs of delays become additional quantities to be found, as in [2]. By using the appropriate test algorithms, we can determine both the value $|V|$ of the speed with a higher accuracy and the direction of motion.

We illustrate the aforementioned statement by considering the data of the experiment in which the parameters of motion of the model (the same model as in the previous experiment) were known in advance. One can see that, for our inclined array, the value of Δ is determined by the simple formula

$$\Delta = \frac{d}{|V|\sqrt{2}}\left(1-\frac{R}{L}\right), \qquad (21)$$

where $d = 19.5$ cm is the distance between the adjacent array elements.

Let us consider the 16-min fraction of the record, which contains two crossings of the path midpoint by the model in two opposite directions. The speed $|V|$ of the model was 0.6 m/s. Formula (21) now yields $\Delta = 0.115$ s. Figure 4 shows the result of the data accumu-

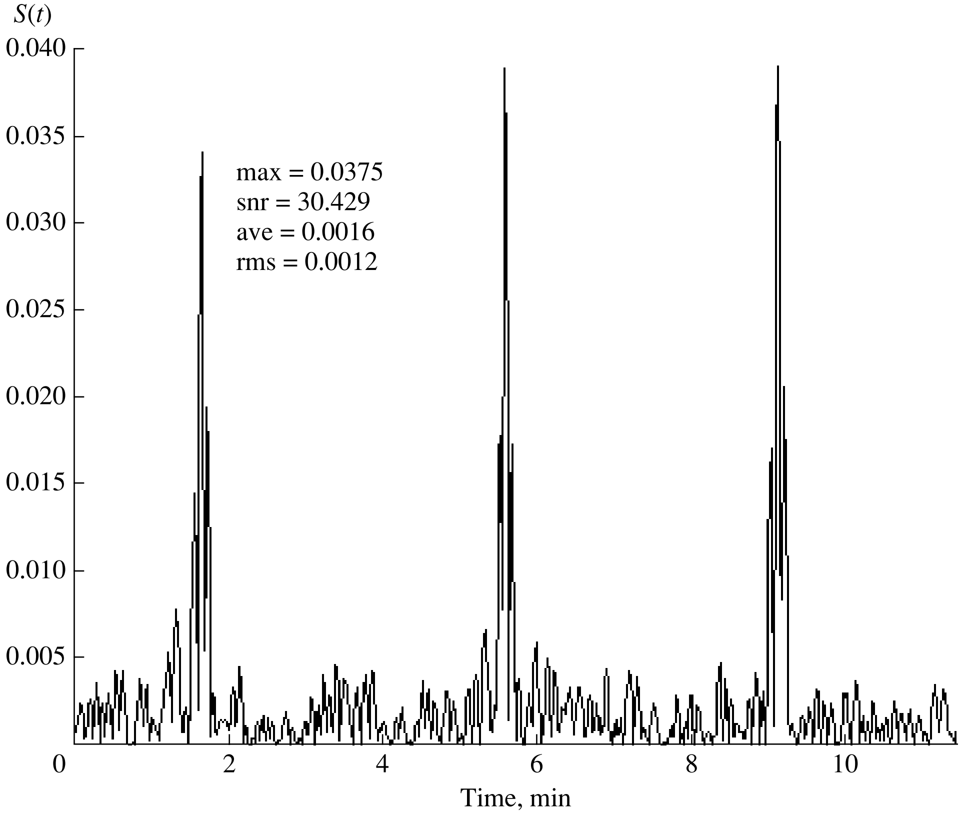

Fig. 3. Result of the secondary matched filtration for the binary pair of two vertical arrays.

lation with shifting for the sign "+" in Eq. (20). It is evident that the second (in time) peak corresponds to the correct choice of the delay sign, while the first peak proves to be noticeably suppressed. In the figure, the values of the signal-to-noise (SNR) ratios are separately shown for the first and second peaks.

Figure 5 shows the result of the same data processing for the sign "–" in Eq. (20). Now, the sharpened and suppressed peaks interchanged their positions. Thus, the inclined array allows one to identify the crossing direction with a sufficient degree of reliability. At the same time, such an array retains all the advantages of the vertical array, as compared to the horizontal one, i.e., the high reliability and reproducibility of observations.

Finally, let us discuss the possibility for a single vertical array to indicate the movement direction in a physically asymmetric channel. Note that the previous case of the inclined array is just an example of this kind of asymmetry produced in an artificial way. However, in realistic environments, the asymmetry may be caused by natural factors, for example, a slight bottom inclination across the propagation path.

Figure 6 shows the results of the experiment carried out in 1998 [10]. The signals were processed according to the simplest aforementioned scheme with normalization, matched filtration, incoherent accumulation over the elements of the vertical array, and frequency averaging. The experimental record, slightly more than 16 min in duration, contains four crossings of the propagation path by the model. The odd (first and third) and even (second and fourth) signal peaks correspond to opposite directions of crossings. In this experiment, the model was presented by a cylindrical body with a length of 6 m and a diameter of 0.45 m. The speed of motion was 0.6 m/s, the path length was 300 m, and the model crossed the middle of the path at nearly a right angle. A monopole sound source was fixed near the bottom and simultaneously produced the acoustic field at four frequencies from 2 to 2.5 kHz.

The figure clearly shows that the even signal peaks exhibit a kind of mirror similarity with respect to the odd ones: the heights of their satellites change in an opposite manner. We succeeded in revealing the mathematical nature of the asymmetry at hand: it manifested itself in the asymmetry of the diffraction-shadow signal, i.e., in a time mismatch of the real and imaginary parts in the exponent of Eq. (6). By introducing an appropriate correction into the structure of the matched filter, we could sharpen the odd peaks and suppress the even ones, and vice versa. Qualitatively, the aforementioned modifications led to results that were similar to

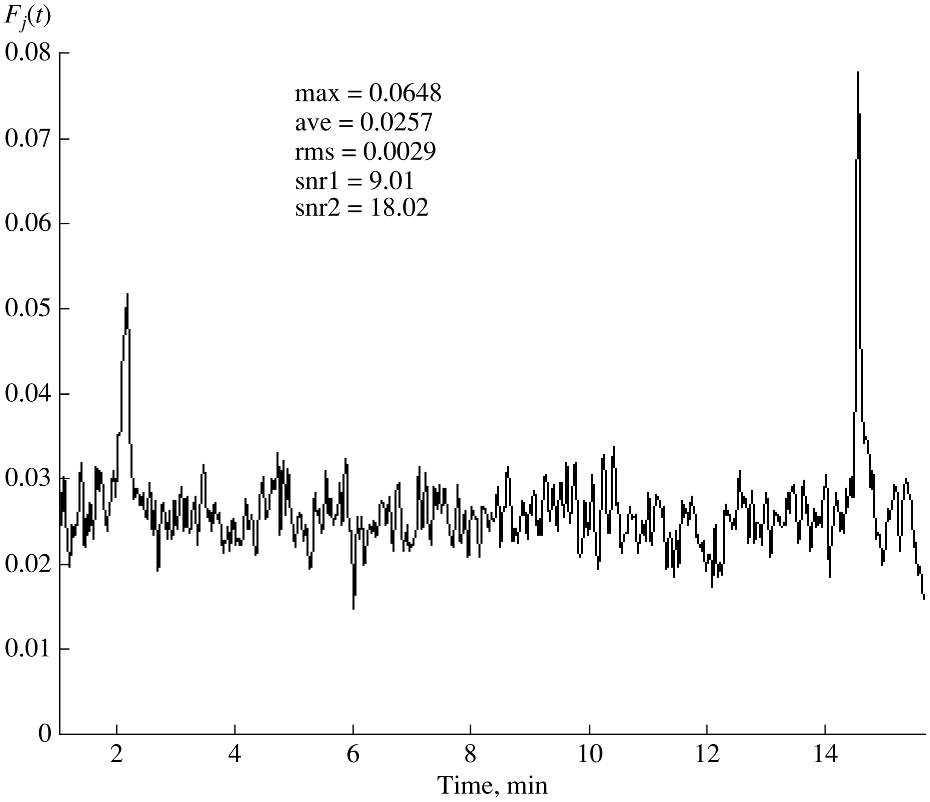

Fig. 4. Incoherent accumulation with the shift "+" for the inclined array.

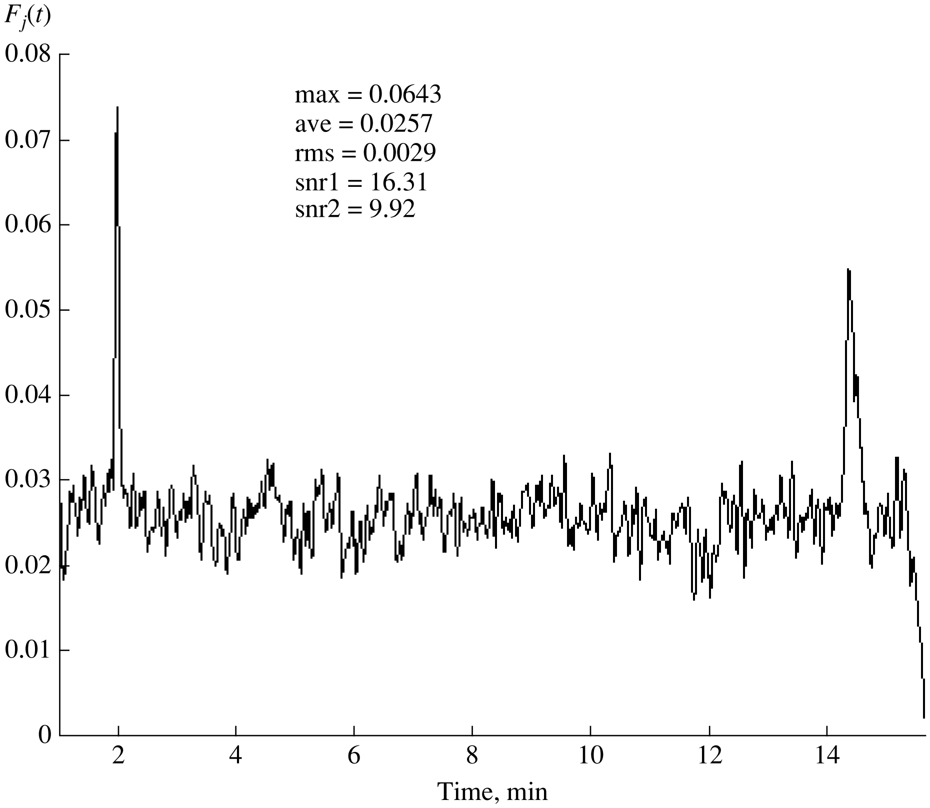

Fig. 5. Incoherent accumulation with the shift "–" for the inclined array.

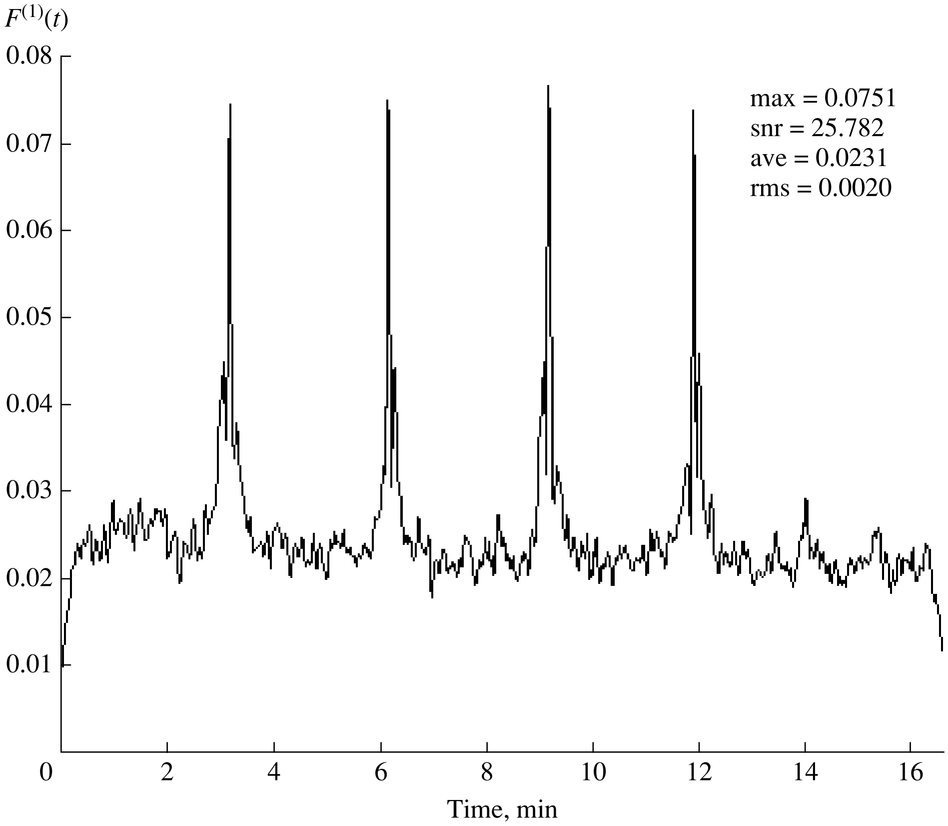

Fig. 6. Result of the incoherent accumulation of the single-array signals after averaging over four operational frequencies.

those obtained with the inclined array. That is why we do not present the corresponding plots here.

Of course, although the aforementioned indication of the direction is of interest in its physical nature, it is hardly useful for practical-purpose applications. The left–right asymmetry of the channel can be caused by factors whose monitoring is difficult or impossible. As to the arrays extended both vertically and horizontally, they are evidently promising for detecting the motion direction. Moreover, they can yield any other information on the trajectory.

We have considered and tested only the simplest versions of spatially extended two-dimensional receiving systems. The analysis showed that such arrays can yield additional information and, in some cases, allow one to use more efficient algorithms of signal processing to implement noise-resistant underwater observations.

According to the present-day trends in improving the instrumentation and theory of underwater-acoustic studies, multielement receiving systems that are extended in two spatial dimensions, namely, two-dimensional arrays and systems of several single vertical arrays, are most promising. From this point of view, the coherent-holographic methods [6, 7] seem to be most advantageous: with the use of spatially extended receiving systems and the appropriate computer software, these methods can provide full visual real-time monitoring of the nonstationary dynamics of the oceanic medium.

ACKNOWLEDGMENTS

We are grateful to V.A. Zverev for useful discussions on signal processing, to P.I. Korotin and B.M. Salin for their efforts in establishing the experimental studies at the Sankhar Lake, and to all researchers of the Institute of Applied Physics, Russian Academy of Sciences, who participated in developing the experimental equipment and in performing the experiment.

This work was supported by the Russian Foundation for Basic Research, project nos. 01-02-17380 and 99-02-16401.

REFERENCES

1. S. M. Gorskiĭ, V. A. Zverev, A. L. Matveev, and V. V. Mityugov, Akust. Zh. **41**, 223 (1995) [Acoust. Phys. **41**, 190 (1995)].
2. V. A. Zverev, A. L. Matveev, and V. V. Mityugov, Akust. Zh. **41**, 591 (1995) [Acoust. Phys. **41**, 518 (1995)].

3. A. L. Matveev, V. V. Mityugov, and B. M. Salin, in *Acoustics of the Ocean: Proceedings of the School–Seminar of Academician L.M. Brekhovskikh* (Geos, Moscow, 1998), p. 151.
4. A. L. Matveev and V. V. Mityugov, Akust. Zh. **46**, 94 (2000) [Acoust. Phys. **46**, 80 (2000)].
5. K. Yoo and T. C. Yang, J. Acoust. Soc. Am. **104**, 3326 (1998).
6. A. L. Matveev, V. V. Mityugov, and A. I. Potapov, in *Acoustics of the Ocean: Proceedings of the School–Seminar of Academician L.M. Brekhovskikh* (Geos, Moscow, 1998), p. 309.
7. A. L. Matveev, V. V. Mityugov, and A. I. Potapov, Akust. Zh. **47**, 246 (2001) [Acoust. Phys. **47**, 202 (2001)].
8. J. Fabrikian, J. L. Krolik, and H. Messer, J. Acoust. Soc. Am. **101**, 241 (1997).
9. W. S. Hodgkiss, H. C. Song, W. A. Kuperman, *et al.*, J. Acoust. Soc. Am. **105**, 1597 (1999).
10. V. A. Zverev, P. I. Korotin, A. L. Matveev, *et al.*, Akust. Zh. **47**, 227 (2001) [Acoust. Phys. **47**, 184 (2001)].
11. N. E. Collison and S. E. Dosso, J. Acoust. Soc. Am. **107**, 3089 (2000).
12. V. A. Grigor’ev and V. M. Kuz’kin, Akust. Zh. **41**, 410 (1995) [Acoust. Phys. **41**, 359 (1995)].

Translated by E. Kopyl

Acoustical Physics, Vol. 48, No. 5, 2002, pp. 584–588. Translated from Akusticheskiĭ Zhurnal, Vol. 48, No. 5, 2002, pp. 661–665.
Original Russian Text Copyright © 2002 by Mironov, Urusovskiĭ.

Damped Waves in a Cylinder Shadow

M. A. Mironov and I. A. Urusovskiĭ
Andreev Acoustics Institute, Russian Academy of Sciences,
ul. Shvernika 4, Moscow, 117036 Russia
e-mail: mironov@akin.ru

Received November 6, 2001

Abstract—The sound field in the region of a deep shadow behind an impedance cylinder is analyzed for the case of plane wave diffraction by the cylinder surface. The main part of the field is represented by a cylindrical wave that has a complex index determined from the boundary conditions and decays with the angular coordinate. An expression for the amplitude of this wave is determined by extracting it from the total field formed in the shadow region. It is demonstrated that this wave approximates more closely the total field behind the cylinder, as compared to the least damped wave in the field representation obtained on the basis of the Watson transform. A way to improve the sound barriers is indicated. *© 2002 MAIK "Nauka/Interperiodica".*

Cylindrical head pieces at barrier edges, which are sufficiently soft acoustically, are used to improve the efficiency of sound barriers screening traffic noise [1]. However, screening by such barriers is inefficient within certain frequency bands. It is of practical and theoretical interest to clarify the origin of this inefficiency, and this is the purpose of the present consideration.

In the case of diffraction of a plane wave of sound pressure $p_i(x) = \exp(ikx)$, where k is the wave number and x is the coordinate along the direction of the wave propagation [the time factor $\exp(-i\omega t)$ is omitted], by a cylinder, the scattered field has the form

$$p_r(r, \phi) = b_0 H_0^{(1)}(kr) + 2\sum_{m \geq 1} i^m b_m H_m^{(1)}(kr)\cos(m\phi),$$

where r is the distance from the cylinder center to the observation point and ϕ is the angle between the direction from the cylinder center to this point and the x axis. Taking into account the identity [2]

$$\exp(ikx) = J_0(kr) + 2\sum_{m \geq 1} i^m J_m(kr)\cos(m\phi),$$

the total field $p = p_i + p_r$ can be represented in the form

$$\begin{aligned} p(r, \phi) &= J_0(kr) + b_0 H_0^{(1)}(kr) \\ &+ 2\sum_{m \geq 1} i^m [J_m(kr) + b_m H_m^{(1)}(kr)]\cos(m\phi). \end{aligned} \tag{1}$$

The boundary condition that is valid at the cylinder surface characterized by the specific acoustic admittance η is as follows:

$$\left(\frac{dp}{dr} + ik\eta p\right)_{r = a} = 0, \tag{2}$$

where a is the cylinder radius. In this case,

$$b_0 = -\frac{J_1(ka) - i\eta J_0(ka)}{H_1^{(1)}(ka) - i\eta H_0^{(1)}(ka)},$$

$$b_m = -\frac{J'_m(ka) - i\eta J_m(ka)}{H_m^{(1)'}(ka) - i\eta H_m^{(1)}(ka)},$$

where the prime denotes a derivative with respect to the argument.

Since the field in the shadow region is formed by the waves arriving from the illuminated region, its main part must have the form of a cylindrical wave decaying in the angle ϕ:

$$p_\nu(r, \phi) = A_\nu \cos(\nu\phi) H_\nu^{(1)}(kr)/H_\nu^{(1)}(ka),$$

where the complex index ν is determined from the boundary condition given by Eq. (2) for the field $p_\nu(r, \phi)$ at the cylinder surface in the space ramified with respect to the angle ϕ:

$$[H_\nu^{(1)'}(ka)/H_\nu^{(1)}(ka)] + i\eta = 0. \tag{3}$$

Substituting the integral representation [2]

$$\begin{aligned} &H_\nu^{(1)}(x) \\ &= \sqrt{\frac{2}{\pi}}\frac{x^\nu}{\Gamma\left(\nu + \frac{1}{2}\right)}\exp\left[i\left(x - \frac{\pi}{2}\nu - \frac{\pi}{4}\right)\right]\int_0^\infty U_\nu(x, t)dt, \end{aligned} \tag{4}$$

where $U_\nu(x, t) = \left[\left(1 + i\frac{t}{2}\right)t\right]^{\nu - \frac{1}{2}}\exp(-xt)$, $\mathrm{Re}(\nu) > -\frac{1}{2}$, and $x > 0$, in Eq. (3), we obtain the following equation for $x = ka$:

$$\frac{\nu}{x} + i - \left[\int_0^\infty U_\nu(x, t)t\,dt \Big/ \int_0^\infty U_\nu(x, t)dt\right] + i\eta = 0.$$

1063-7710/02/4805-0584$22.00 © 2002 MAIK "Nauka/Interperiodica"

In the set of values of ν satisfying Eq. (3), the value of ν with the smallest positive imaginary part corresponds to the wave decaying to the least extent with the increase in the angle $(\pi/2) - \phi$ and, therefore, penetrating deeper than other waves into the shadow zone. It is this value that is of interest for our consideration.

To determine the amplitude A_ν, we represent p in the form $p = p_\perp + p_\nu$, where $p_\perp$ is the part of the total field in the zone of a sufficiently deep shadow $0 \le |\phi| \le \Psi$, $\Psi < \pi/2$ that does not contain the decaying wave p_ν in its angular spectrum, so that $\int_0^\Psi p_\perp \cos(\nu^*\phi)d\phi = 0$, where * is the sign of complex conjugation. Integrating p over ϕ with the weighting function $\cos(\nu^*\phi)$, we obtain

$$A_\nu = \int_0^\Psi p(a, \phi)\cos(\nu^*\phi)d\phi \Big/ \int_0^\Psi \cos(\nu\phi)\cos(\nu^*\phi)d\phi = \frac{4}{S_0}\int_0^\Psi p(a, \phi)\cos(\nu^*\phi)d\phi, \tag{5}$$

where $S_0 = \dfrac{\sin(2\Psi\mathrm{Re}\nu)}{\mathrm{Re}\nu} + \dfrac{\sinh(2\Psi\mathrm{Im}\nu)}{\mathrm{Im}\nu}$.

At $r = a$, with allowance for the identity [2]

$$J_m(z)N_{m-1}(z) - J_{m-1}(z)N_m(z) = \frac{2}{\pi z},$$

Eq. (1) is reduced to the form

$$p(a, \phi) = \frac{2i}{\pi ka}\left[\frac{1}{i\eta H_0^{(1)}(ka) - H_1^{(1)}(ka)} + 2\sum_{m \ge 1} i^m \frac{\cos m\phi}{\left(i\eta - \dfrac{m}{ka}\right)H_m^{(1)}(ka) + H_{m-1}^{(1)}(ka)}\right].$$

Substituting Eq. (5) into Eq. (4) and integrating, we obtain

$$A_\nu = \frac{8i}{\pi ka S_0}\left[\frac{\sin(\nu^*\Psi)}{i\eta H_0^{(1)}(ka) - H_1^{(1)}(ka)}\frac{1}{\nu^*} + \sum_{m \ge 1} i^m \frac{S(m)}{\left(i\eta - \dfrac{m}{ka}\right)H_m^{(1)}(ka) + H_{m-1}^{(1)}(ka)}\right], \tag{6}$$

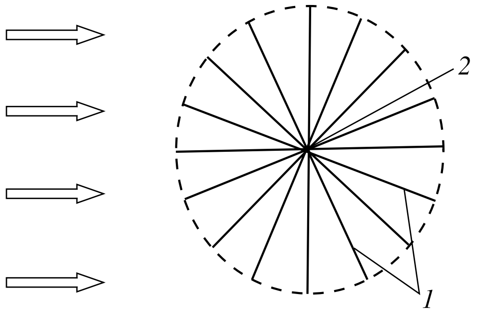

Fig. 1. An impedance cylinder formed by a large number of (*1*) rigid strips with (*2*) a common edge.

where

$$S(m) = 2\int_0^\Psi \cos(m\phi)\cos(\nu^*\phi)d\phi = \frac{\sin[(m + \nu^*)\Psi]}{m + \nu^*} + \frac{\sin[(m - \nu^*)\Psi]}{m - \nu^*}.$$

We select the quantity $\eta = -iJ_1(ka)/J_0(ka)$ as the specific acoustic admittance of the cylinder surface. It is realized for the structure shown in Fig. 1, which consists of a large number N of rigid strips of width a that contact each other along one of their edges in such way that the distances between the neighboring external edges are small in comparison with the sound wavelength ($2\pi ka/N \ll 1$ at equal distances between noncontacting edges).

In the case of the selected η, as our calculations show, the waves under consideration have a relatively large amplitude at a relatively deep penetration into the zone of geometrical shadow behind the cylinder within certain narrow frequency bands. As a result, the efficiency of screening the shadow zone is reduced. Further, we present examples of the field calculations for such frequencies.

At $ka = 7.54444$, which corresponds to a frequency of 408.25 Hz at $a = 1$ m, $i\eta = 0.5618$ and the desired root of Eq. (3) at this η is $\nu = 9.44777 + 0.41256i$, while in the case of a perfectly rigid surface (at $\eta = 0$), the root of Eq. (3) is equal to $\nu_h = 8.30649 + 1.43768i$. Since the imaginary part of ν in this example is much smaller than the imaginary part of ν_h, the corresponding wave for an impedance surface at the indicated frequency decays much slower than in the case of a rigid surface, so that the sound pressure level in the cylinder shadow can be much higher in the first case than in the second. This means that just the damped wave penetrating relatively deep into the shadow zone makes the screening of the zone by a barrier with an impedance cylinder on its top inefficient in the unfavorable cases when the basic angular harmonics forming the sound field are summed almost in phase, even in comparison with the

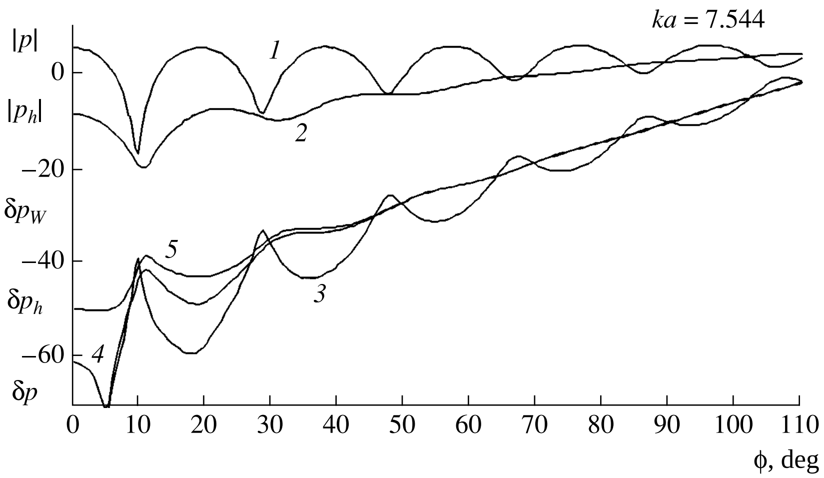

Fig. 2. (*1*) Sound pressure in decibels at the cylinder surface, $p(a, \phi)$, as a function of the angle ϕ for $ka = 7.54444$; (*2*) the same for the sound pressure $p_h(a, \phi)$ at a perfectly rigid surface; (*3, 4*) relative differences δp and δp_h in decibels between these functions and the sound pressures in the corresponding damped waves; and (*5*) relative differences δp_W in decibels between the sound pressures $p(a, \phi)$ and $B_0\cos(\nu_0\phi)$ for the case of a rigid cylinder.

screening by a barrier with a rigid cylinder [1]. Therefore, in designing sound screening barriers, it is necessary to provide for special means against the penetration of damped waves into the shadow zone. We note that the anomalous increase in the amplitude of a damped wave is not connected with the resonance of air oscillations in wedge-shaped cavities of the structure. The value $|\eta| = \infty$ (a soft boundary) would correspond to such a resonance, while in the given example, we have $i\eta = 0.5618$, which corresponds to an elastic-type impedance. Along such an impedance surface, the waves propagate with a relatively small attenuation.

For the considered example at $\Psi = 0.2$, curve *1* in Fig. 2 shows the sound pressure in decibels at the cylinder surface $p(a, \phi)$ as a function of the angle ϕ and curve *2* shows the corresponding dependence for the sound pressure $p_h(a, \phi)$ at a perfectly rigid surface. Curves *3* and *4* represent the relative differences δp and δp_h in decibels between these functions and the sound pressures in the corresponding damped waves $A_\nu\cos(\nu\phi)$ and $A_{\nu h}\cos(\nu_h\phi)$, where $A_{\nu h}$ is equal to the right-hand side of Eq. (6) at $\eta = 0$ with ν replaced by ν_h. As one can see from this figure, the excess of the sound pressure level in $p(a, \phi)$ over the level of $p_h(a, \phi)$ at certain angles in the region of a seemingly deep shadow constitutes more than 10 dB, which demonstrates the inefficiency of the head piece under consideration at the selected frequency.

In the case of $ka = 4.29659$, which corresponds to a frequency of 232.5 Hz at $a = 1$ m, we have $i\eta = 0.4724$, $\nu = 5.44785 + 0.58282i$, and $\nu_h = 4.9204 + 1.21461i$. For this case, the curves similar to those in Fig. 2 are given in Fig. 3. Here, as in Fig. 2, $\Psi = 0.2$.

Now, let us compare the amplitude of the damped wave A_ν obtained above with the corresponding amplitude of the first (the least damped) wave in the field representation in the form of an expansion in damped waves on the basis of the Watson transform [3]. This representation has the form

$$p(r, \phi) = \pi\sum_{s\ge 0} g(\nu_s, ka)\frac{1}{\sin(\nu_s\pi)} \times \exp\left(-i\frac{\pi}{2}\nu_s\right)H^{(1)}_{\nu_s}(kr)\cos(\nu_s\phi),$$

where

$$g(\nu, x) = \sum_{s\ge 0}\left[\frac{d}{dx}H^{(2)}_\nu(x)/\frac{d}{d\nu}\frac{d}{dx}H^{(1)}_\nu(x)\right]$$

and ν_s are the roots of Eq. (3). In this expression, we substitute the integral representations given by Eq. (4) and

$$H^{(2)}_\nu(x) = \sqrt{\frac{2}{\pi}}\frac{x^\nu}{\Gamma\left(\nu+\frac{1}{2}\right)}\exp\left[i\left(\frac{\pi}{2}\nu+\frac{\pi}{4}-x\right)\right]\int_0^\infty V_\nu(x, t)dt,$$

where $V_\nu(x, t) = \left[\left(1 - i\frac{t}{2}\right)t\right]^{\nu-\frac{1}{2}}\exp(-xt)$. Then, for $r = a$, we obtain

$$p(a, \phi) = \sum_{s\ge 0} B_s\cos(\nu_s\phi),$$

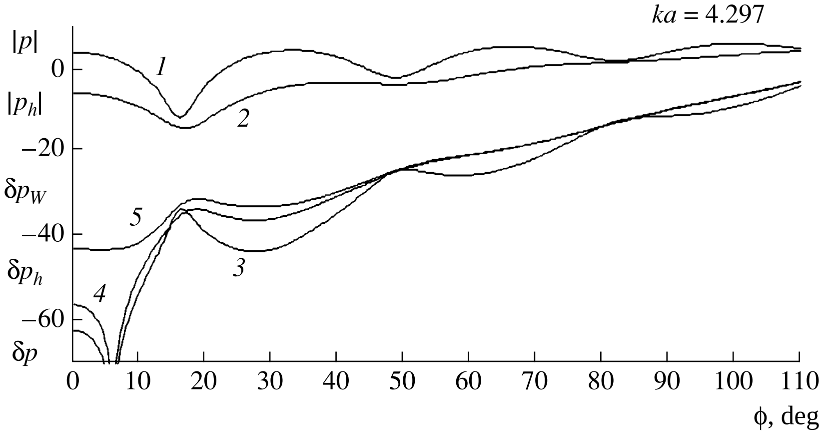

Fig. 3. The same as in Fig. 2 for $ka = 4.29659$.

where

$$B_s = \sqrt{2\pi}\exp\left[i\left(\frac{\pi}{4} - ka\right)\right]G(\nu_s, ka)$$

$$\times \frac{(ka)^{\nu_s}}{\Gamma\left(\nu_s + \frac{1}{2}\right)}\frac{1}{\sin(\nu_s\pi)}\int_0^\infty U(ka, t)dt,$$

$$G(\nu, x) = \exp\left[i\left(2x - \pi\nu - \frac{\pi}{2}\right)\right]g(\nu, x)$$

$$= \left[\left(\frac{\nu}{x} - i\right)\int_0^\infty V_\nu(x, t)dt - \int_0^\infty V_\nu(x, t)tdt\right]/D(\nu, x),$$

$$D(\nu, x) = \left[L(\nu, x)\left(\frac{\nu}{x} + i\right) + \frac{1}{x}\right]\int_0^\infty U_\nu(x, t)dt$$

$$- L(\nu, x)\int_0^\infty U_\nu(x, t)tdt$$

$$+ \int_0^\infty U_\nu(x, t)\left(\frac{\nu}{x} + i - t\right)\ln\left[\left(1 + i\frac{t}{2}\right)t\right]dt,$$

$$L(\nu, x) = \ln x - i\frac{\pi}{2} - \frac{d}{d\nu}\Gamma\left(\nu + \frac{1}{2}\right).$$

To calculate the derivative of the gamma-function, we use its representation [2]

$$\Gamma(z) = \exp(-Cz)\frac{1}{z}\prod_{m \geq 1}\frac{\exp(z/m)}{1 + (z/m)},$$

where $C = 0.577215$ is the Euler constant. This yields

$$\frac{d}{d\nu}\Gamma\left(\nu + \frac{1}{2}\right)$$

$$= -C - \left(\nu + \frac{1}{2}\right)^{-1} + \left(\nu + \frac{1}{2}\right)\sum_{m \geq 1}\left[\left(m + \nu + \frac{1}{2}\right)m\right]^{-1}.$$

Using the equations [2]

$$\sum_{m \geq 1}\frac{1}{m^2} = \frac{\pi^2}{6}, \quad \sum_{m \geq 1}\left[\left(m^2 - \frac{1}{4}\right)m\right]^{-1} = 8\ln 2 - 4,$$

$$\text{and} \quad \sum_{m \geq 1}\frac{1}{m^4} = \frac{\pi^2}{90},$$

the last formula can be reduced to a form that is more convenient for numerical calculations, which contains a rapidly converging series:

$$\frac{d}{d\nu}\Gamma\left(\nu + \frac{1}{2}\right) = -C - \left(\nu + \frac{1}{2}\right)^{-1}$$

$$+ \left(\nu + \frac{1}{2}\right)\frac{\pi^2}{6} - \left(\nu + \frac{1}{2}\right)^2(8\ln 2 - 4)$$

$$+ \left(\nu + \frac{1}{2}\right)^2\sum_{m \geq 1}\left(\nu + \frac{1}{2} + \frac{1}{4m}\right)/\left[\left(m^2 - \frac{1}{4}\right)\left(m + \nu + \frac{1}{2}\right)m\right].$$

For the examples considered, curves *5* in Figs. 2 and 3 represent the relative differences δp_W between the sound pressures $p(a, \phi)$ and $B_0\cos(\nu_0\phi)$ in decibels for the case of a rigid cylinder. One can see from the figures that the damped wave $A_{\nu h}\cos(\nu_h\phi)$ approximates more closely the total field behind the cylinder than the least damped wave in the field representation obtained on the basis of the Watson transform. The corresponding increase in accuracy, on average over the region $0 \leq |\phi| \leq \pi/2$, constitutes 2.15 dB for the first example and

4.33 dB for the second example. For the region of deeper shadow $0 \le |\phi| \le \pi/4$, the corresponding increase constitutes 2.98 and 5.88 dB, respectively. The field $A_{\nu h}\cos(\nu_h\phi)$ proves to be a closer approximation, because it is extracted from the total field only at the part of the cylinder that is located in a relatively deep shadow, while $B_0\cos(\nu_0\phi)$ is extracted from the total field over the total surface of the cylinder. As for the Keller's approximation, in the problem under study, it is reduced to replacing ν and $H_\nu^{(1)}(kr)$ by their approximate values [4], which decreases the accuracy of the approximation.

Further improvement of acoustic barriers is possible by searching for a suitable design of a head piece of a barrier edge that would prevent the penetration of a damped wave deep into the shadow zone.

ACKNOWLEDGMENTS

We are grateful to Yu.I. Bobrovnitskiĭ for a useful discussion.

REFERENCES

1. M. Mözer and R. Volz, J. Acoust. Soc. Am. **106**, 3049 (1999).
2. I. S. Gradshteĭn and I. M. Ryzhik, *Table of Integrals, Series, and Products* (Fizmatgiz, Moscow, 1962; Academic, New York, 1980).
3. H. Hönl, A. W. Maue, and K. Westpfahl, *Theorie der Beugung* (Springer, Berlin, 1961; Mir, Moscow, 1964).
4. E. Skudrzyk, *Die Grundlagen der Akustik* (Springer, Wien, 1954; Springer, New York, 1971; Mir, Moscow, 1976), Vol. 2.

Translated by M. Lyamshev

Acoustical Physics, Vol. 48, No. 5, 2002, pp. 589–597. Translated from Akusticheskiĭ Zhurnal, Vol. 48, No. 5, 2002, pp. 666–674.
Original Russian Text Copyright © 2002 by Passechnik.

The Directivity Pattern of an Interferometer for Measuring Thermal Acoustic Radiation

V. I. Passechnik†

ÉLDIS Research Center, Institute of Radio Engineering and Electronics, Russian Academy of Sciences,
Starosadskiĭ per. 8, Moscow, 101000 Russia
e-mail: passech@orc.ru

Received July 9, 2001

Abstract—The directivity patterns of a pair of piezoelectric transducers for measuring the spatial correlation function of sound pressures produced by sources of thermal acoustic radiation in the megahertz frequency range are calculated. Sources in the form of a heated plane or strip are considered. The signal detection by two circular or rectangular piezoelectric transducers and by focusing transducers is studied. It is demonstrated that, for measuring the correlation function, the piezoelectric transducers must partially overlap. To determine the directivity pattern with a strong dependence on the distance between the heated object and the pair of piezoelectric transducers, focusing piezoelectric transducers should be used. The results obtained offer possibilities for a noninvasive measurement of the absorption coefficient of a medium and also for the realization of the previously proposed [20] passive acoustic thermotomograph, which does not use *a priori* information on the absorption coefficient of the medium. *© 2002 MAIK "Nauka/Interperiodica".*

Noninvasive measurements of temperature within a human body are an important problem for a number of biomedical applications, e.g., for newborn children [1–3]. The data of such measurements agree with the results of the corresponding theoretical calculations [4]. At the same time, the microwave radiometry technique used for this purpose, which is based on detection of thermal electromagnetic radiation, cannot generally provide a high spatial resolution combined with a high sensitivity [5]. This is why efforts to obtain data on the internal temperature with the help of acoustic radiation have been made over the last few years [6–16]. The studies demonstrated the possibility of the development of a passive acoustic thermal tomography operating in the megahertz frequency range with a sensitivity of up to 0.3 K and a spatial resolution of ~1–2 cm [14–16]. It is necessary to remember that the values of the intensity of the intrinsic thermal acoustic emission, which comes from the points on the object surface at different angles to it, are used as initial data for passive thermal tomography (see [17]). The possibility of using correlation measurements of thermal acoustic radiation to improve the characteristics of tomographs have been discussed for years [18, 19].

Now, the major way to improve the quality of temperature reconstruction in passive tomography is connected with the possibility of determining the energy coefficient of absorption γ [20]. This quantity is preset approximately from *a priori* considerations. At the same time, it is involved in all the equations determining the intensity of thermal radiation, and it is impossible to solve the inverse problem of temperature reconstruction without information on its spatial distribution. It is possible to measure the values of γ only on samples, and the scatter in such determinations is very large. It is impossible to measure the absorption by the transmission method, according to the ratio of the intensities of the incident and transmitted waves, because of the geometry of a human body.

Our previous paper [20] proposed to measure the absorption coefficient by a transducer positioned at one side of a human body using the intrinsic thermal acoustic radiation emitted by every part of the human body as the source. The absence of a separate ultrasonic source is an apparent advantage of this technique, but this is also the main difficulty, since any point of the medium is a source of these oscillations, i.e., the source localization is not unambiguous. As is well known, the intensity of thermal radiation emitted by every part of a medium is proportional to the product of the quantity γ by the absolute temperature T [9]. If we measure the radiation intensity by a single sensor, it represents an integral along the acoustic axis of the system with respect to the product γT corrected to the exponential factor taking into account the wave attenuation with propagation from the source to the receiver; i.e., the radiation source is distributed. Unlike the case of the detection of thermal acoustic radiation by a single piezoelectric transducer, the use of the correlation reception by a pair of piezoelectric transducers, i.e., by a two-element interferometer, provides an opportunity to form a directivity pattern with a local peak [9] (remember that, in the case

---

†Deceased.

of such a reception, the signals from the outputs of piezoelectric transducers are multiplied and averaged [20]). With this kind of directivity pattern, it is possible to localize the source of thermal radiation. To determine the absorption coefficient, it is necessary to conduct measurements by sequentially localizing the peak of the directivity pattern at several depths and then solve the corresponding inverse problem.

The main difficulty arose in selecting the directivity pattern of a two-element interferometer. The initial theoretical calculations did not reveal any fundamental difficulties [18]. However, the first experiments [21] already showed that the correlation function of thermal acoustic radiation emitted by a small source and detected by two separated piezoelectric transducers was a function oscillating in space. As the source size grew, the correlated signal decreased in its absolute value and vanished when the source of thermal acoustic radiation covered the aperture of the directivity pattern. Such a directivity pattern makes it impossible to reconstruct the spatial distribution of the absorption coefficient as was proposed earlier [20]. Therefore, it is necessary to clear up whether it is possible, using a pair of some piezoelectric transducers, to form a directivity pattern that would provide the reconstruction of the absorption coefficient in a medium with the help of a two-element interferometer.

In this paper, the problem of studying the directivity patterns of two-element interferometers with different elements is considered for the purpose of developing a technique for the determination of the absorption coefficient. Below, it is demonstrated that overlapping focusing piezoelectric transducers used as interferometer elements provide the necessary directivity patterns.

To calculate the correlation function, we use the generalized Kirchhoff law, which was successfully used for calculating the acoustic brightness temperatures in various cases [22]. According to this law, in the case of the measurement with a single piezoelectric transducer, the volume element *dxdydz* with the thermodynamic temperature τ produces the contribution dT_A to the acoustic brightness temperature T_A. This contribution is proportional to the loss of the intensity $i(x, y, z)$ of an auxiliary unit wave in this volume. We assumed in the calculation that this wave is emitted by a piezoelectric transducer. Then, we have

$$dT_A = \gamma(x, y, z)\tau(x, y, z) \times [i(x, y, z)/\int i(x, y, z)dxdy]\exp\left[-\int_0^z \gamma(z)dz\right]dxdydz. \tag{1}$$

Here, *dxdy* is the area element of the element of the cross section of a wave tube and *dz* is the differential of the path along the ray trajectory. The intensity $i(x, y, z)$ at some point of the tube cross section with the coordinate z is normalized to the total intensity in this cross section. The exponential term describes the attenuation of a wave from the point of its generation to the piezoelectric transducer. The difference between the absolute temperatures of the object and the piezoelectric transducer must be taken as the object temperature τ in Eq. (1): $\tau = T - T_{TR}$ [23, 24]. This is connected with the fact that the transfer of energy and, therefore, its losses are possible only between bodies heated to different temperatures. Note that, if the temperature difference is greater than zero ($T - T_{TR} > 0$), the transducer receives an energy flux from the heated body, and in the opposite case $T - T_{TR} < 0$, the transducer emits radiation.

The directivity pattern of a two-element interferometer must provide the localization of thermal radiation in three coordinates: along the acoustic axis of the system (the z axis) and in the transverse direction (the x and y axes).

First of all, let us consider the possibility of localization in the x, y plane. For this purpose, we place a trial acoustic blackbody with a constant temperature in this plane L at the distance z_B from the transducers. We select a body in the form of a thin layer representing a region where the absorption coefficient is very large: $\gamma(x, y, z) = \gamma(x, y)\delta(z - z_B)$. In the rest of the medium, this coefficient is assumed to be equal to zero. In this case, Eq. (1) is simplified and, after integration with respect to the variable z, we obtain an expression for the increment of the acoustic brightness temperature $\Delta T_A = T_A - T_{TR}$:

$$\Delta T_A(z_B) = \iint \tau(x, y, z_B)\Gamma(x, y) \times i(x, y, z_B)dxdy/\iint i(x, y, z_B)dxdy, \tag{2}$$

where the factor $\Gamma(x, y) = \begin{cases} 0, & \gamma(x, y) = 0 \\ 1, & \gamma(x, y) \longrightarrow \infty \end{cases}$ determines the shape of the radiating body; the radiation is present where the absorption exists and is absent where the absorption is absent. Further, we will denote the z_B coordinate by z without the subscript.

In calculating the correlation effects, we assume that the receiver of thermal radiation is not one but a pair of interferometer transducers. According to the rules of calculation of the acoustic brightness temperature [Eq. (1)], it is necessary to solve the inverse problem, i.e., calculate the radiation intensity produced by this pair of piezoelectric transducers representing a complex source and the corresponding losses.

As is known [25], in the far wave zone in the Fraunhofer approximation, the complex amplitudes of the velocity potentials ϕ_1 and ϕ_2 of the waves radiated by each of the piezoelectric transducers can be represented in the form $\phi_{1,2} = A_{1,2}(r_{1,2})e^{-jkr_{1,2}}$, where j is the imaginary unit, r_1 and r_2 are the distances from the centers of the corresponding piezoelectric transducers to the observation point, $k = 2\pi/\lambda$ is the wave number, $\lambda = f/c$ is the wavelength, f is the frequency, c is the sound velocity, and $A_{1,\,2}$ are the complex amplitudes changing slowly in comparison with the fast oscillating factor. The squares of the absolute values $|A_{1,\,2}|^2$ are the directivity patterns of individual piezoelectric transducers. Two piezoelectric transducers form the velocity potential $\phi_1 + \phi_2$. The intensities of the unit waves produced by each piezoelectric transducer separately (i_1 and i_2) and by two of them together (i) in the plane L have the form (correct to a constant factor)

$$\begin{gathered} i_1 \sim |A_1(r_1)|^2, \quad i_2 \sim |A_2(r_2)|^2, \\ i(r_1, r_2, \vartheta) \sim |A_1(r_1) + A_2(r_2)|^2 \\ = |A_1(r_1)|^2 + |A_2(r_2)|^2 + 2|A_1(r_1)||A_2(r_2)|\cos\vartheta, \end{gathered} \tag{3}$$

where $\vartheta = k(|r_1| - |r_2|)$ is the additional phase shift caused by the path difference between both piezoelectric transducers and the source. If both piezoelectric transducers perform reception independently, the total intensity of the signals produced by them is $i_0(z) \sim |A_1|^2 + |A_2|^2$. Substituting Eq. (3) into Eq. (2), we obtain

$$\begin{gathered} \Delta T_A(z) = \frac{1}{N(z)}\iint \tau(x, y)\Gamma(x, y)[|A_1(r_1)|^2 \\ + |A_2(r_2)|^2 + 2|A_1(r_1)||A_2(r_2)|\cos\vartheta]dxdy, \end{gathered} \tag{4}$$

where $r = r(x, y, z)$ and the normalizing factor is

$$\begin{gathered} N(z) = \iint [|A_1(r_1)|^2 \\ + |A_2(r_2)|^2 + 2|A_1(r_1)||A_2(r_2)|\cos\vartheta]dxdy. \end{gathered} \tag{5}$$

As one can see from Eq. (4), the increment of the acoustic brightness temperature includes three components:

$$\Delta T_A(z) = \Delta T_A^{(1)}(z) + \Delta T_A^{(2)}(z) + 2\Delta T_A^{COR}(z), \tag{6}$$

where $\Delta T_A^{(1)}(z)$ and $\Delta T_A^{(2)}(z)$ are the increments of the acoustic brightness temperatures measured by the first and second piezoelectric transducers separately and proportional to the directivity patterns $|A_1|^2$ and $|A_2|^2$, respectively, and the increment of the so-called correlated temperature ΔT_A^{COR} depending on the difference in distances between the source and both receivers is proportional to the square root of the product of the directivity pattern of both piezoelectric transducers $\sqrt{|A_1|^2|A_2|^2}$. Thus, the quantity formed by the integration of this product over space has the physical meaning of the increment of the acoustic brightness temperature connected with the correlation properties of thermal radiation.

In the experimental studies of thermal acoustic radiation [21], we measure not the square of the sum of voltages at the outputs of both piezoelectric transducers, but each of these values and the correlated signal obtained by averaging the product of these voltages. With such a scheme of measurements, it is evident that

$$\begin{gathered} \Delta T_A^{(1),\,(2)}(z) = \iint \tau(x, y)\Gamma(x, y) \\ \times [|A_{1,\,2}(r_{1,\,2})|^2]dxdy/\iint [|A_{1,\,2}(r_{1,\,2})|^2]dxdy, \end{gathered} \tag{7}$$

$$\begin{gathered} \Delta T_A^{COR}(z) = \iint \tau(x, y)\Gamma(x, y)[|A_1(r_1)||A_2(r_2)|] \\ \times \cos\vartheta(r_1, r_2)dxdy/\iint [|A_1(r_1)||A_2(r_2)|]dxdy. \end{gathered} \tag{8}$$

The normalization for the correlated temperature is selected proceeding from the condition that, in the case of coinciding directivity patterns and zero path difference between the source and both piezoelectric transducers $\vartheta(r_1, r_2) = 0$, its value be equal to $\Delta T_A^{(1)}(z) = \Delta T_A^{(2)}(z)$, and in the case of the path difference equal to half-wavelength, it should have the same value but the opposite sign.

We introduce the correlation coefficient $R(z)$ as a characteristic of the correlation properties of thermal acoustic radiation excluding the temperature difference between the source and the piezoelectric transducers. This coefficient changes within the range from –1 to +1 and is determined by the relation

$$R(z) = \Delta T_A^{COR}(z)/\sqrt{\Delta T_A^{(1)}(z)\Delta T_A^{(2)}(z)}. \tag{9}$$

Using Eqs. (7)–(9), we analyze the directivity patterns of a two-element interferometer for the following sound pressure sensors used as its elements: (1) circular piezoelectric transducers with the radius a; (2) piezoelectric transducers shaped as long strips with the width $2a$; and (3) focusing piezoelectric transducers (circular and shaped as strips). These sensors differ in the forms of their directivity patterns involved in Eqs. (7) and (8).

Consider two sources of thermal acoustic radiation: a long strip with the width Δ and a plane, both of which are heated to a constant temperature. To interpret the results of [21], the correlation coefficients R_Δ (for the source shaped as a strip) and R_P (for a plane) will be analyzed. The last of them is most important, since it determines whether the correlated temperature measured experimentally from big bodies is nonzero. Moreover, in the process of calculation, in many cases we also investigate the relative value of the correlated signal *COR*, which is the normalized (in one way or another) dependence of the correlated temperature on the coordinates. It gives an idea of the dependence of the signal on a number of parameters.

Let us consider two circular piezoelectric transducers (Fig. 1). The source of thermal radiation is located

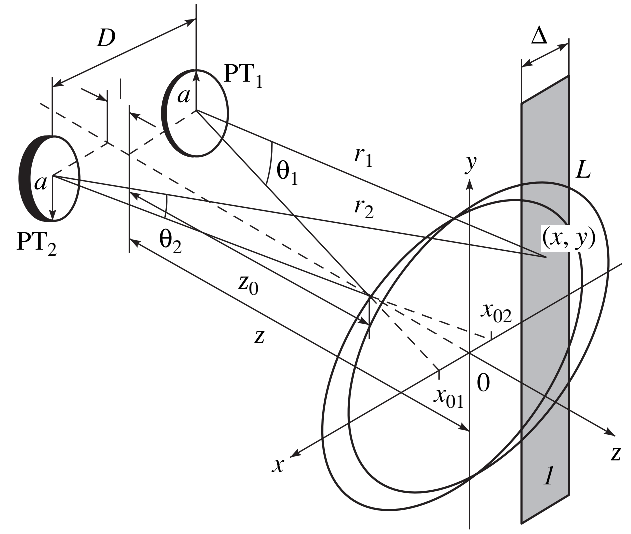

Fig. 1. Schematic diagram of the correlation function measurements for thermal acoustic radiation (according to [21] with some modification). The shift of transducers along the z axis is $l = 0$. For definiteness, $z > z_0$. The description is given in the text.

in the plane L that is separated from the pair of piezoelectric transducers by the distance z. The transducers PT$_1$ and PT$_2$ are separated symmetrically with respect to the acoustic axis of the system by the distances $\mp D/2$ and rotated with respect to each other in such way that their acoustic axes intersect in the plane located at the distance z_0 from the piezoelectric transducers. The coordinates of the intersection points of the acoustic axes of PT$_1$ and PT$_2$, respectively, with the x axis in the plane L are $x_{01} = -x_{02} = x_0 = -(D/2)(1 - z/z_0)$.

The complex amplitudes of the velocity potentials ϕ_1 and ϕ_2 of the waves radiated by each piezoelectric transducer in the far wave zone have the form [25]

$$\phi_{1,2} = -\frac{a^2}{r_{1,2}}\frac{J_1(ka\sin\theta_{1,2})}{ka\sin\theta_{1,2}}e^{-jkr_{1,2}}u_0, \qquad (10)$$

where u_0 is the velocity potential of the corresponding piezoelectric transducer, a is its radius, j is the imaginary unit, r_1 and r_2 are the lengths of the vectors from the centers of PT$_1$ and PT$_2$ to the observation point, θ_1 and θ_2 are the angles between the directions of these vectors and the acoustic axes of the corresponding piezoelectric transducers, and J_1 is the Bessel function of the first order. The finite width of the directivity pattern is taken into account by introducing the frequency characteristic of the receiving device $S(f)$ normalized to unity, which is approximated by an expression with the maximum at the frequency f_0 and the transmission bandwidth at a level of 3 dB δf: $S(f) = (\delta f/2\pi)(1/((f - f_0)^2 + (\delta f/2)^2)$ and $\int_0^\infty S(f)\,df = 1$. In [21], using Eq. (10), it is demonstrated that the correlation function $R_\Delta(x)$ for a source shaped as a strip has the form

$$R_\Delta(x) = \frac{\sin(k_0\Delta D/2z)}{k_0\Delta D/2z}e^{-k_0(\delta f/f_0)(D|x|/z)/2}\cos(k_0Dx/z), \qquad (11)$$

where k_0 is the wave number corresponding to the frequency f_0 of the maximum of the signal spectrum. This formula was derived using the following simplifying assumptions: (1) the transducers are separated by a distance $D > 2a$, (2) the angles $\theta_{1,2}$ in Eqs. (7), (8), and (10) are expressed by the approximate formulas $\theta_{1,2} \approx \sqrt{(x - x_{01,02})^2 + y^2}/z$, and (3) the following approximation of the integrand was used at small values of the argument $\theta_{1,2}$:

$$\frac{J_1(ka\sin\theta_{1,2})}{ka\sin\theta_{1,2}} = (1/2)e^{-(ka\theta_{1,2})^2/8}. \qquad (12)$$

As one can see from Eq. (11), when the strip width Δ increases, a loss of correlation occurs, which is taken into account by the factor $\mathrm{sin}c(\Delta D/\lambda z) = \frac{\sin(k_0\Delta D/2z_0)}{k_0\Delta D/2z_0} \le 1$. If the strip becomes sufficiently wide, this factor vanishes. Therefore, if a plane with a constant temperature is in the field of view of the pair of piezoelectric transducers, the correlation function $R_\mathrm{P} = \lim\limits_{\Delta\to\infty} R_\Delta$ corresponding to this source vanishes also; i.e., there is no correlated signal from the plane. This result does not change, if we take into account the exponential factor depending on the relative transmission band $\delta f/f_0$, which allows for the loss of correlation caused by the nonmonochromaticity of the detected signal.

Let us demonstrate qualitatively that it is possible to obtain a nonzero value of R_P from Eq. (11) if we bring both piezoelectric transducers very close to each other. It is necessary to note that, in reality, a piezoelectric transducer detects a signal not from the total halfspace but only from the region whose dimension does not exceed the diameter d_A of its directivity pattern; i.e., $\Delta \le d_A$ in all cases. Therefore, the condition $\mathrm{sin}c(\Delta D/\lambda_z) \ne 0$ can be taken in the form $k_0d_AD/2z \le \pi/2$. Since, in the Fraunhofer zone, the diameter of the directivity pattern, which is measured at a level of 0.5, is $d_A \approx 0.5\lambda z/a$ [25], this inequality is valid when the centers of both piezoelectric transducers are brought together to a very small distance $D \le a$ that is smaller than or equal to the radius of one piezoelectric transducer. Thus, as this qualitative analysis shows, the value of R_P becomes nonzero when the distance D between the centers of the two piezoelectric transducers is comparable with their radius a.

To obtain a quantitative estimate, we calculate the correlated signal from a heated plane more strictly.

Since the Bessel function in Eq. (10) decreases slowly with the argument growth, we calculate the values of $R_{\rm P}$ and *COR* exactly, without approximation (12) used above. We consider a general case when the acoustic axes of two equal piezoelectric transducers intersect outside the plane L in which the blackbody is located, i.e., at $z \neq z_0$. In this case, the sections of the directivity patterns of the piezoelectric transducers by the plane L in the first approximation are circles *1* and *2* (Fig. 2). The case $z < z_0$ is given in the figure for definiteness. The circles intersect only partially. Their centers formed by the points of intersection of the acoustic axes with the plane L lie on the x axis at the distances $x_{01} = -x_{02} = -\rho_0$, respectively, and the corresponding angles $\mp\theta_0$ (Fig. 1) are $\theta_0 \approx \rho_0/z$. Let the source of thermal radiation be at the point **A** located at the distances ρ_1 and ρ_2 from the centers of the cross sections of the corresponding directivity patterns and at the distance ρ from the origin of coordinates (the point **O**), the interval **AO** forming the angle φ with the y axis. The quantities ρ, ρ_1, and ρ_2 obey the relations

$$\rho_1^2 = \rho_0^2 + \rho^2 - 2\rho_0\rho\sin\varphi; \qquad (13a)$$

$$\rho_2^2 = \rho_0^2 + \rho^2 + 2\rho_0\rho\sin\varphi. \qquad (13b)$$

Introducing the auxiliary variables $\zeta = 2\pi a\rho/\lambda z$, $\zeta_0 = 2\pi a\rho_0/\lambda z$, $\zeta_1 = 2\pi a\rho_1/\lambda z$, and $\zeta_2 = 2\pi a\rho_2/\lambda z$ and using Eqs. (7)–(10), we obtain an expression for the correlation function of thermal radiation from a plane:

$$R_{\rm P} = (1/\pi)\int_0^\infty d\zeta\int_0^{2\pi} d\varphi\,\zeta[J_1(\zeta_1)/\zeta_1] \times [J_1(\zeta_2)/\zeta_2]\cos[\zeta(D/a)\sin\varphi]. \qquad (14)$$

It is necessary to note that, as distinct from Eq. (11), we did not take into account the nonmonochromaticity of thermal radiation in deriving this formula. It will be demonstrated further that this effect can be ignored (see Fig. 4).

Equation (14) is reduced to a simple formula, if the blackbody lies in the plane where the acoustic axes of both piezoelectric transducers intersect, i.e., in the plane located at the distance z_0 from the piezoelectric transducers. In this case, $\rho_0 = 0$ and, then, $\zeta = \zeta_1 = \zeta_2$ and the integral over φ is reduced as follows:

$$\int_0^{2\pi} d\varphi\cos[\zeta(D/a)\sin\varphi] = 2\pi J_0[\zeta(D/a)].$$

This yields

$$R_{\rm P}(D/a) = 2\int_0^\infty [J_1^2(\zeta)J_0(\zeta(D/a))]/\zeta d\zeta. \qquad (15)$$

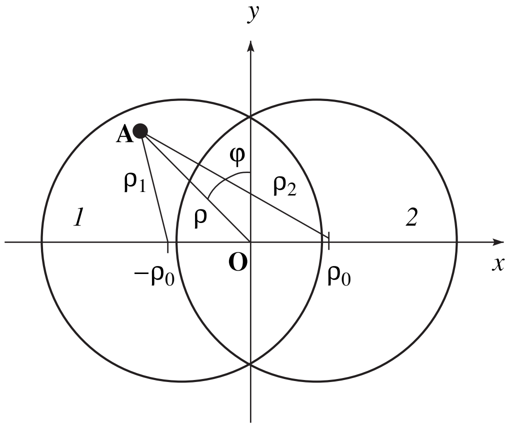

Fig. 2. Scheme for calculating the correlated signal received by two circular piezoelectric transducers ($z < z_0$). The description is given in the text.

As one can see from Eq. (15), the quantity $R_{\rm P}(D/a)$ depends only on the ratio D/a and does not depend on the distance z_0 to the intersection point of the acoustic axes. When D/a increases from zero (both piezoelectric transducers overlap) to the value $D/a = 2$, the value of $R_{\rm P}(D/a)$ decreases from one to zero (Fig. 3, curve *1*, circles). If the distance between the centers of piezoelectric transducers exceeds the sum of the radii of both piezoelectric transducers ($D > 2a$), we have $R_{\rm P}(D/a) \equiv 0$.

If the acoustic axes of two piezoelectric transducers do not intersect in the plane z ($z \neq z_0$), we use the approximation given by Eq. (12) to calculate the correlation function with the help of Eq. (14). In this case, we obtain

$$R_{\rm P}(z, D/a) \approx \exp[-(D/a)^2] \times \exp[-(\pi a^2/2\lambda)^2(D/a)^2(1/z - 1/z_0)^2], \qquad (16)$$

where the dependence of the angle $\theta_0 = \rho_0/z$ on the distance z from the piezoelectric transducers is taken into account in the derivation: $\theta_0 = (D/2)(1/z - 1/z_0)$. Equation (16) provides an opportunity to investigate the correlation function at different z. It shows that $R_{\rm P}$ depends on the distance z and the ratio D/a. In the plane $z = z_0$, where the acoustic axes of both piezoelectric transducers intersect, the approximate dependence $R_{\rm P}(z_0, D/a)$ on D/a (Fig. 3, curve *2*) is close to that for the exact solution at $D/a < 2$ (curve *1*).

Thus, as follows from curves *1* and *2* in Fig. 3, the correlation function $R_{\rm P}$ of the signal from the heated plane does not vanish when two circular piezoelectric transducers overlap.

The shape of flat piezoelectric transducers does not qualitatively influence the dependence of $R_{\rm P}$ on the distance between the piezoelectric transducers. In the case of a rectangular shape of piezoelectric transducers with a width $2a$ (the x axis) and a length (the y axis) greater

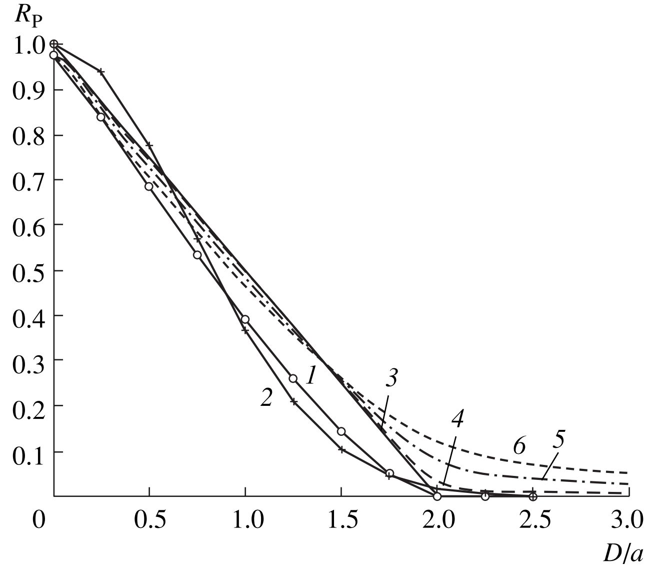

Fig. 3. Dependence of correlation function $R_P(z_0, D/a)$ of the signal from the plane $z = z_0$, where the acoustic axes of both piezoelectric transducers intersect, on the ratio D/a, i.e., the ratio of the distance D between the centers of the piezoelectric transducers to their radius a (curves *1* and *2* for circular piezoelectric transducers) or to the half-width a (curves *3–6* for rectangular piezoelectric transducers) of each of them. Curve *1* for circular piezoelectric transducers is plotted for the exact solution (Eq. 15), and curve *2*, for the approximate one. Curve *3* for rectangular piezoelectric transducers is plotted according to Eq. (19), and curves *4–6*, according to Eq. (18). Curves *1–3* are plotted for a monochromatic signal (the relative transmission bandwidth of the circuit is $\delta f/f_0 = 0$) and curves *4–6*, for the values $\delta f/f_0 = 0.05$, 0.2, and 0.4. The parameters are $a = 5$ mm and $\lambda = 0.75$ mm.

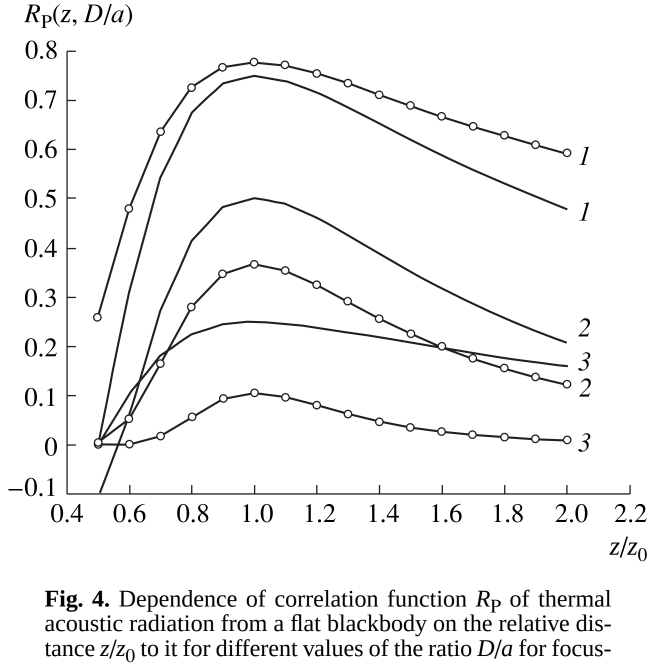

Fig. 4. Dependence of correlation function R_P of thermal acoustic radiation from a flat blackbody on the relative distance z/z_0 to it for different values of the ratio D/a for focusing, rectangular, and circular piezoelectric transducers (the dependences for circular transducers are indicated by circles). Curves *1–3* correspond to $D/a = 0.5$, 1, and 1.5. The parameters are $a = 5$ mm, $\lambda = 0.75$ mm, and $z_0 = 25$ mm.

than the width, the problem becomes one-dimensional and the velocity potential of the waves formed by each piezoelectric transducer (fixed in a rigid screen) has the form [25]

$$\phi_{1,2} = -\frac{a\sqrt{j}}{\sqrt{r_{1,2}\lambda}}\frac{\sin(ka\sin\theta_{1,2})}{ka\sin\theta_{1,2}}\exp[-jkr_{1,2}]u_0, \quad (17)$$

where u_0 is the velocity potential at the surface of a piezoelectric transducer. Using Eq. (17) and the same change of variables as in deriving Eq. (14), we obtain a correlation function for rectangular piezoelectric transducers $R_P^{(2)}(z, D/a)$. In this case, we take into account the signal nonmonochromaticity, which is a generalization of Eqs. (14) and (15) for circular piezoelectric transducers:

$$R_P^2(\theta_0, D/a) = \frac{2}{\pi}\int_0^{\infty}\frac{\sin(\zeta-\zeta_0)}{(\zeta-\zeta_0)}\frac{\sin(\zeta+\zeta_0)}{(\zeta+\zeta_0)} \times \cos(\zeta D/a)\exp\left[-\left(\frac{\delta f}{f_0}\right)\frac{D|\zeta|}{2a}\right]d\zeta. \quad (18)$$

In the particular case of a monochromatic signal ($\delta f/f_0 = 0$), this function has the form

$$R_P^{(2)}(z, D/a) = \begin{cases} (1-D/2a)\operatorname{sin}c\left[\dfrac{2a^2}{\lambda z}\left(1-\dfrac{D}{2a}\right)\dfrac{D}{a}\dfrac{1-z/z_0}{z/z_0}\right], \\ D \le 2a \\ 0, \quad D > 2a, \end{cases} \quad (19)$$

where the function $\operatorname{sin}c(\nu) = \sin(\pi\nu)/(\pi\nu)$. Here, we used the formula $\theta_0 = D/2(1/z - 1/z_0)$.

In the distance range $z > 4a^2/\lambda$, where the Fraunhofer approximation is valid, the approximate expression $R_P^{(2)}(z, D/a) \approx (1 - D/2a)$ for $D \le 2a$ (curve *3* in Fig. 3) follows from Eq. (19). This is a consequence of the fact that the argument of the function $\operatorname{sin}c$ is sufficiently small (the term depending on the ratio D/a does not exceed the maximal value equal to 0.25), so that the value of the function $\operatorname{sin}c$ is approximately equal to unity. Thus, the correlation function is nonzero only when the distance between two piezoelectric transducers is smaller than their width, as for circular piezoelectric transducers (curves *1* and *2*).

The nonmonochromaticity of the signal only slightly affects the dependence of the correlation function $R_P^{(2)}$ on the relative distance D/a between the piezoelectric transducers. The dependence $R_P^{(2)}$ on D/a calculated numerically using Eq. (18) for different rel-

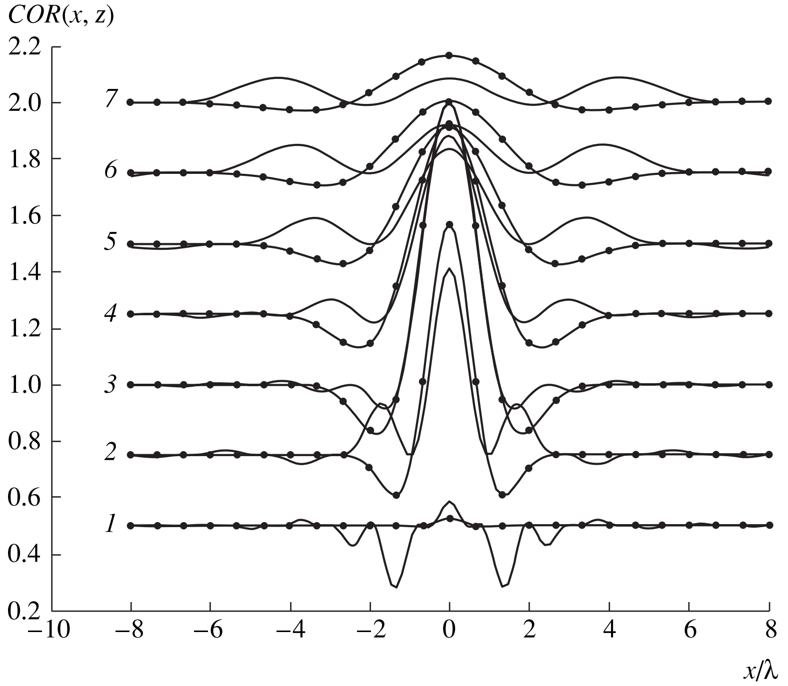

Fig. 5. Dependences of the relative value of the correlated signal $COR(x, z)$ on the x coordinate in several planes separated from the transducer by the relative distances z/z_0 = (*1*) 0.5, (*2*) 0.75, (*3*) 1, (*4*) 1.25, (*5*) 1.5, (*6*) 1.75, and (*7*) 2 for $D/a = 1$. The curves for rectangular piezoelectric transducers are indicated by solid lines and those for circular piezoelectric transducers, by dots. The curves are normalized to the value of $COR(x, z)$ at $z = z_0$. The zero level of each curve (at $x \longrightarrow -\infty$) is shifted upwards to the distance equal to the ratio z/z_0 for a corresponding plane (0.5, 0.75, etc.) for convenience in presenting the results. The parameters are a = 5 mm, λ = 0.75 mm, and z_0 = 25 mm.

ative transmission bandwidths of the circuit $\delta f/f_0 = 0.05$, 0.2, and 0.4 (curves *4–6*, respectively) is slightly different from curve *3* for the monochromatic case. The expansion of the frequency band in comparison with the monochromatic case changes the dependence form for $D/a > 2$ only when the values of the correlation function are small.

Thus, a nonzero correlation signal from a heated plane can be measured only when the piezoelectric transducers overlap partially. The inclusion of the signal nonmonochromaticity does not qualitatively change this result.

Now, let us consider the possibility of the correlation signal localization in depth. As follows from Eqs. (19) and (16), two flat and even partially overlapping transducers cannot provide the localization in depth. The point is that the necessary condition for signal reception from the Fraunhofer zone is the large value of the parameter $S = z\lambda/a^2 > 1$ [25]. However, at such values of this parameter (the Fresnel parameter), the dependence of the correlation function on the distance z becomes very weak for both the function sin*c* [Eq. (19)] and the Gaussian function of Eq. (16). Therefore, it is expedient to use focusing piezoelectric transducers that do not have the aforementioned limitations for the value of S.

For the sensors of a two-element interferometer in the form of focusing piezoelectric transducers, the dependence of the directivity pattern on the scanning angle is given by the same formula as for flat piezoelectric transducers in the Fraunhofer zone. The difference is that the corresponding expressions can be used for small values of the parameter $S = z\lambda/a^2 < 1$ [25]. For example, the correlation function $R_P^{(2)}(z, D/a)$ for the focusing rectangular piezoelectric transducers is also described by Eq. (19). The dependence of the correlation function on the distance z has a peak in the plane z_0 where the acoustic axes of both piezoelectric transducers intersect (Fig. 4, the solid lines) and the strongest dependence $R_P^{(2)}(z, D, a)$ is observed for $z < z_0$. The maximal value of $R_P^{(2)}$ decreases as the distance between the piezoelectric transducers grows (curves *1–3* corresponding to the ratios D/a = 0.5, 1, and 1.5, respectively), which agrees with the results given in Fig. 3.

The shape of the piezoelectric transducers has a weak effect on the dependence of the correlation function on the distance (circles in Fig. 4 indicate the curves that are plotted for a pair of focusing circular piezoelectric transducers according to Eq. (16) for the same values of the ratio D/a).

A comparatively small decrease in the correlation function for a heated plane at $z > z_0$ is presumably related to the increase in the spatial region from which the correlated signal is received by the two-element interferometer. Let a narrow heated strip with the width Δ and orientation along the y coordinate move along the x coordinate in its field of observation, and let us consider the change in the correlated signal $COR_\Delta(x, z)$. Deriving the corresponding formula for a two-element interferometer with circular transducers, we perform the integration in Eq. (14) only over the y axis, reduce the integrand with the help of the approximation given by Eq. (12), and normalize the resulting dependence to the value corresponding to the coordinates $x = 0$ and $z = z_0$. In this case, we obtain

$$COR_\Delta(x, z) = \frac{z_0}{z}\exp\{-(\pi a/\lambda z)^2 \times [(D/2)^2(1 - z/z_0)^2 + x^2]\}\cos[2\pi(D/\lambda)(x/z)]. \quad (20)$$

In deriving the analogous dependence $COR^{(2)}_\Delta(x, z)$ for rectangular piezoelectric transducers, the integrand in Eq. (18) normalized to the corresponding value at $z = z_0$ is used.

In the case of fixed values of z, the dependences of the relative value of the correlated signal $COR(x, z)$ on the x coordinate are similar for both types of piezoelectric transducers. Figure 5 shows these dependences for $D/a = 1$ and for the planes located at the distances $z = z_0 =$ (*1*) 0.5, (*2*) 0.75, (*3*) 1, (*4*) 1.25, (*5*) 1.5, (*6*) 1.75, and (*7*) 2 from the transducer. The case of circular piezoelectric transducers is indicated by dots. For better illustration, the initial level of each of the curves for the strips away from the acoustic axis of the system (formally, at $x \longrightarrow -\infty$) is shifted upwards to the distance equal to the ratio z/z_0 for the corresponding plane (0.5, 0.75, etc.). One can see that the dependences $COR(x, z)$ on the x coordinate have a distinct maximum in the focal region [$z = (0.75–1.25)z_0$, curves *2–4*], which vanishes away from it [$z \le 0.5z_0$ and $z \ge (1.5–2)z_0$, curves *1* and *5–7*]. It is necessary to note that the agreement observed for both types of piezoelectric transducers in the focal plane (curves *2–4*) is good, and it is much worse outside it. Probably, this difference is connected with the utilization of the approximate formula for circular piezoelectric transducers.

From Fig. 5, one can see that, at $z > z_0$, the relative width of the region from which the correlated signal is received increases considerably: from $x = \pm 2\lambda$ at $z = z_0$ to the triple value $x = \pm 6\lambda$ at $z = 2z_0$, although the value of the correlated signal decreases significantly in this case. Apparently the small decrease in the correlation function R_P formed by a heated plane at $z > z_0$ is connected with the expansion of the region where the correlated signal comes from.

Thus, focusing overlapping piezoelectric transducers used as elements of a two-element interferometer provide an opportunity to obtain a spatially localized correlated signal of thermal acoustic radiation from two-dimensional objects. This result does not depend qualitatively on the shape of the utilized elements of the two-element interferometer. Thus, the directivity pattern of a passive acoustic thermotomograph using no *a priori* information on the absorption coefficient of the medium [20] can be realized. The technological difficulty connected with the need to bring the centers of two piezoelectric transducers close to each other can be easily overcome by using various types of acoustic gratings. One can expect that this conclusion will also be valid for the measurements of correlation properties of thermal acoustic radiation emitted by three-dimensional bodies.

ACKNOWLEDGMENTS

I am grateful to A.A. Anosov, Yu.N. Barabanenkov, and L.R. Gavrilov for valuable discussions. This work is supported by the Russian Foundation for Basic Research, project nos. 00-02-16370 and 00-01-00361.

REFERENCES

1. K. Maruyama, S. Mizushina, T. Sugiura, *et al.*, IEEE Trans. Microwave Theory Tech. **48**, 2141 (2000).
2. S. Mizushina, K. Maruyama, T. Sugiura, *et al.*, in *2000 IEEE Microwave Theory and Techniques Symposium Digest* (IEEE, New York, 2000), p. 1033.
3. K. Maruyama, Y. Niwa, S. Mizushina, *et al.*, in *1998 Asia Pacific Microwave Conference Proceedings* (Inst. Electron. Inf. Commun. Eng., Tokyo, 1998), p. 885.
4. G. M. J. van Leeuwen, J. W. Hand, J. J. W. Lagendijk, *et al.*, Pediatr. Res. **48** (3), 351 (2000).
5. A. A. Anosov, V. I. Pasechnik, and V. V. Shablinskiĭ, Akust. Zh. **37**, 610 (1991) [Sov. Phys. Acoust. **37**, 315 (1991)].
6. A. A. Anosov and V. I. Pasechnik, Akust. Zh. **40**, 885 (1994) [Acoust. Phys. **40**, 781 (1994)].
7. Yu. N. Barabanenkov and V. I. Passechnik, J. Acoust. Soc. Am. **99**, 65 (1996).
8. V. A. Burov and E. E. Kasatkina, Akust. Zh. **43**, 162 (1997) [Acoust. Phys. **43**, 135 (1997)].
9. V. I. Pasechnik, A. A. Anosov, and K. M. Bograchev, Biomed. Radioélektron., No. 2, 3 (1999).
10. V. I. Passechnik, A. A. Anosov, and M. G. Isrefilov, Int. J. Hyperthermia **15** (2), 123 (1999).
11. V. I. Passechnik, A. A. Anosov, M. G. Isrefilov, and A. V. Erofeev, Ultrasonics **37**, 63 (1999).
12. V. I. Passechnik, A. A. Anosov, and K. M. Bograchev, in *Forum Acusticum*, CD ROM ed. (Berlin, 1999).
13. E. V. Krotov, S. Yu. Ksenofontov, A. D. Mansfel'd, *et al.*, Izv. Vyssh. Uchebn. Zaved., Radiofiz. **42** (5), 479 (1999).
14. V. I. Pasechnik, A. A. Anosov, and K. M. Bograchev, Biomed. Radioélektron., No. 2, 3 (1999).

15. K. M. Bograchev and V. I. Pasechnik, Akust. Zh. **45**, 742 (1999) [Acoust. Phys. **45**, 667 (1999)].
16. K. M. Bograchev, Candidate's Dissertation in Physics and Mathematics (Inst. of Radio Engineering and Electronics, Russ. Acad. Sci., Moscow, 2000).
17. R. A. Kruger, D. R. Reinecke, and G. A. Kruger, Med. Phys. **26**, 1832 (1999).
18. Yu. N. Barabanenkov and V. I. Pasechnik, Akust. Zh. **41**, 563 (1995) [Acoust. Phys. **41**, 494 (1995)].
19. A. I. Chmill, V. V. Gerasimov, Yu. V. Guluaev, *et al.*, in *Acoustical Imaging-23*, Ed. by S. Lees (Plenum, New York, 1997), pp. 77–86.
20. V. I. Pasechnik, Akust. Zh. **43**, 563 (1997) [Acoust. Phys. **43**, 485 (1997)].
21. A. A. Anosov, M. A. Antonov, and V. I. Pasechnik, Akust. Zh. **46**, 28 (2000) [Acoust. Phys. **46**, 21 (2000)].
22. V. I. Passechnik, Ultrasonics **32** (4), 293 (1994).
23. A. A. Anosov and V. I. Pasechnik, Akust. Zh. **48**, 16 (2002) [Acoust. Phys. **48**, 12 (2002)].
24. G. Kino, *Acoustic Waves. Devices, Imaging, and Analog Signal Processing* (Prentice Hall, Englewood Cliffs, NJ, 1987; Mir, Moscow, 1990).

Translated by M. Lyamshev

Acoustical Physics, Vol. 48, No. 5, 2002, pp. 598–606. Translated from Akusticheskiĭ Zhurnal, Vol. 48, No. 5, 2002, pp. 675–683.
Original Russian Text Copyright © 2002 by Studenichnik.

Space–Time Structure of the Low-Frequency Acoustic Field in an Underwater Sound Channel

N. V. Studenichnik
Andreev Acoustics Institute, Russian Academy of Sciences, ul. Shvernika 4, Moscow, 117036 Russia
e-mail: bvp@akin.ru

Received March 29, 2001

Abstract—Experimental data are presented on the fine structure of the sound field in an underwater sound channel for low and infralow sound frequencies. The experiments are performed in the Black Sea, on a 600-km-long path, with explosive sound sources. The intensity, space–time, and frequency characteristics of the sound field are analyzed. The geometric dispersion of the first normal wave is experimentally studied. The role of the channel inhomogeneities in the violation of the sound field coherence is determined for different frequency bands. On the basis of the experimental data, the vertical distribution of the critical frequencies of the waveguide is obtained, and the validity limits are established for the wave and ray calculation methods. The applicability of the phase methods for calculating the sound fields in waveguides with dispersion is discussed. The frequency–angular dependence of the effective sound attenuation coefficient in an underwater waveguide is revealed and explained. *© 2002 MAIK “Nauka/Interperiodica”.*

Reliable data on the fine structure of the sound field at long and extra-long distances in underwater waveguides are still of high priority in ocean acoustics. These data are required to understand the physical meaning of the processes that occur in the ocean and to solve certain engineering problems. To that end, the main task is to establish the predominant features of the sound field (in appropriate frequency bands), which determine the stable field structure governed by the deterministic ocean inhomogeneities, and the irregular field components governed by random ones. Starting from the 1950s, the author of this paper developed methods for studying sound field structure on the basis of separating and identifying the field components in their propagation times, arrival angles, and frequencies. The methods developed enabled us to establish and, on the basis of the fundamental works of L.M. Brekhovskikh [1], theoretically explain the features of the fine structure of the sound field for various ocean regions, as well as study the mechanisms that produce the fine structure [2–7]. In particular, the following items were studied and analyzed on this basis: the nature and the frequency behavior of the sound field in the shadow zone, the wave activity in the upper ocean layers, the space–time and frequency dependences for the total duration (the “elongation” time) of the signal at different ranges and depths, the possibility for the inverse problems of ocean acoustics to be solved, a ray technique for determining the coordinates of a sound source (from the sound field structure), the phenomenon of prereverberation, the angular width of the (forward) scattering diagram for the refracted field components (under the influence of volume inhomogeneities and surface waves), and the frequency dependence of the lengths of refraction cycles with the associated frequency dependences for the distances from the source where far convergence zones take place.

This paper considers the space–time structure of the sound field and the power “capacity” of the underwater sound channel in certain frequency bands (a 1/3-octave filter is used). We also study the “geometric” dispersion of the sound speed in the underwater channel and the degeneration of the refraction ability of the channel, consider the phase stability of the wave fronts in the waveguide with dispersion, analyze the conditions of the formation of normal waves in a real underwater channel, study the origin and mechanisms for the regular field components to lose their coherence as functions of frequency and range, experimentally determine the critical frequencies for different waveguides and the frequency limits of validity for the ray computation technique along with the limits for using the intensity summation to calculate the sound field in a waveguide with dispersion, and reveal and explain the frequency–angular dependence of the effective attenuation coefficient for an underwater sound channel.

The experiments were performed in the central region of the Black Sea on a path 600 km in length. The path was oriented in the latitudinal direction at an angle of 285° relative to the receiving vessel with a sea depth of 200 m. The hydrological environment was rather steady along the path. The sound speed profile showed a stable underwater sound channel with its axis at the depths 30–50 m and a weakly pronounced surface channel of 5–20 m in thickness. The measured sound speed profiles along the path are presented in Fig. 1. The sea state was Beaufort 1–3. The research vessels drifted at the reception and transmission points. The distance between the vessels was determined by navigational means and recalculated from the measured propagation times of the sound signals. As the sound sources, explosive charges (120 pieces weighing 2.5 kg each) were used. The charges exploded at depths of 10–80 m and at distances of 150, 300, and 600 km. The signals were received by omnidirectional hydrophones at depths of 10, 35, 50, and 80 m. The signals were analyzed at frequencies ranging from 1 Hz to 5 kHz.

To analyze the space–time and power–frequency structures of the sound field and the dispersion properties of the waveguide, let us consider a low-frequency broadband record obtained at a distance of 600 km. The typical shape of the explosion-generated signal received near the channel axis is shown in Fig. 2 for 35-m and 50-m depths of explosion and reception, respectively. The abscissa axis represents the running time, with a linear scale of the signal amplitude on the ordinate axis. The record contains frequencies ranging from 1 to 300 Hz. In the figure, vertical lines are the time marks separated by 100 ms.

The sets of the received signal components corresponding to the ray quartets for the low and infralow sound frequencies are produced by the shock wave and by two oscillations of the gas bubble. The sets are formed purely by water rays: there are no surface and bottom reflections. At the beginning of the record, separate regular components of two sets can be noticed that are generated by the shock wave (signals 1, 2, 3, …) and first oscillation (signals 1', 2', 3', …) with a period of 125 ms. The components produced by the second oscillation have levels which are lower by 10–15 dB than that of the shock wave; they are masked by the latter and weakly pronounced in the record. The signal elongation in the broad band, which is governed by the high-frequency components, is 4.95 s (5.2 s in view of the oscillations). The differences in the delay times are 250, 240, 200, … ms for the initial regular components. For subsequent components, these differences decrease and tend to zero in the limit.

The received sound pressure as a function of time can be associated with a quasi-sinusoidal function that represents the geometric dispersion of the sound speed in the channel. The quasiperiod of this function is equal to the doubled difference in arrival times of the signals in the quartets of rays, for which the number of cycles differs by one. The measured levels of separate components, which are governed by the focusing factors, change by 3–4 dB. In the domain of fully-developed dispersion (the frequencies 40–300 Hz), the general signal level increases by less than 2–3 dB because of the in-phase summation of the regular components. At high frequencies, the characteristic angles (i.e., the angles at which the channel axis is crossed) are within the range ±14° for the rays captured by the waveguide. In the low-frequency band, this angular range strongly depends on the frequency and tends to zero at the critical frequency of the entire waveguide.

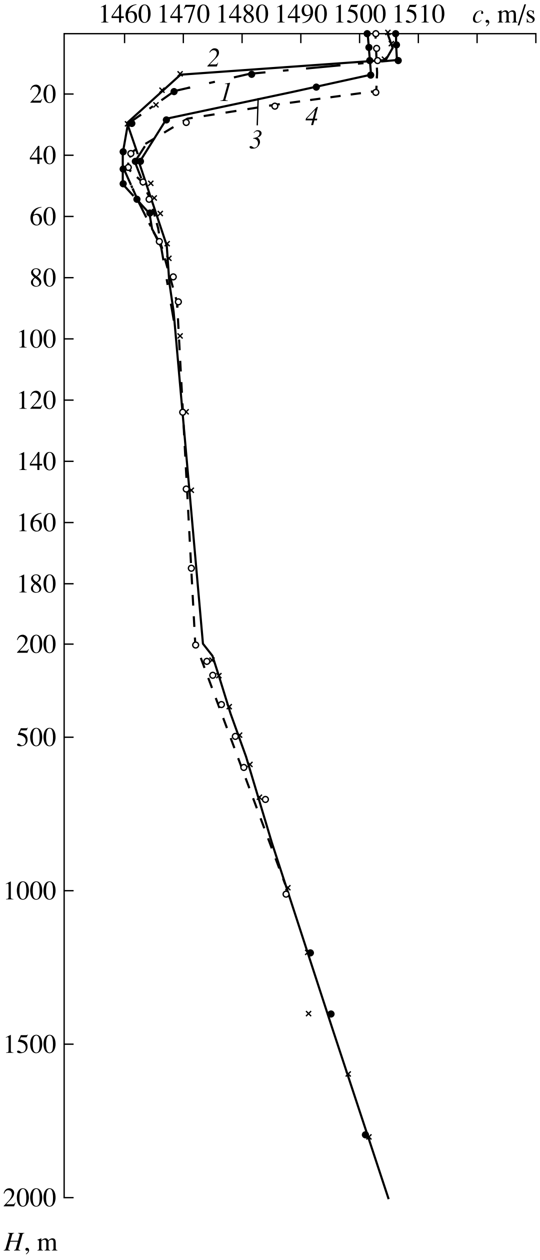

Fig. 1. Vertical profiles of the sound speed along the experimental path at the distances (*1*) 0, (*2*) 150, (*3*) 300, and (*4*) 600 km in the Black Sea.

At the beginning of the record, separate components that are caused by the shock wave are graphically compared with the quasi-sinusoid corresponding to the lowest frequencies of the refracted waves. For the components to be summed nearly in phase and for the dispersion to be well pronounced in the low-frequency spectrum, it is required that the distance be much longer than 600 km. According to the critical frequency of the entire waveguide, the distance must be sufficient to provide equal differences in the arrival times of the first and second, as well as the second and third, signal quartets, which is the condition that can be met nowhere but

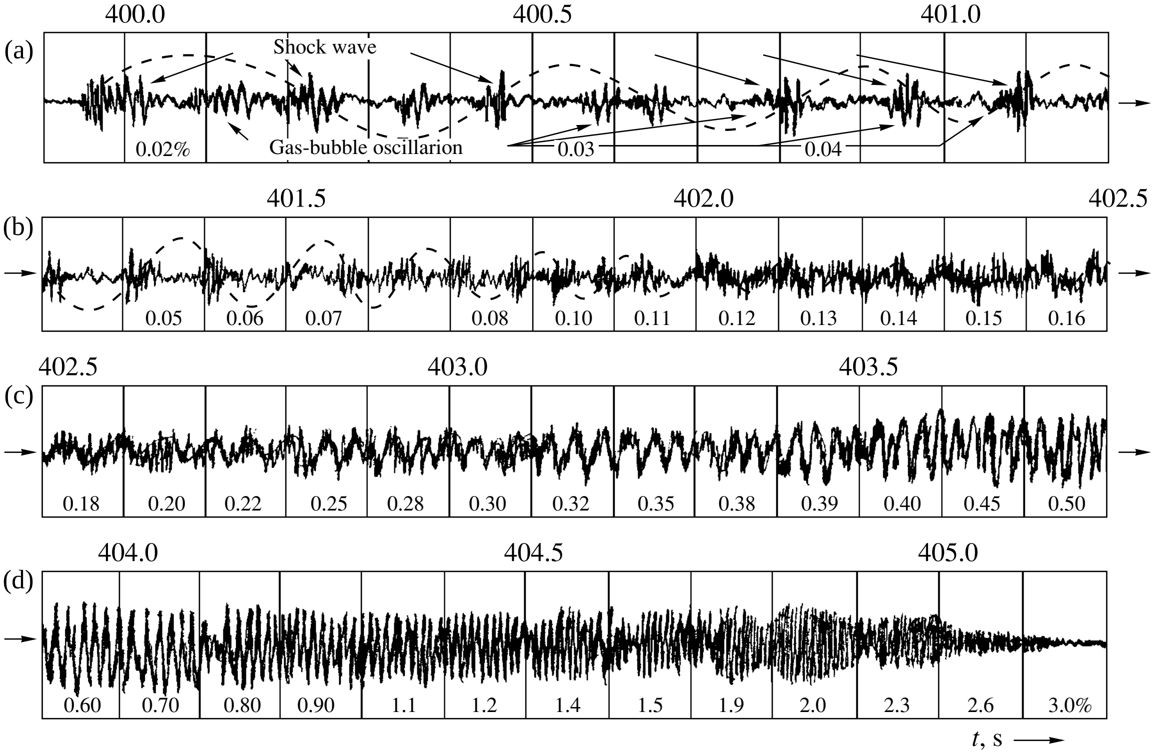

Fig. 2. Structure of the broadband explosion-generated signal in the underwater sound channel at low frequencies. The distance is 600 km. The depths of explosion and reception are 35 and 50 m, respectively. (a–d) Successive fractions of the entire signal set, (1, 2, …) individual arrivals of the quartets generated by the shock wave, and (1', 2', …) quartets of the first gas-bubble oscillation. $f_0 = 100$ Hz.

at an infinite range. Within the limit, this time is equal to the difference in the propagation times for the high-frequency signals propagating over the channel axis and the limiting ray (within a single ray cycle). Being doubled, this value determines the limiting critical frequency of the entire waveguide; for the case at hand, it is equal to 1.8 Hz. The components arriving later propagate in the layers that are closer to the channel axis and govern the dispersion and critical frequencies for higher frequency components of the spectrum. In contrast to a shallow sea where high frequency components of the water signal are the first to arrive, low frequency components and signals of higher modes are the forerunning ones in an underwater (surface) channel [1, 8, 9].

Time intervals in the signal quartets are governed by the positions of the source and the receiver. With the chosen depths of these positions, a visual resolution of separate components is difficult. Several initial quartets are the exception, in which each individual signal can be resolved. For the first quartet, the total signal broadening is 80 ms at a distance of 600 km corresponding to 16 full ray cycles. At a distance of 37 km, i.e., within the first cycle, this value equals 5 ms. As a function of range and number of cycles, the signal duration increases according to the law close to the square one and exhibits a saw-tooth behavior with a period equal to the length of the limiting cycle. At fixed characteristic angles, the delay times in the quartets and between them grow linearly with distance. Strictly discrete space–time and angular structures of regular components exist in layered waveguides. This fact allows one to solve inverse problems of ocean acoustics, namely, to determine the source coordinates [5] and to reconstruct the channel parameters from the sound field structure.

With the reception frequency band broadened up to 2–5 kHz, the shapes of separate components considerably change: first, the front steepness in the quartets increases, and, second, the dispersion, which is quite pronounced in the low-frequency range (Fig. 2), is masked by additional signals and becomes less noticeable. Such a situation is caused by enriching the regular components with high frequencies and, correspondingly, by the higher contribution of prereverberation [2–7]. As a result, starting from the initial five to ten regular components, the intercomponent time intervals are filled with prereverberation signals. The near-axis components are the ones that change most significantly: the levels of regular and prereverberation components become equal in this case. Here, in the tail fraction of the signal set, a continuous noise-like system of regular and incoherent components is formed with a uniform probability distribution of the phases and amplitudes for characteristic angles ranging from 0° to

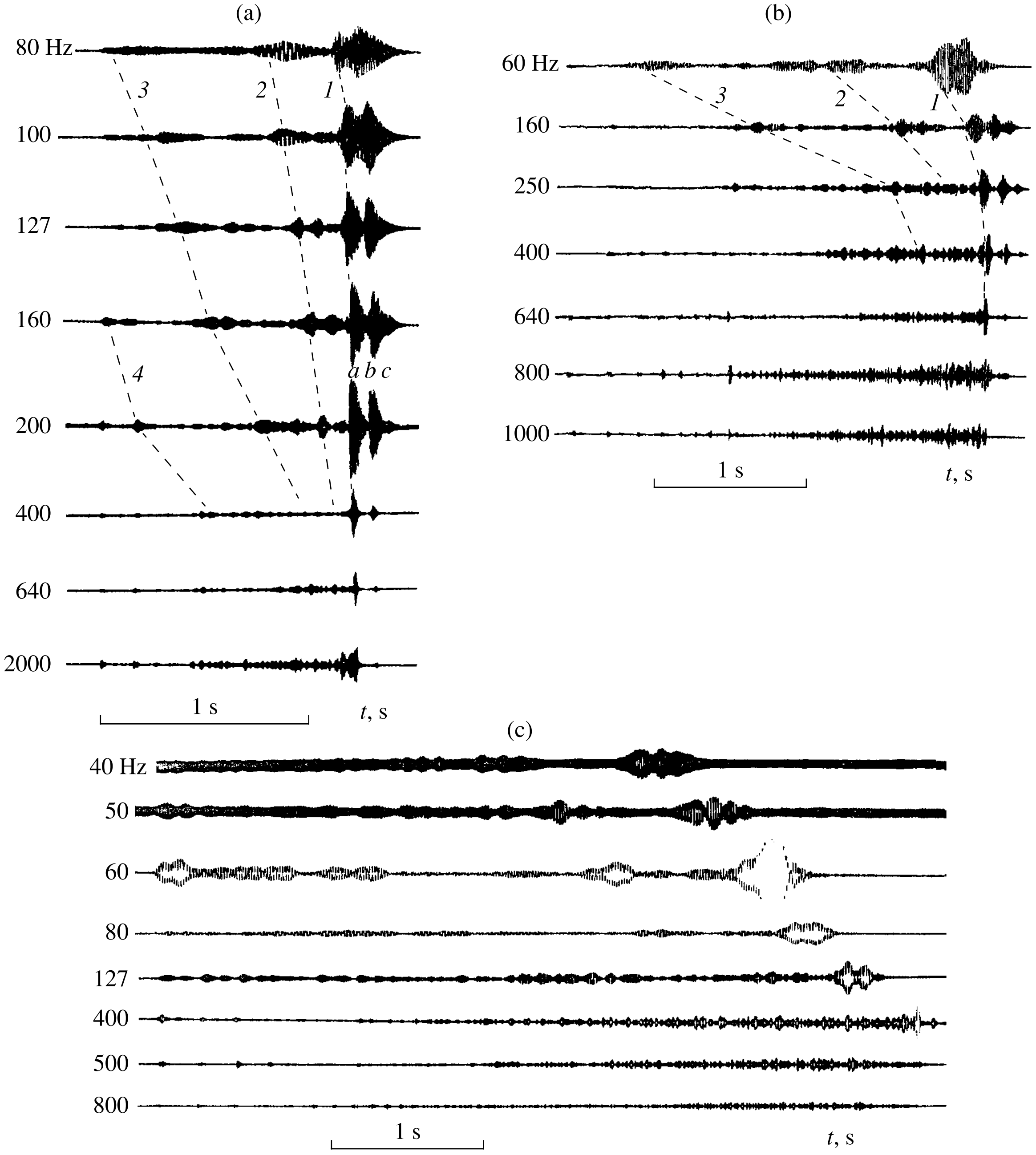

Fig. 3. Structure of the explosion-generated signals in the underwater sound channel for various distances and frequencies. The explosion depth is 35 m and the reception depth is 50 m. The distances are (a) 150 km (frequencies 80–2000 Hz), (b) 300 km (60–1000 Hz), and (c) 600 km (40–800 Hz). Curves *1*, *2*, and *3* approximate the first, second, and third normal waves. The analysis is performed in the 1/3-octave frequency band.

±5°–7°. The only exception occurs for the terminal fractions of the signal sets produced by the first gas-bubble oscillations (which are poor in their high-frequency contents): here, the dispersion is quite pronounced at frequencies 80–300 Hz. The difference in levels of the signals generated by the shock wave and the first oscillation is 15, 10, and 6 dB at the distances 150, 300, and 600 km, respectively, in a broad frequency band (20 Hz to 5 kHz). In the narrow low-frequency band (1–300 Hz), this value is 3–4 dB.

The broadband analysis yields most general and main qualitative characteristics of the sound field in the underwater waveguide. To obtain the fine structure of the field and fundamental quantitative relations, one can use spectral analysis. To that end, signal records are presented in Figs. 3a and 3b, which were obtained in 1/3-octave frequency bands, from 40 Hz to 2 kHz, with the source and receiver located near the channel axis at depths of 35 and 50 m, respectively. The signal amplitudes are shown on a linear scale. The duration of the

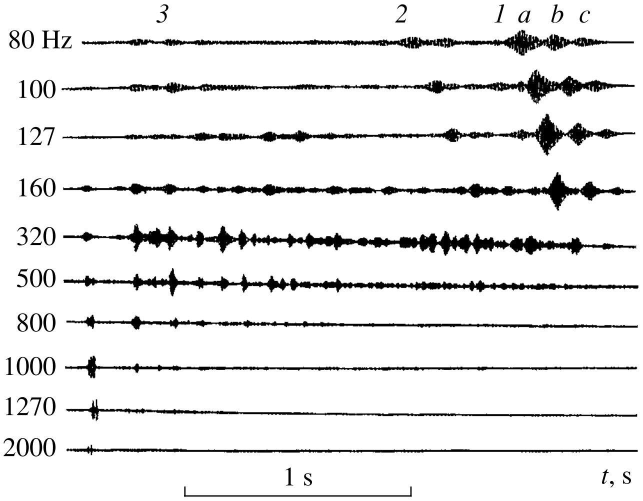

Fig. 4. Structure of the explosion-generated signals at a distance of 300 km in the frequency band 80–2000 Hz. The explosion depth is 16 m. The reception depth is 50 m. The analysis is performed in the 1/3-octave frequency band. The signal groups labeled by numbers *1–3* represent normal waves of the corresponding ordinal numbers. Maxima *a, b,* and *c* correspond to the shock wave and the two initial gas-bubble oscillations.

high-frequency signals is 1250, 2790, and 4950 ms at distances of 150, 300, and 600 km, respectively. At lower frequencies, this duration monotonically decreases and becomes 1110, 2105, and 3100 ms at 40–80 Hz with a fall to zero at the critical frequency (1.8 Hz) of the entire waveguide (Fig. 2). At the high frequencies, the first signals are resolved in time. Starting from the middle of the samples under consideration, the filtered signals overlap, and their levels increase. At lower frequencies (40–200 Hz), the noticeable change in signal shape is caused by high levels of the oscillations and frequency responses of the filters. At the terminal fraction of the samples, pronounced level elevations can be noticed that are frequency dependent and represent the dispersion properties of the channel; here, a nearly in-phase summation of the regular components leads to the formation of normal waves. The terminal maxima correspond to the dispersion of the first normal wave. Other, less pronounced, level elevations correspond to the first and third modes (curves *2* and *3*) and to the fourth mode at a distance of 150 km (for the frequencies 160 and 200 Hz).

At a distance of 150 km (Fig. 3a), the in-phase summation of the field components and the stable formation of the first normal wave occur in the entire frequency band from 80 Hz to 2 kHz. The positive propagation anomaly reaches 15–25 dB in the maxima. The level of the most intense “quasi-in-phase” components exhibit different rates of decay in their propagation. Each individual component decays with distance according to the spherical law (with the focusing factors that are close to zero). The normal waves (for monochromatic processes) follow the cylindrical decay law. In the experiments, we deal not with cw signals but with pulsed broadband signals that undergo a dispersion. Hence, the decay of the in-phase dispersing components obeys the Airy law: $J \sim r^{-5/3}$ [8]. The difference in the decay laws leads to an accumulation of the difference in levels of the corresponding signals as the distance increases. By using the experimental amplitude distributions of the single and phased components, one can easily find the frequency dependence of the transition distance r_0 [1] at which the spherical law changes to the 5/3-law. If the distance 150 km can be considered as allowable for the propagation anomalies of phased components to be reliably estimated in the frequency band 80–2000 Hz, we find that r_0 falls within the range 0.5–5 km. As the frequency decreases, r_0 increases up to tens and even hundreds of kilometers. In accordance with the decay law observed at the distances 100–150 km, the level difference between the components corresponding to the unphased and phased signal quartets must increase proportionally to the distance. However, in real circumstances (even in the rather stable environment of the Black Sea), this behavior does not persist. Moreover, the difference in levels of the unphased and phased signals, which had been reached at a distance of 150 km, decreases with distance instead of increasing. The strongest decrease takes place as the filtering frequency grows and the characteristic angles of the near-axis components diminish. In this case, the violation of the coherence and the strong attenuation of the in-phase components lead to a decrease in their level, which is much deeper than with the spherical spread of the unphased components. Thus, while the coherent components forming the first normal wave at 150 km can be observed with an anomaly of +15–25 dB at all filtering frequencies up to 2000 Hz, and, at 300 km, they are nearly invisible at the frequencies 600–800 Hz, they fully vanish at the distance 600 km even at a frequency of 500 Hz. So, there is a pronounced frequency–angular dependence of the effective attenuation coefficient for the near-axis components in the underwater sound channel. The coherent components that still exist at the frequencies 40–400 Hz and distance 600 km have a positive propagation anomaly, which does not exceed 10–15 dB, this value being much lower than the anomaly at the 150-km distance. For certain values of the waveguide thickness, the decrease in levels of the near-axis components reaches 30–50 dB and even higher at frequencies lower than the critical one, thereby corresponding to the decay law $J \sim r^{-4}$ [1]. On average, the decrease in levels of the near-axis components is 0.02–0.05 dB/km (relative to the spherical decay law) at 80–400 Hz for the whole path. At high frequencies, this value reaches 0.07–0.09 dB/km.

Figure 4 illustrates the structure of the sound field at different frequencies within 80–2000 Hz. These data were obtained at the distance 300 km with the near-surface sound source (at a depth of 16 m) and the near-axis receiver (50 m). In this case, according to ray considerations, the sound field structure should contain a single signal quartet with a characteristic angle close to ±14°. In fact, the sound field structure observed at the frequencies 1000–2000 Hz is somewhat similar to the calculated one. However, even at these frequencies, the field structure contains the second and following signal quartets, which manifest themselves as diffraction components. Their amplitudes are lower by 10–15 dB than the level of the direct signal. At a frequency of 800 Hz, the number of quartets increases to three, and up to ten additional quartets are present as the diffraction components. At the frequencies 320 and 500 Hz, a full set of the refraction signals exists, including all near-axis components that are allowed by the waveguide at these frequencies. In the ray approximation, such a structure can exist only when both source and receiver are located at the channel axis. Similar to Fig. 3 (at near-axis positions of the source and receiver), the same frequency dependences of the field amplitude and time intervals take place at frequencies of 80–320 Hz. In the terminal parts of the signal sets, the in-phase components manifest themselves as the maxima with decreasing amplitudes. They correspond to the first mode and are caused by the shock wave and two initial gas-bubble oscillations with periods of 185 and 165 ms. The maxima that correspond to modes of the first and second numbers can also be noticed. The amplitudes in the maxima of the first normal wave are higher by 10–15 dB than those of the unphased signals. The same structure of the sound field can be observed when positions of the source and receiver are interchanged.

From the aforementioned data obtained at sonic and infrasonic frequencies, the conclusion can be drawn that the ray theory fails to describe the power and space–time characteristics of the low-frequency sound field up to 500–1000 Hz in the underwater sound channel. At frequencies lower than 100–500 Hz, the underwater channel degenerates into a surface one with a pseudo-uniform near-surface layer of some thickness, where an effective minimal sound speed exists. This layer covers horizons above and, partially, below the channel axis. The low-frequency components of the sound field do not undergo refraction in the upper layers. In this frequency band, the field structure is formed by the components that are refracted at deeper layers of the channel. The experimental data obtained for the frequency dependences of the time and amplitude structures of the sound field can be explained by nothing but wave considerations. With these data, the limiting frequency (which limits the ray approximation validity) is about 2–2.5 kHz. According to the validity criterion [9] for the ray considerations, the limiting frequency, at which the refraction phenomena hold when the signal passes the discontinuity layer at low grazing angles, can be found from the relation $f = 0.4Ch^{-1}(\Delta C/C)^{-0.5}$, where C is the sound speed and h is the thickness of the discontinuity layer. For $h = 5$ m and the difference in sound speeds $\Delta C = 37$ m/s, the critical frequency is $f = 750$ Hz, this value being an octave lower than the experimental one. Similar features of low-frequency sound field formation are typical of other ocean regions as well. The only parameters that can change from region to region are the range of critical frequencies and the frequency band within which the in-phase summation of the coherent components occurs and, hence, normal waves can form. In the northwestern part of the Pacific Ocean, for instance, the environment is more variable, and the first normal wave can hardly exist even at frequencies of 60–100 Hz [7].

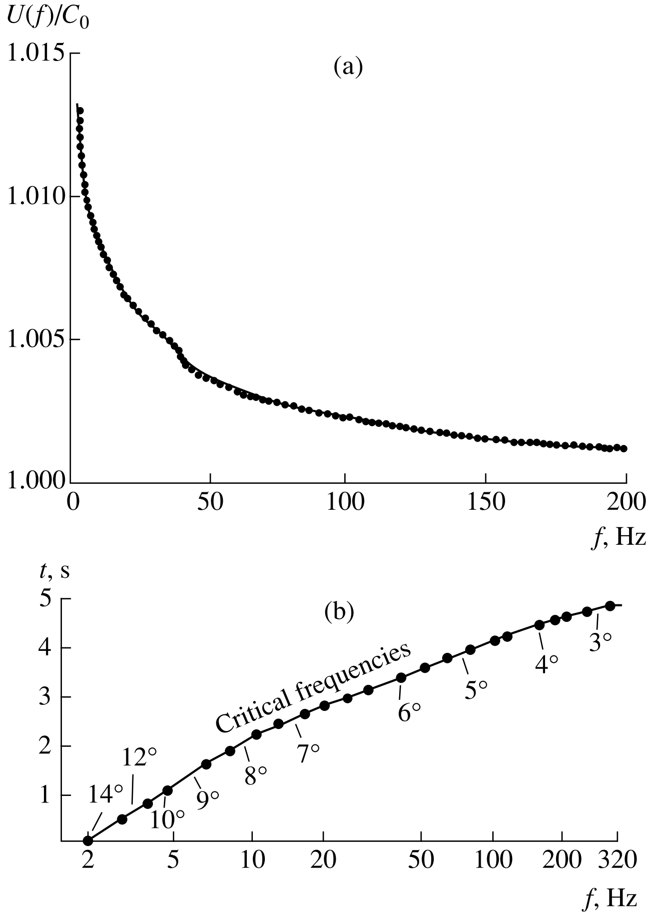

Fig. 5. (a) Dispersion curve for the sound speed and (b) the frequency dependence of the signal duration. The values of the characteristic angles (in degrees) and corresponding critical frequencies are indicated for curve (b). $C_0 = 1460$ m/s.

In the high-frequency band, the mechanism of additional attenuation, which predominates at small characteristic angles, can be attributed to the sound absorption and scattering by the channel inhomogeneities. At low frequencies, in contrast, the decrease in levels of the near-axis components is caused by their mutual suppression at frequencies lower than the critical ones (for near-axis layers of certain thickness). The latter means that there are no refraction components with low characteristic angles in these layers of the channel. As the frequency decreases, the angular range that retains the refraction components becomes narrower. At frequencies lower that the limiting critical one (1.8 Hz in our case), no such components are present in the channel. The shallow-sea waveguide degenerates into a uniform layer in which nothing can propagate but the waves that correspond to straight-line rays [8].

To conclude with considering the structure of the explosion-generated sound field, note that the ratios of amplitudes in signals caused by the shock wave and gas-bubble oscillations change from zero to 25 dB or more at different frequencies. On average, the difference in the levels of the shock wave and the first oscillation is 20–25 dB at 2 kHz, it does not exceed 10 dB at 400 Hz, and it is close to zero at 40–200 Hz. With other masses of charges, these ratios are somewhat different.

By using the ray-calculated and experimental space–time characteristics of the sound field in the waveguide, one can easily analyze and explain the dispersion properties of the channel. The sequence of time intervals separating individual signals in the observed structures (Figs. 2–4), which can be calculated by using ray theory (e.g., [4]), represent the frequency dependence of the group velocity for the first normal wave. The phase velocity is characterized by the sound speed at the turning points of the rays whose characteristic angles allow a certain normal wave to form at the frequency at hand. The sequence of the arriving signal quartets forms a periodic process whose period is equal to the doubled difference in the arrival times of the two adjacent components, which, by summing in phase or out of phase, form the first normal wave at a certain frequency. This frequency can be determined from the relation

$$f_n = 2(t_{n+1} - t_n)^{-1}, \tag{1}$$

where $t_{n+1} - t_n$ is the difference in the arrival times for the signals corresponding to two adjacent signal quartets or to two adjacent maxima or minima in the dispersion curve (Fig. 2).

Equation (1) is identical to the relation determining the critical frequency of the first normal wave in a surface or underwater sound channel:

$$f = 3(l - 1/2)C_0/8h(ah)^{0.5},$$

where h is the thickness of the surface waveguide, a is the relative sound speed gradient given by the relation $\tilde{a} = \Delta C/C_0\Delta h$, C_0 is the sound speed at the channel axis, and l is the ordinal number of the normal wave. For the underwater channel with a bilinear sound speed profile, $\tilde{a}$ is the effective relative gradient of the sound speed

$$1/\tilde{a} = 1/\tilde{a}_1 + 1/\tilde{a}_2,$$

where $\tilde{a}_1$ and $\tilde{a}_2$ are the relative gradients in the layers above and below the channel axis, $h = h_1 + h_2$ is the total channel thickness, and h_1 and h_2 are the thicknesses of the above-axis and below-axis water layers, respectively.

To obtain a steady-state dispersion at a certain frequency, a sufficiently long distance is required starting from which the wave process can be treated as a steady-state one. To meet the conditions for the in-phase summation of the components and the development of the dispersion, it is necessary for the differences in arrival times of successive signals to be equal to π at a given frequency and for the differences in arrival times of signals traveling over adjacent rays to tend to zero; i.e.,

$$\Delta t_1 - \Delta t_2 = |\Delta t_n - \Delta t_{n-1}| - |\Delta t_{n+1} - \Delta t_n| \longrightarrow 0.$$

Within the limit, these conditions can be met only at infinity. If the differences in the arrival times of three adjacent components are less than the wave period or equal to the half-period, the out-of-phase summation takes place. As a result, the components completely suppress each other. At each frequency, a specific angular range exists within which the waves can propagate that arrive in phase or out of phase. Thus, a frequency dependent signal structure is formed in the channel. At high frequencies, the time of elongation of the signal components (with explosion-generated signals, the difference in the times of the first and last near-axis arrivals) reaches its maximum, and the number of components corresponds to the time interval calculated in the ray approximation. As the frequency decreases, the number of the signal components that contribute to the sound field also decreases down to unity, and, correspondingly, the duration of the signal set tends to zero at the critical frequency of the entire waveguide. In wave-theory calculations, the elongation time (the signal duration) is governed by the difference in the group velocities at the frequencies corresponding to the first normal wave. At a certain frequency, this time is determined by the number of relevant normal waves. The signal duration will differ for different frequencies. While at high frequency the range of characteristic angles is ±14.2° for the waveguide-captured signals, this range becomes smaller at lower frequencies and is equal to zero at the lowest critical frequency of the entire channel (we mean the refracted sound waves). The aforementioned features of underwater sound channels are important for calculating and predicting the sound fields, especially in ray-approximation computations. Thus, at high frequencies, several hundreds of rays can arrive at a receiver at ranges of hundreds and thousands of kilometers. At the same time, the low-frequency signal structure can be formed by a few signal components. These phenomena can cause errors in the sound field computations if one does not allow for the wave properties of the channel. Of course, wave-theory calculations are free from such drawbacks.

The dispersion curve obtained from the experimental data (Fig. 2) is shown in Fig. 5a. The frequency is represented by the abscissa axis. The ordinate represents the ratio of the group velocities of the first normal wave to the sound speed at the channel axis. Figure 5b presents the dependence of the duration of the signal set on the frequency for a distance of 600 km with the reception at the channel axis, and the critical frequencies for the corresponding channel thicknesses determined by the characteristic angles shown in the plot. At high frequencies, the duration of the signal set reaches 5 s, while it decreases as low as 4.15, 3.65, 2.25, and 1 s at the frequencies 100, 50, 10, and 4 Hz, respectively. The curve that approximates the critical frequencies serves as the frequency-dependent boundary for the channel filling with the components corresponding to the refracted rays; this curve bounds the domain of angles and frequencies, which allows one to use ray considerations for computing the sound field in the channel.

The recent paper by Buck *et al.* [10] studies the dispersion of normal waves by filtering them in shallow and deep seas. Kuperman *et al.* [11] consider the waveguide invariant B that governs the interference structure of the sound field in the ocean medium and the dependence of the group velocity on the phase velocity for typical oceanic environments.

The attenuation mechanisms considered above for the low- and high-frequency components in the waveguide can be summarized as follows. Every signal fraction in the dispersion curve corresponding to narrow angular and arrival-time ranges of in-phase summation of the components (the main condition for the normal wave to form) is no longer than one period of the wave at a given frequency. These limiting ranges of angles and running times are strongly influenced by various inhomogeneities and are most sensitive to weak changes in the phases of the pair of interacting components. Such a sensitivity is quite natural, because, to the left of the aforementioned signal fraction (at lower frequencies), time intervals lie where the components are summed out of phase at a close frequency, and the resultant sound field vanishes. To the right of that fraction (at higher frequencies), the components are also out of phase, and the signal is steadily suppressed to yield a decay of the signal level according to the law $J \sim r^{-4}$ [1]. Thus, the time interval at hand is highly sensitive to phase changes. For instance, to fully suppress the first normal wave at a frequency of 1000 Hz, the total difference in the propagation paths of the two components should be as small as 0.75 m. Separate unphased components characterized by a spherical spread are not subject to such strict constraints and exhibit low losses. The phase-caused suppression of the near-axis coherent components completely excludes them from the propagation process and determines the critical frequencies for the corresponding waveguide thicknesses.

At frequencies that are higher than the critical ones, strong attenuation of the near-axis components is caused by the processes of prereverberation, forward scattering, and absorption in the inhomogeneous medium. The near-axis components, which propagate along short ray cycles and do not penetrate to deep horizons, travel all the time in water layers where intense turbulent mixing occurs. The inhomogeneities of temperature, density, and sound speed lead to additional attenuation and scattering, which were well studied by Liebermann [12], Mintzer [13], Potter and Murphy [14], Chernov [15], and many others. The components that are summed in phase to form a normal wave at lower frequencies travel mainly in deep water layers in which nearly no inhomogeneities are present, and the additional energy losses caused by scattering and absorption are vanishingly small. The path traveled by these components in near-surface inhomogeneous layers is short in comparison with the total length of deep-water ray cycles. For these components with large characteristic angles, the scattering diagram is much narrower than for the near-axis components.

The aforementioned origin of the higher attenuation of the near-axis components in the high-frequency part of the spectrum (due to the inhomogeneities concentrated near the channel axis) lead to a frequency-angular dependence of the effective absorption coefficient that was previously unknown for an underwater sound channel. The absolute values of such losses far exceed those caused by dissipative processes. As the frequency increases, the effect of additional attenuation becomes stronger.

The experimental data presented in this paper reveal a variety of phenomena governing the structure of the sound field in the channel in a broad frequency band, including the random processes caused by the channel inhomogeneities. The data also lead to the conclusion that, in randomly inhomogeneous waveguides, the method of summing the energies of the signal components, in view of the prereverberation and scattered signals, can be most fruitful.

ACKNOWLEDGMENTS

This work was supported by the Russian Foundation for Basic Research, project nos. 99-02-18359 and 01-02-16636.

REFERENCES

1. L. M. Brekhovskikh, *Waves in Layered Media*, 2nd ed. (Nauka, Moscow, 1973; Academic, New York, 1960).
2. N. V. Studenichnik, in *Abstracts of 9th All-Union Acoustical Conference, Section D* (Acoustics Inst., USSR Academy of Sciences, Moscow, 1977), p. 45.
3. L. M. Brekhovskikh, Yu. P. Lysanov, and N. V. Studenichnik, Dokl. Akad. Nauk SSSR **239** (1), 211 (1978).
4. N. V. Studenichnik, in *Proceedings of Third Seminar on Acoustic Statistical Models of the Ocean* (Acoustics Inst., USSR Academy of Sciences, Moscow, 1981), p. 48.

5. N. V. Studenichnik, in *Proceedings of Fourth Seminar on Acoustic Statistical Models of the Ocean* (Acoustics Inst., USSR Academy of Sciences, Moscow, 1982), p. 19.
6. N. V. Studenichnik, in *Proceedings of Thirteenth All-Union School–Seminar on Statistical Hydroacoustics* (Acoustics Inst., USSR Academy of Sciences, Moscow, 1984), p. 29.
7. N. V. Studenichnik, Vopr. Sudostr., Ser. Akust., No. 18, 39 (1984).
8. C. L. Pekeris, Mem.–Geol. Soc. Am. **27** (October 15, 1948).
9. A. C. Kiblewhite and R. N. Denham, J. Acoust. Soc. Am. **1**, 63 (1965).
10. J. R. Buck, J. C. Preisig, and K. E. Wage, J. Acoust. Soc. Am. **103**, 1813 (1998).
11. W. A. Kuperman, G. L. D’Spain, Hee Chun Song, and A. M. Thode, J. Acoust. Soc. Am. **105**, 983 (1999).
12. L. Liebermann, J. Acoust. Soc. Am. **23**, 563 (1951).
13. D. Mintzer, J. Acoust. Soc. Am. **25**, 922 (1953).
14. D. S. Potter and S. R. Murphy, J. Acoust. Soc. Am. **29**, 197 (1957).
15. L. A. Chernov, *Wave Propagation in a Random Medium* (Akad. Nauk SSSR, Moscow, 1958; McGraw-Hill, New York, 1960).

Translated by E. Kopyl

Acoustical Physics, Vol. 48, No. 5, 2002, pp. 607–617. Translated from Akusticheskiĭ Zhurnal, Vol. 48, No. 5, 2002, pp. 684–694.
Original Russian Text Copyright © 2002 by Shenderov.

Diffraction of Sound by an Elastic or Impedance Sphere Located near an Impedance or Elastic Boundary of a Halfspace[1]

E. L. Shenderov†
Morfizpribor Central Research Institute, Chkalovskiĭ pr. 46, St. Petersburg, 197376 Russia
e-mail: shend@peterlink.ru

Received November 29, 2001

Abstract—An exact solution is obtained to the problem of sound diffraction by an elastic or impedance sphere located near an impedance or elastic boundary of a halfspace. The problem is solved using the Helmholtz integral equation in which the field of a point source in the halfspace with an elastic boundary is used as the Green function. The diffracted field is represented as a series expansion in spherical harmonics. The expansion coefficients are determined from a set of independent algebraic systems of equations. The matrix coefficients of these systems are determined as integrals of the products of the associated Legendre polynomials on the complex plane with respect to the real and complex angles of the sound incidence on the halfspace boundary. To decrease the number of such integrals, expansions using the Klebsh–Gordon coefficients are applied. As a result, algorithms for calculating the scattered field in the halfspace are obtained. *© 2002 MAIK "Nauka/Interperiodica".*

The scattering of a plane sound wave by a sphere near a hard or soft screen was investigated in [1]. This problem was considered in terms of the scattering by two spheres with the use of the addition theorem. Reviews of publications related to the scattering by many objects and, in particular, by two spheres can be found in [1, 2]. It was shown [1] that the calculation of the Klebsh–Gordon coefficients appearing in the addition theorem for spherical harmonics presents the main difficulty in obtaining a numerical solution for the scattered field. This paper offers an efficient method for calculating these coefficients, as well as the algorithms for calculating the scattered field in the halfspace.

If the screen is neither acoustically hard nor acoustically soft, the problem cannot be reduced to the scattering by two spheres. In this case, other methods should be used. The consideration presented below is concerned with the sound scattering by an impedance or elastic sphere located near an impedance or elastic halfspace. The surface of the halfspace may be covered by an elastic plate. The sphere may exhibit either impedance or elastic properties. In particular, it may be covered by an elastic shell.

To illustrate the suggested method and to introduce the notation, two approaches to the solution of a simple and well-known problem of the diffraction of a plane sound wave by an impedance sphere are presented below.

CLASSICAL SOLUTION

Let a plane wave with the wave vector **k** be incident on a sphere (Fig. 1a). The vector **k** is assumed to lie in the *xz* plane, so that $\varphi_0 = 0$. For an isolated sphere, one can set $\theta_0 = 0$; however, if this sphere is located near a screen, one should consider the case with $\theta_0 \neq 0$. Hence, the direction of the wave incidence does not coincide with the direction of the *z* axis in this example. We represent the total sound pressure in the form

$$p = p_{\mathrm{i}} + p_{\mathrm{s}}, \tag{1}$$

where

$$p_{\mathrm{i}} = \exp[-ik(x_1\sin\theta_0 + z_1\cos\theta_0)], \tag{2}$$

or (see, e.g., [2])

$$p_{\mathrm{i}} = 2\sum_{n=0}^{\infty}\sum_{m=-n}^{n}\frac{(-i)^n}{N_{mn}}j_n(kr_1) \times P_n^m(\cos\theta_0)P_n^m(\cos\theta_1)\exp(im\varphi_1), \tag{3}$$

$$p_{\mathrm{s}} = \sum_{n=0}^{\infty}\sum_{m=-n}^{n}b_{mn}h_n^{(1)}(kr_1)P_n^m(\cos\theta_1)\exp(im\varphi_1), \tag{4}$$

where r_1, θ_1, and φ_1 are the coordinates of the observation point; b_{mn} are the unknown coefficients; and

$$N_{mn} = \frac{2}{2n+1}\frac{(n+m)!}{(n-m)!}. \tag{5}$$

The total sound pressure *p* is related to the normal velocity ν through the relationship

$$\frac{\partial p}{\partial r_1} = i\omega\rho\nu. \tag{6}$$

---

†Deceased.

[1] The paper was prepared for publication by M.D. Smaryshev and V.E. Glasanov.

1063-7710/02/4805-0607$22.00 © 2002 MAIK "Nauka/Interperiodica"

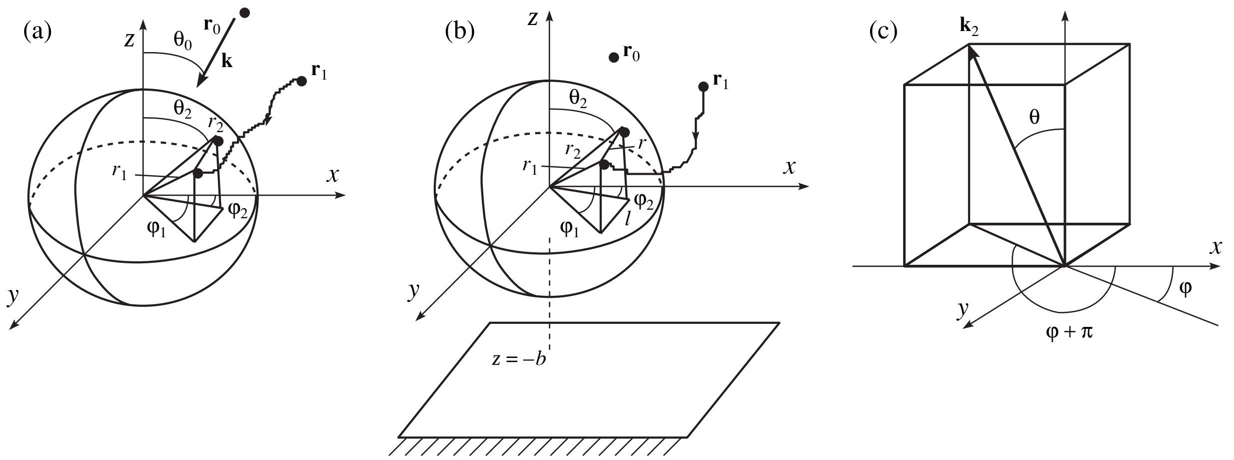

Fig. 1. Coordinate systems for (a) the diffraction of a plane wave by a sphere in the free space, (b) the diffraction of a spherical wave by a sphere located near the surface of a halfspace, and (c) the vector $\mathbf{k}_2$ in Eq. (23).

We represent these quantities on the sphere surface in the form of the following series expansions:

$$p = \sum_{n=0}^{\infty} \sum_{m=-n}^{n} a_{mn} P_n^m(\cos\theta_1) \exp(im\varphi_1), \tag{7a}$$

$$\nu = \sum_{n=0}^{\infty} \sum_{m=-n}^{n} \nu_{mn} P_n^m(\cos\theta_1) \exp(im\varphi_1). \tag{7b}$$

The coefficients a_{mn} and ν_{mn} are related as follows:

$$a_{mn}/\nu_{mn} = -w_n, \tag{7c}$$

where w_n are the sphere impedances normalized by the product ρc taken for the surrounding medium. These impedances are independent of the spherical harmonic number when the sphere surface is described by a normal impedance. Conversely, in the case of an elastic sphere (e.g., an elastic shell), the impedances depend on the aforementioned number. It should be noted that, to describe the motion of the sphere, it is necessary to know the mechanical impedances of only axially symmetric modes even in the case of an axially asymmetric excitation. Hence, the impedances depend only on the number n and are independent of the number m. Such impedances of spherical shells for different exact and approximate models can be found in [3, 4].

From Eqs. (1)–(7), one can obtain the coefficients

$$b_{mn} = -2\frac{(-i)^n}{N_{mn}} P_n^m(\cos\theta_0) \frac{j_n(ka) - iw_n j_n'(ka)}{h_n^{(1)}(ka) - iw_n h_n^{(1)'}(ka)}. \tag{8}$$

With the use of the identity

$$j_n'(ka) h_n^{(1)}(ka) - h_n^{(1)'}(ka) j_n(ka) = -i/(ka)^2, \tag{9}$$

from Eqs. (3), (4), and (8), we obtain

$$a_{mn} = 2\frac{(-i)^n}{N_{mn}} P_n^m(\cos\theta_0) \times \frac{w_n}{(ka)^2 [h_n^{(1)}(ka) - iw_n h_n^{(1)'}(ka)]}. \tag{10}$$

Solution with the Use of the Helmholtz Equation

The total sound pressure must satisfy the Helmholtz equation

$$p(\mathbf{r}_1) = -ik\rho c Q G(\mathbf{r}_0, \mathbf{r}_1) + \int_S \left[p(\mathbf{r}_2) \frac{\partial G(\mathbf{r}_1, \mathbf{r}_2)}{\partial n_2} - \frac{\partial p(\mathbf{r}_2)}{\partial n_2} G(\mathbf{r}_1, \mathbf{r}_2) \right] dS_2, \tag{11}$$

where Q is the source strength, G is the Green function, $\mathbf{r}_0$ is the position of the source, $\mathbf{r}_1$ is the position of the observation point, and $\mathbf{r}_2$ is the point on the sphere surface (Fig. 1b). The subscript 2 indicates that the differentiation and integration in Eq. (11) are performed with respect to the variable $\mathbf{r}_2$. In this section, we use the free-space Green function

$$G_0 = \frac{\exp(ikr)}{4\pi r}, \tag{12}$$

where $r = |\mathbf{r}_0 - \mathbf{r}_1|$ for the first term on the right-hand side of Eq. (11) and $r = |\mathbf{r}_1 - \mathbf{r}_2|$ for the integrand. Since we consider a plane wave, we can set $r \gg a$ in the first term on the right-hand side. Then, we have

$$kr \approx kr_0 - (\mathbf{k} \times \mathbf{r}_1) = kr_0 - k(x_1 \sin\theta_0 + z_1 \cos\theta_0).$$

Thus, the first term takes on the form $-ik\rho c Q \times \frac{\exp(ikr_0)}{4\pi r_0} \exp(-i\mathbf{k} \times \mathbf{r}_1)$. Assuming that the source generates the incident wave of unit amplitude, we obtain the first term in the form coincident with Eq. (2).

On the sphere surface, we have

$$\frac{\partial p_2}{\partial n_2} = i\omega\rho v_2, \tag{13}$$

where p_2 and v_2 are obtained from Eqs. (7a) and (7b) by replacing the subscript 1 with the subscript 2. Then, we can rewrite Eq. (11) in the form

$$\begin{aligned} p(\mathbf{r}_1) = {} & \exp(-i\mathbf{k}\times\mathbf{r}_1) + \int\limits_S \sum_{n=0}^{\infty}\sum_{m=-n}^{n} a_{mn}P_n^m(\cos\theta_2) \\ & \times\cos(m\varphi_2)\left[\frac{\partial G(\mathbf{r}_1,\mathbf{r}_2)}{\partial n_2} + \frac{ik}{w_n}G(\mathbf{r}_1,\mathbf{r}_2)\right]dS_2. \end{aligned} \tag{14}$$

In this section, we will use expression (12) as the Green function in the integrand with both points located at the sphere surface. However, differentiating with respect to n_2 requires that we first write the Green function for different $\mathbf{r}_1$ and $\mathbf{r}_2$. If $\mathbf{r}$ is the vector whose ends are described by the spherical coordinates ($\mathbf{r}_1$, θ_1, φ_1) and ($\mathbf{r}_2$, θ_2, φ_2), we have [2]

$$\begin{aligned} G_0 = {} & \frac{ik}{2\pi}\sum_{n=0}^{\infty}\sum_{m=-n}^{n}\frac{1}{N_{mn}}P_n^m(\cos\theta_1)P_n^m(\cos\theta_2) \\ & \times\exp[im(\varphi_1-\varphi_2)]\begin{cases} j_n(kr_1)h_n^{(1)}(kr_2), & r_2 > r_1 \\ j_n(kr_2)h_n^{(1)}(kr_1), & r_1 > r_2. \end{cases} \end{aligned} \tag{15}$$

To obtain a correct result, we must first differentiate the Green function at the integration points $\mathbf{r}_2$ and then set the observation point $\mathbf{r}_1$ tending to the surface. Consequently, we must assume that $r_1 > r_2$ and take the lower row of Eq. (14). Note that series (15) is divergent at $r_1 = r_2 = a$; however, this fact does not prevent us from obtaining the solution, because we can assume that r_1 is somewhat greater than r_2 in the intermediate rearrangements. In this case, the series converges, so that we can reduce the orders of summation and integration and set $r_1 = a$ only in the final expressions.

Substituting Eqs. (3), (7a), (7b), (13), and (15) in Eq. (14), we obtain

$$\begin{aligned} & \sum_{n=0}^{\infty}\sum_{m=-n}^{n} a_{mn}P_n^m(\cos\theta_1)\exp(im\varphi_1) \\ & = 2\sum_{n=0}^{\infty}\sum_{m=-n}^{n}\frac{(-i)^n}{N_{mn}}j_n(ka)P_n^m(\cos\theta_0)P_n^m(\cos\theta_1) \\ & \times\exp(im\varphi_1) + \frac{i(ka)^2}{2\pi}\int_0^{\pi}\int_0^{2\pi}\sum_{q=0}^{\infty}\sum_{s=-q}^{q} a_{sq}P_q^s(\cos\theta_2) \\ & \times\exp(is\varphi_2)\sum_{n=0}^{\infty}\sum_{m=-n}^{n}\frac{1}{N_{mn}}\left[j_n'(ka) + \frac{i}{w_n}j_n(ka)\right] \\ & \times h_n^{(1)}(ka)P_n^m(\cos\theta_1)P_n^m(\cos\theta_2) \\ & \times\exp[im(\varphi_1-\varphi_2)]\sin\theta_2 d\theta_2 d\varphi_2. \end{aligned}$$

Taking into account the orthogonality of the spherical harmonics, we arrive at the expressions

$$\begin{aligned} & \int_0^{\pi} P_q^s(\cos\theta_2)P_n^m(\cos\theta_2)\sin\theta_2 d\theta_2 \\ & = \begin{cases} N_{mn}, & m = s, \quad n = q \\ 0 & \text{for other } m \text{ and } n, \end{cases} \end{aligned} \tag{16a}$$

$$\int_0^{2\pi}\exp[i(s-m)\varphi_2]d\varphi_2 = \begin{cases} 2\pi, & s = m \\ 0, & s \ne m. \end{cases} \tag{16b}$$

Equating the coefficients of the harmonics with identical indices, we represent the coefficients in the form

$$\begin{aligned} a_{mn} = {} & 2\frac{(-i)^n}{N_{mn}}j_n(ka)P_n^m(\cos\theta_0) \\ & + i(ka)^2 a_{mn}h_n^{(1)}(ka)\left[j_n'(ka) + \frac{i}{w_n}j_n(ka)\right]. \end{aligned}$$

Applying identity (9) to the expression in square brackets, we obtain Eq. (10).

The calculations with this approach are longer than the classical solution. However, it allows one to solve more complicated problems for a sphere located near a plane screen.

Solution for a Sphere Located near a Screen

The following boundary condition can be written for the screen surface:

$$p = -\frac{w_p}{ik}\frac{\partial p}{\partial z}\bigg|_{z=-b}, \tag{17}$$

where w_p is the normalized impedance of the plane surface. The reflection coefficient of the screen is

$$A(\theta) = \frac{w_p\cos\theta - 1}{w_p\cos\theta + 1}. \tag{18}$$

This expression does not restrict the further consideration to surfaces with a normal impedance. Under the assumption that the impedance w_p is a function of the angle of incidence θ, all expressions remain valid not only for the impedance plane, but also for an arbitrary elastic surface. For example, in the case of a liquid–liquid interface, we can write

$$\begin{aligned} w_p = w_1/\cos\theta_1, \quad w_1 = \rho_1 c_1/(\rho c), \\ \cos\theta_1 = \sqrt{1-(c_1/c)^2\sin^2\theta}, \end{aligned} \tag{19a}$$

where the subscript 1 refers to the parameters of the medium in the lower halfspace.

For a liquid–solid interface, we have

$$w_p = w_l \cos^2 2\theta_t/\cos\theta_t + w_t \sin^2 2\theta_t/\cos\theta_t, \qquad (19b)$$

where

$$w_l = \rho_1 c_l/(\rho c); \quad w_t = \rho_1 c_t/(\rho c),$$
$$\cos\theta_l = \sqrt{1-(c_l/c)^2\sin^2\theta},$$
$$\cos\theta_t = \sqrt{1-(c_t/c)^2\sin^2\theta},$$

and the subscripts *l* and *t* indicate the parameters of the longitudinal and transverse waves, respectively, in the lower halfspace.

For a thin elastic plate positioned at a liquid–liquid interface, we obtain

$$w_p = \{-i\omega M[1-(c_b/c)^4\sin^4\theta] + \rho_1 c_1/\cos\theta_1\}/(\rho c), \qquad (19c)$$

where $M = \rho_m h_m$ is the surface density of the plate, c_b is the velocity of the bending wave, and the subscript 1 indicates the parameters of the medium in the lower halfspace.

In all the examples presented above, the angle θ should be determined not only for real but also for complex values.

We use Eq. (11) and represent the integral as the sum $\int_{S_{\text{sph}}} + \int_{S_{\text{pl}}}$, where S_{sph} and S_{pl} denote the sphere surface and the plane surface, respectively. We chose the Green function to satisfy the boundary condition at the plane surface

$$G = -\frac{w_p}{ik}\frac{\partial G}{\partial z}\bigg|_{z=-b}, \qquad (20)$$

which coincides with the boundary condition for the sound pressure. In this case, the integral over the plane disappears, and we can integrate only over the sphere surface.

Now, we present several forms of the Green function. Consider a vector of length *r* between two points with the respective coordinates

$$x_1 = r_1\sin\theta_1\cos\varphi_1, \quad y_1 = r_1\sin\theta_1\sin\varphi_1, \quad z_1 = r_1\cos\theta_1 \text{ and}$$

$$x_2 = r_2\sin\theta_2\cos\varphi_2, \quad y_2 = r_2\sin\theta_2\sin\varphi_2, \quad z_2 = r_2\cos\theta_2$$

(Fig. 1b). For the free space, the Green function can be represented in the form [5]

$$G_0 = \frac{\exp(ikr)}{4\pi r} = \frac{ik}{8\pi^2}\int_0^{\pi/2-i\infty}\int_0^{2\pi}\exp\{ik[\alpha(x_1-x_2) + \beta(y_1-y_2) + \gamma|z_1-z_2|]\}\sin\theta\, d\theta\, d\varphi, \qquad (21)$$

where $\alpha = k\sin\theta\cos\varphi$, $\beta = k\sin\theta\sin\varphi$, and $\gamma = k\cos\theta$. The angles θ and φ determine the direction of an elementary plane wave, including the case of complex-valued angles θ. Every plane wave is reflected from the screen with the reflection coefficient given by Eq. (18) and a phase shift of $2ib\gamma$. Hence, the Green function for an elastic halfspace can be written in the form

$$G = \frac{ik}{8\pi^2}\int_0^{\pi/2-i\infty}\int_0^{2\pi}\exp\{ik[\alpha(x_1-x_2)+\beta(y_1-y_2)]\} \times [\exp(i\gamma|z_1-z_2|) + A(\theta)\exp(i\gamma(z_1+z_2+2b))] \times \sin\theta\, d\theta\, d\varphi. \qquad (22a)$$

The exponent in the second term is not negative, and we can omit the sign of the absolute value. It can be easily verified that the function determined by Eq. (22a) satisfies boundary condition (20).

Now, we write several useful representations of the Green function. We rearrange the first factor in the integrand of expression (22a) into the form $\exp(ikl\sin\theta\cos(\varphi - \psi))$, where $l = \sqrt{l_1^2 + l_2^2 - 2l_1l_2\cos(\varphi_1-\varphi_2)}$ is the projection of *r* on the *xy* plane; $\cos\psi = (x_1 - x_2)/l$; and l_1 and l_2 are the projections of r_1 and r_2, respectively. Then, we use the expression

$$\int_0^{2\pi}\exp(ikl\sin\theta\cos(\varphi-\psi))\,d\varphi = 2\pi J_0(kl\sin\theta)$$

to obtain

$$G = \frac{ik}{4\pi}\int_0^{\pi/2-i\infty} J_0(kl\sin\theta)[\exp(ik|z_1-z_2|\cos\theta) + A(\theta)\exp(ik(z_1+z_2+2b)\cos\theta)]\sin\theta\, d\theta.$$

Using the formulas $J_0 = (H_0^{(1)} + H_0^{(2)})/2$ and $H_0^{(2)}(-u) = H_0^{(1)}(u)$, we can reduce the latter integral to an integral along a symmetric path [5]:

$$G = \frac{ik}{8\pi}\int_{-\pi/2+i\infty}^{\pi/2-i\infty} H_0^{(1)}(kl\sin\theta)[\exp(ik|z_1-z_2|\cos\theta) + A(\theta)\exp(ik(z_1+z_2+2b)\cos\theta)]\sin\theta\, d\theta. \qquad (22b)$$

Now, we represent the Green function in the form of a series expansion in spherical harmonics. We write Eq. (22a) as $G = G_0 + G_1$, where G_0 is the Green function given by Eq. (21) for free space and G_1 is the remainder. The first term is determined by Eq. (15) in which the lower row is used. Consider the second term and represent it in the form

$$G_1 = \frac{ik}{8\pi^2}\int\limits_0^{\pi/2-i\infty} A(\theta)\exp(i2\gamma b) \times \int\limits_0^{2\pi}\exp(i\mathbf{k}\times\mathbf{r}_1)\exp(i\mathbf{k}\times\mathbf{r}_2)\sin\theta d\theta d\varphi, \tag{23}$$

where the vector $\mathbf{k}_2$ is directed as shown in Fig. 1c. In the integrand, plane waves can be represented in the form of the following expansions:

$$\exp(i\mathbf{k}\times\mathbf{r}_1) = 2\sum_{n=0}^{\infty}\sum_{m=-n}^{n}\frac{i^n}{N_{mn}}j_n(kr_1) \times P_n^m(\cos\theta)P_n^m(\cos\theta_1)\exp[m(\varphi_1-\varphi)],$$

$$\exp(i\mathbf{k}\times\mathbf{r}_2) = 2\sum_{n=0}^{\infty}\sum_{m=-n}^{n}\frac{i^n}{N_{mn}}j_n(kr_2) \times P_n^m(\cos\theta)P_n^m(\cos\theta_2)\exp[im(\varphi_2-\varphi+\pi)].$$

Substituting these two expressions in Eq. (23), we replace the summation indices n, m with n_1, m_1 and n_2, m_2 and use Eq. (16b). Then, only the terms with $m_1 = -m_2 = m$ will be retained, and one of sums will disappear. Using the formula

$$P_n^{-m}(x) = (-1)^m\frac{(n-m)!}{(n+m)!}P_n^m(x), \tag{24}$$

we obtain

$$G_1 = \frac{ik}{\pi}\sum_{n_1=0}^{\infty}i^{n_1}j_{n_1}(kr_1)\sum_{n_2=0}^{\infty}i^{n_2}j_{n_2}(kr_2)\sum_{m=-n_{\min}}^{n_{\min}}(-1)^m \times \frac{f^m_{n_1,n_2}}{N_{mn_1}N_{mn_2}}P^m_{n_1}(\cos\theta_1)P^m_{n_2}(\cos\theta_2)\exp[im(\varphi_1-\varphi_2)], \tag{25}$$

where

$$f^m_{n_1,n_2} = \int\limits_0^{\pi/2-i\infty}A(\theta)P^m_{n_1}(\cos\theta)P^m_{n_2}(\cos\theta) \times \exp(i2kb\cos\theta)\sin\theta d\theta. \tag{26}$$

To determine the values of n_1 and n_2, we use the fact that the index $|m|$ cannot exceed the minimal values of n_1 and n_2. Thus, the summation runs in the region $m = \pm n_{\min}$, where $n_{\min} = \mathrm{Min}(n_1, n_2)$. Using Eq. (15) with the lower row and Eq. (25), we replace n_2 with n to obtain

$$G = \frac{ik}{2\pi}\sum_{n=0}^{\infty}\sum_{m=-n_{\min}}^{n_{\min}}\frac{1}{N_{mn}}j_n(kr_2)P_n^m(\cos\theta_2) \times \exp[im(\varphi_1-\varphi_2)][h_n^{(1)}(kr_1)P_n^m(\cos\theta_1) + 2i^n(-1)^m s_{nm}(r_1,\theta_1)] \quad (r_1 > r_2), \tag{27a}$$

where

$$s_{mn}(r,\theta) = \sum_{n_1=0}^{\infty}i^{n_1}j_{n_1}(kr)\frac{f^m_{n_1,n}}{N_{mn_1}}P^m_{n_1}(\cos\theta). \tag{27b}$$

In the case $r_2 > r_1$, we should use formula (15) with the upper row. Then, we obtain

$$G = \frac{ik}{2\pi}\sum_{n=0}^{\infty}\sum_{m=-n_{\min}}^{n_{\min}}\frac{1}{N_{mn}}j_n(kr_1)P_n^m(\cos\theta_1) \times \exp[im(\varphi_1-\varphi_2)][h_n^{(1)}(kr_2)P_n^m(\cos\theta_2) + 2i^n(-1)^m s_{nm}(r_2,\theta_2)] \quad (r_2 > r_1). \tag{27c}$$

Now, let us represent the total sound field on the sphere surface as the expansion

$$p(\mathbf{r}_{1,2}) = \sum_{n=0}^{\infty}\sum_{n=-m}^{m}a_{mn}P_n^m(\cos\theta_{1,2})\exp(im\varphi_{1,2}), \tag{28}$$

where the subscript 1 refers to the observation point on the sphere surface and the subscript 2 refers to the integration point on this surface. Using boundary conditions (7b), from Eq. (11) we obtain

$$p(\mathbf{r}_1) = -ik\rho cQG(\mathbf{r}_0,\mathbf{r}_1) + \int\limits_{S_{\mathrm{sph}}}\sum_{n=0}^{\infty}\sum_{m=-n}^{n}a_{mn} \times P_n^m(\cos\theta_2)\exp(im\varphi_2)\left[\frac{\partial G(\mathbf{r}_1,\mathbf{r}_2)}{\partial n_2} + \frac{ik}{w_n}G(\mathbf{r}_1,\mathbf{r}_2)\right]dS_2. \tag{29}$$

Let the point $\mathbf{r}_1$ tend to the sphere surface. Substituting Eq. (27a) in integral (29) and replacing m and n in the first sum with q and s, respectively, we obtain

$$\int\limits_{\mathrm{sph}} = \frac{i(ka)^2}{2\pi}\int\limits_0^{\pi}\int\limits_0^{2\pi}\sum_{q=0}^{\infty}\sum_{s=-q}^{q}a_{sq}P_q^s(\cos\theta_2)\exp(is\varphi_2) \times \sum_{n=0}^{\infty}\sum_{m=-n_{\min}}^{n_{\min}}\frac{1}{N_{mn}}P_n^m(\cos\theta_2)\left[j_n'(ka) + \frac{i}{w_n}j_n(ka)\right] \times \exp[im(\varphi_1-\varphi_2)][h_n^{(1)}(ka)P_n^m(\cos\theta_1) + 2i^n(-1)^m s_{mn}(a,\theta_1)]\sin\theta_2 d\theta_2 d\varphi_2.$$

The integration with respect to θ_2 and φ_2 is carried out with the use of the orthogonality of spherical harmonics [see Eqs. (16a) and (16b)]. Then, two sums disappear, and we have

$$\int\limits_{\text{sph}} = i(ka)^2\sum_{n=0}^{\infty}\sum_{m=-n_{\min}}^{n_{\min}} a_{mn}\left[j'_n(ka)+\frac{i}{w_n}j_n(ka)\right] \tag{30}$$
$$\times\exp(im\varphi_1)[h_n^{(1)}(ka)P_n^m(\cos\theta_1)+2i^n(-1)^m s_{mn}(a,\theta_1)].$$

Substituting Eqs. (27a), (28), and (30) in Eq. (29), we obtain the relationship

$$\sum_{n=0}^{\infty}\sum_{m=-n}^{n} a_{mn}P_n^m(\cos\theta_1)\exp(im\varphi_1) = \frac{k^2\rho cQ}{2\pi}$$
$$\times\sum_{n=0}^{\infty}\sum_{m=-n_{\min}}^{n_{\min}}\frac{1}{N_{mn}}j_n(ka)P_n^m(\cos\theta_1)\exp(im(\varphi_0-\varphi_1))$$
$$\times[h_n^{(1)}(kr_0)P_n^m(\cos\theta_0)+2i^n(-1)^m s_{mn}(r_0,\theta_0)$$
$$+i(ka)^2\sum_{n=0}^{\infty}\sum_{m=-n}^{n} a_{mn}\left[j'_n(ka)+\frac{i}{w_n}j_n(ka)\right] \tag{31}$$
$$\times h_n^{(1)}(ka)P_n^m(\cos\theta_1)\exp(im\varphi_1)$$
$$+i(ka)^2\sum_{n=0}^{\infty}\sum_{m=-n_{\min}}^{n_{\min}} a_{mn}\left[j'_n(ka)+\frac{i}{w_n}j_n(ka)\right]$$
$$\times\exp(im\varphi_1)2i^n(-1)^m s_{mn}(a,\theta_1).$$

Let us perform the following rearrangements:

(i) Normalize the sound pressure in the incident and scattered waves by the sound pressure generated by the source in free space at the distance r_0, i.e., divide the first term on the right-hand side by

$$p_0 = -ik\rho cQ\frac{\exp(ikr_0)}{4\pi r_0}. \tag{32}$$

(ii) Replace n with q and then n_1 with n in the threefold sum containing the factor $s_{mn}(a, \theta_1)$.

(iii) Replace m with $-m$ in the sums containing the factor $\exp[(im(\varphi_0 - \varphi_1)]$ and take into consideration Eqs. (5) and (24). Equating the coefficients of spherical harmonics $P_n^m(\cos\theta_1)\exp(im\varphi_1)$ with the same indices, we obtain

$$a_{mn} = \frac{1}{N_{mn}}i2kr_0j_n(ka)\exp(-ikr_0)\exp(-im\varphi_0)$$
$$\times[h_n^{(1)}(kr_0)P_n^m(\cos\theta_0)+2i^n(-1)^m s_{nm}(r_0,\theta_0)]$$
$$+i(ka)^2a_{mn}\left[j'_n(ka)+\frac{i}{w_n}j_n(ka)\right]h_n^{(1)}(ka)$$
$$+2i(ka)^2i^nj_n(ka)(-1)^m$$
$$\times\sum_{q=0}^{\infty}i^qa_{mq}\left[j'_q(ka)+\frac{i}{w_n}j_q(ka)\right]\frac{f_{q,n}^m}{N_{mn}}.$$

Using identity (9), after some rearrangements we obtain the system of algebraic equations

$$\sum_{q=0}^{\infty}a_{mq}Z_{q,n}^m = c_{mn},\quad n = (0, 1, \ldots\infty), \tag{33}$$
$$m = (-\mathrm{Min}(q,n), \ldots\mathrm{Min}(q,n));$$

$$Z_{q,n}^m = 2i^{n+q}(-1)^m$$
$$\times\frac{j_q(ka)-iw_aj'_q(ka)}{h_n^{(1)}(ka)-iw_ah_n^{(1)'}(ka)}\frac{f_{q,n}^m}{N_{mn}}+\delta_{qn}; \tag{34}$$

$$c_{mn} = \frac{2ikr_0\exp(-ikr_0)\exp(-im\varphi_0)}{(ka)^2N_{mn}}$$
$$\times\frac{w_n}{h_n^{(1)}(ka)-iw_nh_n^{(1)'}(ka)} \tag{35a}$$
$$\times[h_n(kr_0)P_n^m(\cos\theta_0)+2i^n(-1)^m s_{mn}(r_0,\theta_0)],$$

where δ_{qn} is the Kronecker delta. Without the loss of generality, we can assume that the source lies in the xz plane, i.e., $\varphi_0 = 0$. In this case, using Eqs. (5), (24), and (33) and introducing new coefficients $\tilde{a}_{mn} = a_{mn}P_n^m(\cos\theta_1)$, one can show that the terms in Eq. (33) are symmetric under the transformation $m \longrightarrow -m$. Thus, we can limit our consideration to the values of m from the interval (0, min(q, n)).

As a result, we obtain a set of independent systems of equations of different orders. The first system corresponding to $m = 0$ has all rows and columns. In the second system corresponding to $m = 1$, the first row and the first column are absent. In the third system corresponding to $m = 2$, two rows and two columns are absent, and so on. If we limit the maximal value of n by the value $n_{\max}$, the last system corresponding to $m = n_{\max}$ will contain only one term in which m–n–q–$n_{\max}$.

If the screen is absent, we should set $A(\theta_0) = A(\theta_1) = 0$. The coefficients $f^m_{q,n}$ disappear, and the systems retain only the diagonal terms from Eq. (33). In this case, we obtain Eq. (10) for a sphere in the free space.

In matrix (34), the elements are independent of both the source position and the observation point position. Equation (35a) holds for a spherical incident wave. To obtain the solution for a plane incident wave, we set the source position tending to infinity. The details of the corresponding transformation are given in the Appendix. For a plane incident wave, we obtain

$$c_{mn} = \frac{2(-i)^n}{(ka)^2 N_{mn}}\frac{w_n}{h_n^{(1)}(ka) - iw_n h_n^{(1)\prime}(ka)} \qquad (35b)$$

$$\times P_n^m(\cos\theta_0)[1 + (-1)^{m+n}A(\theta_0)\exp(2ikb\cos\theta_0)].$$

The determination of the coefficients $f^m_{q,n}$ given by Eq. (26) is the main difficulty in the numerical solution of system (33). The calculation of any individual coefficient is not as difficult, but the problem is that one should calculate a great number of such coefficients. Taking into account the symmetry of n_1 and n_2, every system of order N requires the determination of $N(N + 1)/2$ coefficients. Then, the total number of coefficients for all systems is determined by the series

$$\frac{1\times 2}{2} + \frac{2\times 3}{2} + \ldots + \frac{(n_{\max}+1)(n_{\max}+2)}{2} = \frac{(n_{\max}+1)(n_{\max}+2)(n_{\max}+3)}{6}.$$

For example, if $ka = 10$, one should set the value of $n_{\max}$ at about 15. Hence, one should calculate $16 \times 17 \times 18/6 = 816$ integrals. Since the angular scattering pattern is independent of the source and observation point positions, its calculation for a single value of the parameter kb requires that the coefficients be calculated only once. However, an exhaustive investigation requires that all coefficients be calculated for every point of the curve, which can result in long calculations.

The number of integrals can be considerably reduced by using the following formula for the associated Legendre polynomials:

$$P^m_{n_1}(\cos\theta)P^m_{n_2}(\cos\theta) = \sum_{n=|n_1-n_2|}^{n_1+n_2} b_n^{(n_1,m,n_2,m)}P_n(\cos\theta), \qquad (36)$$

where the coefficients

$$b_n^{(n_1,m,n_2,m)} = (-1)^m\left[\frac{(n_1+m)!(n_2+m)!}{(n_1-m)!(n_2-m)!}\right]^{1/2} \times (n_1, n_2, 0, 0|n, 0)(n_1, n_2, m, -m|n, 0) \qquad (37)$$

are expressed through the Klebsh–Gordon coefficients (see [2]). Then, integrals (22) can be rewritten in the form

$$f^m_{n_1,n_2} = \sum_{n=|n_1-n_2|}^{n_1+n_2} b_n^{(n_1,m,n_2,m)}g_n, \qquad (38)$$

where

$$g_n = \int_0^{\pi/2 - i\infty} A(\theta)P_n(\cos\theta)\exp(2ikb\cos\theta)\sin\theta d\theta. \qquad (39)$$

With the use of series (38), the calculation of only $2n_{\max} + 1$ integrals is sufficient. Such a rearrangement reduces the calculation of a great number of integrals to the calculation of the Klebsh–Gordon coefficients (see [1]).

If the boundary is hard or soft, the function $A(\theta)$ is equal to 1 or –1 and is independent of θ. Hence, it can be factored out from under the integral sign. In this case, we can use the expression [2]

$$i^n h_n^{(1)}(2kb) = \int_0^{\pi/2 - i\infty} P_n(\cos\theta)\exp(i2kb\cos\theta)\sin\theta d\theta. \qquad (40)$$

Then, from Eqs. (38) and (39) we obtain

$$f^m_{n_1,n_2} = \pm\sum_{n=|n_1-n_2|}^{n_1+n_2} i^n b_n^{(n_1,m,n_2,m)}h_n^{(1)}(2kb). \qquad (41)$$

To calculate integrals (39), we can represent them as sums $g_n = g_n^{(1)} + g_n^{(2)}$, where $g_n^{(1)}$ is the integral over the interval $(0, \pi/2)$ and $g_n^{(2)}$ is the integral over the interval $(\pi/2, \pi/2 - i\infty)$. In the expressions for $g_n^{(1)}$ and $g_n^{(2)}$, we apply the respective changes of variables $u = \cos\theta$ and $iu = \cos\theta$ in the integrands. As a result, we obtain integrals over the segments $(0, 1)$ and $(0, \infty)$, respectively:

$$g_n^{(1)} = \int_0^1 A_1(u)P_n(u)\exp(i2kbu)du; \qquad (42a)$$

$$g_n^{(2)} = -i\int_0^\infty A_2(u)P_n(iu)\exp(-2kbu)du. \qquad (42b)$$

The functions $A_{1,2}(u)$ can be represented as follows.

In the case of a liquid–liquid interface,

$$A_1(u) = \frac{w_1u - \sqrt{1-\bar{c}_1^2(1-u^2)}}{w_1u + \sqrt{1-\bar{c}_1^2(1-u^2)}}; \qquad (43a)$$

$$A_2(u) = \frac{iw_1u - \sqrt{1-\bar{c}_1^2(1+u^2)}}{iw_1u + \sqrt{1-\bar{c}_1^2(1+u^2)}}, \qquad (43b)$$

where $w_1 = \rho_1c_1/(\rho c)$ and $\bar{c}_1 = c_1/c$.

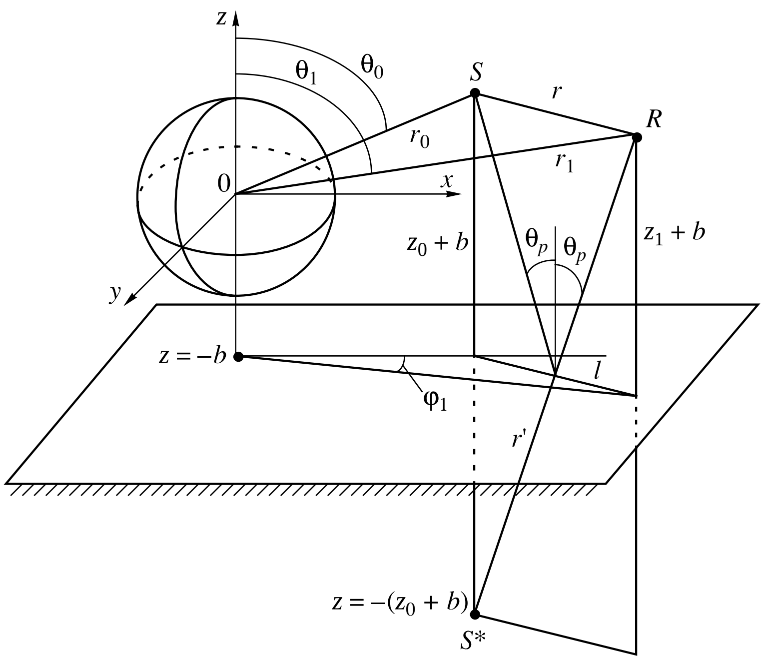

Fig. 2. Coordinate system for the calculation of the scattered and reflected sound pressure. The source S lies in the xy plane. The imaginary source is at the point S^*.

In the case of a liquid–solid interface,

$$A_1(u) = \frac{uF_1(u) - \sqrt{1 - \bar{c}_l^2(1 - u^2)}}{uF_1(u) + \sqrt{1 - \bar{c}_l^2(1 - u^2)}}, \tag{44a}$$

$$A_2(u) = \frac{iuF_2(u) - \sqrt{1 - \bar{c}_l^2(1 + u^2)}}{iuF_2(u) + \sqrt{1 - \bar{c}_l^2(1 + u^2)}}, \tag{44b}$$

where $\bar{c}_l = c_l/c$, $\bar{c}_t = c_t/c$, $w_l = \rho_1 c_l/(\rho c)$, $w_t = \rho_1 c_t/(\rho c)$, and

$$F_1(u) = w_l[1 - 2\bar{c}_l^2(1 - u^2)]^2 + 4w_t\bar{c}_t^2(1 - u^2)\sqrt{[1 - \bar{c}_l^2(1 - u^2)][1 - \bar{c}_t^2(1 - u^2)]}; \tag{45a}$$

$$F_2(u) = w_l[1 - 2\bar{c}_l^2(1 + u^2)]^2 + 4w_t\bar{c}_t^2(1 + u^2)\sqrt{[1 - \bar{c}_l^2(1 + u^2)][1 - \bar{c}_t^2(1 + u^2)]}. \tag{45b}$$

In the case of a thin elastic plate at a liquid–liquid interface,

$$A_1(\theta) = \frac{u[-iz_M(1 - \bar{c}_b^4(1 - u^2)^2)s_1(u) + w_1] - s_1(u)}{u[-iz_M(1 - \bar{c}_b^4(1 - u^2)^2)s_1(u) + w_1] + s_1(u)}; \tag{46a}$$

$$A_2(\theta) = \frac{iu[-iz_M(1 - \bar{c}_b^4(1 + u^2)^2)s_2(u) + w_1] - s_2(u)}{iu[-iz_M(1 - \bar{c}_b^4(1 + u^2)^2)s_2(u) + w_1] + s_2(u)}; \tag{46b}$$

where $\bar{c}_b = c_b/c$; $\bar{c}_1 = c_1/c$; $w_1 = \rho_1 c_1/(\rho c)$; $s_1(u) = \sqrt{1 - \bar{c}_1^2(1 - u^2)}$; $s_2(u) = \sqrt{1 - \bar{c}_1^2(1 + u^2)}$; $z_M = \omega M/(\rho c)$ and $M = \rho_m h_m$ is the surface density of the plate.

In the case of an impedance boundary,

$$A_1(\theta) = \frac{w_p u - 1}{w_p u + 1}; \tag{47a}$$

$$A_2(\theta) = \frac{iw_p u - 1}{iw_p u + 1}. \tag{47b}$$

For the liquid–liquid interface, both integrands have no poles on their integration paths, which follows from the absence of surface waves at this kind of boundary. For the boundaries of other types listed above, the denominators of the function $A_2(\theta)$ can vanish at certain points of the integration paths. Consequently, the integrands may have poles. Poles on the integration path appear either in the case of a hard lossless medium, or in the case of plates located at the liquid–vacuum interface for frequencies exceeding the critical frequency of the plate, or in the case of an impedance boundary characterized by a normally positive, purely reactive impedance (a flexible surface). These poles are related to the generation of surface waves. In all these cases, we must calculate the principal value of the integral and add half the residue at every pole. A much simpler approach is to introduce losses in the hard medium or the plate and to use complex-valued velocities of elastic waves. In this case, the poles are shifted from the integration path and cause no difficulties in the calculations.

Now, we write formulas describing the sound pressure at an arbitrary observation point $\mathbf{r}_1$ (Fig. 2). For this purpose, we use Eq. (29) and represent it as the sum of the incident wave p_i, the wave reflected from the plane in the absence of the sphere p_r, and the scattered wave p_s:

$$p(\mathbf{r}_1) = p_i(\mathbf{r}_1) + p_r(\mathbf{r}_1) + p_s(\mathbf{r}_1). \tag{48}$$

As before, we normalize all pressures by the value given in Eq. (32). The incident and reflected waves are described by the first and second terms of Eq. (22b), respectively. The normalized incident wave can be represented as follows:

$$p_i(\mathbf{r}_1) = \frac{-ik\rho cQ}{p_0}\frac{\exp(ikr)}{4\pi r}, \tag{49}$$

where p_0 is determined by Eq. (32). The quantity

$$r = (r_1^2 + r_0^2 - 2r_1 r_0 \cos(\mathbf{r}_0\ \mathbf{r}_1))^{1/2} \tag{50}$$

is the distance between the source and the observation point, where

$$\cos(\mathbf{r}_0\ \mathbf{r}_1) = \sin\theta_1 \sin\theta_0 \cos\varphi_1 + \cos\theta_0 \cos\theta_1. \tag{51}$$

Expression (49) can be simplified:

$$p_i(\mathbf{r}_1) = \frac{r_0}{r}\exp[ik(r - r_0)]. \tag{52}$$

The normalized reflected field is determined as the second term of Eq. (22b) divided by p_0:

$$\begin{aligned} r_r(\mathbf{r}_1) = \frac{ikr_0}{2}\exp(-ikr_0) \int\limits_{-\pi/2 + i\infty}^{\pi/2 - i\infty} A(\theta) H_0^{(1)}(kl\sin\theta) \\ \times \exp(ik(z_1 + z_0 + 2b)\cos\theta)\sin\theta d\theta. \end{aligned} \tag{53}$$

The integral in Eq. (29) describes the scattered field. It can be calculated by substituting Green function (27a) and expansion (28) in the integrand. Integration with respect to θ_2 and φ_2 is carried out with the use of the orthogonality of the spherical harmonics (see Eqs. (16a) and (16b)), as it was done in the derivation of Eq. (30). Then, two sums disappear, and we obtain the scattered field as

$$\begin{aligned} p_s(\mathbf{r}_1) = i(ka)^2 \sum_{n=0}^{\infty} \sum_{m=-n_{\min}}^{n_{\min}} a_{mn}\left[j'_n(ka) + \frac{i}{w_n} j_n(ka)\right] \\ \times \exp(im\varphi_1)[h_n^{(1)}(kr_1) P_n^m(\cos\theta_1) \\ + 2i^n(-1)^m s_{mn}(r_1, \theta_1)], \end{aligned} \tag{54}$$

where $n_{\min} = \mathrm{Min}(n, n_1)$ and n_1 is the summation index in Eq. (27b). Only certain changes in the arguments of the spherical Bessel and Hankel functions make the difference between this expression and Eq. (30).

If $\varphi_1 = 0$, i.e., if the observation point is located in the same vertical plane as the source and the center of the sphere, all terms of the sum with respect to the index m vanish except for the term with $m = 0$, and the threefold sum transforms to the twofold sum.

To obtain the scattering pattern in the far zone, one should assume that $kr_1 \gg 1$. Then, the integrals appearing in Eq. (54) with the factor s_{mn} can be calculated using the saddle-point method. Details of this calculation coincide with those described in the Appendix with r_0 and θ_0 replaced by r_1 and θ_1. Instead of Eq. (A5), we obtain

$$\begin{aligned} s_{mn}(r_1, \theta_1) \approx -\frac{i}{2}\frac{\exp(ikr_1)}{kr_1} A(\theta_1) \\ \times P_n^m(\cos\theta_1)\exp(2ikb\cos\theta_1) \quad (kr_1 \gg 1). \end{aligned} \tag{55}$$

Using this expression for the sum together with the identity

$$h_n^{(1)}(x) \approx (-i)^{n+1}\exp(ix)/x \quad (x \gg 1), \tag{56}$$

we obtain the scattered sound pressure in the far zone:

$$\begin{aligned} p_s \approx \frac{\exp(ikr_1)}{kr_1}(ka)^2 \sum_{n=0}^{\infty} \sum_{m=-n}^{n} a_{mn}(-i)^n \\ \times [ij_n(ka)/w_n + j'_n(ka)] P_n^m(\cos\theta_1) \\ \times [1 + (-1)^{m+n} A(\theta_1)\exp(2ikb\cos\theta_1)]\exp(im\varphi_1). \end{aligned} \tag{57}$$

As was mentioned above, $a_{-mn}P_n^{-m}(\cos\theta_1) = a_{mn}P_n^m(\cos\theta_1)$ when $\varphi_0 = 0$. In this case, the scattering pattern can be written in the form

$$f_\infty(\theta_0, \theta_1, \varphi_1) = \left|\frac{2r_1}{a} p_s\right|, \tag{58}$$

where

$$\begin{aligned} f_\infty(\theta_0, \theta_1, \varphi_1) = \Bigg| 2i(ka) \sum_{n=0}^{\infty} \sum_{m=0}^{n} (2 - \delta_{0m}) a_{mn}(-i)^n \\ \times [j_n(ka) + iw_n j'_n(ka)]/w_n P_n^m(\cos\theta_1) \\ \times [1 + (-1)^{m+n} A(\theta_1)\exp(2ikb\cos\theta_1)]\cos(m\varphi_1) \Bigg|. \end{aligned} \tag{59}$$

For an acoustically soft screen, the impedances are $w_n = 0$, and the denominator vanishes. However, the coefficients a_{mn} are proportional to the coefficients c_{mn} whose numerators contain w_n, so that the scattered field remains finite. Note that the mechanical impedances of an elastic sphere w_n depend only on the index n and are independent of the index m despite the fact that the oscillations of the sphere are axially asymmetric, except for the case with $\theta_0 = 0$. The proof of this statement can be found in [6]. Thus, all terms containing these impedances can be eliminated from the sum with respect to the index m.

The normalized sound pressure in the incident wave is described by Eq. (52). When $r_1 \gg r_0$, the distance r can be represented in the form

$$r \approx r_1 - r_0\cos(\mathbf{r}_0\ \mathbf{r}_1)\quad (r_1 \gg r_0). \tag{60}$$

In the opposite case $r_0 \gg r_1$, we deal with the diffraction of a plane wave. From Eq. (50), we have

$$r \approx r_0 - r_1\cos(\mathbf{r}_0\ \mathbf{r}_1)\quad (r_0 \gg r_1). \tag{61}$$

As a consequence, we obtain the standard expression for the plane wave

$$\begin{aligned} p_{\mathrm{i}} &= \exp(-ikr_1\cos(\mathbf{r}_0, \mathbf{r}_1)) \\ &= \exp[ik(-x_1\sin\theta_0 - z_1\cos\theta_0)]. \end{aligned} \tag{62}$$

Consider the normalized reflected wave described by Eq. (53). The integral in this expression is calculated by the saddle-point method, as described in [5]. For the far field, we can use the asymptotic properties of the Hankel functions to obtain the normalized sound pressure in the form

$$\begin{aligned} p_{\mathrm{r}} \approx \frac{ikr_0}{2}\sqrt{\frac{2}{\pi kl}}\exp(-ikr_0 - i\pi/4)\int\limits_{-\pi/2 + i\infty}^{\pi/2 - i\infty} A(\theta) \\ \times \exp[ik(l\sin\theta + (z_1 + z_2 + 2b)\cos\theta)]\sqrt{\sin\theta}\,d\theta. \end{aligned} \tag{63}$$

The saddle point θ_p is determined from the equality $\tan\theta_p = l/(z_1 + z_2 + 2b)$. The angle θ_p is the angle of incidence of the plane wave on the surface of the halfspace. As in the derivation of Eq. (35b), we calculate the integrals by neglecting the contributions of the poles that may be intersected by the integration path as a result of its transformation to the saddle-point path. It should be noted that, neglecting these poles in calculating integral (63), we do not neglect the effect of surface waves on the scattering, because integrals (26) and (39) include this effect through the definition of the coefficients a_{mn}.

As a result of the calculation, we obtain

$$p_{\mathrm{r}} = \frac{r_0}{r'}\exp(ik(r' - r_0))A(\theta_p), \tag{64}$$

where

$$r' = (l^2 + (z_0 + z_1 + 2b)^2)^{1/2} \tag{65}$$

is the distance between the observation point and the imaginary source (Fig. 2). Since $l^2 + (x_0 - x_1)^2 + y_1^2$, $r_0^2 = x_0^2 + z_0^2$, $\sin\theta_0 = x_0/r_0$, and $\cos\theta_0 = z_0/r_0$, we can write

$$\begin{aligned} r' = r_0\{1 - 2x_1\sin\theta_0/r_0 + 2(z_1 + 2b)\cos\theta_0/r_0 \\ + [x_1^2 + y_1^2 + (z_1 + 2b)^2]/r_0^2\}^{1/2}. \end{aligned} \tag{66}$$

To consider the diffraction of a plane wave, we should assume that $r_0 \gg r_1$. Neglecting the second-order term, we obtain

$$r' \approx r_0 - x_1\sin\theta_0 + (z_1 + 2b)\cos\theta_0. \tag{67}$$

For a distant source, we have $\theta_p \approx \theta_0$, and we can set $r_0 \approx r'$ in the amplitude factor of expression (64). As a consequence, for a plane incident wave, Eq. (64) yields a plane reflected wave

$$\begin{aligned} &p_{\mathrm{r}} \\ &= A(\theta_0)\exp(ik(-x_1\sin\theta_0 + (z_1 + 2b)\cos\theta_0)). \end{aligned} \tag{68}$$

APPENDIX.

TRANSFORMATION OF EXPRESSION (35a) FOR A PLANE INCIDENT WAVE

Using representation (26), we write the factor $s_{mn}(r_0, \theta_0)$ in Eq. (35a) as follows:

$$\begin{aligned} s_{mn}(r_0, \theta_0) = \int\limits_{0}^{\pi/2 - i\infty} A(\theta)\exp(i2kb\cos\theta)P_n^m(\cos\theta) \\ \times \sin\theta\sum_{n_1 = 0}^{\infty}\frac{i^{n_1}}{N_{mn_1}}j_{n_1}(kr_0)P_{n_1}^m(\cos\theta_0)P_{n_1}^m(\cos\theta)d\theta. \end{aligned} \tag{A1}$$

Consider the expansion (see [2])

$$\begin{aligned} &\exp(ikr_0(\cos\theta\cos\theta_0 + \sin\theta\sin\theta_0\cos\varphi)) \\ &= \sum_{n = 0}^{\infty}\sum_{m = -n}^{n}\frac{i^n}{N_{mn}}j_n(kr_0)P_n^m(\cos\theta_0)P_n^m(\cos\theta)\exp(im\varphi). \end{aligned} \tag{A2}$$

Multiplying its both sides by $\exp(-is\varphi)$, where s is an arbitrary number ($s \le n$), and integrating over the interval $(0, 2\pi)$, we obtain the sum involved in Eq. (A1) in the form

$$\exp(ikr_0\cos\theta\cos\theta_0)J_0(kr_0\sin\theta\sin\theta_0)/2. \tag{A3}$$

Using expression (A3) and the identities $J_0(x) = (H_0^{(1)}(x) + H_0^{(2)}(x))/2$ and $H_0^{(2)}(-x) = -H_0^{(1)}(x)$, we can transform expression (A1) into an integral with a symmetric part:

$$\frac{1}{4}\int_{-\pi/2+i\infty}^{\pi/2-i\infty} A(\theta)\exp(i2kb\cos\theta)P_n^m(\cos\theta) \tag{A4}$$
$$\times\exp(ikr_0\cos\theta\cos\theta_0)H_0^{(1)}(kr_0\sin\theta\sin\theta_0)\sin\theta d\theta.$$

Now, we assume that $kr_0 \gg 1$. Using the asymptotic formula for the Hankel function, we write

$$\frac{1}{4}\int_{-\pi/2+i\infty}^{\pi/2-i\infty} A(\theta)\exp(i2kb\cos\theta)P_n^m(\cos\theta)$$
$$\times\sqrt{\frac{2}{\pi kr_0\sin\theta\sin\theta_0}} \tag{A5}$$
$$\times\exp(ikr_0\cos((\theta-\theta_0)-i\pi/4))\sin\theta d\theta.$$

In this case, we can use the saddle-point method. As a result of the transformation of the integration path, the latter may intersect several poles of the function $A(\theta)$. The residues of these poles correspond to surface waves that rapidly decrease with distance from the surface. Note (see [5]) that the reflected field depends on the sum $z_0 + z_1$ rather than on the distances z_0 and z_1 (see Fig. 2) separately. Consequently, we can neglect the contribution of poles for a distant source. A simple calculation of integral (A5) by the saddle-point method yields

$$s_{mn}(r_0,\theta_0) \approx -\frac{i}{2}\frac{\exp(ikr_0)}{kr_0} \tag{A6}$$
$$\times A(\theta_0)P_n^m(\cos\theta_0)\exp(2ikb\cos\theta_0) \quad (kr_0 \gg 1).$$

Substituting expression (A6) in Eq. (35a), we obtain Eq. (35b).

REFERENCES

1. G. C. Gaunaurd and H. Huang, IEEE Trans. Ultrason. Ferroelectr. Freq. Control **43**, 690 (1996).
2. E. A. Ivanov, *Electromagnetic Wave Diffraction by Two Bodies* (Nauka i Tekhnika, Minsk, 1968).
3. E. L. Shenderov, *Wave Problems in Hydroacoustics* (Sudostroenie, Leningrad, 1972).
4. E. L. Shenderov, *Generation and Scattering of Sound* (Sudostroenie, Leningrad, 1989).
5. L. M. Brekhovskikh, *Waves in Layered Media*, 3rd ed. (Nauka, Moscow, 1982; Academic, New York, 1980).
6. E. L. Shenderov, Akust. Zh. **45**, 281 (1999) [Acoust. Phys. **45**, 245 (1999)].

Translated by A. Vinogradov

Acoustical Physics, Vol. 48, No. 5, 2002, pp. 618–619. Translated from Akusticheskiĭ Zhurnal, Vol. 48, No. 5, 2002, pp. 695–696.
Original Russian Text Copyright © 2002 by Konovalov.

SHORT COMMUNICATIONS

The Effect of the Matching Layer Thickness on the Duration of Pulses Generated by a Transducer

S. I. Konovalov
St. Petersburg State Electrotechnical University,
ul. Prof. Popova 5, St. Petersburg, 197376 Russia
e-mail: root@post.etu.spb.ru

Received July 4, 2001

Recent publications (e.g., [1, 2]) testify that the problem of investigating the pulsed-mode operation of piezotransducers and choosing the optimal parameters of their components remain topical.

Among the problems of applied acoustics, the need for the generation of short acoustic pulses by a transducer is rather common. One of the possible ways of meeting this need is the use of quarter-wave matching layers. The problem of choosing the optimal value of the specific acoustic impedance of the matching layer is considered, in particular, in [3, 4]. In manufacturing high-frequency transducers (with resonance frequencies of about several MHz), special attention should be given to the accuracy of fabricating a layer of the required thickness. This factor is of particular importance when it is necessary to obtain identical characteristics of transducers within a batch where a scatter in this parameter is unavoidable. This paper is devoted to the numerical analysis of the dependence of the pulse form generated by a transducer on the small deviations of the matching layer thickness from the quarter-wavelength. The transducer is considered as a piezoceramic plate (of the TsTBS-3 type) whose rear side is loaded by a damper with the specific acoustic impedance z_d and, on the other side, the radiation is emitted into the water medium through a quarter-wave matching layer with the specific acoustic impedance z_l. The damper is assumed to be semi-infinite. The electric excitation pulse is taken in the form of a half-cycle of a sine voltage with the period T_0 equal to the period of natural oscillations of the piezoceramic plate. The technique for calculating the form of the generated pulse was described in [5, 6]. As before, we estimate the pulse duration by the amplitude decrease to a level of 0.1, i.e., by 20 dB. We introduce a parameter α characterizing in percent the deviation of the matching layer thickness from the quarter-wavelength. The value $\alpha = 0$ corresponds to the case when the matching layer thickness is equal to the quarter-wavelength. The value $\alpha = \pm 10\%$ characterizes the deviation of the thickness from the quarter-wavelength toward greater or smaller values by one tenth, and so on.

The figure shows a family of curves characterizing the dependence of the duration τ of the pulse generated by the transducer on the parameter α for various degrees of damping. Curve *1* corresponds to the specific acoustic impedance of the damper $z_d = 0$, curve *2*, to $z_d = 5 \times 10^6$ Pa s/m, and curve *3*, to $z_d = 10 \times 10^6$ Pa s/m. As is seen from the figure, in the absence of the damper, even rather small variations of the parameter α (within about ±4%) result in a noticeable increase in the pulse duration relative to its minimal value equal to 7.5 half-periods. With an increase in z_d, the effect of α decreases. For the case with $z_d = 5 \times 10^6$ Pa s/m (curve *2*), the deviation α within ±(8–10)% does not lead to an increase in the acoustic pulse duration, as compared to its minimal value of 6.5 half-periods. For stronger damping ($z_d = 10 \times 10^6$ Pa s/m, which corresponds to curve *3*), the influence of the parameter α decreases still further, so that the minimal pulse duration equal to five half-periods is retained even for deviations of α of ±15%.

For comparison, it is appropriate to give the values of the duration of pulses generated in the absence of the matching layer. For $z_d = 0$, the pulse duration exceeds 20 half-periods. For $z_d = (5, 10, 15, \text{and } 20) \times 10^6$ Pa s/m,

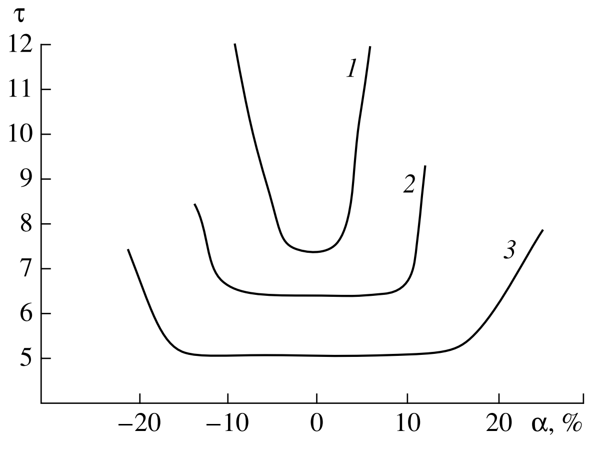

Figure.

the values of τ are 11.4, 6.6, 5.3, and 4.2 half-periods, respectively. When z_d is equal to the value of the specific acoustic impedance of piezoceramics, $\tau = 2.7$.

It should be noted that the indicated small variations in the layer thickness only slightly affect the magnitude of the maximum and the form of the main part of the pulse. Only the pulse tail is considerably modified, while for low values of mismatch of the parameter α, the growing amplitudes of separate parts of the pulse in the indicated region still do not reach the level of 0.1 of the maximum. This explains the presence of the flat parts of the curves shown in the figure.

Thus, the calculations make it possible to determine the approximate limits of the allowable values for the deviation of the matching layer thickness from the quarter-wavelength. For various values of z_d, the value of the parameter α can be as follows: for $z_d = 0$, $\alpha \approx \pm3\%$; for $z_d = 3 \times 10^6$ Pa s/m, $\alpha \approx \pm6\%$; for $z_d = 5 \times 10^6$ Pa s/m, $\alpha \approx \pm10\%$; for $z_d = 7 \times 10^6$ Pa s/m, $\alpha \approx \pm12\%$; and for $z_d = 10 \times 10^6$ Pa s/m, $\alpha \approx \pm15\%$. For greater values of z_d, the determination of the values of α is of little interest, because the fabrication of layers whose thickness satisfies the condition $\alpha = \pm15\%$ does not present any technological difficulties.

REFERENCES

1. V. N. Danilov, Defektoskopiya, No. 4, 58 (2001).
2. N. Lamberti, F. M. de Espinosa, N. Pérez, *et al.*, in *Proceedings of 2000 International IEEE Ultrasonics Symposium, San Juan, Puerto Rico, 2000* (IEEE, Piscataway, NJ, 2000), Vol. 2, p. 1105.
3. S. I. Konovalov and A. G. Kuz’menko, Akust. Zh. **44**, 119 (1998) [Acoust. Phys. **44**, 100 (1998)].
4. S. I. Konovalov and A. G. Kuz’menko, Akust. Zh. **45**, 568 (1999) [Acoust. Phys. **45**, 507 (1999)].
5. S. I. Konovalov and A. G. Kuz’menko, Akust. Zh. **42**, 724 (1996) [Acoust. Phys. **42**, 638 (1996)].
6. S. I. Konovalov and A. G. Kuz’menko, Defektoskopiya, No. 8, 3 (1998).

Translated by A. Svechnikov

Acoustical Physics, Vol. 48, No. 5, 2002, pp. 620. Translated from Akusticheskiĭ Zhurnal, Vol. 48, No. 5, 2002, pp. 697.
Original Russian Text Copyright © 2002 by Andreeva, Kulikov, Samokishchuk.

CONFERENCES AND MEETINGS

XI Session of the Russian Acoustical Society

The XI Session of the Russian Acoustical Society was held in Moscow on November 19–23, 2001. The scope of the session covered a wide range of problems of modern acoustics, and the participants of the session included acousticians from almost all regions of Russia. Considerable interest was aroused among the participants by the section “Speech Acoustics and Acoustic Problems of Applied Linguistics.” The editorial board of *Acoustical Physics* decided to publish part of the papers presented at this section and devoted to the most topical problems of this promising field of research. Three more papers in addition to those published in the previous issue are presented below (the publication will be continued in the following issues). The papers were not additionally refereed before publishing.

1063-7710/02/4805-0620$22.00 © 2002 MAIK “Nauka/Interperiodica”

Acoustical Physics, Vol. 48, No. 5, 2002, pp. 620–622. Translated from Akusticheskiĭ Zhurnal, Vol. 48, No. 5, 2002, pp. 697–700.
Original Russian Text Copyright © 2002 by Andreeva, Kulikov, Samokishchuk.

CONFERENCES AND MEETINGS

Common Features of the Amplitude–Frequency Characteristics of Vowels in Different Forms of Speech

N. G. Andreeva, G. A. Kulikov, and A. P. Samokishchuk
St. Petersburg State University, Universitetskaya nab. 7/9, St. Petersburg, 199034 Russia
e-mail: kulikovga@mail.ru

Abstract—According to classical concepts, the relationship between the first two formants is the feature that determines the identification of long vowels in speech. However, the characteristics of vowels may considerably vary depending on the conditions of their production. Thus, the aforementioned features that are valid for adult speech cannot be extended to speech signals with high fundamental frequencies, such as infant speech or singing. On the basis of the studies of preverbal infant vocalizations, singing, and speech imitation by talkingbirds, it is shown that the stable features of vowel-like sounds are the positions and amplitude ratios of the most pronounced spectral maxima (including those corresponding to the fundamental frequency). The results of the studies suggest that precisely these features determine the categorical identification of vowels. The role of the relationship between the frequency and amplitude characteristics in the vowel identification irrespective of the way the vowel is produced and the age and state of the speaker, as well as in the case of speech imitation by talkingbirds, is discussed. *© 2002 MAIK “Nauka/Interperiodica”.*

Among many aspects of the problem of speech recognition, the analysis of the features responsible for the identification of vowels remains topical. According to classical concepts [1, 2], such features of vowels are certain relationships between the frequency values of the first two formants. However, it is well known that the characteristics of vowels may considerably vary in the course of one's individual development or with changes in the conditions of the vowel production. In particular, sounds produced by infants have high fundamental frequencies (usually, within 300–600 Hz) and, hence, are characterized by other values of the first two formants, as compared to those typical of adults. Moreover, the formant values in infant vocalizations exhibit no noticeable differences for different vowels [3, 4]. This means that the aforementioned classical concepts cannot be transferred to preverbal infant vocalizations. A similar discrepancy is observed for sung vowels, where the fundamental frequency range and articulation considerably differ from ordinary speech [5]. Meanwhile, in listening to both infant vocalizations and singing, adult auditors are capable of ascribing the vowels they hear to certain phonetic groups.

To form the speech sounds peculiar to a given language environment, on the basis of imitation an infant must reveal the speaker-independent common features that determine the vowel categorical perception. The ability of an infant to reveal the similarity of vowels pronounced by different adults and to establish their relation to the infant's own sounds is evidenced by the very possibility of imitation. A correction of such a sound imitation by an acoustic feedback cannot shift the formant values to those of adults. However, in listening to the vowel-like sounds produced by infants, adult auditors are capable of categorizing them with certain phonetic groups. Hence, infants, like adult auditors, can reveal some universal features in the vowels of the same phonetic group, and these features, which determine the categorical perception, cannot be reduced to the positions of formants in the two-formant plane. Presumably, similar speculations are valid for the vowels in the words imitated by talkingbirds, which have a specific vocal apparatus.

1063-7710/02/4805-0620$22.00 © 2002 MAIK “Nauka/Interperiodica”

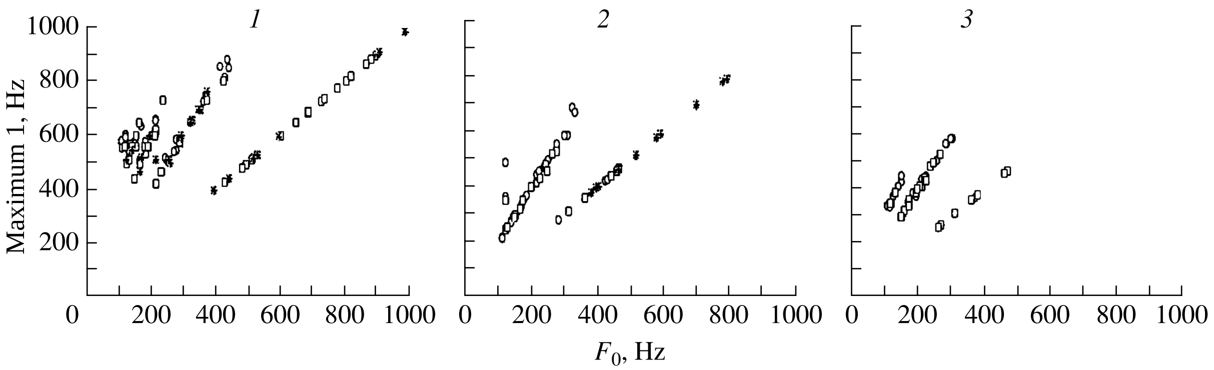

Fig. 1. Relation between the frequency corresponding to the first spectral maximum and the fundamental frequency for three vowels (*1*) [a], (*2*) [i], and (*3*) [u] sung by (0) a tenor, (□) a countertenor, and (∗) a soprano.

To determine the stable features of vowels in different forms of speech, both instrumental and phonetic analyses were performed for the following sounds: vowel-like sounds recorded in the course of a longitude study of ten healthy infants (from 1 to 12 months old), cardinal vowels sung by professional singers (tenor, countertenor, and soprano) with different fundamental frequencies, and the vowels [a] and [i] in the words imitated by *Gracula religiosa*. To estimate the temporal and spectral characteristics of sounds, the licensed Cool 96 program was used. The spectral analysis was based on the fast Fourier transform, and the data were weighted by the Hamming window. For the signals and their individual components, which were selected on the basis of their dynamic spectrum and sounding, the fundamental frequencies, the formant frequency values, and the relative amplitudes of the corresponding spectral maxima were estimated.

The studies showed that infant vocalizations contain a wide variety of phonetic units. It was found that the first speechlike elements observed in infants coincide with the sounds that accompany emotional reactions and innate behavioral acts. This fact may be responsible for the certain universality of the phonetic repertoire of preverbal infants. The phonetic analysis showed that, despite the wide variety of sounds in early infant vocalizations, the latter are characterized by the predominant production of sounds described as front vowels (66%) and, to a lesser extent, central vowels (33%). Note that none of the infants from the age group 1–6 months was found to produce all the vowels presented in the IPA. At the same time, these infants produced some vowel-like sounds that none of the auditors could ascribe to any definite category of vowels.

On the basis of the spectral analysis of infant vocalizations, it was shown that, as a rule, the possibility to ascribe vowel-like sounds to a definite category is not determined by their formant values and, hence, is not determined by the features that are significant for the identification of vowels in adult speech. It was found that the vowel-like sounds of infants are characterized by other relationships between the first two formant values, as compared to those observed for adults, and occupy a wide region in the two-formant plane, this region corresponding to different vowels of adult speech. The data obtained from our studies suggest that the stable features that possibly determine the categorical identification of the sounds under investigation should be the positions and amplitude ratios of the spectral maxima, including those corresponding to the fundamental frequency.

In the course of the comparative analysis of the sound production at the stage of the appearance of the first words (some authors believe that this stage is unrelated to innate phonations [6]), it was shown that precisely these features make it possible to separate the cardinal vowels. Thus, the spectral characteristics of vowel-like early vocalizations of infants and the spectral characteristics of the first words do not differ from each other. This fact agrees well with the concept of the continuity between the stage of babble and the stage of the first words. The latter result can be considered as evidence in support of the succession in the speech development on the basis of a set of innate vowel-like sounds.

With the aim to test the generality of the aforementioned stable features, a study of sung vowels (academic singing) was carried out. In addition, vowels of ordinary adult speech were recorded and analyzed as reference. For the sung vowels, it was found that, when fundamental frequencies are higher than 250–400 Hz, the spectral components most pronounced in amplitude are those corresponding to the fundamental frequencies (Fig. 1). As the fundamental frequency increases, the first and second formants approach the two-formant plane region corresponding to the concentration of the first formants of vowel-like sounds produced by infants. At the same time, as the fundamental frequency increases, different vowels of singing begin to exhibit specific variations of the amplitude ratio of the spectral maxima (Fig. 2). These variations, as in infants, are statistically significant stable features of the corresponding speech sounds. Similar stable features are characteristic of vowels taken from the words imitated by talk-

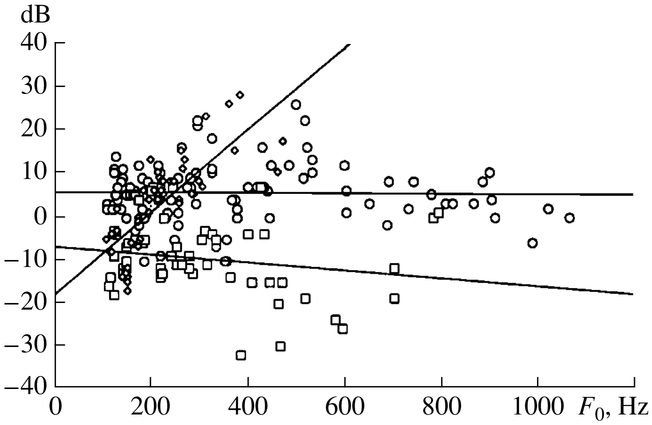

Fig. 2. Amplitude ratios of the first and second formants of three vowels (○) [a], (□) [i], and (◇) [u] sung by different professional singers with different fundamental frequencies.

ingbirds. The results of the reference records and the analysis of the vowels of ordinary adult speech proved to agree well with the known data on the ordered positions of the first and second formants in the two-formant domain [1, 7].

Thus, although the formant frequencies are accepted as a feature essential for vowel recognition, they are not invariant with respect to the character and ways of speech production. From the results of the studies described above, it follows that, at high fundamental frequencies, the positions and the amplitude ratios of the spectral maxima are stable features of specific vowels, and these features are present in different forms of speech and in preverbal infant vocalizations. This suggests that precisely these features determine the categorical identification of vowels, whatever the way the vowel is produced and the age and state of the speaker, including the case of the imitation of vowels by talkingbirds.

ACKNOWLEDGMENTS

This work was supported by the Russian Humanitarian Foundation (project no. 01-06-00185a), the Ministry of Education in Support of Humanitarian Sciences (grant no. G00-1.7-130), and the program “Universities of Russia-2000” (project no. 992616).

REFERENCES

1. L. C. Peterson and H. L. Barney, J. Acoust. Soc. Am. **24**, 175 (1952).
2. L. A. Chistovich, A. V. Ventsov, M. P. Granstrem, *et al.*, *Physiology of Speech. Speech Perception by Human* (Nauka, Leningrad, 1976).
3. P. K. Kuhl and A. N. Meltzoff, J. Acoust. Soc. Am. **100**, 2425 (1996).
4. G. A. Kulikov, N. G. Andreeva, E. E. Lyakso, and M. I. Pavlikova, Sens. Sist. **13** (1), 62 (1999).
5. V. P. Morozov, in *Mechanisms of Speech Formation and Perception of Complex Sounds* (Nauka, Moscow, 1966), pp. 73–86.
6. R. Jakobson, *Child Language Aphasia and Phonological Universals* (Mounton, Hague, 1968).
7. M. F. Derkach, R. Ya. Gumetskiĭ, B. M. Gura, and M. E. Chaban, *Dynamic Spectra of Speech Signals* (Lvov Gos. Univ., Lvov, 1983).

Translated by E. Golyamina

Acoustical Physics, Vol. 48, No. 5, 2002, pp. 623–625. Translated from Akusticheskiĭ Zhurnal, Vol. 48, No. 5, 2002, pp. 701–704.
Original Russian Text Copyright © 2002 by Vorob'ev, Davydov.

CONFERENCES AND MEETINGS

Synthesis of Speechlike Signals

V. I. Vorob'ev and A. G. Davydov
Belarussian State University of Informatics and Radio Engineering,
ul. P. Brovki 6, Minsk, 220660 Belarus
e-mail: nil53@bsuir.edu.by

Recent publications concerned with speech synthesis include some papers that consider so-called speechlike signals (SLS). The main areas of application of these signals are expected to be psychology and information security [1, 2].

The SLSs already used in the aforementioned areas are understood as signals phonetically similar to speech, but carrying no meaningful information that could be extracted by conventionally used simple means (primarily, by direct listening to these signals by the called party).

In psychological experiments, SLSs are formed, in particular, by a frequency inversion of the spectrum of ordinary speech signals. In the case of information protection (masking) by SLSs, the latter are formed as a result of the summation of three arbitrary speech signals [3].

In both cases mentioned above, the use of the term “speechlike signal” is not quite correct, because the signals formed in these cases still contain in a hidden form the meaningful information carried by the initial speech signals. By subjecting such SLSs to a suitable processing, this information can be extracted. Cases are known when users understood the basic meaning of spectrum-inverted speech without any explicit transformation of the arriving acoustic signals to the initial speech signals. At a subconscious level, a user, independently of his own wish, can perform a kind of spectral inversion of the received signals, and the meaning of the initial speech can be extracted from the resulting data by the user's brain.

It is desirable that the term “speechlike signals” has its own meaning independent of the way these signals are formed and processed. We will interpret the SLSs as acoustic signals that are similar to speech in their temporal and spectral characteristics and in the perception by ear but carry no meaningful information in whatever form.

With allowance for the data on the typical parameters of speech signals [4–7], the main features that determine the similarity between the SLSs and speech can be defined as follows:

(1) the burst-type character of the time variations of SLSs with a burst duration of 15–120 ms;

(2) the grouping of bursts into packets containing two to eight bursts each with an interval between individual bursts within 10–50 ms and an interval between packets from 10 ms to 1 s;

(3) the presence of a fundamental tone with a frequency of 75–300 Hz in the SLS spectrum;

(4) the presence of an SLS envelope with a spectrum concentrated in the frequency band 9–60 Hz;

(5) the shape of the envelope of a burst-type signal can be preset analytically with a parameter variation, or it can be chosen in a random way from a set of preliminarily prepared signals;

(6) the presence of three to five formants in the spectrum, these formants being formed according to the law

$$f_n(t) = A_n \exp(-t/t_n)\sin(\omega_n t - \varphi_n).$$

Here, A_n is the amplitude of the nth formant, where $n = \overline{1, N}$ and N is the total number of formants; t is the running time of reading, which varies from the beginning of the fundamental period to its end; t_n is the time interval within which the amplitude decreases by a factor of e (the duration of this interval is within 1.5–30 ms); φ_n is the initial phase of the harmonic carrier of the nth formant; and ω_n is the circular frequency of the formant ($\omega_n = 2\pi fn$). The cyclic frequencies of the formants lie approximately in the following frequency bands [4, 6, 7]: f_1 = 300–1000 Hz, f_2 = 1000–2000 Hz, f_3 = 2000–3000 Hz, f_4 = 3000–4000 Hz, and f_5 = 4000–5000 Hz.

One may notice that the literature data on the parameters of the bursts and their packets to some extent contradict the aforementioned numerical values of the time and frequency characteristics of the SLS envelope. However, this fact cannot hinder the subsequent consideration.

The formation of the SLSs on the basis of the features listed above should be performed so as to satisfy the following additional conditions:

—It is expedient to divide the SLS realization under construction into segments with durations from 5 to 15 fundamental periods. It is necessary that, within these segments, the initial phases and formant carrier frequencies vary within no more than 10% of their initial values. The character of the variations of the initial phases and formant frequencies can be similar to that of the burst envelope.

Table 1. Absolute probabilities of the letters of the Russian alphabet

Space	0.175	К	0.028		
О	0.090	М	0.026	Ч	0.012
Е	0.072	Д	0.025	Й	0.010
А	0.062	П	0.023	Х	0.009
И	0.062	У	0.021	Ж	0.007
Т	0.053	Я	0.018	Ю	0.006
Н	0.053	Ы	0.016	Ш	0.006
С	0.045	З	0.016	Ц	0.004
Р	0.040	Ь, Ъ	0.014	Щ	0.003
В	0.038	Б	0.014	Э	0.002
Л	0.035	Г	0.013	Ф	0.002

—In passing from one segment to another, the fundamental frequency, the formant frequencies, the amplitudes, and the decay time of formant signals may vary in a stepwise manner by 20–70% in any direction.

—In passing from one burst to another, the burst parameters may change in an arbitrary way within the limits indicated above.

For the formation of SLSs, two approaches can be used:

—at the signal level, i.e., by a direct formation of a process with temporal and spectral parameters obeying the requirements proposed above for the SLSs;

—at the text level, i.e., by generating texts according to specially developed algorithms, so that the conversion of these texts to sound by specially designed means yields the SLSs.

Below, we mainly consider the second approach, which, at this stage of investigation, allows a simpler computer simulation of the SLSs under discussion. Within this approach, several methods of the SLS formation can be proposed.

The most simple method is the formation of “words” with the use of the absolute probabilities of the appearance of letters and spaces in the texts of the modeled language (see Table 1).

The advantage of this method is the automated separation of the words of the resulting text by spaces, which appear with a probability of 0.175.

An example of a text obtained by this method has the form: “омтгбусп гаднн ааб р чйдвднугейнбнмтию а т иреьрн пкс схлтиеикиуятиожд рл аюас лкнонеб прунчщ ьиэь тк нкнйбеобот еммявщтн ма гуиотдесад а твисьлсинжн ймоттееадзо еошедеола ивауа млиц лпаянуауот рбиут обнем ре овееопкааоонодоз ые ондусоoююерешро чмумлккшеусоыойп.”

Another method of SLS formation is the synthesis of words on the basis of the probabilities of the appearance of different syllables. In this case, the difference in the probabilities of the appearance of a given syllable after different numbers of other syllables preceding it in the word is taken into account. To separate the syllables themselves, it is expedient to use the following assumptions: (a) one syllable should contain a single vowel; (b) a syllable can consist of a single vowel; (c) a syllable terminates with a vowel; (d) the consonants standing at the end of the word and remaining untapped after the formation of syllables according to the first three assumptions should be considered as a separate syllable.

The assumptions listed above are illustrated by the following example.

The initial word: ПОЛУПРОВОДНИК (semiconductor).

The correct partition: ПО-ЛУ-ПРО-ВОД-НИК.

The partition on the basis of the aforementioned assumptions: ПО-ЛУ-ПРО-ВО-ДНИ-К.

One can see that the assumptions yield a practically correct partition. Errors occurred only in the formation of the syllables ВОД and НИК. However, even in the case of such a partition, the resulting elements of the word continue “sounding.”

At the end of the word, the syllable “К” appeared. This syllable is incorrect. However, it may occur only at the end of the word and with a low probability. In this connection, it is necessary to introduce a correction: all syllables characterized by a total probability of their appearance smaller than a certain value should be discarded as incorrect (nonexistent) ones.

An example of a text formed by the second method is as follows: “тиебщеля позовща амниваде фапенаяльно педостаегомы всетоктие издерье эне ко растогайе ма осоко незниднынонныт сстьенййчно икдей мнокрорайв ворый чтопострой идныснеятся пдпгухйсате у тре аспозутьнтныя листрользува свяраниниватся вбще золевнюа поктобрани нальшехнтао нетилняель о тимячкиткеюм атрировя тинфибраво вымяфинибра дляляму дапри дватоймхнно.”

For the formation of SLSs, text formation on the basis of using the probabilities of the appearance of different sounds in the language is also of interest. The probabilities of the appearance of different sounds in the separated parts of words are shown in Table 2.

Owing to lack of space, we do not discuss here the algorithmic details of the text formation by the third method. We only present an example of a text formed by this method: “пуздату панофакы насиху п еасаматай пазешиф сапрыпаноша ним дликахаф шяпаныфехя ситья ватажихята ромахоту шт сте егтопасьяти напрота нявето со фсафо вувёкийете понасеть певойеши рар пинееиком ласвайой самехай гамынимэ му чиштисатьим тамыкакуф кепот е боноха к совнеташ сынь в.”

After the formation of the sequences of sounds or letters by any of the aforementioned methods, it is nec-

Table 2. Occurrence of sounds (in percent)

Consonants and their groups								Vowels (stressed) in the middle of a word
initial				terminal				
Б	П	ВН	ПЛ	Й 17.0	С	ЗМ 0.1	МЬ 0.08	А 32.5
3.7	11.6	0.3	0.3	К 5.5	2.9	ЗНЬ 0.2	ПЬ 0.03	Е 19.6
В	Р	ГЛ	ПР	Л 7.7	СЬ	КП 0.1	ФЬ 0.03	Е 1.3
7.3	3.6	0.2	3.7	ЛЬ 0.4	3.5	КТ 0.3	ПЬФЧ	И 14.3
Г	С	ГР	СВ	М 14.1	Т	СК 0.1	0.05	О 14.6
2.0	8.4	0.1	0.7	Н 5.1	12.8	СТ 0.2		У 7.0
Д	Т	ДВ	СК	НЬ 0.8	ТЬ	СТЬ 1.1		Ы 6.1
4.8	6.4	0.3	0.4	П 0.2	9.3	РК		Э 1.2
Ж	Ф	ДЛ	СП	Р 1.3	Ф	0.03		Ю 0.6
0.8	2.1	0.4	0.2	РЬ	4.8	РП		Я 2.8
З	Х	ДР	СТ	0.5	Х	0.03		
3.9	1.0	0.3	1.1		8.4	ФК		
К	Ц	ЗД 0.4	ТР		Ц	0.03		
4.9	0.3	ЗН	0.6		0.4			
Л	Ч	0.6	ФС		Ч			
1.6	1.3	КВ	1.1		0.8			
М	Ш 1.1	0.1	ЧТ		Ш			
4.8	Щ	КР	0.9		2.9			
Н	0.1	0.3	ШТ		Щ			
12.6			0.9		0.3			
At the beginning of a word: е, ё, ю, я—4.8.								

essary to obtain an analog representation of the SLSs. For this purpose, there exist a number of computer techniques and algorithms [7–10] that differ in their complexity and computer memory requirements.

The text examples formed for SLS generation can be subjectively estimated by reading them aloud. A comparative analysis of different methods of SLS synthesis is beyond the scope of this paper. The current status of the studies concerned with the problems of the formation and use of speechlike signals of probabilistic character testifies that these signals can be used for protecting speech messages in communication channels by masking the intervals between the communication sessions, for noise masking in audio systems of information protection from leakage through acoustic channels, and for generating a special noise in security and fire alarm systems. A possible area of application of the SLSs is psychology.

REFERENCES

1. G. V. Davydov and A. V. Potapovich, Izv. Bel. Inzh. Akad., No. 1(9)/1, 123 (2000).
2. *Physiological Acoustics*, http://psi.webzone.ru/st/005300.htm.
3. S. V. Kalinin, http://www.MASCOM.ru/vib_st.html.
4. M. A. Sapozhnikov, *Speech Signal in Cybernetics and Communication (Speech Transformation as Applied to Engineering and Cybernetics Problems)* (Svyaz'izdat, Moscow, 1963).
5. M. A. Sapozhkov and V. G. Mikhaĭlov, *Vocoder Communication* (Radio i Svyaz', Moscow, 1983).
6. J. D. Markel and A. H. Gray, *Linear Prediction of Speech* (Springer, Berlin, 1976; Svyaz', Moscow, 1980).
7. N. V. Petlyuchenko, in *Proceedings of XI Session of the Russian Acoustical Society: Modern Speech Technologies* (GEOS, Moscow, 1999), p. 112.
8. T. A. Brovchenko, V. G. Voloshin, and O. F. Chernov, in *Proceedings of XI Session of the Russian Acoustical Society: Modern Speech Technologies* (GEOS, Moscow, 1999), p. 108.
9. M. K. Rumyantsev, M. I. Kaplun, B. V. Pospelov, and K. I. Dolotin, in *Proceedings of XI Session of the Russian Acoustical Society: Modern Speech Technologies* (GEOS, Moscow, 1999), p. 103.
10. O. F. Krivnova, L. M. Zakharov, N. V. Zinov'eva, *et al.*, *Proceedings of XI Session of the Russian Acoustical Society: Modern Speech Technologies* (GEOS, Moscow, 1999), p. 93.

Translated by E. Golyamina

Acoustical Physics, Vol. 48, No. 5, 2002, pp. 626–633. Translated from Akusticheskiĭ Zhurnal, Vol. 48, No. 5, 2002, pp. 705–712.
Original Russian Text Copyright © 2002 by Mikhaĭlov.

CONFERENCES AND MEETINGS

Diagnostic Articulation Tables

V. G. Mikhaĭlov

Faculty of Philology, Moscow State University,
Vorob'evy gory, Moscow, 119899 Russia
e-mail: rfc-lsve@mtu-net.ru

Abstract—In recent years, considerable progress has been made in the development of instrumental methods for general speech quality and intelligibility evaluation on the basis of modeling the auditory perception of speech and measuring the signal-to-noise ratio. Despite certain advantages (fast measurement procedures with a low labor consumption), these methods are not universal and, in essence, secondary, because they rely on the calibration based on subjective-statistical measurements. At the same time, some specific problems of speech quality evaluation, such as the diagnostics of the factors responsible for the deviation of the speech quality from standard (e.g., accent features of a speaker or individual voice distortions), can be solved by psycholinguistic methods. This paper considers different kinds of diagnostic articulation tables: tables of minimal pairs of monosyllabic words (DRT) based on the Jacobson differential features, tables consisting of multisyllabic quartets of Russian words (the choice method), and tables of incomplete monosyllables of the _VC/CV_ type (the supplementary note method). Comparative estimates of the tables are presented along with the recommendations concerning their application. © *2002 MAIK "Nauka/Interperiodica".*

The quality of speech is determined by a set of features characterizing its naturalness, identifiability, and intelligibility, as well as its loudness and the presence of irrelevant sounds and noise. The purpose of testing is to determine how much the speech quality fits the adopted standards and also to reveal the sources of distortions and the ways of eliminating them. Testing vocalized speech is necessary in such areas as telephony (the evaluation of the transmission quality of communication channels), medicine (the determination of speech defects and hearing impairments), criminology (voice identification), etc. The methods of testing are classified into subjective-statistical (psycholinguistic) ones, which are realized with the participation of speakers and listeners, and instrumental methods realized with the help of calculations and automated measurement procedures. The subjective-statistical measurements have a long history of their application and improvement. Major contributions to the development of methods based on the user's estimates of the transmission quality were made by L.R. Zinder (1951), M.A. Sapozhkov (1959), N.B. Pokrovskiĭ (1962), Yu.S. Bykov (1959), H. Fletcher (1929), G. Fairbanks (1958), and K. Kryter (1965). In recent years, new interesting results concerned with the testing problem were published by R.K. Potapova (1986), L.V. Zlatoustova (1986), G.V. Vemyan (1985), D. Pisoni (1989), and W. Voiers (1983).

In Russia, the methods of measurement are regulated by state standards. The GOST R 50840-95 standard, which has been effective since 1997, refers to the measurement of the transmission quality, intelligibility, and voice identification in speech communication channels [6]. For testing, both methods of measurement based on articulation tables (words, syllables, phrases) and methods of verbal description of the speech quality (opinions, pairwise comparisons, etc.) are used. The word and syllable articulation measurements are performed using tables with words and syllables. The main purpose of the tables of words is to measure the intelligibility in communication channels with the limiting allowable quality in the presence of intense acoustic noise. Because of the limited number of these tables (a total of 50) and their ability to be easily memorized, a frequent use of these tables is impermissible. Measurements can also be performed with tables of phrases and two-digit numbers. The former type of tables is almost never used because of their redundancy and, hence, low sensitivity to distortions in the communication channel. For example, the intelligibility of phrases obtained for a channel of reasonable quality amounts to 95–97%, for a channel of good quality, to 97–99.5%, and for a channel of excellent quality, to 99.5–100%. Numerical tables are used in the specific conditions of a rather low intelligibility (below 25%), which is impermissible for telephone communication.

A certain relationship had been established between different types of intelligibility [1]. Tables of syllables have several disadvantages: the prosodic parameters of speech (the envelope of the fundamental tone, the rhythmic structure, and the speech rate) are not represented; the spectral characteristics of sounds in syllables have an exaggerated form; and, finally, for obtaining the necessary value for the coefficient of experimental practice of an articulation team (z = 0.96–0.98), long-term training is required, especially when the task includes the perception of synthesized speech [2].

In this respect, the tables of words have certain advantages. The tables contain words with rhythmic structures that vary in the number of syllables and stress position. They provide a natural enunciation, and the training time required for the articulation team of listeners is small. However, the tables of words possess a considerable redundancy, and, hence, their sensitivity to speech signal distortions is low. The results of measuring the intelligibility of words and syllables are represented in the form of statistically average estimates of the transmission quality without description of linguistic factors that cause the distortions of the speech units. The diagnostic articulation tables serve to eliminate this drawback.

THE DRT DIAGNOSTIC TABLES

The known types of diagnostic articulation tables include tables of minimal pairs of monosyllabic words called Diagnostic Rhyme Tests, which were developed on the basis of Jacobson differential features [4], tables of multisyllable quartets of Russian words (the choice method) [5], and tables of incomplete syllables of the _VC/CV_ type with one (initial or terminal) consonant omitted (the supplementary note method) [6].

The DRT tables were developed at the Cambridge Naval laboratory, USA, to evaluate the effect of signal distortions in a communication channel on the discriminability of the differential features of phonemes. The tables consist of 112 pairs of monosyllabic English words, for example:

beam-peen	need-deed	feet-peat	seem-theme	peach-teach	she-see	*teal-keel
gin-chin	mitt-bit	fin-pin	chink-kink	bid-did	shift-sift	tilt-kilt
dent-tent	mend-bend	fend-pend	jest-guest	pest-test	yen-wen	pen-ken
vast-fast	nab-dab	fan-pan	champ-camp	bad-dad	cast-past	ram-yam

* The seventh pair of the row is chosen by the experimentalist.

The pairs of words, in order of their sequence, differ by one differential feature of English consonants (the so-called minimal pairs): voicing, nasality, sustention, sibilation, graveness, and compactness. The seventh pair of words has a feature chosen by the experimentalist. In total, the table contains 16 groups with seven pairs of words in each group. The words contain front vowels /i, e/ and back vowels /u, o/, high rising and low rising ones. The authors of the table followed the one word pair–one feature principle, although in some cases, deviations take place; for example, the consonants /k–p, g–b/ differ in both compactness and simplicity.

In the measurements, the table is repeated four times, which lasts 10 min (1.3 s per word). The feature of a word pair intended for reading, e.g., voiced/unvoiced, is chosen in an arbitrary way and is repeated twice during the test. The listeners mark the transmitted word in the printed chart containing the full table. The test is performed with a team of one or two speakers possessing trained voices and eight listeners with normal hearing. The discriminability of consonants estimated by the formula $d = 100(R - r)/T$, where R is the number of correct marks, r is the number of erroneous marks, and $T = 448$ is the number of transmitted words, proved to be close to the intelligibility of 256 phonetically balanced monosyllabic words.

The DRT tables are widely used outside Russia for measuring the intelligibility of synthesized speech. The degree of consonant distortions in their distinctive features is included in the Diagnostic Acceptability Measure (DAM) of speech communication [4]. The intelligibility measurements in the presence of noise and frequency distortions in a communication channel with a passband of 200–4000 Hz showed that noise produces different effects on the discriminability of the differential features of phonemes. The features most sensitive to noise were found to be interruption, simplicity, and compactness, while the voicing and nasality features proved to be less sensitive. Noise was also found to have different effects on contrasting features; for example, the sharpness feature proved to be more sensitive to noise than the simplicity feature. As under the effect of noise, a strong limitation of the frequency band from above noticeably affects the interruption, simplicity, and compactness features and, to a lesser extent, the voicing and nasality ones. At the same time, the discriminability of consonants under distortion remains fairly high, which is caused by the relatively stable auditory perception of the lexical meanings of words in minimal pairs. According to the data of many measurements, the discriminability is close to 70–95%.

DIAGNOSTIC TABLES OF CHOICE

Attempts to develop diagnostic tables on the basis of the Russian language encounter some difficulties. The system of differential features used for contrasting the consonants of the English language cannot be transferred to Russian without changes, and not only because of the difference in features. In the Russian language, the number of monosyllabic lexical units is limited. In addition to the vowels а, ы, э, у, and о, there

Table 1

Intelligibility (%) for test tables			
speaker	syllables	diagnostic (words)	diagnostic (paired sound combinations)
Male	85.6	99.2	94.6
Male	83.4	98.8	98.0
Female	84.1	98.8	97.5
Average	84.4	98.9	96.7

exist palatal versions я, е, ю, and ё; the use of some of the aforementioned vowels (e.g., ы or э) after some consonants may lead to combinations that are not typical of the Russian language (e.g., кы, гю, хе, etc.). In some cases, it is impossible to find minimal pairs of monosyllabic words with consonants differing in a single feature. Therefore, a new method has been proposed: the so-called choice method [5]. It consists in the transmission of three tables of 27 words each through the communication channel under test. The receiving operators (no less than three persons) must mark the transmitted word in the table consisting of 27 groups of phonetically similar (similarly sounding) words, with four words in each group; for example: the word БАНТ from the group БЛАНК, ПЛАН, БАНТ, БАНК, or the word ГРЕТЬ from the group УГОРЕТЬ, ГОРЕТЬ, БОЛЕТЬ, БАЛЕТ, etc. The measure of the speech quality (intelligibility) is the average number of errors per table: two errors correspond to the superior class, five errors, to class I, eight errors, to class II, and eleven errors, to class III. In total, ten tables of choice have been designed.

The number of variants in reading a single table can be fairly large. With a reading rate of one word in three seconds, the transmission time for one table is 1.5 min, and the time of one test of 30 tables is about 60 min (with intervals between the tables from 6 to 8 min). No special requirements are imposed on the team training. The latter consists in that the operators are given several tables to listen to just before testing. If the average score of errors does not decrease from table to table, the training is considered as sufficient.

At the laboratory of Applied Linguistics of Moscow State University, diagnostic tables for the Russian language were developed in the form of tables of paired CVC sound combinations selected on the basis of contrasting the initial or terminal consonants in one of the distinctive features of the Russian consonants (fricative/sonorous, place of formation, way of formation, voiced/unvoiced, hard/soft) [7]. During the test, the listener marks the perceived sound combination in the table of minimal pairs.

EVALUATION OF THE DRT TABLES AND TABLES OF CHOICE

To compare the sensitivities of the aforementioned diagnostic tables to speech signal distortions, articulation measurements of the intelligibility of synthesized speech were performed using the LPC-10 vocoder with a transmission rate of 2.4 kbit/s. A team of three speakers and four listeners took part in the measurements. The results are shown in Table 1.

One can see that, compared to the tables of syllables of the GOST R 50840-95 standard, the tables of choice exhibit a considerable redundancy (the corresponding intelligibility values are 84.4 against 98.9 and 96.7%). The intelligibility values for the tables of paired sound combinations proved to be lower than for the tables of word choice because of the lack of lexical meaning in the sound combinations (according to Zinder [9], the sound combinations may have some conditional meaning). This is no surprise, because, although the dichotomy principle is convenient for describing the system of distinctive features of phonemes in the domain of acoustic–articulation correlates and is used in the design of diagnostic tables, it proves to be a simplification. In reality, the relation between the articulation and perceptive features is much more complicated. Let us demonstrate it by an example. We use the method of diagnostic tables to measure the properties of the voiced/unvoiced differential feature. For this purpose, a test table was designed, part of which is presented below:

Быс-пыс
Дым-тым
Гуть-куть
Ждось-щтось
Дрит-трит
зэс-сэс
крыз-крыс
вяв-вяф
ег-ек
бяз-бяс
фиж-фиш
нюдь-нють
грыс-крыс
сущ-зущ
гар-кар
дац-тац
зой-сой
вур-фур
дамь-тамь
жась-шась
здам-стам
даз-дас
руд-рут
чтаз-чтас
лув-луф
маж-маш
зуг-зук
ребь-репь
скез-скес
луд-лут

The whole table consisted of 400 pairs of syllables. In half of these syllables, random changes of the initial consonants took place, while in the other half, the terminal consonants were changed. The enunciation of the terminal voiced consonant in the CVC sound combinations without loss of voicing required some attention of the speaker. Table 2 shows the consonant contents in Russian speech and the contents of initial consonants in the test table.

For the terminal consonants, the contents are the same. The numbers of voiced and unvoiced consonants included in the table are equal.

The test was performed using a setup that contained a spectral-band vocoder. The vocoder had 19 channels of equal articulation width in the frequency band between 150 and 7000 Hz. To separate the fundamental tone (FT) signal from speech, a laringophone and a peak FT pulse separator were used. A tone–noise signal was formed by the FT pulses. The tone signal corresponded to the presence of pulses, and the noise signal, to their absence. The vocoder with the aforementioned devices for separating the FT and tone-noise signals provided high qualitative indices: the syllable intelligibility of speech was 94–96% and the quality of synthesized speech proved to be close to the transmission quality in a standard telephone channel.

The test table was recorded for three modes of operation. In mode 1, the synthesizer was driven by a signal that was formed by the tone–noise signal from the FT pulses and the signal produced by a noise generator; in mode 2, pulses with a frequency of 140 Hz were used to drive the synthesizer, and in mode 3, a noise excitation signal was used.

In the course of recording, the speaker read one of the two syllables from each pair (in the test table, this syllable was underlined). The listener's task was to mark the perceived syllable in the printed chart of the test table. Then, the relative number of errors was calculated for the initial and terminal consonants separately. This number characterized the effect of the type of the driving signal on the consonant discrimination with respect to the voiced/unvoiced feature. The experiments were performed with two speakers (a man and a woman) and four listeners. The results of the voiced and unvoiced consonant discrimination are shown in Table 3.

From the data of this experiment, one can see that the score of errors in unvoiced consonants is greater than that in voiced consonants with all types of excitation. However, no effect of the type of excitation could be detected for the discriminability of synthesized consonants with respect to the voiced/unvoiced feature. On the contrary, voiced consonants were better discriminated with the noise excitation than with the tone excitation (the error scores are 2.5 and 6.9%, respectively).

It should also be noted that the percentages of errors in three different modes differ only slightly (8.5, 15, and 11.2%). Therefore, the intelligibility of synthesized speech in the aforementioned modes of excitation was also almost the same. The measurements performed with a team of four speakers and four listeners showed that the syllable intelligibility of speech was 93.9, 94.0, and 94.3% in modes 1, 2, and 3, respectively.

Table 2

Consonants	Probability of occurrence in Russian speech (%)		Percentage of consonants in the test table (%)	
	hard	soft	hard	soft
/ж, ш/	4.36	–	40 (5.76)	–
/б, п/	6.32	1.52	48 (6.90)	12 (1.74)
/г, к/	6.71	0.91	48 (6.90)	12 (1.74)
/в, ф/	6.89	0.72	48 (6.90)	12 (1.74)
/з, с/	8.41	2.56	48 (6.90)	12 (1.74)
/д, т/	12.71	5.47	84 (12.06)	36 (5.22)
Total	45.40	12.18	316 (45.42)	84 (12.18)

Table 3

Consonants	Percentage of errors for different types of excitation (%)		
	FT pulses	140-Hz pulses	noise
Voiced	3.0	6.9	2.5
Unvoiced	5.5	8.1	8.7
Including:			
Initial			
voiced	1.6	3.1	0.7
unvoiced	0.9	1.6	3.1
Terminal			
voiced	1.4	3.8	1.8
unvoiced	4.6	6.5	5.6

Let us compare the spectra of voiced consonants and of the corresponding unvoiced consonants. At frequencies above 1000 Hz, the spectra of these sounds differ only slightly. At frequencies below 600 Hz, the spectral density is higher for voiced consonants than for unvoiced ones by 20–40 dB. This difference in the spectral shape is retained for synthesized sounds independently of the type of the driving signal (tone or noise), which facilitates the correct perception. On the other hand, the limitation of the frequency band of the speech signal from the side of low frequencies reduces the difference between the spectral shapes of consonants, which should adversely affect their perception. Table 4 presents the data obtained by listening to the tables when a high-pass filter with a cutoff frequency of 600 Hz was inserted in the channel.

From Table 4, one can see that the limitation of the frequency band of the speech signal caused almost no increase in the number of errors in mode 1, because in this mode the tone/noise feature of the spectrum type is retained. In mode 2 and, especially, in mode 3, the limitation of the frequency band from below causes a sharp

Table 4

Mode of excitation	Type of the driving signal	Percentage of errors (%) with a limited frequency band (Hz)	
		70–7000	600–7000
1	FT pulses	2.8/4.9*	3.4/5.5
2	140-Hz pulses	4.5/10.0	22.0/20.0
3	Noise	3.5/6.2	10.0/12.0

* The numerator shows the percentage of errors for voiced consonants, and the denominator, for unvoiced consonants.

Table 5

Mode of excitation	Type of the driving signal	General speech quality, score	Percentage of errors (%)	
			speaker identification	perception of voice and intonation
1	FT pulses	7.8	11	3 (2/3)*
2	140-Hz pulses	4.2	25	49 (52/45)
3	Noise	2.9	17	24 (40/7)

* The numerator shows the percentage of errors in the intonation perception for a male voice, and the denominator, for a female voice.

increase in the number of errors, although some other discriminative features of consonants are retained. In fact, the voiced and unvoiced consonants of correlative pairs of sounds, e.g., /в-ф, з-с/, differ not only in the type of spectrum but also in spectral shape (the voiced consonants are lower in pitch), duration (the voiced consonants are shorter than the unvoiced ones, and the occlusive phase is also shorter), intensity (the voiced consonants are louder), and the fundamental frequency at the consonant-to-vowel transition [3, 10].

Let us consider the effect of the type of driving signal on the quality of synthesized speech. Some standard phrases were read by six speakers (three men and three women) in modes 1–3. The speech quality was evaluated by ten-point scores by the method of paired comparisons with the participation of six to ten listeners. A record of natural speech in the frequency band 300–3400 Hz was used as the reference. The results are shown in Table 5.

One can see that the general quality of synthesized speech largely depends on the type of the driving signal. The minimal percentage of errors was obtained with the synthesizer driven by FT pulses.

In addition to the general evaluation of the synthesized speech quality, the speaker identification feature and the intonation perception were also evaluated.

The experiment on the speaker identification was performed as follows. Six standard phrases read by four male speakers at random were recorded. At the end of each phrase, the speaker announced his personal number. The listeners were initially not acquainted with the speakers' voices. Before the test, all speakers in turn read twice a single phrase to make their voices known to the listeners. After listening to the whole recording, each listener gave 24 answers. As could be expected, the highest identification index was obtained with mode 1, although with modes 2 and 3, the identification scores were also high.

To estimate the effect of the type of driving signal on intonation perception, the following method was used. In modes 1–3, a standard phrase read by one speaker with three different intonations was recorded: interrogative, narrative, and affirmative. The listeners were asked to determine the kind of intonation they perceived. The test team consisted of eight speakers (five men and three women) and ten listeners. The results of the test are presented in Table 5. One can see that, in mode 1, the intonation was transmitted properly, whereas in modes 2 and 3, it suffered severe distortions. It should be also noted that, in the case of the noise-type excitation, the number of errors for female voices was relatively small (7%) while for male voices it reached 40%. Presumably, this result can be explained by the higher fundamental frequencies of female voices, for which the resolution of the synthesizer in frequency was sufficiently good.

The data presented above testify to the validity of the statement that the perceptive parameters determining the phonetic quality of speech, namely, the timbre, loudness, and pitch, correlate not with individual acoustic parameters of speech separately but with their entire set: spectrum, intensity, fundamental frequency, and durations of stressed and unstressed syllables. The voicing feature is represented in speech not only by the fundamental harmonics but also by a higher intensity of voiced segments and a more distinct formant structure, as compared to unvoiced segments: the softness feature is represented in the *i*-type track of the second formant F2 on the adjacent vowel, the frequency F2 about 1.8–2.6 kHz, and the reduced intensity of components in the frequency band 1.2–1.8 kHz. From the aforesaid, we can conclude that the sensitivity of DRT tables to distortions of individual features of the speech signal is fairly weak.

THE SUPPLEMENTARY NOTE METHOD

The GOST R 50840-95 standard includes all diagnostic tables of supplementary notes, in which the listeners have to add the initial/terminal consonants to incomplete _VC/CV_ syllables [3]. The tables used by the speakers are standard syllable tables. Examples of the speaker's and listener's tables (fragments) are presented below.

Speaker's table:

СЯК	КУЛЬ	СЮЩ	НЯТ	СВУМ
КОСЬ	ПИШ	СТАЛ	МУРЬ	ХАК

Listener's table:

_ЯК_АК	_ЮЛЬ_УЛЬ	_ЮЩ_УЩ	_ЯТ_АТ	_ВУМ
_ЕСЬ_ОСЬ	ПИ_	_ТАЛ	_ЮРЬ_УРЬ	ХА_

In the listener's tables, the syllables lack the initial/terminal consonants (hard or soft). In the course of measurements, the listener fills the gaps with the sounds perceived by hearing. Table 6 shows the relation between the syllable intelligibility *S* and the consonant discrimination by the supplementary note method *Q*.

The supplementary note method was subjected to long-term experimental testing in a number of institutions and was included in the GOST R 50840-95 standard as a method for the diagnostic evaluation of speech signal distortions in speech communication channels.

Compared to the standard technique used for syllable intelligibility measurements, the supplementary note method considerably reduces the requirements imposed on the training of the articulation team. Special measurements had been carried out to estimate the progress in training an inexperienced team of three listeners in the course of the perception of tables of syllables of synthesized speech by the GOST R standard and by the supplementary note method. The tests were performed within three days with a daily perception of 20 tables recorded through a channel of synthesized speech (an LPC vocoder with a transmission rate of 4.8 kbit/s) with the voice of a single male speaker. It was found that the coefficient of the experimental practice of the team *Z* (*Z* = Ai/At, where Ai is the experimental value of the formant intelligibility for an inexperienced team and At is the same for a well trained team) slowly increased (up to 0.5) during three days in the case of the perception of syllable tables, while in the case of the perception of tables of supplementary notes, it exceeded 0.78 by the second day of training. In practice, within approximately a week of everyday work, an inexperienced team can reach the necessary value of *Z* (above 0.9). If the test tables are each time formed anew by an automated method (as is prescribed by the GOST R 50840-95 standard), the possibility of memorizing the tables of supplementary notes is excluded.

A listener is supplied with a personal computer equipped with a sound board and a KPEC software package for an IBM PC. All testing and data processing procedures are automated. The monitor screen shows the tables of incomplete syllables, the gaps in which should be filled through the keyboard. The rate of syllable presentation is 3 s per syllable and the input rate is 20 symbols per minute, which does not require any special training of the operators. As a result of the data processing, the following values are calculated: the discriminability of each individual phoneme, the group intelligibility of correlative phoneme series, and the speech intelligibility for some preset statistics of sound occurrence in vocalized speech. In the tables of supplementary notes, the probability of phoneme occurrence can differ from that in real speech, which provides a fairly high reliability of the estimate of sound intelligibility (discrimination) for speech sounds of both frequent (e.g., /т, п/) and rare occurrence (e.g., /ФЬ/ and /ХЬ/). Thus, the long-term discussion concerning the allowable deviation of the sound content in articulation tables from that in real speech, the choice of a representative set of texts for evaluating this content, and the methods suitable for the phonetic transcription of texts and for statistical data processing ceases being topical. The result of the measurements is the estimate of the probability of errors in the perception of individual sounds q_i, while the sound content of speech is taken into account (e.g., for local or professional conditions) by the weighted average sound intelligibility $D_j = 1 - Q_j$, where $Q_j = \Sigma p_{ij} q_i$ is the sound intelligibility loss, p_{ij}

Table 6

S	35	40	45	50	55	60	65	70
Q	61	65	69	73	77	80	83	86
S	75	80	85	87.5	90	92.5	95	97.5
Q	89	92	95	96	97	98	99	99.5

is the probability of the *i*th sound occurrence in the table according to the *j*th statistics (e.g., for public telephone communication networks, military communication lines, etc.), and q_i is the error probability in the perception. The syllable intelligibility determined according to the *j*th statistics of sound occurrence in speech is

$$S = 0.8D_j^3 + 0.2D_j^4.$$

The method of supplementary notes is free of the drawback inherent in the DRT diagnostic tables, that is, their relation to the Jacobson model of differential features and their consequent low sensitivity to speech signal distortions.

Consider an example of studying the matrices of auditory errors (mishearings) obtained from the intelligibility measurements for speech sounds [11]. The intelligibility was measured with a team of four speakers (two men and two women) and four listeners. The measurements provided full error matrices of 36 consonants for four types of speech signals, including natural speech (with a signal-to-noise ratio of 10 dB) and two models of speech analysis–synthesis (an LPC vocoder with a transmission rate of 2.4 kbit/s and a semivocoder with a transmission rate of 9.6 kbit/s). The total volume of measurements was about 100 000 sounds, which provided statistically stable results (presumably, for the first time for the Russian language).[1]

The error matrices were processed by an IBM PC/AT with the use of multidimensional statistical analysis of data. By the method of statistical regression analysis of auditory error (mishearing) matrices, the following ranks and weights (in arbitrary units) of the group features of phonemes (in decreasing order) were determined: hard/soft, 5; voiced/unvoiced, 3; sonorous/fricative, 2; and occlusive/glottal, 1.

The group features, unlike the differential ones, have rather stable acoustic characteristics independent of the manner of enunciation and positional and combinatorial changes in phonemes. On the other hand, the sound production sites during the excursion and recursion phases are not constant, and their acoustic correlates in the holding phase are not always detectable because of the reduction and assimilation.

The distribution of auditory errors (mishearings) depends on the probability of occurrence of consonants (sound types) in Russian speech: the more frequent the sound type, the better its discrimination. The difference between the natural and synthesized speech manifests itself primarily in an increased regression coefficient and an increased multiple correlation for natural speech. One can expect that, in conditions when the perception of synthesized speech by the distinctive features of sound types is more difficult than that of natural speech, listeners more or less rely on the probability of the sound occurrence.

Perceptual errors (mishearings) possess the property of retaining their association with the group distinctive features of the corresponding sounds. In our experiment, the total amount of errors in the discrimination of hard consonants of natural speech was 8%. Among these errors, 7% retained their association with the group of hard consonants and only 1% were classed with the soft consonants. The total number of mishearings for soft consonants was also equal to 8%, and 6% of them retained the association with the soft type while 2% were classed with the hard type. Thus, 75–88% of mishearings remained within the corresponding hard/soft group.

Similar statistics were observed for other features: the voiced/unvoiced feature was perceived with a total error percentage of 5–12%, and 75–80% of these mishearings remained within the respective groups. For sonorous consonants, the total amount of errors was 4%, and 80% of them remained with their group. For the glottal consonants, the corresponding numbers were 4 and 70%, and for the occlusive consonants, they were 13 and 75%. It should be noted that, of all the mishearings for the sonorous consonants, 2/3 were classed with occlusive and 1/3 with glottal consonants. The sounds that lost their glottal and occlusive features were perceived as sonorous and occlusive in the first case and sonorous and glottal in the second case.

In the case of synthesized speech, the group distinctive features of sound types proved to be less stable, as compared to natural speech. When the number of errors in the discrimination of consonants of all groups increased by a factor of about 2–2.5, the relative number of mishearings, in which the group distinctive features of sounds were lost, increased as follows: for sonorous consonants, up to 50% (instead of 20% for natural speech), with 15% of them being classed with the occlusive group and 35% with the glottal one; for occlusive consonants, 70% (instead of 30% for natural speech) with 18% of them being classed with the sonorous group and 2% with the glottal one; and for glottal consonants, 48% (instead of 25% for natural speech) with 16% of them being classed with the sonorous group and 32% with the occlusive one. For the hard/soft and voiced/unvoiced distinctive features, the proportions of the mishearings that retained the initial group (or changed it) were almost the same in natural and synthesized speech. Proceeding from the aforesaid, the following explanation can be proposed for the certain discrepancy between the intelligibility indices obtained for synthesized speech and the user's estimate of the intelligibility of phrases: the latter is determined not only by the average discriminability of consonants (in our example, by the hard/soft feature, 82–84%; voiced/unvoiced, 78–88%; sonorous, 89%; occlusive,

---

[1] Note that one of the first studies of auditory error matrices was performed by Miller and Nicely (in 1955) and Singh (in 1968) [12]. In the first study, the authors used 200 open syllables of the CV type, which included 16 consonants and the vowel /a/ of the English language. The second study was performed with minimal pairs of monosyllabic words. However, the limited amount of data allowed no representative statistical analysis at that time.

85%; and glottal, 77%), but also by the stability in retaining particular distinctive features of the sound types in distorted speech.

REFERENCES

1. N. B. Pokrovskiĭ, *Calculation and Measurement of Speech Intelligibility* (Svyaz'izdat, Moscow, 1962).
2. V. G. Mikhaĭlov and L. V. Zlatoustova, *Measurement of Speech Parameters* (Radio i Svyaz', Moscow, 1987).
3. V. G. Mikhaĭlov, in *Proceedings of International Workshop "Specom-99"* (Moscow, 1999), p. 149.
4. W. D. Voiers, in *Proceedings of 1977 IEEE ICASSP* (1977), p. 204.
5. G. V. Vemyan, *Speech Transmission through Electrocommunication Networks* (Radio i Svyaz', Moscow, 1985).
6. *GOST* (State Standard) *R 50840-95: Speech Transmission through Communication Channels. Methods of Estimating the Quality, Intelligibility, and Identifiability.*
7. *Speech Tests and Their Application*, Ed. by L. V. Zlatoustova (Mosk. Gos. Univ., Moscow, 1986).
8. R. K. Potapova, *Speech: Communication, Information, Cybernetics* (Radio i Svyaz', Moscow, 1997).
9. L. R. Zinder, *General Phonetics* (Vysshaya Shkola, Moscow, 1979).
10. L. G. Zubkova, *Phonetic Realization of Consonant Contrasting in the Russian Language* (Univ. Druzhby Narodov, Moscow, 1974).
11. V. G. Mikhaĭlov, Akust. Zh. **39**, 879 (1993) [Acoust. Phys. **39**, 464 (1993)].
12. G. Miller and P. Nicely, J. Acoust. Soc. Am. **27**, 338 (1955); S. Singh, IRAL, No. 6, 37 (1968).

Translated by E. Golyamina

Acoustical Physics, Vol. 48, No. 5, 2002, pp. 634–635. Translated from Akusticheskiĭ Zhurnal, Vol. 48, No. 5, 2002, pp. 713–714.
Original Russian Text Copyright © 2002 by the Editorial Board.

CHRONICLE

Sergey Viktorovich Egerev (On His 50th Birthday)

July 22, 2002, marks the 50th birthday of Sergey Viktorovich Egerev, one of the leading researchers of the Andreev Acoustics Institute, a well-known expert in the field of laser photoacoustics.

In 1974, Egerev graduated with honors from the Moscow Institute of Electronic Engineering (now Moscow Institute of Electronics and Mathematics) having specialized in a new field of science, namely, the physics of the interaction of laser radiation with matter. Just such an expert was needed by one of the laboratories of the Acoustics Institute, where research at the interface of optics and acoustics was developing under the supervision of professors L.M. Lyamshev and K.A. Naugol’nykh. A new field of science emerged: the laser photoacoustics of liquid media.

Mechanical and hydrodynamic effects in liquids affected by laser radiation were studied actively from the beginning of the 1960s. The light-hydraulic effect and laser generation of plasma in gases and metal targets were already observed at that time. However, the problems of communication, technology, and medical diagnostics required full knowledge of the acoustic fields formed in liquids in the process of their irradiation by a laser beam. There were many questions, and the field of research seemed vast. Correspondingly, the interest in the problem throughout the scientific community of the country was very large. It is enough to say that such outstanding Soviet scholars as R.V. Khokhlov, S.A. Akhmanov, and F.V. Bunkin headed the research in photoacoustics in other research centers. Such an effectively cooperating community of scientists from different institutions would today be called an invisible college.

Egerev started to work actively together with other young researchers from Moscow State University and the Physical Institute of the USSR Academy of Sciences (later the research was conducted at the General Physics Institute of the USSR Academy of Sciences). His contribution to the common achievements of the Soviet school of photoacoustics was considerable. The effect of thermal nonlinearity studied by him theoretically was an outstanding result. This effect manifests itself in the process of the irradiation of liquids at a temperature close to the point of the maximal density. Later, the predicted distinctive features of the effect were confirmed not only in photoacoustic experiments but also in experiments conducted with accelerators of elementary particles, which was an important event in radiation acoustics.

Experimental and theoretical studies conducted by Egerev provided an opportunity to understand what the effects of photoacoustic conversion in two-phase liquids and also in liquids subjected to intense laser irradiation are. These results were appreciated by the research community both in this country and abroad. In 1981, Egerev got the degree of Candidate of Science (Phys.–Math.), and in 1984 he received the Lenin’s Komsomol Prize for achievements in science and technology together with other researchers.

In the 1980s, Egerev several times headed the research expeditions of the Acoustics Institute exploring the photoacoustic diagnostics of shallow-water marine regions. It was discovered that powerful acoustic pulses generated remotely by laser radiation at the sea surface are an excellent instrument for the detailed monitoring of marine media parameters, namely, wind waves, bottom character, etc. The Acoustics Institute pioneered the study of this field, and researchers from other countries started such investigations 5–6 years later. The results of Egerev's studies in the field of photoacoustic oceanography were generalized in a series of papers and an international scientific treatise. Now, since the need for the development of new techniques for navigation and oceanography has risen, in particular, in connection with the construction of ports in the Baltic Sea, these results have become especially important.

The development of the fundamental concept of the combined mechanism of photoacoustic conversion by Egerev belongs to the same period. This concept assumes that contributions of different origin to the acoustic response of an irradiated liquid exist simultaneously. It played an important role in both the development of theoretical ideas and practical applications, that is, for the development of new techniques for the diagnostics and monitoring of liquid media for biomedical applications.

Now, Egerev has concentrated his research interests mostly in the field of the photoacoustics of scattering liquid media. Together with his students and collaborators, he has developed a technique for the low-threshold cavitation photoacoustic diagnostics of suspensions with superlow concentrations. The effect of the emission of a sound pulse by a cavitation bubble that develops at a particle heated by a laser pulse is used in this technique. In this case, the intensity of laser radiation is significantly smaller than that needed for the development of a laser spark (breakdown).

In 1994, Egerev got the degree of Doctor of Science (Phys.–Math.). In 1995–1997, he worked for the administration of the President of the Russian Federation as a consultant on the scientific and technological policy of the country. The outcome of this work was his book entitled *Sensitive Points of Science* (1998).

Egerev gives much time to teaching at Moscow State Pedagogical University. Several of his postgraduate students have become Candidates of Science. Egerev got the title of professor in 2000. Now, Egerev is the first deputy director of research at the Andreev Acoustics Institute.

Egerev is the author of more than one hundred papers in leading Russian and foreign scientific journals. He is a member of the Russian Acoustical Society and the Acoustical Society of America. He is also a member of the Bureau of the Scientific Council on Acoustics of the Russian Academy of Sciences and takes an active part in international scientific meetings on acoustics.

At fifty, Sergey Viktorovich Egerev is full of various creative plans. We wish him good health and many new achievements.

Translated by M. Lyamshev

Acoustical Physics, Vol. 48, No. 5, 2002, pp. 636–637. Translated from Akusticheskiĭ Zhurnal, Vol. 48, No. 5, 2002, pp. 715–716.
Original Russian Text Copyright © 2002 by the Editorial Board.

CHRONICLE

Viktor Dar'evich Svet (On His 60th Birthday)

May 17, 2002, marked the 60th birthday of Viktor Dar'evich Svet, doctor of science (Phys.–Math.), head of a laboratory at the Andreev Acoustics Institute, and a well-known specialist in applied acoustics.

In 1963, Svet first appeared at the Acoustics Institute as a student to work on his undergraduate project. In 1964, he graduated from the Department of Radio Systems of Moscow Electrotechnical Institute of Communication and was offered a permanent position at the Acoustics Institute. There, Svet has been working for more than 38 years on problems related to the reception and processing of acoustic signals.

His first research projects were concerned with studying nonlinear correlations in acoustic signals and noise generated by high-power mechanisms with rotary units. The theory of the methods of nonlinear correlation analysis, which had been developed at that time, not only explained and predicted the appearance of combination components in the noise spectrum, but also allowed one to determine the sources of the signals producing these components. On the basis of this theory, new efficient methods for the acoustic remote sensing of aircraft engines and turbines were developed. The results of theoretical and experimental studies on the methods of nonlinear correlation analysis were summarized by Svet in his candidate's thesis, which he defended in 1971.

The following research projects carried out by Svet were concerned with the development and application of the ideas and methods of coherent optics and holography for space–time signal processing in underwater acoustic observation systems. Svet was among the first to use these methods for signal processing in multielement antenna arrays and also for the development of acoustooptic sound detectors. One of the merits of Svet's approach to his work is that he always tries to put scientific concepts and ideas into practice. For example, such devices as the first Russian high-speed optical processor intended for signal processing in planar arrays, liquid-crystal acoustooptic hydrophones with optic-fiber communication lines, and acoustooptic antennas were developed and tested under his supervision.

Several tens of research projects and several large research-and-development projects have been supervised by Svet, for which he has received state awards.

Svet is also known for his organizational work. He has supervised twelve expeditions to various regions of the ocean, which were carried out on the ships of both the Acoustics Institute and the Navy.

Svet is the author of more than 130 papers and two monographs, and he owns 20 inventor's certificates and patents. Four candidate's theses have been prepared under his supervision.

For years, Svet has been a member of the Scientific Council of the Acoustics Institute. He is a member of the Russian Acoustical Society and a member of the New York Academy of Sciences.

His erudition, benevolence, and unprejudiced view on various complex problems have won him the respect of the scientists of the Acoustics Institute and other related institutions.

In the last few years (in view of the difficulties that have prevented the organization of full-scale oceanic experiments), Svet has concentrated on the development of new methods for obtaining ultrasonic images of dynamic objects located in inhomogeneous media with scattering. This new area of research, which is related to acoustic speckle interferometry, is interesting and promising from the point of view of many possible applications, such as medical diagnostics, flaw detection, and underwater acoustic imaging.

Svet celebrates his 60th birthday in the prime of his creative life. He is as full of energy and creative ideas as ever.

We wish Viktor Dar’evich Svet good health and success in all his undertakings.

Translated by E. Golyamina

Acoustical Physics, Vol. 48, No. 5, 2002, pp. 638–639. Translated from Akusticheskiĭ Zhurnal, Vol. 48, No. 5, 2002, pp. 717–718.
Original Russian Text Copyright © 2002 by the Editorial Board.

CHRONICLE

In Memory of Viktor Ivanovich Passechnik (July 28, 1943–March 17, 2002)

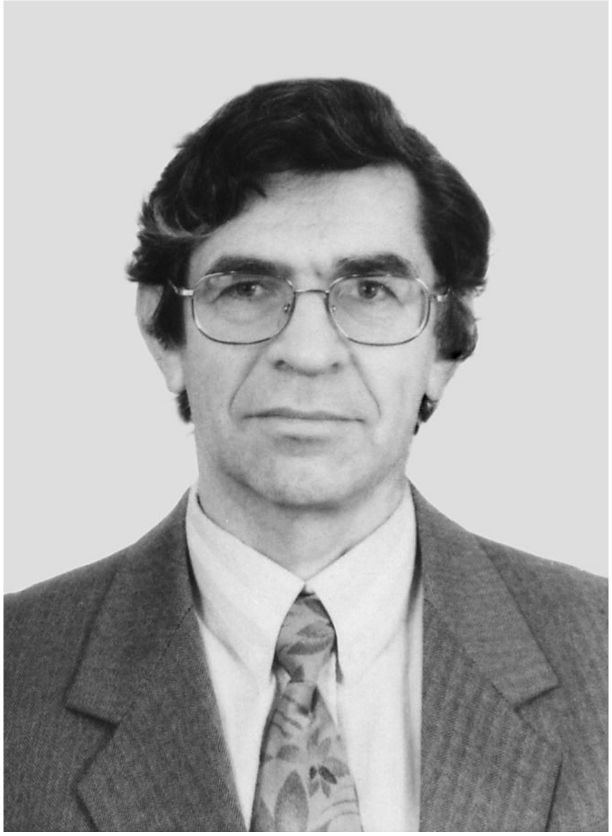

On March 17, 2002, Viktor Ivanovich Passechnik, professor of the Physics Department of Sechenov Medical Academy, head of the Acoustothermography Laboratory of the Institute of Radio Engineering and Electronics of Russian Academy of Sciences, a prominent scientist, an excellent teacher, and a wonderful person, passed away.

Passechnik was born on August 28, 1943, in Ufa. The first half of his career in science was associated with the Physics Faculty of Moscow State University. After his graduation in 1966, Passechnik continued working at the biophysics department of this university. He carried out a number of theoretical and experimental studies of the dynamics of viscoelastic properties of muscles and biological membrane models. The results of these studies have formed the basis of Passechnik's candidate and doctoral theses, which he successfully defended in 1969 and 1983, respectively. The studies of the viscoelastic properties of biological membranes proved to be most fruitful and made him one of the leading specialists in this field of research. In particular, together with Professor T. Hianik from Bratislava University, Passechnik published two monographs devoted to this subject, which appeared in Czechoslovakia and in England in 1991 and 1995.

The second half of Passechnik's career in science was of special interest from the point of view of acoustics and was associated with his work at the Institute of Radio Engineering and Electronics, Russian Academy of Sciences. From 1983, Passechnik, together with Academician Yu.V. Gulyaev and Dr. Sci. (Phys.–Math.) É.É Godik, carried out theoretical and experimental studies aimed at the development of acoustothermography methods for medical diagnostics. In this connection, it should be noted that a human organism generates not only weak thermal radio-wave radiation but also thermal acoustic radiation, which carries the information on the spatial temperature distribution and the functional dynamics of heat generation in the organism, especially in the ultrasonic frequency range (the megahertz frequencies with wavelengths of about 1 mm). The ultrasonic waves of thermal acoustic noise of the organism tissues travel toward the surface from a depth of 5–10 cm and, in real time, carry the information on the functioning of, for example, such an important organ as the liver. One of the topical directions of research in modern acoustics is the use of proper thermal acoustic radiation for monitoring the temperature distribution in the depth of a human body during hyperthermia procedures in oncology or during thermal ablation (a microwave heating of tissue by a needle). The methods developed under Passechnik's supervision for solving the inverse problem in passive acoustic thermotomography laid the foundation for the design of a passive acoustic tomograph.

Passechnik has left a vast scientific heritage: about 300 scientific publications, 150 of which are papers in Russian and foreign reviewed journals. As a professor of Sechenov Medical Academy, Passechnik supervised the work of young scientists, three of whom prepared and defended candidate's theses and one, a doctoral thesis. In the recent years, Passechnik published two textbooks: *Biophysics* (Moscow, 2000) and *Laboratory Studies in Biophysics* (Moscow, 2001).

The works by Passechnik received wide recognition both in Russia and abroad. Beginning from 1972

1063-7710/02/4805-0638$22.00 © 2002 MAIK “Nauka/Interperiodica”

(when he first presented a report on the viscoelastic properties of biological membrane models), Passechnik took part in International Congresses on Biophysics. In the 1990s, he received the support for his COPERNICUS and INTAS projects related to this area of research. The acoustothermography problems were the subject of his cooperative work with the National Institute of Health (Bethesda, USA) and the National Oncology Institute (Rockville, USA). Passechnik's projects concerned with acoustothermography were supported by the Russian Foundation for Basic Research.

In 1999, in relation to the 275th birthday of the Russian Academy of Sciences, Passechnik received a certificate of gratitude for his long and fruitful work in science from the Russian Academy of Sciences, which was signed by President of the Academy Yu.S. Osipov.

The colleagues of Viktor Ivanovich Passechnik deeply mourn the premature death of their friend, a person of ready sympathy and modesty, whose shining memory will last for many years to come.

Translated by E. Golyamina

Acoustical Physics, Vol. 48, No. 5, 2002, pp. 640–641. Translated from Akusticheskiĭ Zhurnal, Vol. 48, No. 5, 2002, pp. 719–720.
Original Russian Text Copyright © 2002 by Svet.

BOOK REVIEW

V. A. Zverev and A. A. Stromkov: *Signal Extraction from Interference by Numerical Methods*

(V. A. Zverev and A. A. Stromkov, *Vydelenie signalov iz pomekh chislennymi metodami,* Institut prikladnoĭ fiziki RAN, Nizhni Novgorod, 2001)

Having read the title of this book, an expert in signal detection will surely think “Here is another book on statistical signal detection methods, plenty of which have already been published.” However, this expert will be greatly mistaken.

Firstly, the book does not even mention any of the standard probabilistic approaches to solving such problems. Secondly, it considers a completely different physical situation when a great number of applications are characterized by a fairly high input signal-to-noise ratio, and the main interference is represented by random phase modulation of the signal rather than by an independent additive noise. In some cases, this phase modulation is nothing but a strong interference, while, in other cases, it can be a source of useful information.

Thirdly, the book is written by a physicist and renowned expert in the field of wave processes. Therefore, it primarily focuses on the physical mechanisms of the phenomena and completely lacks the statistical formalism commonly used in detection problems. The author follows the excellent traditions of L.I. Mandel’shtam’s scientific school by illustrating complex phenomena and methods in the physics of oscillatory processes by similar well-understood phenomena from different fields of science.

What makes the book interesting?

Primarily, the novelty of the research area and the contents. The book is devoted to problems in which useful information or interference is contained in the random phase modulation of the signal; i.e., it considers multiplicative signal models.

Methodologically, the monograph is also original. It aptly combines the statement and description of rather complex physical problems with practical solution tools elaborated into particular application programs. These programs are provided in each chapter and, moreover, many of the theoretical examples are illustrated and corroborated by experimental data, which makes these programs more valuable.

The next feature of the book is that it applies correlation-, spectral-, and nonlinear-analysis methods to describing complex wave propagation phenomena observed in inhomogeneous scattering media: forward scattering location, multipath propagation, phase distortions, reverberation, etc. Approaches to signal extraction in these media that are proposed in the book are novel and were previously published only in journal papers.

The presence of original scientific information and its presentation as a tutorial make the book particularly attractive.

The monograph consists of five chapters.

Chapter 1, “Spectrum and Cepstrum,” primarily focuses on numerical methods of correlation, spectral, and cepstral analysis and, especially, on the so-called complex-cepstrum method, which is insufficiently covered in the literature. This nonlinear transformation is, however, a very powerful tool for extracting weak multiplicative signals. An easy-to-understand description of the procedure (and program) that calculates the argument of a function far beyond the 2π interval without phase jumps is provided.

The chapter ends by discussing the numerical methods for the representation of random signals. Each section of the chapter is illustrated by a ready-to-use program written in the Mathcad 6.0 Plus software package. Having spent a certain amount of time learning this package, any Windows user can thus oneself check the numerical results presented and create an application program.

Chapter 2 is devoted to physical principles of the forward scattering location.

The problem is actually reduced to the extraction of a very weak signal scattered from an inhomogeneity of the channel in the presence of an intense direct signal. This problem differs from the classical problem of detecting a weak signal in the presence of noise primarily in that both the weak scattered useful signal and the intense direct signal are produced by the same source. Such known methods for suppressing strong signals as adaptive processing and placing nulls in the directivity pattern are therefore ineffective in this case. The authors analyze the potentialities of the dark-field method (a direct analogy with optics) at, however, much smaller wave dimensions of the receiving aperture than in optics.

The main algorithm for extracting a weak signal relies on nonlinear transformations and primarily uses the phase information contained in the received field. An extremely representative experiment described at the end of Chapter 2 clearly illustrates the potentialities of the method.

Chapter 3, which considers the possibilities of increasing the space or time resolution that are far from trivial, is very interesting. In particular, it shows that the dark-field method can be effective enough if the field is measured over a large receiving aperture. However, as one of the authors previously wrote: "In spite of the entirely positive and proven result of applying the dark-field method in optics, no one has tried to create a cyclopean acoustic antenna whose wave dimensions were similar to those of the optical antenna."

The authors draw the reader's attention to the fact that, if a weakly scattering object moves, the antenna resolution can be increased through the synthesis of the receiving antenna aperture, the aperture synthesis method proposed in the book being essentially different from the receiving-antenna aperture synthesis due to the antenna motion applied in side-scan radar.

Chapter 4, "Phase Noise and Reverberation," details nonlinear filtering methods based on cepstral analysis that are capable of effectively separating multiplicatively related signals. If, after taking a logarithm of the received signal, the spectra of the logarithms of the summands do not overlap, the multiplicatively related signals can be effectively separated. Certainly, this is a known fact, and a similar approach has been used previously in the time-domain processing of signals with a random phase or with an amplitude modulation. However, the effective use of the same approach for spatial signal processing seems, at first sight, paradoxical, because the authors' assertion is actually as follows. Let a plane wave signal be received with a moving flexible linear antenna. As the antenna moves, its shape unpredictably changes, so that the signal phase distortions many times greater than 2π occur in each antenna receiver. The authors do not want to accurately measure these distortions and compensate for them; they, however, assert that, under certain conditions and with an appropriate signal processing, such an irregular antenna will operate as good as a straight one. If we recall that, in good antennas, phase distortions even on the order of $\lambda/32$ are regarded inadmissible and designers try to eliminate them, the above assertion really seems paradoxical at first sight.

Nevertheless, using the nonlinear analysis methods described in the foregoing chapters, the authors clearly demonstrate the possibility of phasing such strongly curved antennas. Of course, everything has its price, and the price is, in particular, a restricted angular coverage, if there are several signal sources. It should be noted that the method proposed by the authors has very interesting potentialities for use not only in antennas. It offers a completely new approach to improving resolution of distorted apertures and to tracing the trajectory of a sound source moving in a medium whose parameters cannot be measured or predicted.

Chapter 5, "Analysis of Acoustic Paths Using Maximal-Length Sequences," actually illustrates all signal extraction methods considered in the book by examples of particular oceanic propagation tracks: stationary (such as ATOC), nonstationary, and seismic ones and tracks between two ships. The final section of the chapter concentrates on the cepstral method for measuring the fluctuations in the multipath signal delays.

On the whole, the book is an original work that describes new nontrivial methods for solving complex problems of acoustic wave propagation in inhomogeneous media and modern practical numerical techniques serving for these purposes.

The book clearly presents the new methods from the point of view of physics, widely resorts to various analogies, uses simple and easily understood mathematical tools, and illustrates the material with numerous specific practical programming examples. All this makes the book interesting for experts and post- and undergraduate students specializing in physics, as well as for engineers, whatever their discipline, with a background in Fourier analysis.

It is however a pity that the size of the edition is so small (300 copies), which has already made it a rarity.

V. D. Svet

Translated by A. Khzmalyan